Characterization, Orientation, and Deformation Behavior of the Double Gyroid Phase in Elastomeric Triblock Copolymers

by
Benita Jean Dair

B.S., Materials Science and Engineering, 1994
Cornell University, Ithaca, NY

Submitted to
the Department of Materials Science and Engineering and
the Program in Polymer Science and Technology
in Partial Fulfilment of the Requirements for the Degree of

Doctor of Philosophy in Polymers

at the

Massachusetts Institute of Technology

February 1999

Author .....
Materials Science and Engineering
January 8, 1999

Certified by .....
Edwin L. Thomas
Morris Cohen Professor of Materials Science and Engineering
Thesis Advisor

Accepted by .....
Linn W. Hobbs
John F. Elliott Professor of Materials
Chairman, Departmental Committee on Graduate Students

Characterization, Orientation, and Deformation Behavior of the Double Gyroid Phase in Elastomeric Triblock Copolymers

by

Benita Jean Dair

Submitted to the Department of Materials Science and Engineering and
the Program in Polymer Science and Technology
on January 8, 1999 in Partial Fulfilment of the Requirements for the Degree of
Doctor of Philosophy in Polymers

ABSTRACT

An oriented polystyrene-polyisoprene-polystyrene (SIS) double gyroid (DG) nanocomposite comprised of two separate interpenetrating glassy networks embedded in a rubbery matrix is studied as a function of applied strain to elucidate the anisotropic deformation microstructure and mechanisms. The morphologies of 34%-36% S SIS triblock copolymer thermoplastic elastomers were characterized to have double gyroid (DG) morphology by a combination of transmission electron microscopy (TEM), small-angle x-ray scattering (SAXS), simulations of level set surfaces using TEMsim, laser diffraction, and fast Fourier transforms (FFT). The polymers were then processed via roll casting, which produced oriented cylinder (34%S) and lamellar (36%S) films. Annealing treatment enabled nucleation and growth of the equilibrium oriented DG phase in the 34%S. The <111> DG directions nucleated from the cylinder axes, and twinned {110}-type DG planes nucleated in the plane of the film.

Mechanical properties and deformation microstructures were investigated via synchrotron SAXS and simultaneous load-deformation measurements, as well as TEM of microtomed sections from stretched DG fixed by high energy electron crosslinking. In the flow [111] direction, along the tightly wound continuous PS 3-fold screw helices, the modulus is 5 times larger than in the transverse direction, there is yielding with a distinct neck, 50% higher mechanical hysteresis, and immediate residual strain of 100%. SAXS and TEM indicate that yielding and necking occur via plastic deformation of the PS domains, which then elongate and draw upon further stretching. At the highest strains, some pullout of PS endblocks is seen. In the transverse direction, samples do not neck, but rather undergo distributed yielding, indicative of defects and many grains in this direction. SAXS and TEM show that strain in this direction is accomodated by rotation of grains into the stretch direction followed by buckling of the [111] PS helices. The remarkable anisotropy of the mechanical properties is due to the high PS connectivity in the flow direction, and no continuous PS domains in the transverse. These materials were also found to have both microscopic and macroscopic memory and recover fully upon annealing above the glass transition temperature of PS.

Thesis Supervisor: Edwin L. Thomas
Title: Morris Cohen Professor of Materials Science and Engineering

Acknowledgments

I would like to thank my commitee, Prof. Edwin Thomas, Prof. Bernhardt Wuensch, and Prof. Mary Boyce, for providing me opportunities and guidance throughout my graduate school years, being encouraging, supportive and helpful, and taking interest in my professional and academic development. I am also grateful to Prof. Edward Kramer, previously at Cornell University, now at UC Santa Barbara, for encouragement, support, and advice during my formative undergraduate years at Cornell, and continuing throughout my graduate schooling. I am very thankful to Christian Honeker, who became my friend, teacher, and adviser ever from the start of tenure in the group.

The research would not have been possible without the help of the following people:

- Prof. Nikos Hadjichristidis and Apostolos Avgeropoulos from the University of Athens, Greece, for synthesizing the two SIS polymers with double gyroid composition, on which this thesis is based.
- Brian Walther, previously at DEXCO, now at to DOW, for synthesizing the commercial analogs to the prototype triblocks at DEXCO.
- Malcolm Capel at NSLS beamline X12B, and Kenneth Wright at the MIT High Voltage Laboratory for their expertise and assistance at the respective facilities.
- Prof. Lorna Gibson and Prof. Ali Argon for their generous time and scientific insight.
- Carl Zimba (NIST) and Stephane Joly for assistance at BNL, Ariel Eisen for assistance with spectra and birefringence measurements, AnneValerie Ruzzette and Rob Lammertink for assistance in rheology and ODT measurements, Jorgen Bergstrom for his assistance with finite element modelling
- Ramon Albalak for the design of the rollcaster, Christian Honeker and Carl Zimba for the design and modification of the stretcher and Jim Hoffman for providing TEMsim,
- Mme. Sylvia Deplanque at the Librarie de Laboratoire de Minéralogie-Cristallographie, Université Pierre-et-Marie-Curie, Paris, France, for sending crystallography references, from which the introductory chapter on gyroid history developed.
- Lew Fetters (Exxon), Prof. Andrew Keller (University of Bristol), Prof. Yachin Cohen, Prof. Edward Merrill, Michael Shin, Hartmut Rudmann, Yot Boontongkong, Anuj Bellare, and Olivera Kesler for helpful scientific and experimental discussions.

I thank the National Science Foundation and the Society of Automative Engineers for my financial support, and the Air Force Office for Scientific Research and National Science Foundation for research funds.

Thanks to all my family and friends, especially Berkland Baptist Church, for generous love and support throughout.

Most of all, I thank God for His grace, love, mercy, and faithfulness for me to complete the thesis.

Table of Contents

Page Number

List of Figures

List of Tables

List of Symbols and Abbreviations

ABA	generic triblock copolymer with the two endblocks of the same component
ABC	generic triblock terpolymer with three different blocks
BCC	body centered cubic
BNL	Brookhaven National Laboratory
C_6H_6	benzene
CaH_2	sodium hydride
$CdCl_3$	cadmium chloride
$Cl_2Si(CH_3)_2$	dichlorodimethylsilane
CMC	constant mean curvature (surface)
CT	constant thickness (surface)
CYL	cylinders
d_{hkl}	interlayer spacing of the {hkl} planes
DD	double diamond
DG	double gyroid
DMA	dynamic mechanical analysis
DMTA	dynamic mechanical thermal analysis
dn/dc	refractive index increments
FFT	fast Fourier transform
G	gyroid, or sometimes double gyroid (an old notation)
G*	double gyroid (old notation)
GPC	gel permeation chromatography
H-NMR	nuclear magnetic resonance
HeNe	helium-neon (laser)
HPL	hexagonally perforated layers
$I4_132$	cubic space group #214, to which the single gyroid belongs
I(q)	intensity as a function of the scattering vector
$Ia\bar{3}d$	cubic space group #230, to which the double gyroid belongs
$Im\bar{3}m$	cubic space group, to which the spheres morphology belong
IMDS	intermaterial dividing surface
IPN	interpenetrating network
λ	wavelength of radiation (Chapter 4)
λ	extensional ratio (Chapter 7)
LALLS	low-angle laser photometer
LAM	lamellae
LC	lamellar catenoid
ML	modulated layers
M_n	number-average molecular weight
MO	mineral oil
mSImS	poly(alpha-methylstyrene) - polyisoprene - poly(alpha-methylstyrene) triblock copolymer
M_w	weight-average molecular weight
n-BuLi	n-butyl lithium
NSLS	National Syncrotron Light Source at Brookhaven National Laboratory
OBDD	ordered bicontinuous double diamond
OBS	ordered bicontinuous structure
OsO_4	osmium tetroxide
OT	optical transform

Π	osmotic pressure
p6mm	hexagonal plane group to which the cylinder morphology belongs
PB	poly(1,4-butadiene)
PDI	polydispersity index
PI	poly(1,4-isoprene)
PL	perforated layers
$Pn\bar{3}m$	cubic space group #224, to which the double diamond belongs
PS	poly(styrene)
PSNa	polystyrylsodium
$\mathbf{q}$	scattering vector
q_n	magnitude of the scattering vector of the nth peak
q_{hkl}	magnitude of the scattering vector of the {hkl} reflection
SAXS	small angle x-ray scattering
SBS	poly(styrene)-poly(1,4 butadiene)-(poly)styrene
SEC	size exclusion chromatography
SIS	poly(styrene)-poly(1,4 isoprene)-(poly)styrene
TEM	transmission electron microscopy
TEMsim	transmission electron microscopy simulation program
T_g	glass transition temperature
T_g^{PS}	glass transition temperature of polystyrene, 100°C
θ	half of the scattering angle
THF	tetrahydrofuran
TPE	thermoplastic elastomer
UV/SEC	ultraviolet size exclusion chromatography
vol %	volume per cent
wt %	weight per cent
w/v	weight per volume
X12B	beamline at the National Syncrotron Light Source at Brookhaven National Laboratory

Chapter 1: Thesis Overview and Organization

1.1 Opening Remarks

I was convinced of studying mechanical properties in graduate school. My reasons were not so clear other than I just liked it. As an undergraduate, I was enthralled with the classes which pertained to the molecular and morphological impacts on mechanical properties, and through this, I discovered Materials Science. Perhaps first as some psychological compensation for my youth, I developed a curiosity for breaking things, which was later fueled by my senior thesis project on understanding the fracture behavior of reinforced polymer interfaces from a molecular behavior point of view.

In my search for graduate advisors, I happened to visit Prof. Thomas after he had just finished a paper reporting the discovery of the novel double gyroid microphase in block copolymers. As his mind was fresh on the double gyroid and on the novel interconnected phases, he proposed that I study "the mechanical properties of the interconnected cubic phases". Although I did not have a real understanding of either the double gyroid or the double diamond morphologies or the types of mechanical tests that would be involved, I was drawn in by the *mechanical properties* opportunity.

In the 4+ years that I have spent on the project, I have been exposed to many subjects in addition to mechanical properties, such as electron microscopy, diffraction, scattering, mathematical surfaces, phase behavior, polymer physics, thermodynamics, and kinetics, to name a few. The initial challenges were not with the mechanical properties, but rather with finding an appropriate polymer system, and then with characterizing the oriented morphology. It was only after these issues were resolved could the mechanical and deformation behavior be interpreted in light of the morphology.

1.2 Overview

This thesis reports on the characterization and the mechanical properties of oriented or polygranular double gyroid morphologies in elastomeric block copolymer systems. In hindsight, the project can be separated into three main stages: morphological characterization of the novel phases, orientation, and mechanical properties. Materials systems were chosen to be compatible with existing industries, such that novel morphologies could provide options for improved or varied properties. Through collaborations with groups at the University of Athens, Greece and at DEXCO, a series of elastomeric triblock copolymers were obtained in composition windows appropriate for the novel morphologies. The morphologies of these polymers were then characterized, and two polymers were found to be double gyroid.

The double gyroid morphology has cubic $Ia\bar{3}d$ symmetry and hence the potential for anisotropic mechanical properties. The properties of isotropic or polycrystalline samples are superpositions of the responses of the structure to deformation along many different orientations, which complicate interpretation. By producing highly textured DG, mechanical properties along the different directions of the mechanically anisotropic DG phase could be investigated. Therefore, the polymers were oriented and textured via roll casting, a processing technique developed in the Thomas lab, in order permit sampling the anisotropic mechanical behavior. However, the oriented polymers were not obviously double gyroid and were subsequently characterized for their morphology.

Roll cast double gyroid samples were then deformed and observed via synchrotron small angle x-ray scattering and transmission electron microscopy. The high energies and high flux of synchrotron radiation allow for increased spatial and temporal resolution, respectively. The diffraction patterns could be taken in 30 seconds or less, allowing deformation to be monitored *in situ* as a function of strain. TEM complemented the diffraction information by providing a real space correspondence to the SAXS patterns. Samples stretched to different strains were first crosslinked to retain the stretched state, before preparing them for microscopy. The combination of SAXS and TEM information allowed models to be developed for deformation and evolution of structures up to large strains in the different directions.

1.3 Thesis Organization

Chapter 2 provides the motivation for the project, the background of block copolymer architectures and morphologies through polymer physics principles, and the justification of the chosen system. Chapter 3 gives the historical framework of gyroids, the origin of the term, and its use in the crystallography and in the mathematics community. The double gyroid is then described for insight into the geometry of this novel phase found in block copolymers. Chapter 4 details the experimental procedures used in the morphological characterization of polymers, in producing roll cast films, in mechanical testing, and in small-angle x-ray and transmission electron microscopy investigations into the deformation behavior.

Chapter 5 describes the collaborations that ensued on finding an appropriate polymer system. It discusses the characterization of the novel phases through electron microscopy, small-angle scattering, and theoretical simulations based on mathematical models of the surfaces between the two microphases. Chapter 6 discusses the morphology and indexing of the scattering patterns from roll-cast polymers that would otherwise be double gyroid if quiescently cast. Chapter 7 presents the mechanical properties and

deformation behavior of the double gyroid phase, isotropic or oriented, through mechanical testing, *in situ* synchrotron scattering, and electron microscopy. The behavior is interpreted in light of the morphological response of the double gyroid. Chapter 8 offers a beam-bending model to predict the [111] modulus of the double gyroid. Finally, Chapter 9 summarizes the results and conclusions and presents the future outlook and possible paths to continue the research in the various areas.

Chapter 2: Background and Motivation

This chapter provides the motivation and background for the project. First, the general issues and factors affecting mechanical behavior of composite materials are discussed. Then, block copolymer morphology and phase behavior are reviewed, followed by copolymer architecture considerations, in order to better understand the reasoning behind the choice of polymer system.

Then, the preliminary observations of the enhanced mechanical properties of the interconnected cubic phases are recounted as a historical framework behind this formal study of the mechanical properties of the double gyroid phase in elastomeric triblock copolymers.

2.1 Project Objective and Motivation

The objective of this thesis project was to conduct a formal study of the mechanical behavior of the double gyroid cubic phase in a rubbery polystyrene-polyisoprene-polystyrene (PS-PI-PS) triblock system. There were several reasons for choosing the system and the project.

First, two studies, Bi and Fetters (1976) and Alward and Thomas (1985) demonstrated enhanced mechanical performance of block copolymers with the then-unknown interconnected morphologies. These two preliminary studies provided the present impetus for embarking on a formal study of the mechanical properties of the cubic systems.

Morphology studies in 1986 showed that cubic phases existed in AB and star-diblock copolymer systems. For mechanical robustness, at least a triblock architecture is necessary. By appropriate choice of composition, the tricontinuous cubic phase could possibly be achieved in triblock copolymers, since a triblock copolymer is architecturally intermediate between a diblock and a starblock. As an interconnected cubic phase had not yet been observed in triblock systems, a composition range over which cubic phases existed could only be estimated. In particular, diblock styrene-diene systems were found to form cubic morphologies in the range 32 - 38 wt. % styrene (Anderson and Thomas, 1988).

Glassy-rubbery triblock copolymers have already been used extensively in the thermoplastic elastomer (TPE) industry (Holden, Legge, Quirk, and Schroeder, 1996). Existing production facilities and synthesis knowledge and experience are available, with only minor shifts in the composition of the TPEs that are currently produced, materials with enhanced mechanical properties may be achieved. This should prove to be valuable from

an industrial standpoint as different properties would open up possibilities for new and improved applications.

2.2 Composites as Insight into Block Copolymer Properties

It is widely known that the behavior of a composite will be unlike each of its constituent phases. Several factors contribute to the behavior of the overall composite, including

- the difference in constituent properties
- the length scales of the structures compared to stress gradients
- the geometry and topology of the structures within the composite (i.e., the morphology), and
- the strength of the interface between components.

It has been of interest to the engineering community to characterize or predict the mechanical properties of such composite materials. Such efforts have resulted in compilations of mechanical properties data and rules of mixtures.

If the two constituent phases of a composite have very different individual mechanical properties, the mechanical properties of the composite phase will have properties distinct from either of the two constituents alone. The most interesting properties arise if the composite is a mixture of constituents containing vastly different properties (e.g., one phase is conducting and the other insulating, or one phase is hard and brittle while the other is soft and ductile).

In addition to composition, the length scales of the constituent domains can be varied to give macro-, micro-, or even nano-composites. Typical engineering composites, such as concrete, are examples of macrocomposites. Here, the diameter of the steel reinforcing bars is on the order of centimeters and lengths of meters. Rock aggregates are also millimeter/centimeter composites, while sand is composed of micrometer- to millimeter- sized particles. Microcomposites, e.g., fiberglass and nanocomposites, e.g., silicate ceramic composites, have characteristic length scales on the order of micrometers and nanometers, respectively.

Accompanying the length scales is a corresponding change in surface-to-volume ratio of the different types of composites and this will affect the properties of the overall composite. Macrocomposites will have the smallest surface-to-volume ratio, while nanocomposites will have the largest surface-to-volume ratio.

Length-scale-dependent mechanical properties arise due to the size of the stress field relative to the size of the different materials in the composite and the characteristic dimensions of deformation structures. For example, in engineering composites such as

fiberglass, if the spacing between the fibers is small and the applied load is high such that the stress fields of the fibers overlap, then the composite will behave differently than if the fibers were far apart enough to act independently. Thus, one key question is at what length scale does the composite stop acting as a heterogeneous medium and start acting like a homogeneous material? For instance, concrete is at one extreme and normally acts as a heterogeneous composite; a miscible polymer blend, however, is at the other extreme and responds as a homogeneous material.

Often one of the components is much stiffer and stronger than the other and is designated the reinforcing component. The interfacial strength between the reinforcing component and the matrix also affects the overall mechanical behavior of the composite. If the strength of the interface is the limiting factor, then the main mode of deformation will be concerned with crack initiation and propagation along the interface. However, if the interface between components is sufficiently strong, then the deformation of the whole will concern cooperative deformation and the influence of the deformation mechanism of one phase on that of the other.

2.3 Block Copolymers as Polymer Composites

One of the most widely studied polymer composite materials are those that are formed by block copolymers, whereby two or more different polymer chains are chemically joined together. These polymer composites typically consist of a glassy component (e.g., styrene) and a rubbery component (e.g., diene) with the purpose of combining the beneficial properties and minimizing the disadvantageous properties of both. These polystyrene-polydiene block copolymers are interesting systems for several reasons.

First, the reinforcing structures typically have a length scale on the order of 100 Å . The interfacial width is a function of $\chi(T)$, and is approximately 40 Å for polystyrene-polyisoprene. Here, microphase separation occurs at 120 °C. These factors, suggest that the polydiene phase may not act rubbery and the polystyrene phase may not act glassy when the material is deformed. Hence, the composite may exhibit mechanical properties and deformation mechanisms that are unlike the bulk component materials.

Secondly, the two components are bonded by a covalent bond every ~400 $Å^2$ along the surface separating the components. Therefore the deformation behavior of the composite is not, as is the case for many other types of composites, only limited by the delamination of the phases from one another.

Thirdly, the microstructure of the composite can vary widely. Different morphologies will result depending on the relative amounts of A and B. By manipulating the composition of the minority phase and thus the morphology of the sample, the

macroscopic properties can be tailored. In particular, the properties and behavior of the sample will depend on the morphology within the sample; e.g., a rubbery matrix with glassy spheres packed in a body-centered cubic matrix will have different mechanical properties than a rubbery matrix with glassy cylinders on a hexagonal lattice.

2.3.1 Block Copolymer Physics

A block polymer is one in which each chain is composed of two or more different polymer chains which are chemically joined together. The different components may or may not be compatible with one another. The compatibility is quantitatively embodied in $\chi(T)$, the segment-segment interaction parameter, which is a function of temperature. In an A/B block copolymer system, if $\chi_{AB} > 0$, the two components have a tendency to demix. The higher the total number of Kuhn lengths N, i.e., the number of polymer "units" whose positions in space are uncorrelated with its adjacent neighbors, the higher the number of interactions between the two incompatible components. The enthalpy arising from these unfavorable interactions dominates over the entropy of mixing for long chains (large χN), and the system will microphase separate as the copolymer is cooled from the high temperature homogeneously mixed state. Block copolymer systems of sufficient $\Delta(\chi N) = (\chi N - (\chi N)_{critical})$ self-assemble into ordered microcomposites upon cooling from the melt. For example, the immiscibility of the two constituents causes the A blocks to segregate away from the B blocks, so as to minimize the number of unfavorable contacts. However, because the A blocks are covalently joined to the B blocks, they cannot completely phase separate; rather, they form microdomains, which have a shape and a periodicity (Leibler, 1980), (Bates and Fredrickson, 1990). The blocks arrange themselves to form an interface between the constituent phases, called the intermaterial dividing surface (IMDS). This interface adopts a shape that tends to minimize the contacts between the two components, and hence minimizes its surface area to approximate constant mean curvature (CMC) (Thomas, Anderson, Henkee, and Hoffman, 1988), (Lambert, Radzilowski, and Thomas, 1996). However, an entropic penalty must be paid with the chains stretching away from the IMDS on both sides to preserve a constant density throughout space. The chain stretching is relieved to a certain extent by allowing the longer blocks more room relative to the shorter blocks, and hence the IMDSs adopt a curvature towards the domains containing the shorter blocks. The balance between area minimization and chain stretching results in the arrangement of the domains into a morphology, which consists of the types of domain structures formed and their packing and arrangement in space. The ratio of the block lengths and the architecture of the molecule will determine the exact shape and spacing of the IMDS .

Helfand and Wasserman (1976,1978,1980) built upon the pioneering work of Meier (1969, 1973) and of Leibler (1980) to develop the theory of microphase separation for block copolymers in the strong segregation regime (where the interface thickness, ξ, is small compared to the domain periodicity, D) using mean field theory (Helfand, 1974,1975) Ohta and Kawasaki (1986) later furthered this work to develop an expression for the free energy of a microphase-separated morphology and the equilibrium domain sizes. For example, the free energy of a lamellar morphology can be expressed as

$$\Delta F = \Delta H - T\Delta S = \frac{2\sigma}{\rho_o}\frac{N}{D} + \frac{3k_B T}{8a^2}\frac{D^2}{N} \tag{2.1}$$

where σ is the interfacial energy (arising from the unfavorable interactions between the two components, ρ_o is the number of monomer units per volume (which needs to be kept constant throughout volume and hence causes the chain stretching), k_B is the Boltzmann constant, T is temperature in Kelvin, a is the Kuhn statistical segment length, D is the domain spacing, and N is the degree of polymerization. At equilibrium,

$$\frac{\partial \Delta F}{\partial D} = 0 \tag{2.2}$$

such that the equilibrium spacing can be found as

$$D = 2\left(\frac{\sigma a^2}{3\rho_o}\right)^{1/3} N^{2/3}, \tag{2.3}$$

the predicted 2/3 power law. Using equations 2.1 and 2.3, the ratio of the enthalpy and entropy contributions to the free energy at equilibrium are calculated to be

$$\left(\frac{\Delta H}{\Delta F}\right)_{D\,eq.} = \frac{2}{3} \text{ and } \left(\frac{\Delta S}{\Delta F}\right)_{D\,eq.} = \frac{1}{3}. \tag{2.4}$$

Thus, at equilibrium conditions, the enthalpic interactions are twice as important as the entropic chain stretching factors, and the equilibrium morphology attempts to first reduce the number of unfavorable contacts between the components and then to increase entropy by reducing chain stretching.

2.3.2 Block Copolymer Morphologies

The three traditional morphologies recognized in block copolymers in a two component system, upon variation of composition are spheres of one component in a matrix of the other, cylinders, and lamellae (good reviews can be found in (Burke and Weiss, 1973), (Holden et al., 1996), (Riess, Hurtrez, and Bahadur, 1986)). This is shown in figure 2.1. In styrene-diene thermoplastic elastomer systems, spheres correspond to discrete glassy reinforcements in a 3-dimensionally continuous rubbery matrix, cylinders correspond to 1-dimensionally continuous glassy reinforcements in a 3-dimensionally continuous rubbery matrix, and lamellae correspond to a stack of 2-dimensionally continuous alternating layers of glassy reinforcement with rubber. (Holden et al., 1996) and (Quirk and Morton, 1996) are good reviews of mechanical properties work done on the classical phases.

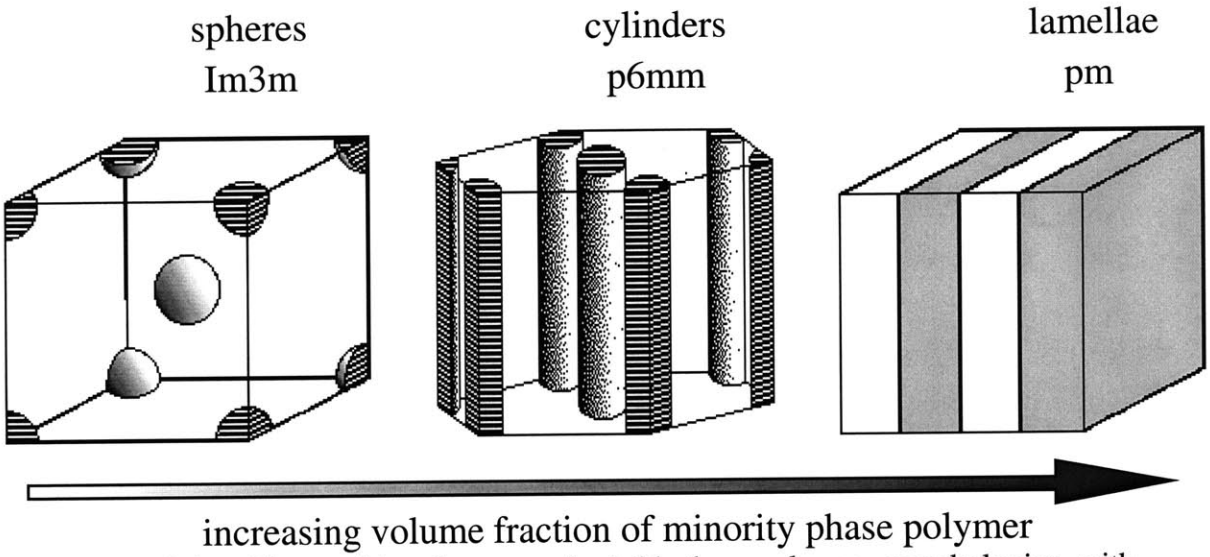

Figure 2.1: The traditionally recognized block copolymer morphologies with increasing volume fraction of minority component are spheres, cylinders, and lamellae.

Novel phases have recently been discovered in copolymer systems in both the weakly segregated- and strongly segregated- regimes, in composition ranges between that for cylinders and lamellae. The ordered tricontinuous double diamond morphology (DD) was thought to exist in styrene-isoprene star-block copolymers (Thomas, Alward, Kinning, Martin, Handlin, and Fetters, 1986) and in styrene-isoprene diblock copolymers (Hasegawa, Tanaka, Yamasaki, and Hashimoto, 1987). (However, some of these samples have been re-evaluated to be double gyroid (DG). This will be elaborated further in

Section 4.1 on the history of the DD and DG). Since then, DD has been observed in AB mikto-arm star systems (Tselikas, Hadjichristidis, Lescanec, Honeker, Wohlgemuth, and Thomas, 1996) and in ABC triblock copolymers (Mogi, Mori, Matsushita, and Noda, 1992), (Matsushita, Tamura, and Noda, 1994). Another ordered tricontinuous morphology, the double gyroid (DG), was discovered in 1994 in AB diblock systems (Hajduk, Harper, Gruner, Honeker, Kim, Thomas, and Fetters, 1994), (Schulz, Bates, Almdal, and Mortensen, 1994). They each have a tricontinuous nature and are ordered with cubic space lattices. Figure 2.2 shows the unit cells of both the DG and the DD morphologies.

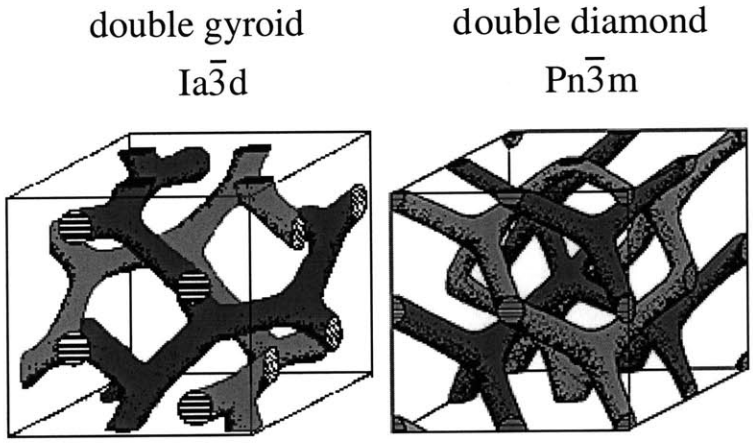

Figure 2.2: Ordered tricontinuous double gyroid and double diamond morphologies. Each structure consists of two connected networks, here shown in dark and grey shading. The space groups of each structure are given above each figure. (after Seddon, et al., 1993)

These novel morphologies have two 3-dimensionally continuous reinforcing networks embedded in a 3-dimensionally continuous matrix. The two labyrinthine networks interpenetrate but do not intersect. In particular, DG consists of arrays of struts which lie along <110> directions and meet in planar tri-functional nodes. DD consists of arrays of struts which lie along <111> directions and meet in tetrafunctional nodes. DG conforms to the symmetries of the Ia$\bar{3}$d space group (Hajduk et al., 1994), while DD conforms to that of the Pn$\bar{3}$m space group (Thomas et al., 1986). In this manner, they can be considered interpenetrating networks (IPNs) having long range order and periodicity.

Because of the different physical nature in which the composite incorporates the reinforcing styrene phase into the matrix, and because of the cubic crystal structure of the composite material, the mechanical properties of the tricontinuous, interpenetrating

morphologies are anticipated to be markedly different than those of the three traditional block copolymer morphologies.

2.4 Block Copolymer Architectures

Anionic polymerization has made possible many different block polymer architectures. The simplest architectures are linear block copolymers (Fetters, 1969), (Morton and Fetters, 1975), which have junctions connecting two or more blocks. Figures 3a-c shows some possibilities of linear block polymers. The simplest block copolymer architecture, the linear diblock, is depicted in figure 3a. Figure 3b shows a linear ABA triblock copolymer, where the block B is connected on both ends by A blocks. Figure 3c shows a linear ABC terpolymer, which contains three different blocks. Longer, more complex linear multiblocks are also possible with having more types of blocks in one chain and with having different block sequences.

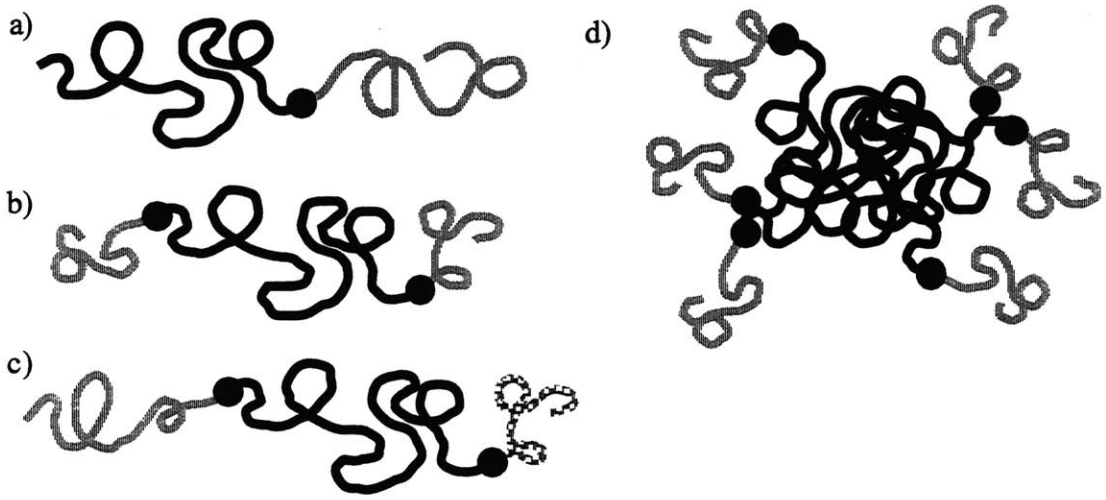

Figure 2.3: Schematics of linear block copolymers: a) AB diblock, b) ABA triblock, c) ABC triblock, d) 6-arm star diblock copolymer. The junctions between blocks are indicated by black dots.

More complex architectures can be made using connectors which join more than two blocks (Bi, Fetters, and Morton, 1974), (Bi et al., 1976), (Alward, Kinning, Thomas, and Fetters, 1986), (Iatrou and Hadjichristidis, 1992, 1993), (Avgeropoulos, Hadjichristidis, Dair, Thomas, in preparation). For example, figure 3d shows a star diblock copolymer; a molecule consisting of six linear AB diblock copolymers radiating from a common center. Complex architectures such as these require anionic synthesis

techniques more advanced than those for di- or triblocks. Such molecules are highly interesting for studies into their morphologies and property characterization.

2.5 Triblock Copolymers as Thermoplastic Elastomers

Both the composition and the architecture of a molecule affects the morphology of the block copolymer which, in turn, affects the mechanical properties. However, the composition and architecture also has some direct influences on the processability and hence, usefulness of a block copolymer.

In particular, styrene-diene-styrene SDS *tri*block copolymers (such as polystyrene-b-polybutadiene-b-polystyrene (SBS) and polystyrene-b-polyisoprene-b-polystyrene (SIS); figure 2.3b), in which the polydiene phase is the majority component, have been an industrial mainstay for more than 30 years because of their excellent composite properties (Legge, 1989). It has been found that these triblock copolymer systems can form useful thermoplastic elastomeric materials, referred to as thermoplastic elastomers (TPEs) in industry. These materials are composites in that the polystyrene and the polydiene phases still retain some of their homopolymer characteristics. In particular, the material as a whole exhibits two glass transition temperatures characteristic of the two phases (Hendus, Illers, and Ropte, 1966), (Kraus, Childers, and Gruver, 1967), (Beecher, Marker, Bradford, and Aggarwal, 1969), (Holden, Bishop, and Legge, 1969), indicating that the structure of the material is phase separated. At room temperature, the rubbery middle block is anchored by the glassy ends on either side, which have microphase separated into their own domains. These glassy domains act as physical crosslinks for the rubbery matrix, preventing permanent flow. Unlike elastomers which are crosslinked by chemical means, these triblock copolymer "physical crosslinks" are thermoreversible. Upon passing through the order-disorder transition through solvation or heating, the system randomizes into a homogeneous state, melting the physical crosslinks. It is this characteristic which allows these materials to be re-processed.

The diblock counterparts (see figure 3a) to these elastomeric materials, however, are less useful as TPEs. Diblocks have only one end of the polymer anchored in a glassy phase. The other end is free to move and permanent flow can occur upon deforming these materials. Thus, by themselves, diblock copolymers cannot be made into mechanically useful elastomeric materials (Morton, 1971). In fact, addition of diblock materials have shown to have a detrimental effect on the mechanical properties of triblock elastomers (Smith and Dickie, 1969), (Berglund and McKay, 1993).

Other architectures which have rubbery midblocks attached to glassy end blocks (e.g., the star block copolymers depicted in figure 3d) can also be used as mechanically

useful elastomeric materials (Bi et al., 1974,1976). However, the synthesis of these materials is more involved than for linear di- and triblock copolymers. The commercial star block copolymers made by Philips (K Resins) are known to be quite polydisperse due to it containing large amounts of the diblock precursors of various segment molecular weights (Fetters, private communication), which can have a malevolent effect on the mechanical properties, as previously mentioned. It is the triblock copolymer which is the predominant architecture used in the TPE industry, as it is the simplest architecture that forms mechanically useful elastomers.

2.6 Enhanced Mechanical Properties of the Interconnected Phases

Many studies have been carried out to characterize the mechanical properties of styrene-diene-styrene systems of the more traditional morphologies. However, the mechanical properties of the more recently-discovered morphologies, such as the interconnected cubic DD and DG, remain minimally touched.

In previous studies on block copolymers with bicontinuous morphologies, that are now understood to be DD or DG, there seemed to be a surprising enhancement in mechanical properties over those triblocks of cylindrical morphology (Bi et al., 1974, 1976), (Alward, 1985). Here, two studies will be reviewed, Bi and Fetters (Bi et al., 1976), and Alward and Thomas.

Bi and Fetters (Bi et al., 1976) characterized the stress-strain curves of styrene-butadiene and styrene-isoprene star-block copolymer systems. The polymers consisted of styrene-diene arms connected with a multi-functional divinyl-benzene (DVB) molecule (as opposed to chlorosilane) so that arm number per molecule was polydisperse across the material.

Bi and Fetters made comparisons between star-blocks as a function of arm number, all having an equivalent composition ~30% PS, segment molecular weights, and PS as the outer blocks . The molecules they studied ranged in average arm number from 2-arms (i.e., a linear triblock) to 29-arms. Although Bi and Fetters used TEM to characterize the morphologies of all the copolymers, they claimed that all of the polymers, the linear triblock and the multiarm stars, had a sphere morphology with body-centered cubic (BCC) arrangements. They explained their TEM observations of continuous PS phase in the samples as the array of BCC spheres seen at an angle to give a 2D projection of continuous lines. Implicit in their claim was that the copolymers had the same morphology, regardless of arm number.

Today the star block copolymers having 2 arms (triblock) would be interpreted to have cylinder morphology, and the 6 arm star, whose stress-strain behavior is shown in

figure 2.4, would be identified as having an ordered bicontinuous morphology. It is unclear why the authors did not interpret the TEM images of stripes and dots as those belonging to axial and end-on views of cylinders, as the classical morphologies of spheres, cylinders, and lamellae had been identified by 1970 (Molau, 1970).

The mechanical properties of the block copolymers can now be interpreted keeping the correct morphologies in mind. It was found that the stress-strain properties of the stars, particularly with arms of 6 or greater, exhibited yielding, necking, higher ultimate tensile strengths, smaller extension ratios for a given stress, and lower residual strains than the linear counterparts. Figure 2.4 is a reproduction from references (Bi et al., 1974) and (Bi et al., 1976) of the stress-strain curves for the block copolymers and shows that the 6-arm star has enhanced mechanical properties over the linear triblock. Again, the morphology of the linear triblock is probably one of cylinders while the morphology of the 6-arm star block is probably one of the interconnected cubic phases. It can now be inferred that the difference in mechanical properties between the starblock and the triblock is due to the morphology difference between the two materials, as both materials have the same composition of 30 wt.% PS. This study suggests an enhanced stress-strain behavior of interconnected cubic phases over that of the cylindrical phase.

Bi and Fetters also observed a yielding phenomenon in a 32 wt.% PS (PS-PI) 7-arm star. However they insisted that the morphology was BCC spheres and that the yield point was *not* due to "the existence of interconnected polystyrene domains". However, this sample too, was most likely to have an interconnected cubic morphology. However, today the sample would be recognized to have an interconnected cubic morphology, and that the yield point is, in fact, related to "the existence of interconnected polystyrene domains".

Alward (1985), (Alward et al., 1986), and subsequently reported in (Kinning, Thomas, Alward, Fetters, and Handlin, 1986) studied the morphological and mechanical behavior of polystyrene-polybutadiene star block copolymers synthesized by Fetters. These star block copolymers have diblocks as arms, connected by a multi-functional chlorosilane molecule such that the number of arms per molecule had a low polydispersity (e.g., average 5.9 arms for an expected 6 arm star). He studied a series with different arm numbers and different arm molecular weights, but with the same arm and overall composition of about 30 wt% PS. It was found that these star block copolymers were polymorphic: at low arm numbers and/or arm molecular weights, the

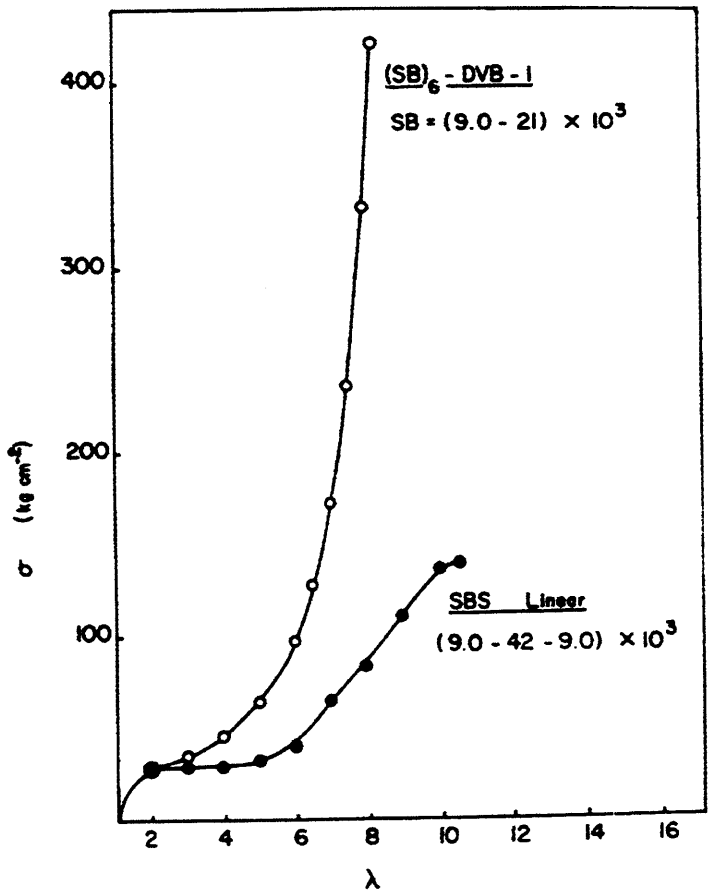

Figure 2.4: Stress-strain curves for linear triblock (probably cylinders) and for star block copolymer (interconnected cubic). σ is the stress in kg/cm^2, while λ is the extensional ratio (i.e., engineering strain). (Bi et al., 1974, 1976)

stars exhibited cylindrical morphology, but increasing arm number and/or increasing arm molecular weight produced an ordered bicontinuous structure (OBS). In particular, it was shown that a 5-arm star composed of diblock arms with 30% overall PS composition and a molecular weight of 10,000 had a cylinder morphology. However, the 6-arm star was an ordered, bicontinuous structure (Kinning et al., 1986). The study was the first to show that at constant composition, the molecular architecture could affect the domain morphology.

Alward conducted dynamic mechanical thermal analysis (DMTA) at a strain rate frequency of 1 Hz on the SI stars. DMTA is a mechanical test sensitive to PS connectivity; the drop in E', the elastic modulus (the modulus in phase with the oscillatory shear stress), as the T_g of the polydiene phase is traversed is indicative of the relative roles that the polydiene phase plays in bearing the load as compared to the polystyrene phase. A large

drop indicates that the load bearing capacity of the material is borne by the polydiene; i.e., the polydiene is continuous, and the polystyrene phase is discrete. A small drop indicates that the polydiene phase does not play a large role in the load bearing capacity of the material; i.e., the polystyrene may also form a continuous phase in the continuous polydiene phase.

Figure 2.5 shows a comparison of the DMTA results for the 5-arm (cylinder morphology) and the 6-arm star (OBS), taken from (Kinning et al., 1986). As the T_g of the PI phase is crossed, the drop in E' is more severe for the 5-arm star than for the 6-arm star. The figure shows that the modulus of the 6-arm star is approximately one order of magnitude higher than that for the 5-arm star, with only a minor increase in total molecular weight. The fact that the two samples have the same composition and only a 16% difference in total molecular weight indicates that the drastic change in mechanical behavior is due to the difference in morphology. The PS domains in OBS play a large load-bearing role in the mechanical response of the material, and indicate that the PS is probably a continuos phase. These observations were of the first indications that the OBS phase may

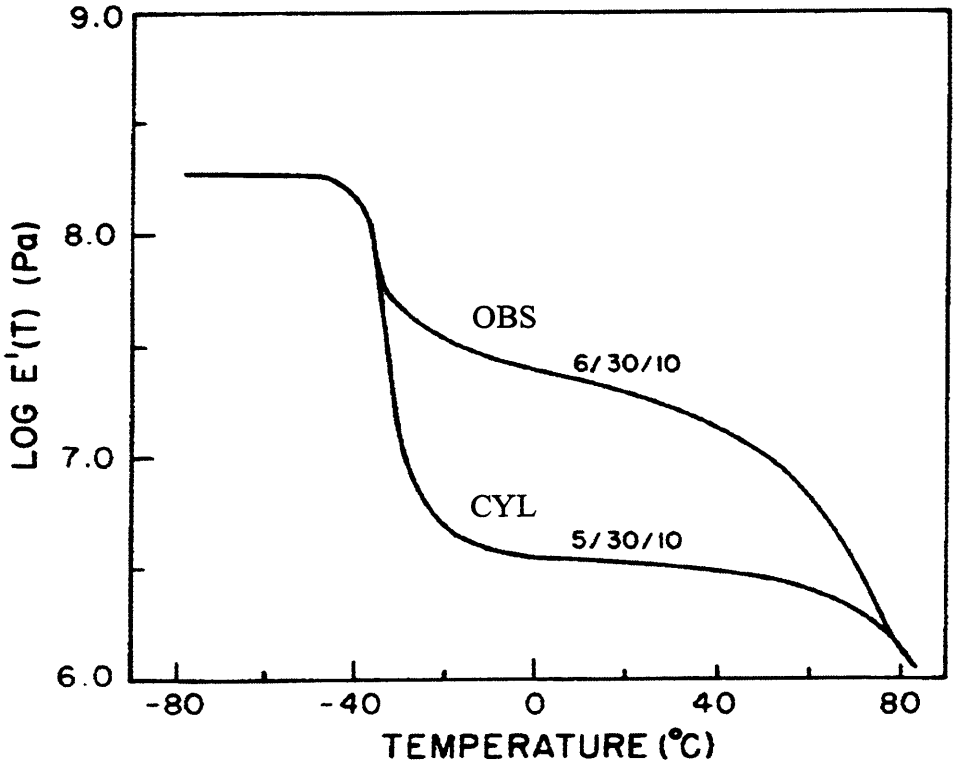

Figure 2.5: DMTA results for a 5-arm and 6-arm star, reproduced from (Kinning et al., 1986). The sample identification 5/30/10 represents a 5-arm star having diblock arms of 30% PS and 10K (10,000) molecular weight. The 5-arm star has a cylinder morphology, while the 6-arm star has the OBS morphology.

have enhanced mechanical properties over that of the cylindrical morphology, even with the same PS content.

Figure 2.6 shows unpublished data from Alward's thesis on the stress-strain curves of isotropic cylinder and an OBS starblock. Note that the OBS phase exhibits yielding and necking phenomenon, but that the cylinder phase does not. The stress required to deform the sample is higher for the OBS phase than for the cylinder phase at all strains shown, indicating that the work involved for deformation , given by the area underneath the curve, is higher for the OBS phase. This is yet another example that the OBS phase has enhanced mechanical properties over that of the cylinder phase.

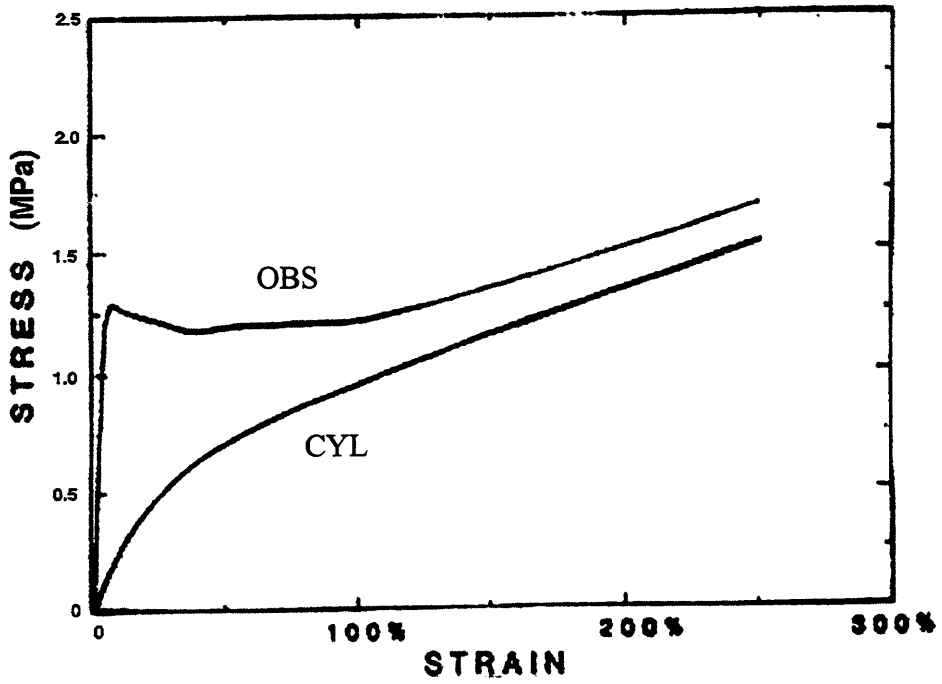

Figure 2.6: Unpublished data from Alward (1985) comparing the stress-strain behavior of the OBS phase and the cylinder phase.

2.7 Related Materials and Models

2.7.1 Interpenetrating Networks

The tricontinuous, interpenetrating glassy networks nature of these cubic systems may be considered as ideal interpenetrating networks (IPNs). IPNs consist of two molecularly intertwined 3D networks. They are made by forming a solution of two different monomers and polymerizing the two components separately, or by forming a polymer-monomer solution and polymerizing the monomer while keeping a single misciblesystem (which becomes harder as the polymerization progresses). In either case, there is usually neither long range order nor controllable dimensions of the components.

The term 'interpenetrating polymer network' was coined before the full consequences of phase separation were realized. Actual IPNs usually do not correspond to this ideal since as the molecular weight of the two polymerizing species increases, phase separation of the components occurs and the final morphology consists of a chaotic interspersion of nanodomain networks. Molecular interpenetration occurs only in the case of total mutual solubility; however, most IPNs phase separate to a greater or lesser extent. Thus molecular interpenetration may be restricted or shared with supermolecular levels of interpenetration. In some cases, true molecular interpenetration is thought to take place only at the phase boundaries.

(Klempner, Sperling, and Utracki, 1994) and (Sperling, 1981) are general introductions to IPNs for the interested reader. Some IPNs combine polyurethanes and epoxies or PET and castor oil, PS and PMMA, or SBR and PS. Most of the IPN literature are concerned with engineering properties, such as ultimate tensile strength, impact properties, dynamic mechanical moduli, and the effect of chemistry, conversion, and cross-link density on the mechanical properties. The studies relevant to this thesis concern those on blends of SB copolymers with PS, PMMA, or PS-PMMA copolymers (Curtius, Covitch, Thomas, and Sperling, 1972), (Donatelli, Sperling, and Thomas, 1976, 1976, 1977), (Sardelis, Michels, and Allen, 1987), (Byun, Burford, and Mai, 1989), (Yamaoka, 1995, 1996, 1998). These studies involve the morphology and engineering properties mentioned above, but some do mention the mechanisms of failure, which include debonding of the components from one another. Only one IPN study showing a full stress-strain diagram was found. This was done on an IPN system based on polymerized castor oil and PS (Devia, Manson, and Sperling, 1979). Curtius et al. (1972) compared the properties of polystyrene-polybutadiene IPNs with commercially available block copolymers found that the tensile properties of PS-PB IPNs were inferior to their block copolymer TPE counterparts.

If IPN development were to progress such that the ideal IPN were achieved, then the deformation behavior of either the DD or DG materials can be useful as an ideal version of IPNs. In the interpenetrating cubic block copolymer microphase separated phases, both components fully interpenetrate, and there is a chemical junction joining the two phases such that the mechanical properties are neither governed by conversion of the networks nor by the debonding of the components. The cubic morphology polymers are a special case of IPNs in that they have longer range order and regular, controllable microphase dimensions. Hence, there may be better control of properties, which may mean more reproducible results after processing. This may be interesting from an industrial or commercial standpoint, particularly for quality control purposes.

Since the interpenetrating cubic morphologies are highly ordered structures, they may be probed to investigate the directional dependence of properties. That is, whereas the disordered IPNs will form a film isotropic in character for all physical properties, a film made of a highly textured cubic morphology can be mechanically anisotropic.

2.7.2 Cellular Materials

Cellular materials consist of arrays of struts or faces of a solid phase interconnected to one another to form either honeycomb (two dimensional) or foam (three dimensional) structures. Gibson and Ashby have written a good reference on such materials (Gibson and Ashby, 1997). Insight into the deformation mechanisms of the interpenetrating network DD and DG structures can be provided by those of open celled cellular solids, which consist of interconnected struts.

Gibson and Ashby find that honeycomb and foam structures deform by similar mechanisms. In tension, cells deform first by bending, giving linear elasticity, and then rotation of the cell edges toward the tensile axis, thereby increasing the stiffness of the structure along the tensile axis. The rotation occurs by plastic bending of the struts, by bending of the plastic hinges between two struts, or by formation of plastic hinges within one strut. In compression, the linear elastic region is also due to bending of the struts. When a critical stress is reached the cells collapse by buckling of the cell walls for elastic materials and by formation or deformation of plastic hinges in materials which yield. Further deformation compresses the cells and the stress rises from the densification.

Air is the medium surrounding the struts of cellular materials, whereas polyisoprene rubber, an incompressible solid, surrounds the PS struts in the block copolymer phases. Although the moduli of both are negligible in comparison to the hard phase, the two surrounding media are very different in nature such that the large strain deformation behavior of the block copolymers may deviate from those found in cellular materials. Nevertheless, deformation mechanisms, such as rotation of the struts and opening of the "hinges" connecting struts, can be used in the analysis of the mechanical behavior of the DD or DG.

2.7.3 Theoretical Moduli Predictions for Interpenetrating-Phased Composites

Davies developed a theory for predicting the modulus for systems with two continuous phases, ideally used for a polymer composite "containing two interpenetrating networks which separate into two phases" (Davies, 1971). Davies used equations by Hashin and Shtrikman (1963) and Budiansky (1965) for elastic constants of composite

materials and a method by Looyenga (1965) to predict properties of a continuous, interpenetrating composite. The general results will be briefly described here.

Hashin and Shtrikman (1963) developed equations for the elastic constants for an isotropic material composed of one phase dispersed in a matrix of another phase:

$$\frac{3K + 4G_1}{(K - K_1)} = \frac{1}{\phi_2}\frac{3K_2 + 4G_1}{(K_2 - K_1)} \tag{2.5a}$$

$$\frac{G + G_1\dfrac{9K_1 + 8G_1}{6K_1 + 12G_1}}{G_2 + G_1\dfrac{9K_1 + 8G_1}{6K_1 + 12G_1}} = \frac{1}{\phi_2}\frac{G - G_1}{G_2 - G_1} \tag{2.5b}$$

where the subscripts 1 and 2 refer to the matrix and dispersed components, respectively, and unsubscripted quantities refer to the composite. G is the shear modulus, K is the bulk modulus, and ϕ_2 is the volume fraction of the dispersed component 2. They found that the two equations describe the lower bounds to the elastic constants when $K_1 < K_2$ and $G_1 < G_2$ (i.e., dispersed component having higher moduli than the matrix). The lower bound to K is achieved if the material consists of spheres of phase 2 dispersed in phase 1, and the lower bound to K is exact if $G_1 = G_2 = G$.

Budiansky (1965) also derived formulae for the elastic constants based on a self-consistent model of spheres of phase 2 embedded in the effective medium having constants K and G, where

$$\phi_2 = \frac{K_1 - K}{K_1 - K_2}\frac{3K_2 + 4G}{3K + 4G} \tag{2.6a}$$

$$\phi_2 = \frac{G_1 - G}{G(G_1 - G_2)}\left\{G + \frac{6}{5}\left(\frac{K + 2G}{3K + 4G}\right)(G_2 - G)\right\} \tag{2.6b}$$

Davies (1973) modified the method of Looyenga (1965) (used to predict the dielectric constants) and used the formulae above to derive a formula for the shear modulus of an isotropic and homogeneous composite materials having two co-continuous, interpenetrating phases. He considered a material having volume fraction ϕ_2 of the disperse phase in a matrix of phase 1 as a composite of material A, which has a slightly larger volume fraction of phase 2 than the average, and material B, which has a slightly smaller volume fraction of phase 2 than the average. He assumed that the bulk modulus K is a

function of the shear modulus G. He expressed the changes in K for the altered materials based on Taylor expansions about the original composition. The materials needed to be "combined" to make a composite with the overall moduli G and K. The problem then became to solve for the correct volume fraction of phase 2 which would be required, which in turn became a function of G and K. The solution of the series of differential equations with consideration of boundary conditions gave

$$\phi_2 = \frac{G^{1/5} - G_1^{1/5}}{G_2^{1/5} - G_1^{1/5}}. \tag{2.7}$$

Equation 2.7 can be re-written with Young's moduli as

$$E^{1/5} = \phi_1 E_1^{1/5} + \phi_2 E_2^{1/5}. \tag{2.8}$$

Consideration of the boundary conditions suggest that this model be used for domains which are phase separated but form continuous paths, and where the domains have perfect cohesion between the two phases to satisfy continuous strain across the boundaries. Both of these conditions can be met with the novel interconnected phases.

2.8 Mechanical Anisotropy of Cubic Materials

For cubic materials, all symmetric second rank property tensors, such as thermal expansion α_{ij} and dielectric constant ε_{ij}, are isotropic. However, the symmetries of cubics are not sufficient to render isotropic a fourth rank tensor property, such as the elasticity tensors **C** and **S** (with components C_{ijkl} and S_{ijkl}, respectively). For example, the elasticity tensors consists of three independent components, S_{1111}, S_{1122}, and S_{2323} (or S_{11}, S_{12}, and S_{44} in Voigt notation). This property of the cubics may be of value in cases where different properties may be desired in different directions. A general review of stress, strain, and the elasticity tensor can be found in (McClintock and Argon, 1966), (Nye, 1957), and (Zener, 1948), and a brief review will be provided here.

2.8.1 Stress

Both stress σ and strain ε are second rank tensors. In the most general case, there are $3^2 = 9$ components for each, as given by

$$\sigma = \begin{bmatrix} \sigma_{11} & \sigma_{12} & \sigma_{13} \\ \sigma_{21} & \sigma_{22} & \sigma_{23} \\ \sigma_{31} & \sigma_{32} & \sigma_{33} \end{bmatrix} \quad \text{and} \quad \varepsilon = \begin{bmatrix} \varepsilon_{11} & \varepsilon_{12} & \varepsilon_{13} \\ \varepsilon_{21} & \varepsilon_{22} & \varepsilon_{23} \\ \varepsilon_{31} & \varepsilon_{32} & \varepsilon_{33} \end{bmatrix} . \tag{2.9}$$

Stress is defined as the force per unit area, applied at a point. A general stress can be resolved, first into three components along a chosen set of three mutually orthogonal axes. Each of these component can be, in turn, further resolved into three components, (with a total of 9 components) corresponding to stresses which act on the different planes normal to the three axes. Figure 2.7 shows the resolved components of a general stress. By convention, the first subscript, i, for a given stress component refers to the axis to which the applied stress is parallel and the second subscript, j, to the outward normal of the cube face at which the stress is applied. Elements on the diagonal of the stress tensor (which have the form σ_{ii}) are tensile stresses, while the off-diagonal elements (which have the form $\sigma_{i\neq j}$) are shear stresses.

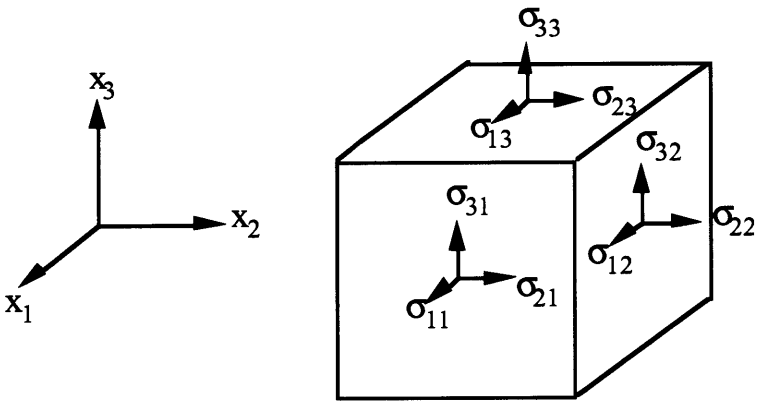

Figure 2.7: Resolved components of a generalized stress (adapted from (Zener, 1948), p. 10).

Equilibrium considerations, namely $\Sigma F = 0$ and $\Sigma M = 0$, impose restrictions on the shear stresses such that $\sigma_{ij} = \sigma_{ji}$. The stress tensor is thus symmetric, and the number of independent components reduces to six:

$$\sigma = \begin{bmatrix} \sigma_{11} & \sigma_{12} & \sigma_{13} \\ & \sigma_{22} & \sigma_{23} \\ (\text{sym.}) & & \sigma_{33} \end{bmatrix} . \tag{2.10}$$

2.8.2 Strain

The general displacement of a body can be described by a second rank tensor,

$$\mathbf{e} = \begin{bmatrix} e_{11} & e_{12} & e_{13} \\ e_{21} & e_{22} & e_{23} \\ e_{31} & e_{32} & e_{33} \end{bmatrix} \tag{2.11}$$

where $e_{ij} = \frac{\partial u_i}{\partial x_j}$ is the displacement in the "i" direction with position in the "j" direction.

Figure 2.8 shows the displacement vector for a deformed body.

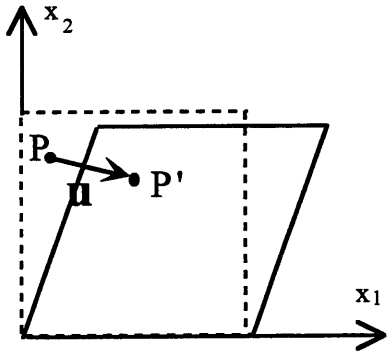

Figure 2.8: After deformation, a point originally at P moves to P', with a corresponding displacement vector **u**.

The diagonal elements e_{ii} represent the fractional change in tensile length of the object along the x_i axis. For small deformations, the off-diagonal elements e_{ij} represent the angle of rotation of x_j towards x_i.

General displacement is a superposition of pure deformation and of rigid body rotation, as shown in figure 2.9. Because it is the deformation resulting from an applied stress which is the only quantity of interest, it would be useful to extract only the pure deformation component from the displacement tensor.

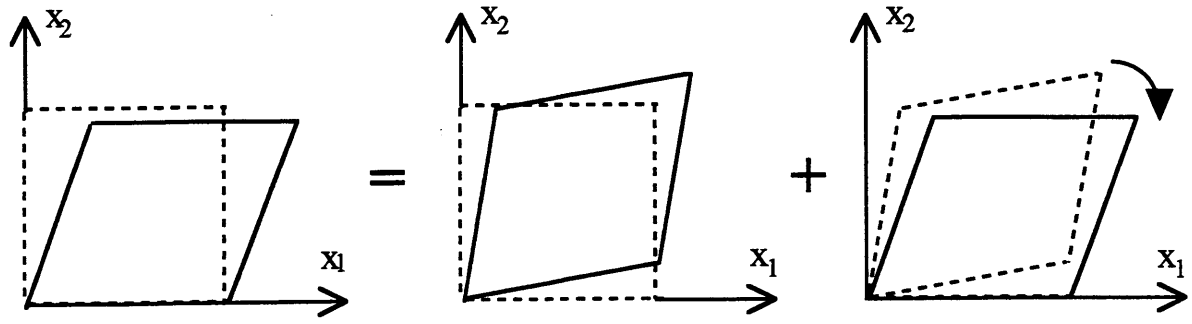

Figure 2.9: General displacement = pure deformation + rigid body rotation

As a property of tensors and matrices, a tensor can be decomposed into the sum of two separate tensors. Thus, e_{ij} can be decomposed into

$$e_{ij} = \varepsilon_{ij} + \omega_{ij} \tag{2.12}$$

where ε_{ij} is a purely deformational component described by the symmetric tensor

$$\varepsilon_{ij} = \frac{1}{2}(e_{ij} + e_{ji}) \tag{2.13 a}$$

and ω_{ij} is a purely rotational component described by the anti-symmetric tensor

$$\omega_{ij} = \frac{1}{2}(e_{ij} - e_{ji}) \,. \tag{2.13 b}$$

Strain is defined as the symmetric part of the relative deformation tensor and hence also has only six independent components:

$$\varepsilon = \begin{bmatrix} \dfrac{\partial u_1}{\partial x_1} & \dfrac{1}{2}\left(\dfrac{\partial u_1}{\partial x_2} + \dfrac{\partial u_2}{\partial x_1}\right) & \dfrac{1}{2}\left(\dfrac{\partial u_1}{\partial x_3} + \dfrac{\partial u_3}{\partial x_1}\right) \\ \dfrac{1}{2}\left(\dfrac{\partial u_1}{\partial x_2} + \dfrac{\partial u_2}{\partial x_1}\right) & \dfrac{\partial u_2}{\partial x_2} & \dfrac{1}{2}\left(\dfrac{\partial u_2}{\partial x_3} + \dfrac{\partial u_3}{\partial x_2}\right) \\ \dfrac{1}{2}\left(\dfrac{\partial u_1}{\partial x_3} + \dfrac{\partial u_3}{\partial x_1}\right) & \dfrac{1}{2}\left(\dfrac{\partial u_2}{\partial x_3} + \dfrac{\partial u_3}{\partial x_2}\right) & \dfrac{\partial u_3}{\partial x_3} \end{bmatrix} = \begin{bmatrix} \varepsilon_{11} & \varepsilon_{12} & \varepsilon_{13} \\ & \varepsilon_{22} & \varepsilon_{23} \\ (\text{sym.}) & & \varepsilon_{33} \end{bmatrix} \tag{2.14}$$

2.8.3 Elasticity Tensor

Stress and strain are related through fourth rank tensors,

$$\sigma_{ij} = \sum_{k=1}^{3}\sum_{l=1}^{3} C_{ijkl}\,\varepsilon_{kl} \quad \text{and} \quad \varepsilon_{ij} = \sum_{k=1}^{3}\sum_{l=1}^{3} S_{ijkl}\,\sigma_{kl}. \tag{2.15 a and b}$$

where **C** is the stiffness and **S** the compliance tensors. **S** and **C** are related through $\mathbf{S} = \mathbf{C}^{-1}$. In general, **S** and **C** both have $3^4 = 81$ components. However, the equalities $\sigma_{ij} = \sigma_{ji}$ and $\varepsilon_{ij} = \varepsilon_{ji}$ reduce the number of constants to 36. This allows the 4-dimensional tensor to be represented by a 2-dimensional matrix with compressed (Voigt) notation:

$$\begin{aligned} '11' &= '1' \quad '23' = '4' \\ '22' &= '2' \quad '13' = '5' \\ '33' &= '3' \quad '12' = '6' \end{aligned} \quad .$$

The compliance matrix, for example, becomes

$$\mathbf{S} = \begin{bmatrix} S_{11} & S_{12} & S_{13} & S_{14} & S_{15} & S_{16} \\ S_{21} & S_{22} & S_{23} & S_{24} & S_{25} & S_{26} \\ S_{31} & S_{32} & S_{33} & S_{34} & S_{35} & S_{36} \\ S_{41} & S_{42} & S_{43} & S_{44} & S_{45} & S_{46} \\ S_{51} & S_{52} & S_{53} & S_{54} & S_{55} & S_{56} \\ S_{61} & S_{62} & S_{63} & S_{64} & S_{65} & S_{66} \end{bmatrix} . \tag{2.15}$$

A further reduction arises from the fact that deformation work is a function of only the strain and is path independent; $\dfrac{\partial^2 U}{\partial \varepsilon_{ij}\, \partial \varepsilon_{kl}} = \dfrac{\partial^2 U}{\partial \varepsilon_{kl}\, \partial \varepsilon_{ij}}$, where U is the strain energy function. Thus, $C_{ijkl} = C_{klij}$, $S_{ijkl} = S_{klij}$, (the elasticity matrix becomes symmetric, and the number of independent components reduces to 21:

$$\mathbf{S} = \begin{bmatrix} S_{11} & S_{12} & S_{13} & S_{14} & S_{15} & S_{16} \\ & S_{22} & S_{23} & S_{24} & S_{25} & S_{26} \\ & & S_{33} & S_{34} & S_{35} & S_{36} \\ & & & S_{44} & S_{45} & S_{46} \\ & (\text{sym.}) & & & S_{55} & S_{56} \\ & & & & & S_{66} \end{bmatrix} \tag{2.16}$$

The above case is applicable to the triclinic crystal class, which is the most general of the crystals, since it contains no inherent symmetries, save for translation or inversion. Crystal symmetry reduces the number of independent components even further. The higher the symmetry, the fewer the independent elastic constants. Cubics have the highest symmetry of the crystal classes. The elasticity tensor for cubic crystals is composed of three independent components, S_{11}, S_{12}, and S_{44}:

$$\mathbf{S} = \begin{bmatrix} S_{11} & S_{12} & S_{12} & 0 & 0 & 0 \\ & S_{11} & S_{12} & 0 & 0 & 0 \\ & & S_{11} & 0 & 0 & 0 \\ & & & S_{44} & 0 & 0 \\ & (\text{sym.}) & & & S_{44} & 0 \\ & & & & & S_{44} \end{bmatrix} \tag{2.17}$$

The relation between **S** and **C** is simplified and the individual components are related by the following equations:

$$S_{44} = \frac{1}{C_{44}} \tag{2.18 a}$$

$$S_{11} - S_{12} = \frac{1}{C_{11} - C_{12}} \tag{2.18 b}$$

$$S_{11} + 2S_{12} = \frac{1}{C_{11} + 2C_{12}} \tag{2.18 c}$$

Because of the three independent constants, the mechanical properties of cubic materials are anisotropic, and the anisotropy can be sampled by observing the mechanical properties of an oriented material in different directions.

Table 2.1 shows the moduli and the anisotropy of different cubic metals in different directions (from (Dieter, 1986). The anisotropy, A, is the ratio of the moduli in two different directions. Note that the anisotropy of the materials is typically around 1 with an upper value of approximately 3.

Table 2.1: Moduli of cubic metals in various directions and the anisotropy ratios

Material	**E_{100} GPa**	**E_{110} GPa**	**E_{111} GPa**	**A 111/110**	**A 110/100**	**A 111/100**
Al	64	73	76	1	1.1	1.2
Cu	67	130	190	1.5	1.9	2.8
Fe	125	210	273	1.3	1.7	2.2
W	384	385	385	1	1	1

2.8.4 Criteria for Isotropy of Modulus

Cubics have only one component more than that of an elastically isotropic material. Elastically isotropic materials hold the upper limit for symmetry and have 2 independent elastic constants:

$$\mathbf{S} = \begin{bmatrix} S_{11} & S_{12} & S_{12} & & & & \\ & S_{11} & S_{12} & & & & \\ & & S_{11} & & & & \\ & & & 2(S_{11} - S_{12}) & 0 & 0 & \\ & (\text{sym.}) & & & 2(S_{11} - S_{12}) & 0 & \\ & & & & & 2(S_{11} - S_{12}) & \end{bmatrix}$$

It has been known in crystallography that planes having 6-fold symmetry are elastically isotropic in the plane. Less obvious is the fact that 3-fold symmetry also renders the plane elastically isotropic. These two facts will become useful later in interpretation of the mechanical properties of the oriented interconnected cubic materials.

Christensen also showed that in low density materials in which loads are transferred via micro-material struts (i.e., foams and other cellular structures), 6 axes of 5-fold symmetry are sufficient for isotropy of moduli in 3-dimensional space (Christensen, 1987). The interconnected cubic phases consist of micro-struts of the glassy phase similar to a cellular foam. Depending on the desired applications, these materials can be appropriately processed to give the necessary properties in different directions, along different planes, or throughout 3-dimensional space.

2.9 References

Alward, D. and E. L. Thomas (1985). "unpublished results."

Alward, D. B. (1985). A Morphological Study Of A Series Of Multiarmed Star Block Copolymers Of Polyisoprene And Polystyrene. Ph. D. thesis, University of Massachusetts.

Alward, D. B., D. J. Kinning, E. L. Thomas and L. J. Fetters (1986). "Effect Of Arm Number And Arm Molecular Weight On The Solid-State Morphology Of Poly(Styrene-Isoprene) Star Block Copolymers." Macromolecules **19**: 215-224.

Anderson, D. M. and E. L. Thomas (1988). "Microdomain Morphology Of Star Copolymers In The Strong-Segregation Limit." Macromolecules **21**: 3221-3230.

Avgeropoulos, A., N. Hadjichristidis, B. Dair and E. L. Thomas. "Morphological Behavior Of Miktoarm Star Block Copolymers Of The (Ps-B-Pi)2ps, (Ps-B-Pi)3ps Type, Super H-Shaped Block Copolymers Of The (Ps-B-Pi)3ps(Pi-B-Ps)3 And Their Blends With Homopolymer Hps." in preparation.

Bates, F. S. and G. H. Fredrickson (1990). "Block Copolymer Thermodynamics: Theory And Experiment." Annual Review in Physics and Chemistry **41**: 525-557.

Beecher, J. F., L. Marker, R. D. Bradford and S. L. Aggarwal (1969). "Morphology And Mechanical Behavior Of Block Polymers." Journal of Polymer Science Part C **26**: 117-134.

Berglund, C. A. and K. W. McKay (1993). "Viscoelastic Properties Of A Styrene-Isoprene-Styrene Triblock Copolymer And Its Blends With Polyisoprene Homopolymer And Styrene-Isoprene Diblock Copolymer." Polymer Engineering and Science **33**(18): 1195-1203.

Bi, L.-K. and L. J. Fetters (1976). "Synthesis And Properties Of Block Copolymers. 3. Polystyrene-Polydiene Star Block Copolymers." Macromolecules **9**: 732-742.

Bi, L.-K., L. J. Fetters and M. Morton (1974). "The Synthesis, Mechanical Behavior And Morphology Of Star Triblock Copolymers." Polymer Preprints ACS Polymer Chemistry Division **15**(2): 157-163.

Budiansky, B. (1965). "On The Elastic Moduli Of Some Heterogeneous Materials." Journal of Mechanics and Physics of Solids **13**: 223-227.

Burke, J. J. and V. Weiss, Eds. (1973). Block and Graft Copolymers. Syracuse, Syracuse University Press.

Byun, H. S., R. P. Burford and Y.-W. Mai (1989). "Morphology Of Interpenetrating Polymer Networks Based On Block Styrene-Butadiene Copolymers And Ps." Materials Forum **13**: 26-34.

Christensen, R. M. (1987). "Sufficient Symmetry Conditions For Isotropy Of The Elastic Moduli Tensor." Transaction of the ASME **54**(December): 772-777.

Curtius, A. J., M. J. Covitch, D. A. Thomas and L. H. Sperling (1972). "Polybutadiene/Polystyrene Interpenetrating Polymer Networks." Polymer Engineering and Science **12**: 101-108.

Davies, W. E. A. (1971). "The Elastic Constants Of A Two-Phase Composite Material." Journal of Physics D: Applied Physics **4**: 1176-1181.

Davies, W. E. A. (1971). "The Theory Of Elastic Composite Materials." Journal of Physics D: Applied Physics **4**: 1325-1339.

Devia, N., J. A. Manson and L. H. Sperling (1979). "Simultaneous Interpenetrating Networks Based On Castor Oil Elastomers And Polystyrene. Iv. Stress-Strain And Impact Loading Behavior." Polymer Engineering and Science **19**: 878-882.

Dieter, G. E. (1986). Mechanical Metallurgy. New York, McGraw-Hill.

Donatelli, A. A., L. H. Sperling and D. A. Thomas (1976). "Interpenetrating Polymer Networks Based On Sbr/Ps. 1. Control Of Morphology By Level Of Cross-Linking." Macromolecules **9**: 671-675.

Donatelli, A. A., L. H. Sperling and D. A. Thomas (1976). "Interpenetrating Polymer Networks Based On Sbr/Ps. 2. Influence Of Synthetic Detail And Morphology On Mechanical Behavior." Macromolecules **9**: 676-680.

Donatelli, A. A., L. H. Sperling and D. A. Thomas (1977). "A Semiempirical Derivation Of Phase Domain Size In Interpenetrating Polymer Networks." Journal of Applied Polymer Science **21**: 1189-1197.

Fetters, L. J. (1969). "Synthesis Of Block Polymers By Homogeneous Anionic Polymerization." Journal of Polymer Science Part C. **26**: 1-35.

Gibson, L. J. and M. F. Ashby (1997). Cellular Solids. Cambridge, UK, Cambridge University Press.

Hajduk, D. A., P. E. Harper, S. M. Gruner, C. C. Honeker, G. Kim, E. L. Thomas and L. J. Fetters (1994). "The Gyroid: A New Equilibrium Morphology In Weakly Segregated Diblock Copolymers." Macromolecules **27**: 4063-4075.

Hasegawa, H., H. Tanaka, K. Yamasaki and T. Hashimoto (1987). "Bicontinuous Microdomain Morphology Of Block Copolymers. 1. Tetrapod-Network Structure Of Polystyrene-Polyisoprene Diblock Polymer." Macromolecules **20**: 1651-1662.

Hashin, Z. and S. Shtrikman (1963). "A Variational Approach To The Theory Of The Elastic Behavior Of Multiphase Materials." Journal of Mechanics and Physics of Solids **11**: 127-140.

Helfand, E. (1974). "Block Copolymer Theory. Ii. Statistical Thermodynamics Of The Microphases" in Recent Advances in Polymer Blends, Grafts, and Blocks. L. H. Sperling. New York, Plenum. **4:** 141-156.

Helfand, E. (1975). "Block Copolymer Theory. Iii. Statistical Mechanics Of The Microdomain Structure." Macromolecules **8**: 552-556.

Helfand, E. and Z. R. Wasserman (1976). "Block Copolymer Theory. 4. Narrow Interphase Approximation." Macromolecules **9**(6): 879-888.

Helfand, E. and Z. R. Wasserman (1978). "Block Copolymer Theory, 5. Spherical Domains." Macromolecules **11**(5): 960-966.

Helfand, E. and Z. R. Wasserman (1980). "Block Copolymer Theory. 6. Cylindrical Domains." Macromolecules **13**: 994-998.

Hendus, H., K.-H. Illers and E. Ropte (1966). "Strukturuntersuchungen An Sbs Blockcopolymeren." Colloid and Polymer Science **216-217**: 110-119.

Holden, G., E. T. Bishop and N. R. Legge (1969). "Thermoplastic Elastomers." Journal of Polymer Science Part C **26**: 37-57.

Holden, G. and N. R. Legge (1996). "Styrenic Thermoplastic Elastomers" in Thermoplastic Elastomers. G. Holden, N. R. Legge, R. P. Quirk and H. E. Schroeder. New York, Hanser Publishers: 48-69.

Holden, G., N. R. Legge, R. P. Quirk and H. E. Schroeder, Eds. (1996). Thermoplastic Elastomers. New York, Hanser Publishers.

Iatrou, H. and N. Hadjichristidis (1992). "Synthesis Of A Model 3-Miktoarm Star Terpolymer." Macromolecules **25**: 4649-4651.

Iatrou, H. and N. Hadjichristidis (1993). "Synthesis And Characterization Of Model 4-Miktoarm Star Co- And Quaterpolymers." Macromolecules **26**: 2479-2484.

Kinning, D. J., E. L. Thomas, D. B. Alward, L. J. Fetters and D. L. J. Handlin (1986). "Sharpness Of The Functionality Induced Structural Transition In Poly(Styrene-Isoprene) Star Block Copolymers." Macromolecules **19**: 1288-1290.

Klempner, D., L. H. Sperling and L. A. Utracki, Eds. (1994). Interpenetrating Polymer Networks. Advances in Chemistry Series, American Chemical Society.

Kraus, G., C. W. Childers and J. T. Gruver (1967). "Properties Of Random And Block Copolymers Of Butadiene And Styrene. I. Dynamic Properties And Glassy Transition Temperatures." Journal of Applied Polymer Science **11**: 1581-1591.

Lambert, C. A., L. H. Radzilowski and E. L. Thomas (1996). "Triply Periodic Level Surfaces As Models For Cubic Tricontinuous Block Copolymer Morphologies." Philosophical Transactions of the Royal Society of London A **354**: 2009-2023.

Legge, N. R. (1989). "Thermoplastic Elastomers - Three Decades Of Progress." Rubber Chemistry and Technology **62**: 529-547.

Leibler, L. (1980). "Theory Of Microphase Separation In Block Copolymers." Macromolecules **13**: 1602-1617.

Looyenga, H. (1965). "Dielectric Constants Of Heterogeneous Mixtures." Physica **31**: 401-406.

Matsushita, Y., M. Tamura and I. Noda (1994). "Tricontinuous Double-Diamond Structure Formed By A Styrene-Isoprene-2-Vinylpyridine Triblock Copolymer." Macromolecules **27**: 3680-3682.

McClintock, F. A. and A. S. Argon (1966). Mechanical Behavior of Materials. Reading, MA, Addison-Wesley.

Meier, D. J. (1969). "Theory Of Block Copolymers. I. Domain Formation In A-B Block Copolymers." Journal of Polymer Science: Part C: Polymer Symposia **26**: 81-98.

Meier, D. J. (1973). "Block Copolymer-Solvent Systems: Thermodynamics And Morphology" in Block and Graft Copolymers. J. J. Burke and V. Weiss. Syracuse, Syracuse University Press: 105-120.

Mogi, Y., K. Mori, Y. Matsushita and I. Noda (1992). "Tricontinuous Morphology Of Triblock Copolymers Of The Abc Type." Macromolecules **25**: 5412-5415.

Molau, G. E. (1970). "Colloidal And Morphological Behavior Of Block And Graft Copolymers" in Block Polymers. S. L. Aggarwal. New York, Plenum Press: 79-106.

Morton, M. (1971). "Styrene-Diene Block Copolymers" in Encyclopedia of Polymer Science and Technology. M. Bikales. New York, Wiley-Intersciene. **15:** 508-530.

Morton, M. and L. J. Fetters (1975). "Anionic Polymerization Of Vinyl Monomers." Rubber Chemistry and Technology **48**: 359-409.

Nye, J. F. (1957). Physical Properties of Crystals. Oxford, Clarendon Press.

Ohta, T., and K. Kawasaki (1986). "Equilibrium Morphology Of Block Copolymer Melts." Macromolecules **19**: 2621-2632.

Quirk, R. P. and M. Morton (1996). "Research On Anionic Triblock Copolymers" in Thermoplastic Elastomers. New York, Hanser Publishers: 72-100.

Riess, G., G. Hurtrez and P. Bahadur (1986). "Block Copolymers" in Encyclopedia of Polymer Science. H. F. Mark, M. Bikales, C. G. Overberger, G. Menges and J. I. Kroshwitz. New York, John Wiley & Sons. **2:** 349-434.

Sardelis, K., H. J. Michels and G. Allen, FRS (1987). "Toughened polystyrene containing block, graded, and randomized copolymers of butadiene-styrene." Polymer **28**: 244-250.

Schulz, M. F., F. S. Bates, K. Almdal and K. Mortensen (1994). "Epitaxial Relationship For Hexagonal-To-Cubic Phase Transition In A Block Copolymer Mixture." Physical Review Letters **73**(1): 86-89.

Seddon, J. M. (1990). "Structure Of The Inverted Hexagonal (H2) Phase, And Non-Lamellar Phase Transitions Of Lipids." Biochimica et Biophysica Acta **1031**: 1-69.

Seddon, J. M., and R. H. Templer (1993). "Cubic Phases Of Self-Assembled Amphiphilic Aggregates." Philosophical Transactions of the Royal Society of London A **344**: 377-401.

Smith, T. L. and R. A. Dickie (1969). "Viscoelastic And Ultimate Tensile Properties Of Sbs Block Copolymers." Journal of Polymer Science Part C **26**: 163-187.

Sperling, L. H. (1981). Interpenetrating Polymer Networks and Related Materials. New York, Plenum Press.

Thomas, E. L., D. B. Alward, D. J. Kinning, D. C. Martin, D. L. Handlin Jr. and L. J. Fetters (1986). "Ordered Bicontinuous Double-Diamond Structure Of Star Block Copolymers: A New Equilibrium Microdomain Morphology." Macromolecules **19**: 2197-2202.

Thomas, E. L., D. M. Anderson, C. S. Henkee and D. Hoffman (1988). "Periodic Area-Minimizing Surfaces In Block Copolymers." Nature **334** (6184): 598-601.

Tselikas, Y., N. Hadjichristidis, R. L. Lescanec, C. C. Honeker, M. Wohlgemuth and E. L. Thomas (1996). "Architecturally-Induced Tricontinuous Cubic Morphology In Compositionally Symmetric Miktoarm Starblock Copolymers." Macromolecules **29**: 3390-3396.

Yamaoka, I. (1995). "Toughened Polymer Blends Composed Of A Ductile Styrene-Butadiene-Styrene Matrix With Brittle Methyl-Methacrylate-Styrene Particles." Polymer **36**: 3359.

Yamaoka, I. (1996). "Effects Of Morphology On Mechanical Properties Of Styrene-Butadiene-Styrene Triblock Copolymer/Methyl Methacrylate-Styrene Copolymer Blends." Polymer **37**(4): 5343-5356.

Yamaoka, I. (1998). "Anisotropic Behavior Of Styrene-Butadiene-Styrene Triblock Copolymer / Methyl Methacrylate-Styrene Copolymer Blends." Polymer **39**: 1081-1093.

Zener, C. (1948). Elasticity and Anelasticity of Metals. Chicago, University of Chicago Press.

Chapter 3: History and Description of G and DG

This chapter discusses the first observations regarding gyroid materials. First a report of the term "gyroid" and related terms in crystallographic text is presented. Next an account of the discovery of **double** gyroid (DG) materials in macromolecular systems is presented, including lipid, surfactant, and polymer systems. Then, the gyroid surface and double gyroid surfacesas seen by mathematicians are discussed. Finally, the DG structure is extensively described for a better understanding of the TEM, SAXS and mechanical behavior of block copolymer materials with this interesting microdomain morphology.

3.1 Crystallographic History of Gyroid

The term "**gyroid**" by itself does not appear in the Oxford English Dictionary (Oxford University Press, 1971). However, the term "**gyroidal**" does appear, which means 'having a spiral arrangement, as certain planes, etc.' and is derived from '**gyre**' + '**-oid**' + '**-al**' (p. 531). "**Gyre**" (verb) (from the Latin "**gyrare**", to move in a circle) means 'to turn or whirl round; to revolve round'. The suffix "**-oid**" (from the Latin "**-oïdes**" and the Greek "**-oeidës**", from **-o-** + **eidos**, meaning "appearance" or 'form') is either a noun suffix meaning 'something resembling a specified object or having a specified quality', or an adjective suffix meaning 'resembling; having the form or appearance of'. "**Gyroid**" would hence mean an object having the appearance of a spiral arrangement.

It is unclear as to exactly when the term "gyroidal" was applied in the science of crystallography. The earliest reference found is the term "gyroidisch", which was used in Klockmann's *Textbook of Mineralogy* (1st edition in 1891) and "gyroëdrisch" in Groth's *Physical Crystallography* (1st edition in 1895) to describe the class of materials of the 432, or "pentagonal-icosi-tetrahedral" symmetry. Point group 432 is one of the 32 possible crystallographic point groups. Class 432 materials have three 4-fold, four 3-fold, and six 2-fold axes, but is one of six crystal classes which do not have inversion or mirror symmetry. Structures that are enantiomorphic can thus have the 432 structure. In optics, "**gyroidal**" means 'having the property of turning the plane of polarization to the right or left; rotatory in respect to polarized light'. Both Klockmann and Groth observed a distinct handedness to "gyroid" compounds. Presumably crystallographers associated the term "gyroid" to the pentagonal-icosi-tetrahedral class of materials because the faceted surfaces of these crystals to seem to "**gyrate**" to the left or right (**gyrate**: adapted from the Latin "**gyratus**", past participle of "**gyrare**", 'to move in a circle or spiral; to rotate, whirl').

Class 432 is one of two crystal classes which have dubious representatives, as mentioned by Buerger (1956). Crystals of these materials are rare and include ammonium

chloride (NH_4Cl) and cuprite (Cu_2O) as mentioned in Klockmann and in Groth. However, according to Buerger (1956), only the "spurious" forms of these two materials have the gyroidal symmetry. They normally exhibit $\frac{4}{m}\bar{3}\frac{2}{m}$ symmetry, but can exhibit 432 symmetry if precipitated from a medium containing optically active matter. Figures 3.1 a and b show schematics of {321} crystals of left and right gyroid, respectively. The chiralities of the surface gyrations are particularly clear on these two {321} gyroid crystals in that the observer is lead to turn (or gyrate) to the left or right with the surfaces.

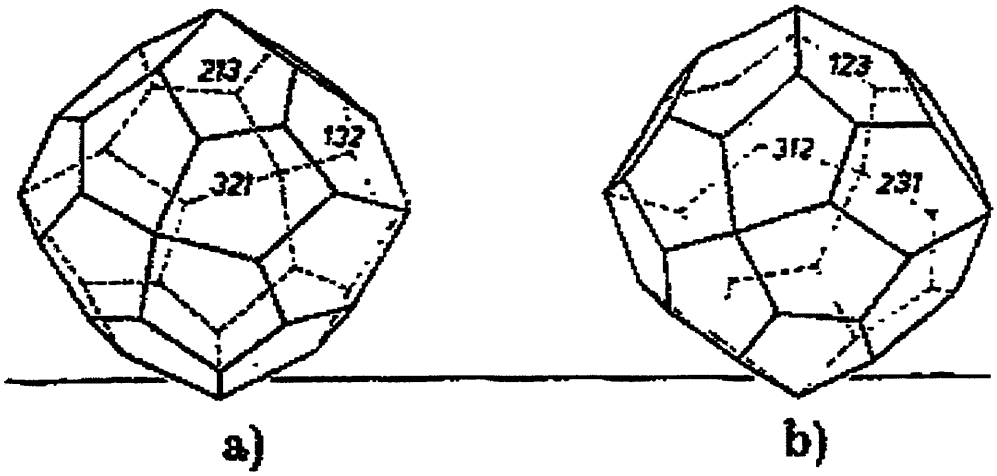

Figure 3.1: Schematics of a) left and b) right gyroid with {321} faces (reproduced from Klockmann's Lehrbuch der Mineralogie). It is particularly clear on these two {321} gyroid crystals that the surfaces lead the eye to turn to the left or right.

(A bit of trivia: On the California Institute of Technology campus in Pasedena, CA, there stands a giant ferritin crystal serving as the fountain piece in front of the Beckmann Institute. This ferritin crystal has 432 space group symmetry. The crystal and its symmetry group is described on a plaque ~50 feet away.)

According to both Klockmann and Groth, the common faces of class 432 ammonium chloride are in the order {211}, {110}, {100}, {111}, while that for cuprite are the opposite: {111}, {100}, {110}, {211}. Later it will be discussed that in DG materials, i.e. materials having two interpenetrating gyroid networks with composite symmetry $Ia\bar{3}d$, the {211} and {110} planes are preferential planes.

Gross at the Institute for Mineralogy and Petrography, published an article in 1918 entitled "Zur Frage der Gyroedrie des Steinsalzes / *On the question of the Gyrohedry of Rocksalts*" (in which he tried to prove wrong the theory of Bragg and Bragg that rocksalts consist of two interpenetrating fcc lattices of each type of atom) (Gross, 1918). In that article, he used the terms "**gyroedrie**" or "**gyroiedrisch-**" (gyrohedry, gyrohedric) to

describe symmetries and symmetry character in his exposition. He used it rather freely, stopping nowhere to define his use of these terms. Their frequent use without definition or explanation causes one to believe that by 1922 the mineralogy, geology, and crystallography community is familiar with the root "**gyr-**".

At around the same time, (1922), Rinne at the University of Leipzig used the terms "**gyrish-**" and "**gyroidish-**" in his book, *Das feinbauliche Wesen der Materie nach dem Vorbilde der Kristalle / The Atomistic Construction of Materials* (Rinne, 1922). He used them to define them as two elementary symmetry operations, where a "gyrisher Rhythmus" is a simple rotation, and a "gyroidischer Rhythmus" is a combination of a rotation and a reflection together. These two operations are used to generate the 32 crystal classes from the 1-, 2-, 3-, 4-, 6-fold, and isometric "rhythms". It appears that the usage of "gyrish" as a rotation operation is directly from the Latin meaning of "gyrare", but it is unclear why a combination of rotation and reflection is dubbed "gyr*oid*isch", especially since the "gyroidische Klasse", known at the time as the 432 class, only has rotation axes but neither centers of inversion nor mirror planes.

The use of the term "gyroid", which started in crystallography to describe crystals with chiral surfaces or rotation operations in crystal theory, has remained ever since as the descriptive name for the 432 class of crystals. By the 1950's, "gyroid" had been established as an alternate name for the general hkl crystals of class 432, pentagon-trioctahedron or pentagon-icositetrahedron (Buerger, 1956). It is now used in the International Tables of Crystallography as an alternative name for class 432 (Hahn, 1993).

3.2 History of the Discovery of Double Gyroid in Soap Systems

We now move from mineralogy to the morphology and crystallography of macromolecular systems. The classical phases in block copolymer systems, as well as in lipid/water/surfactant systems, are spheres, cylinders, and lamellae, typically designated Q($Im\bar{3}m$), H, and L_α by the surfactant community and S, C, and L by the block copolymer community. Spheres are the minority component discrete in its continuity and periodic in 3 dimensions (represented by 0-3, whereby the first number represents the dimensions of continuity, and the second represents the dimensions of periodicity). Cylinders are continuous in 1 dimension and periodic in 2 dimensions (1-2). Lamellae are continuous in 2 dimensions and periodic in 1 dimension (2-1).

In the 1960's during his Ph.D. thesis, Spegt and his advisor Skoulios at the CNRS Centre de Recherches sur les Macromolecules in Strasbourg, France, detected a phase in six different one-component strontium soap systems which did not fit the classical (Q, H, L_α) phases via x-ray crystallography. From the peak intensities, it was determined to be a

body-centered cubic phase, but the detailed structure was left unsolved (Spegt and Skoulios, 1966).

Luzzati, a colleague of Skoulios who had recently moved from Strasbourg to the CNRS Laboratoire de Genetique Physiologique in Paris, undertook to elucidating the structure, and invited Spegt as a collaborator. From the x-ray scattering data, Luzzati and Spegt first characterized the strontium soap structures as belonging to the space group $Ia\bar{3}d$. They modeled the x-ray scattering as arising primarily from the strontium ions and that the electron density was distributed evenly throughout a unit cell, and that the strontium ions occupied special Wyckoff positions to account for structural integrity or rigidity of the cell to which the paraffinic regions do not contribute. They found that if the strontium ions occupied Wyckoff positions "g" in the International Tables of Crystallography (at $(\frac{1}{8}, y, \frac{1}{4} - y)$-type positions), which correspond to lines along the <110> directions, then the calculated amplitudes of the structure factors were in very good agreement with those observed. They postulated a 3-D interconnected cubic structure which would fit the $Ia\bar{3}d$ space group and satisfy all the physico-chemical requirements of the surfactant system, envisioning that "the polar groups are arranged so as to form interwoven three-dimensional networks embedded in a continuous matrix formed by disordered paraffin chains", as depicted in figure 3.2a. The white and black struts in figure 3.2a represent the loci of the strontium ions belonging to two separate non-intersecting but interpenetrating networks . The Sr ions are distributed uniformly throughout the struts, which in turn, are separated by a medium of paraffin chains as shown in Type IIa in figure 3.2c.

This new cubic phase was the first example of an interconnected soap structure, completely different from the classical spheres, cylinders, and lamellae. Luzzati et al. later described this $Ia\bar{3}d$ structure as having two separate networks of polar groups which are separated by a medium of paraffin chains, and that the two media are 3-dimensionally continuous throughout the 3-D structure (Luzzati et al., 1968).

3.3 History of the Discovery of Gyroid in Mathematical Minimal Surfaces

In the 1960's, Schoen, an applied mathematician working for the National Aeronautics and Space Administration (NASA) on algorithms for infinite periodic minimal surfaces (IPMS) without self intersections, discovered the *gyroid* surface (Schoen, 1970). A minimal surface is one which minimizes the *local* area based on local constraints; i.e., over a given closed boundary loop, it is the surface with least area.

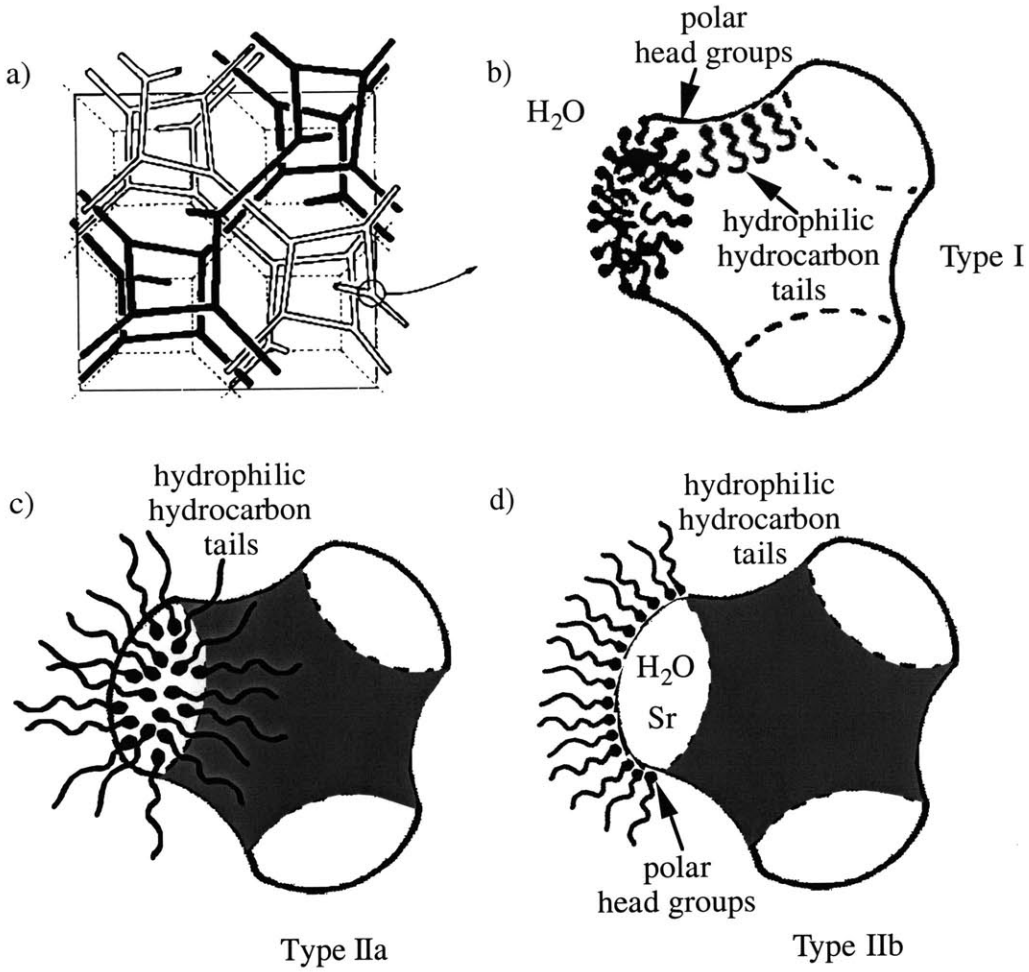

Figure 3.2: (a) A unit cell of the skeletal graph representation of the tricontinuous periodic $Ia\bar{3}d$ structure viewed slightly off a <100> direction. (b-d) Three enlargements of the node where three struts come together. The system in which the paraffin chains are on the inside of the struts is termed "type I", while that in which the paraffin chains are on the outside is termed "type II". b) Type I represents the cases where the struts are composed of entire molecules with the polar head groups laying on the surface of the strut. c) Type IIa represents the cases where the struts are composed of the heads of the molecules in water and the matrix is composed of the hydrocarbon tails and d) type IIb represents the cases where the struts are loci of the polar head groups, with the struts themselves composed of water, while the matrix is composed of the hydrocarbon tails. (Adapted from references (Rançon and Charvolin, 1987) and (Luzzati and Spegt, 1967)

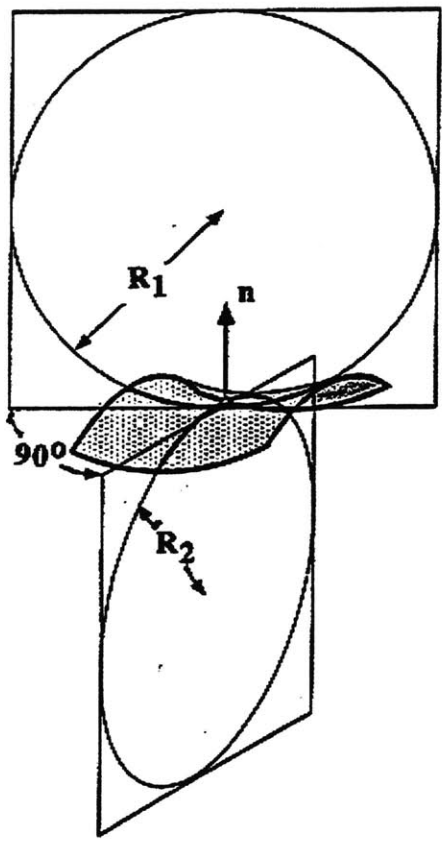

Figure 3.3: Schematic of a portion of a surface (shaded region). At any given point on the surface, the local normal is **n** and the two principal radii of curvature, R_1 and R_2, which are the maximum and minimum radii of curvature of the surface, respectively. The principal curvatures, C_1 and C_2, are defined as and $C_2 = -\frac{1}{R_2}$.

It has everywhere zero mean curvature; i.e., $H = \frac{C_1 + C_2}{2} = 0$ (or equivalently, $C_1 = -C_2$ everywhere) where C_1 and C_2 are the principal curvatures defined by the principal radii of curvature R_1 and R_2 by the relations $C_1 = \frac{1}{R_1}$ and $C_2 = \frac{-1}{R_2}$. R_1 and R_2 are defined to be on opposite sides of the surface. If R_1 and R_2 are on the same side of the surface, then C_1 and C_2 are of the same sign. Figure 3.3 shows a portion of a surface with R_1 and R_2 indicated. An IPMS is a minimal surface which is infinitely periodic, where periodicity can range from one to three dimensions, and its unit of repetition partitions space into two subvolumes. When modeling physical systems such as surfactant and polymer systems, the IMPS partitions space into subvolumes of matter; on either side of the IMPS are phase-separated materials. Hence the partition is named the intermaterial dividing surface (IMDS).

In 1970, Schoen reported the discovery of eleven new IPMS which were free of self-intersections, one of which he called "gyroid", G, which has the cubic space group number 214, with symmetry $I4_132$. Schoen called the new surface the gyroid, rumored because the surface gyrated throughout space. The gyroid minimal surface that he described in the NASA Technical Note (Schoen, 1970) was one in which the mean curvature was zero and divided space into two equal subvolumes, which are "labyrinths" of the two components. Just like the pentagonal-icosi-tetrahedral crystals, the gyroid surface has a chirality such that its gyrations have a preferential handedness.

Schoen invented the concept of skeletal graphs to help himself envision the minimal surface. A skeletal graph is formed by joining nodes in a network by a series of straight segments which are representations of nodes and struts of the two labyrinths defined by the surface. Since a triply periodic IPMS partitions space into two subvolumes or labyrinths, two skeletal graphs are associated with an IPMS, located on either side of the surface and each representing one of the continuous subvolumes.

For the G minimal surface the two skeletal graphs have opposite handedness. Although Schoen did discuss the enantiomorphic skeletal graphs of the two labyrinths on either side of the IMDS of minimal gyroid, he did not consider the symmetry of the composite structure of the two G skeletal graphs together, which would have resulted in an overall cubic symmetry $Ia\bar{3}d$ (space group #230). Schoen did not make a connection between the structure formed by the two skeletal graphs of the two minimal G labyrinths to the interpenetrating networks found by Luzzati and Spegt (1967) having $Ia\bar{3}d$ symmetry, described via the use of representative straight lines for the loci of the strontium ions. It is believed that Schoen did not know about the work of Luzzati and Spegt, though structures considered by the two groups are, in fact, the same.

3.4 Double Gyroid in Subsequent Physical Systems

In 1976, Scriven, a mathematician at the University of Minnesota, proposed that bicontinous structures may be present in liquid-crystal-like phases which were "regarded as dispersions of spheres, cylinders, and lamellae" (Scriven, 1976). He defined "bicontinuous partitioning of a volume" as a case in which space was divided into subvolumes, each of which are filled with a distinct medium and is continuous across the specimen. Scriven argued that cubics, as mathematically described by Schoen, were particularly expected, and he highlighted Neovius's simple cubic and Schoen's gyroid BCC lattices. He proposed that experiments be done with microemulsions and mesomorphic liquid crystals in search of bicontinuous phases, which could then be modeled after appropriately chosen mathematical surfaces of a particular genus. He

mentioned that no example of bicontinous structures had yet been found in the literature of "macroemulsions, periodic colloid structures, microemulsions, micellar solutions, mesomorphous phases and lyotroic crystals", so it is presumed that the work of Luzzati and Spegt (1967) and subsequent work by Luzzati and co-workers on other novel morphologies in surfactant systems, was unbeknownst to Scriven at the time.

The 3D interpenetrating network morphology with $Ia\bar{3}d$ symmetry has been frequently found in surfactant systems since the first discovery by Luzzati and Spegt (Rançon and Charvolin, 1988), (Mitchell et al. 1983), (Luzzati et al., 1997). For amphiphilic systems of the lyotropic liquid crystals $C_{12}OE_6$ (hexa-ethyleneglycol mono n-dodecyl ether) / water system as studied by Rançon and Charvolin, the white and black struts represent the central axes of the amphiphilic rods. The polar head groups lie on the surrounding surface of the struts and nodes, and the hydrophilic hydrocarbon tails lie on the interior, which has been termed "type I" and is shown in figure 3.2b. The first mention of any $Ia\bar{3}d$ structure in block copolymer systems was by Gobran (1990), who speculated in his Ph.D. thesis that a 10k-17k SI diblock was possibly $Ia\bar{3}d$. It was only in 1994 that the DG was discovered in low-molecular weight diblock copolymer systems (Hajduk et al., 1994), incidentally the same system as studied by Gobran. (Förster et al., 1994) also found it in a blend by using a combination of SAXS, TEM, and TEM simulations based on level surfaces. Due to the striking similarity of the 3-fold (so-called "wagon wheel" projections of these two structures, the ordered bicontinuous structures (Alward, 1985), first identified in high molecular weight star-block copolymers in 1986 as double diamond (DD) with space group number Pn3m, were then re-evaluated, and the data found to better fit to DG. This was made possible with higher-precision x-rays, which made the determination of peak ratios $\frac{q_n}{q_1}$ more accurate (Hajduk et al., 1995). The DG microdomain structure has since been found in triblock copolymers of the ABA type (Laurer et al., 1997), (Avgeropoulos, Dair, Hadjichristidis, Thomas, 1997), (Avgeropoulos et al., 1998) as well as in blends of diblocks (Sakurai et al., 1998), or diblocks and triblocks with homopolymer (current research in the Thomas group by R.G.H Lammertink, and A. Avgeropoulos). A double gyroid structure was found in a triblock of the ABC type (Matsushita, Suzuki, Seki, 1998) but which has the space group I4132, since the two labyrinths are no longer mirror related equivalents; one labyrinth is composed of polymer A, while the labyrinth having the opposite handedness is composed of polymer C.

It has been found that interpenetrating networks in surfactant and polymer systems have *two* intermaterial dividing surfaces, both non-intersecting to either itself or to the other surface. Hence space is divided into three subvolumes, and the two IMDSs minimize their

area to conform to the volume constraints. One method to construct the IMDSs is to take the two aforementioned skeletal graphs as one type of material and inflate the struts and nodes such that the volume fraction of the two networks together correspond to that of the total minority fraction composition of the real system.

Usually when the volumes are not equally divided, then the surface does not have zero mean curvature; instead, the surfaces will minimize their area based on the volume constraints. This gives rise to a family of surfaces, which are based on the original minimal surface (e.g., gyroid). There are several different IMDSs which could be constructed 1) constant mean curvature (CMC), 2) constant thickness (CT), and 3) level surfaces The result is two labyrinths, and hence two IMDSs of one type of component in a matrix of the other component. The two surfaces are related by inversion symmetry and have opposite chirality. The composite symmetry is that of $Ia\bar{3}d$ and has no overall chirality.

The physical systems that exhibit the double gyroid morphology are experimentally observed to do so at compositions less than 50 vol. %. Hence, these surfaces are no longer minimal surfaces and must be described by level surfaces or CMCs (Lambert, Radzilowski, Thomas, 1996), (Grosse-Brauckmann, 1997). The minority components constitute the labyrinths, and are embedded in a matrix of the majority component. The skeletal graphs (Schoen, 1970), (Grosse-Brauckmann, 1997) of the labyrinths bear exact resemblance to the morphology of the strontium soaps first postulated by Luzzati and Spegt.

3.5 Description Of The *Double* Gyroid

Figure 2.2 shows a schematic of one unit cell of DG, and figure 3.2a shows the skeletal graph. Examination of the skeletal graph (Schoen, 1970), (Grosse-Brauckmann, 1997) of the double gyroid in figure 3.2a shows that the structure consists of short struts or finite rods which all lie in <110> type directions. The struts define two infinite three-dimensional networks, mutually interwoven, and otherwise unconnected (Luzzati et al., 1967). Each end of a strut is joined to two others to form a node, as shown in figure 3.4. At each node, three struts meet with 120° angles and define a plane (the nodal plane) with local 3-fold symmetry, the axis of which is perpendicular to the plane of the struts. There are 8 nodes per network per unit cell and hence, 16 nodes per unit cell of double gyroid. To each node belongs $\frac{3}{2}$ struts; therefore, 12 struts are in one unit cell of a single gyroid network, and 24 struts are contained in one double gyroid unit cell.

Neighboring nodal planes are twisted by 70.53° relative to one another, as shown schematically in figure 3.4b. The twisting action gives rise to a chirality of the network.

The DG structure consists of two networks, each of opposite handedness, related to one another by inversion. In the structure there exist screw axes of the 2_1, 3_1, 3_2, 4_1, and 4_3 type, but the surface contains no straight lines or plane lines, which renders the structure without mirror symmetry.

The length of each strut (from one node to another) is $\frac{a\sqrt{2}}{4}$ where a is the translational period of the unit cell (Grosse-Brauckmann, 1997). Notice that a strut is thinnest at its center and broadens out upon approaching the node. In the small composition window in which DG is found, the length-to-diameter ratio of a strut at its center is 3:1.

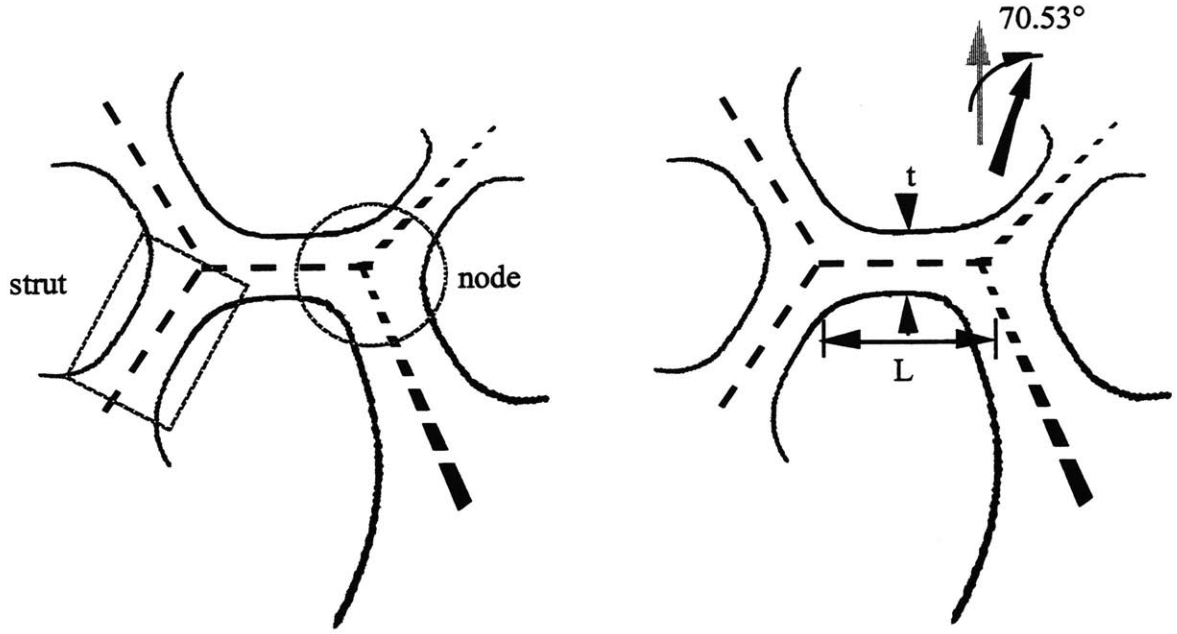

Figure 3.4: Schematic of DG struts and nodes at 34 vol. % minority (17 vol. % per network). a) A strut is indicated by the rectangle, while a node is indicated by a circle. b) Neighboring nodal planes are twisted by 70.53°, which gives rise to the spiraling or gyrating nature of the networks. At this volume fraction minority, the length-to-diameter ratio of a strut is 3:1.

Rançon and Charvolin also determined in monocrystals of the $C_{12}OE_6$ (hexa-ethyleneglycol mono n-dodecyl ether) / water system (type I) that the {211} planes are the those with the highest density of matter in the $Ia\bar{3}d$ 3D interconnected phase. In other words, for DG which consist of struts of surfactant (having the higher density) surrounded by water (having the lower density), the planes of highest density material are those of the {211} planes. In addition, the {211} planes have the highest interplanar spacings. These {211} planes correspond to the {001} planes of lamellae and {10} planes of cylinders,

which are the planes having highest density and highest interplanar spacing of their respective phases (Rançon et al., 1988). Figure 6.6b is a skeletal graph representation showing the lamellar planes and their relation to the dense {211} DG planes and to the dense {10} cylinder planes. These observations were consistent with those made of freeze-fracture planes and facets of bubbles trapped in monocrystals of the $Ia\bar{3}d$ 3D interconnected phase (DG). In particular, Delacroix et al. found in the same type of lyotropic liquid crystal system that fracture of DG occurs preferentially along the {211} planes, then along {110} planes, and lastly along {100} planes. The {211} fracture planes were very flat and more uniform with less cross-over into higher and lower planes than in either the {110} or the {100} planes, indicating that the {211} planes are the planes of highest density in the $Ia\bar{3}d$ 3D interconnected phase (Delacroix, Mariani, and Gulik-Krzywicki, 1990), (Delacroix, Gulik-Krzywicki, Mariani, and Risler, 1993). Sotta found that bubbles in a monocrystal of this same lyotropic liquid crystal system facet preferentially with {211}-type planes. The {211}-type planes having the highest density, having the largest interplanar spacing, and being preferential cleavage planes indicate that these planes are those of lowest energy.

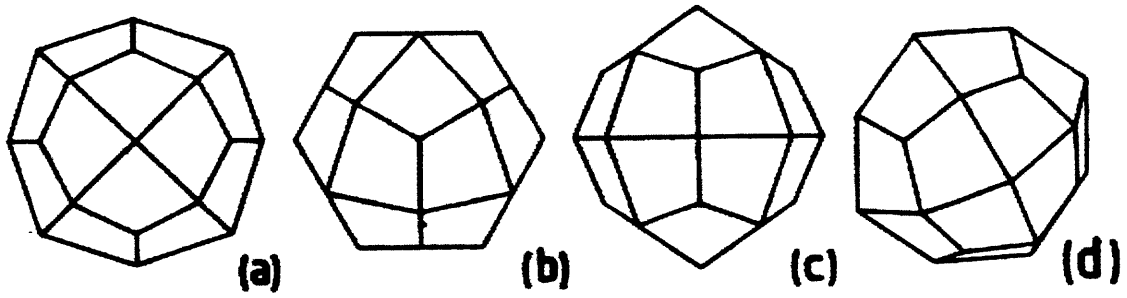

Figure 3.5: Views along different axes of a 'negative' DG crystal (air bubbles in the monocrystal) having {211} facets, as seen in the $C_{12}OE_6$ / water system (from (Sotta, 1991).

A 3D model of a crystal with {211} facets, as shown in figure 3.5, can be constructed using 8 of the unit panels shown in figure 3.6. The centers of each panel, when folded correctly, form the 3-fold axes, while the 4 corners come together to form axes with 4-fold symmetry, and the flat edges come together to form 2-fold rotation axes at the center.

Hashimoto et al. (1997), also found in a blend of SI diblock copolymer and homopolystyrene systems having 66 wt% total PS that DG freeze-fractures preferentially

along the {211} planes. For a case such as the I-rich SIS triblock copolymers used in this thesis, the "highest density planes" would correspond to those of highest PS density.

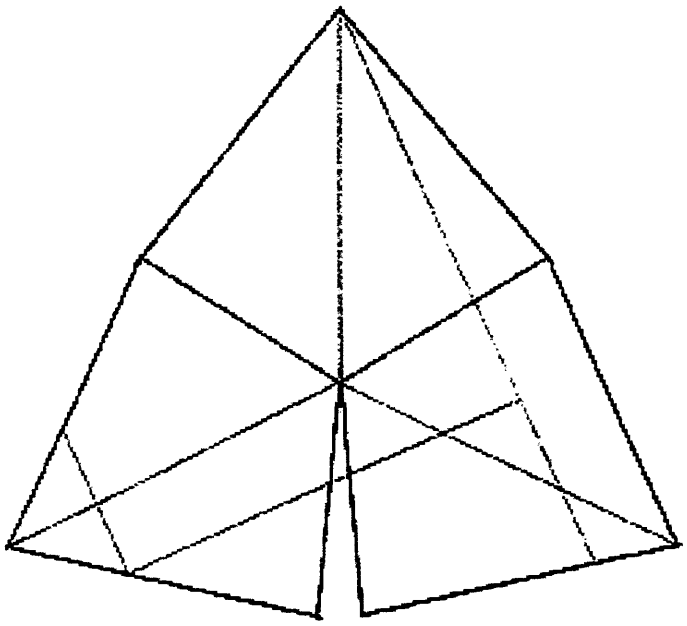

Figure 3.6 To form a unit panel, cut along the bold lines, folding along the dotted lines such that the bolded edges of the slit touch. Eight such panels can be joined together to form the 3D DG crystal having {211} type facets; each corner touches 4 others, while each side touches 1 other. (Provided by P. Sotta and M. Weber of the Laboratoire de Physique de Solides, Université Paris-Sud, Orsay Cedex, France.)

[111] Direction

The [111] direction deserves special attention because it contains the most compact, direct, and continuous paths of PS in the DG structure. There are three types of 3-fold axes in a <111> direction in the DG: the $\bar{3}$, 3_1, and 3_2 axes. One-third of the 3-fold axes are the $\bar{3}$ axes, while two-thirds of are the screw axes. The $\bar{3}$ axis consists of a stack of trifunctional nodes from alternating networks, as shown by Figure 3.10 by Rançon and Charvolin. Each node along this axis is a Wyckoff "b" position having 3-fold symmetry. This axis is the origin of the <111> projection having p6mm symmetry. Halfway between each subsequent node along the $\bar{3}$ axis is an inversion center, as indicated by the dot in figure 3.10.

The 3_1, and 3_2 axes are screw axes of opposite handedness, each belonging to a separate network. These are the most compact, direct, and continuous paths of PS in the DG structure which, as will be seen later, bear the load for the initial modulus and are the

most interesting units for interpretation of mechanical behavior in the different directions. These <111> screw axes contain 6 strut segments over a lattice repeat of $\sqrt{3}$*a, with all

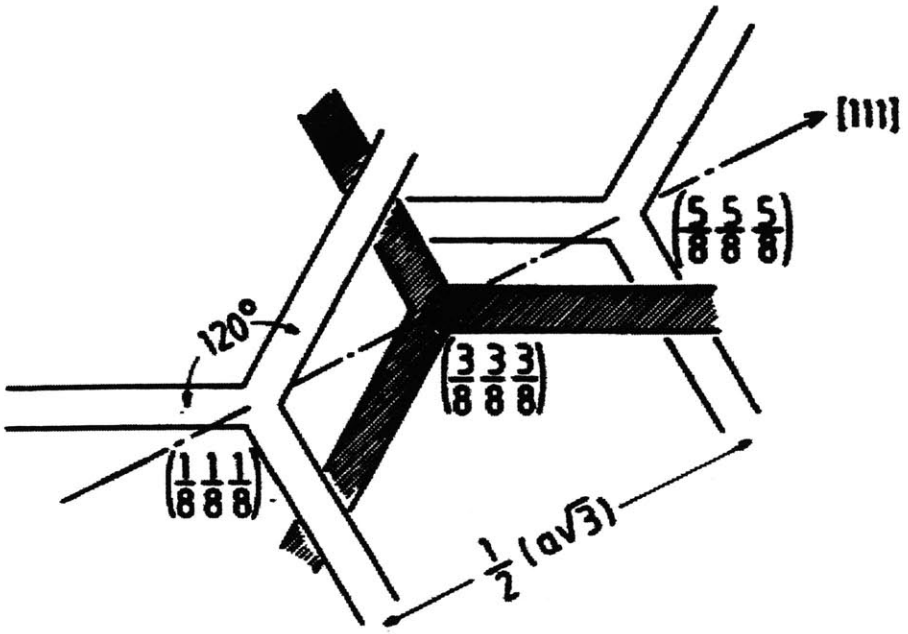

Figure 3.7: from (Rançon et al., 1987). Schematic of the $\bar{3}$ axis of the [111], which consists of a stack of nodes from alternating networks.

struts ~35° from [111] forming equal numbers of tight 3_1 or 3_2 helices. The structure has $\sqrt{3}$ of these helical PS paths per a^2 (where a is the unit cell parameter of the DG).

Transverse to the [111]

Along either the <$\bar{1}$ 10>- or <11$\bar{2}$>-type directions, the most direct continuous PS path is much more serpentine. In the [11$\bar{2}$], 10 struts span a lattice repeat of $\sqrt{6}$*a; 6 of the struts make an angle of 30° with the [11$\bar{2}$], 2 struts make an angle 54.7°, and 2 others make an angle of 73.2°. In the [$\bar{1}$ 10], 6 struts span a lattice repeat of $\sqrt{2}$*a; 4 of the struts make an angle of 60° with [$\bar{1}$ 10] and 2 struts are oriented along the [$\bar{1}$ 10] direction but these two are non-collinear. The structure has $\sqrt{2}$ of these PS paths per a^2. Perhaps the most striking aspect to note is that only serpentine paths of continuous PS struts can be found in directions transverse to the [111].

3.6 References

Alward, D. B. (1985). A Morphological Study Of A Series Of Multiarmed Star Block Copolymers Of Polyisoprene And Polystyrene. Ph. D. thesis, University of Massachusetts.

Avgeropoulos, A., V. Z.-H. Chan, V. L. Lee, D. Ngo, R. D. Miller, N. Hadjichristidis and E. L. Thomas (1999). "Synthesis And Morphological Behavior Of Silicon-Containing Triblock Copolymers For Nanolithographic Applications." Chemistry of Materials: accepted for publication.

Avgeropoulos, A., B. J. Dair, N. Hadjichristidis and E. L. Thomas (1997). "The Tricontinuous Double Gyroid Cubic Phase In Triblock Copolymers Of The Aba-Type." Macromolecules **30**: 5634-5642.

Buerger, M. J. (1956). Elementary Crystallography: An Introduction to the Fundamental Geometrical Features of Crystals. New York, John Wiley and Sons Inc.

Delacroix, H., T. Gulik-Krzywicki, P. Mariani and J.-L. Risler (1993). "Freeze-Fracture Electron Microscopy Of Lyotropic Lipid Systems. Quantitative Analysis Of Cubic Phases Of Space Group Ia3d (Q230)." Liquid Crystals **15**: 605-625.

Delacroix, H., P. Mariani and T. Gulik-Krzywicki (1990). "Image Analysis Of Freeze-Fractures Lipid-Water Cubic Phases Of Space Group Ia3d." Colloque de Physique **C7**(23): C7-119-C7-129.

Förster, S., A. K. Khandpur, J. Zhao, F. S. Bates, I. W. Hamley, A. J. Ryan and W. Bras (1994). "Complex Phase Behavior Of Polyisoprene-Polystyrene Diblock Copolymers Near The Order-Disorder Transition." Macromolecules **27**: 6922-6935.

Gobran, D. A. (1990). Phase Separation And Morphology Of Diblock And Segmented Block Copolymers. Ph. D. thesis, University of Massachusetts.

Gross, R. (1918). "Zur Frage Der Gyroedrie Des Steinsalzes." Centralblatt für Mineralogie, Geologie, und Paläontologie (January): 1-19.

Grosse-Brauckmann, K. (1997). "On Gyroid Interfaces." Journal of Colloid and Interface Science **187**: 418-428.

Groth, P. (1895). Elemente Der Physikalischen Und Chemischen Kristallographie. First Edition. München, Germany, Oldenbourg Press.

Hahn, T., Ed. (1993). International Tables for Crystallography. Dordrecht, Holland, D. Reidel Publishing Company.

Hajduk, D. A., P. E. Harper, S. M. Gruner, C. C. Honeker, G. Kim, E. L. Thomas and L. J. Fetters (1994). "The Gyroid: A New Equilibrium Morphology In Weakly Segregated Diblock Copolymers." Macromolecules **27**: 4063-4075.

Hajduk, D. A., P. E. Harper, S. M. Gruner, C. C. Honeker, E. L. Thomas and L. J. Fetters (1995). "A Reevaluation Of Bicontinuous Cubic Phases In Starblock Copolymers." Macromolecules **28**: 2570-2573.

Hashimoto, T., K. Tsutsumi and Y. Funaki (1997). "Nanoprocessing Based On Bicontinuous Microdomains Of Block Copolymers: Nanochannels Coated With Metals." Langmuir **13**: 6869-6872.

Klockmann (1891). Lehrbuch der Mineralogie. First Edition. Stuttgart, Germany, Ferdinand Enk-erlag.

Lambert, C. A., L. H. Radzilowski and E. L. Thomas (1996). "Triply Periodic Level Surfaces As Models For Cubic Tricontinuous Block Copolymer Morphologies." Philosophical Transactions of the Royal Society of London A **354**: 2009-2023.

Laurer, J. H., D. A. Hajduk, J. C. Fung, J. W. Sedat, S. D. Smith, S. M. Gruner, D. A. Agard and R. J. Spontak (1997). "Microstructural Analysis Of A Cubic Bicontinuous Morphology In A Neat Sis Triblock Copolymer." Macromolecules **30**: 3938.

Luzzati, V., H. Delacroix, A. Gulik, T. Gulik-Krzywicki, P. Mariani and R. Vargas (1997). "The Cubic Phases Of Lipids" in Lipid Polymorphism and Membrane Properties. R. M. Epand. New York, NY, Academic Press. **44:** 3-24.

Luzzati, V. and P. A. Spegt (1967). "Polymorphism Of Lipids." Nature **215**: 701-704.

Luzzati, V., A. Tardieu, T. Gulik-Krzywicki, E. Rivas and F. Reiss-Husson (1968). "Structure Of The Cubic Phases Of Lipid-Water Systems." Nature **220**: 485-488.

Matsushita, Y., J. Suzuki and M. Seki (1998). "Surfaces Of Tricontinuous Structure Formed By An Abc Triblock Copolymer In Bulk." Physica B. Condensed Matter **248**: 238.

Mitchell, D. J., G. J. T. Tiddy, L. Waring, T. Bostock and M. P. McDonald (1983). "Phase Behaviour Of Polyoxyethylene Surfactants With Water." Journal of the Chemical Society, Faraday Transactions I **79**: 975-1000.

Oxford University Press (1971). The Compact Edition of the Oxford English Dictionary. Oxford, England.

Rançon, Y. and J. Charvolin (1987). "Displacement Disorder In A Liquid Crystalline Phase With Cubic Symmetry." Journal de Physique **48**: 1067-1073.

Rançon, Y. and J. Charvolin (1988). "Epitaxial Relationships During Phase Transformations In A Lyotropic Liquid Crystal." Journal of Physical Chemistry **92**: 2646-2651.

Rinne, F. (1922). Das feinbauliche Wesen der Materie nach dem Vorbilde der Kristalle. Berlin, Gebrüder Bornträger.

Sakurai, S., H. Irie, H. Umeda, S. Nomura, H.-H. Lee and J.-K. Kim (1998). "Gyroid Structures And Morphological Control In Binary Blends Of Polystyrene-Block-Polyisoprene Diblock Copolymers." Macromolecules **31**: 336.

Schoen, A. H. (1970). Infinite periodic minimal surfaces without selfintersections, NASA.

Scriven, L. E. (1976). "Equilibrium Bicontinuous Structure." Nature **263** (5573): 123-125.

Sotta, P. (1991). "Equilibrium Shape Of Lyotropc Cubic Monocrystals." Journal de Physique France **1**: 763-772.

Spegt, P. P. A. and A. E. Skoulios (1966). "Structure Des Savons De Strontium En Fonction De La Temperature." Acta Crystallographica **21**: 892-897.

Chapter 4: Experimental Procedures

Section 4.1 describes the procedures to characterize the morphology of the novel phases. Section 4.2 details the orientation technique, roll casting, and further describes the symmetry of the materials so processed. Section 4.3 describes the experimental procedures for tensile sample preparation and mechanical testing.

4.1 General Procedures for Morphological Characterization

This section details the methods for morphological characterization. Section 4.2.1 describes the procedures and parameters for experimental data, while section 4.2.2 describes the modeling of the DG and DD morphologies, which are then used to generate expected TEM and diffraction images. The experimental and theoretical images are then compared to for insight into differentiation between the two morphologies.

4.1.1 Experimental Procedures

For SAXS and TEM characterization, 0.7 -1.0 mm thick films of the materials were cast from a dilute solution (~5 wt%) with a nonselective solvent (toluene) in glass crucibles over a period of 1 week at ambient conditions. Irganox, a stabilizer was added at < 0.25wt % to the solution in order to prevent oxidation of the isoprene double bond when annealed at high temperature. Films were easily removed from the glass crucibles by submerging the crucible in liquid nitrogen and quickly pushing out the hardened disk. The polymer films were dried for 2 days under vacuum at room temperature and were subsequently annealed at 120° C for 10 days under vacuum to promote long range order and equilibrium microstructure.

4.1.1.1 Small-Angle X-ray Scattering

The X-ray diffraction (SAXS) data were acquired at the Time-Resolved Diffraction Facility (station X12B) at the National Synchrotron Light Source at Brookhaven National Laboratory (BNL) using a custom-built two-dimensional gas-delay line detector (10 x 10 cm, 512 x 512 pixels) (Capel, Smith, and Yu, 1995). The optical system provides a doubly-focused (spot size, 0.5 x 0.5 mm fwhm) monochromatic X-ray beam with a wavelength of $\lambda = 1.54$ Å. Sample-to-detector distances ranged from 215-260 cm.

SAXS data is represented by plots of scattered intensity as a function of the scattering vector q, which is defined as

$$q = \frac{4\,\pi\,\sin\theta}{\lambda} \tag{4.1}$$

where θ is half of the scattering angle 2θ, and λ is the wavelength of the x-rays. Using this relation and Bragg's law for scattering,

$$\lambda = 2\,d_{hkl}\,\sin\theta, \tag{4.2}$$

the spacing of the scattering hkl planes, d_{hkl}, are related to the scattering vector by the following equation:

$$d_{hkl} = \frac{2\,\pi}{q_{hkl}} \tag{4.3}$$

For polycrystalline or isotropic samples, the scattered intensity is weighted with q^2 in order to take into account the spreading of intensity in reciprocal space over the surface of a sphere, the area of which increases as q^2. Observed scattering peaks are then assigned from the subsequent plots. The scattering ratios $\frac{q_n}{q_1}$ are then compared with the theoretically allowed ratios of different plane or space groups found in the International Tables for Crystallography (Hahn, 1993). Table 4.1a lists the theoretically allowed reflections of space groups of the classical morphologies, and table 4.1b lists those of the novel DG and DD phases.

In a cubic system (to which DD and DG belong), the ratio of two q-vectors $q_{h_1k_1l_1}$ and $q_{h_2k_2l_2}$ is

$$\frac{q_{h_1k_1l_1}}{q_{h_2k_2l_2}} = \frac{\sqrt{h_2^{\,2}+k_2^{\,2}+l_2^{\,2}}}{\sqrt{h_1^{\,2}+k_1^{\,2}+l_1^{\,2}}}, \tag{4.4}$$

whereas in a hexagonal system (to which cylinders belong), the ratio of two q-vectors $q_{h_1k_1}$ and $q_{h_2k_2}$ is

$$\frac{q_{h_2k_2}}{q_{h_1k_1}} = \frac{\sqrt{h_2^{\,2}+k_2^{\,2}+h_2{*}k_2}}{\sqrt{h_1^{\,2}+k_1^{\,2}+h_1{*}k_1}}. \tag{4.5}$$

Since

$$d = \frac{2\pi}{q}, \tag{4.6}$$

q's are inversely proportional to d's in any given coordinate system, and

$$\frac{d_1}{d_2} = \frac{q_2}{q_1}. \tag{4.7}$$

For example, in the hexagonal coordinate system,

$$\frac{q_{11}}{q_{10}} = \sqrt{3} \quad \text{and} \quad \frac{d_{11}}{d_{10}} = \frac{1}{\sqrt{3}} \tag{4.8}$$

The spacing of any (hkl) plane in the cubic system is related to its indices and the lattice parameter, a, of the unit cell by the identity

$$d_{hkl} = \frac{a}{\sqrt{h^2 + k^2 + l^2}}, \tag{4.9}$$

while the analog of (hk) planes in the hexagonal system is related to its indices by

$$d_{hk} = \frac{a}{\sqrt{h^2 + k^2 + hk}} \tag{4.10}$$

4.1.1.2 Transmission Electron Microscopy

For TEM investigation, 500-1500 Å thick sections were cryo-ultramicrotomed at approximately -120° C using a Reichert-Jung FC 4E cryo-ultramicrotome equipped with a diamond knife. Although the section thicknesses varied between 500-1500 Å thick, only the thinnest sections (500-1000 Å thick) were used for the images and their subsequent optical transforms (OTs). The thickness of the high symmetry projection grains was determined by spraying two different sizes of PS spheres, one size on each side of the section using an atomizer. From images taken before and after a known amount of specimen tilt, measurement of the relative separation distance of a pair of different size spheres permited calculation of the average sample thickness. Sections were picked up on 600-mesh copper grids and then placed in the vapors of a 4% osmium tetroxide (OsO_4)-

water solution for two hours for selective staining of the PI phase. A JEOL 200CX electron microscope, operated at 200kV in the bright field mode, was used to examine the stained sections. Images of high symmetry were obtained using a goniometer stage with ±45° tilt capability on the x-axis and ±27° on the y-axis of a double tilt holder. The double tilt holder in the TEM allowed selection of grains of the required orientation.

Optical transforms (OTs) of the TEM negatives were taken with a custom-built optical diffractometer using a 5mW polarized UniPhase HeNe laser with a wavelength of 633 nm. The diffractometer was equipped with a camera shutter, and diffraction patterns were recorded using Polaroid type 55 film. The diffraction patterns or OTs of high symmetry areas were in most cases very clear, exhibiting up to third order peaks, and were qualitatively comparable with those obtained from fast Fourier transforms (FFTs) of appropriate computer simulated projections. Several different exposures were required of the OTs in order to capture and observe different order diffraction peaks due to the limited dynamic range of the film. Image areas on the negatives (from which OTs were taken) were scanned at high resolution (1200 - 2400 dpi) and fast Fourier transformed (FFT) using NIH Image, version 1.28b6.

Table 4.1a: Theoretically Allowed Reflections of Sphere, Cylinder, and Lamellar Morphologies

Spheres	$Im\bar{3}m$	Cylinders	p6mm	Lamellae	pm
reflection	$\frac{q_{hkl}}{q_{100}}$	reflection	$\frac{q_{hk}}{q_{10}}$	reflection	$\frac{q_{hkl}}{q_{100}}$
{100}	1.00	{10}	1.00	{100}	1
{110}	$\sqrt{2}$, 1.41	{11}	$\sqrt{3}$, 1.73	{200}	2
{200}	$\sqrt{3}$, 1.73	{20}	$\sqrt{4}$, 2.00	{300}	3
{210}	$\sqrt{4}$, 2.00	{21}	$\sqrt{7}$, 2.65	{400}	4
{300}	$\sqrt{5}$, 2.24	{30}	$\sqrt{9}$, 3.00	{500}	5
{220}	$\sqrt{6}$, 2.45	{22}	$\sqrt{12}$, 3.46	{600}	6
{310}	$\sqrt{7}$, 2.65	{31}	$\sqrt{13}$, 3.61	{700}	7
{400}	$\sqrt{8}$, 2.83	{40}	$\sqrt{16}$, 4.00	{800}	8
{320}	$\sqrt{9}$, 3.00	{32}	$\sqrt{19}$, 4.36	{900}	9
{410}	$\sqrt{10}$, 3.16	{41}	$\sqrt{21}$, 4.58	{10 0 0}	10
{500}	$\sqrt{11}$, 3.32	{50}	$\sqrt{25}$, 5.00	{11 0 0}	11
{330}	$\sqrt{12}$, 3.46	{33}	$\sqrt{27}$, 5.20	{12 0 0}	12
{420}	$\sqrt{13}$, 3.61	{42}	$\sqrt{28}$, 5.29	{13 0 0}	13
{510}	$\sqrt{14}$, 3.74	{51}	$\sqrt{31}$, 5.57	{14 0 0}	14

Table 4.1b: Theoretically Allowed Reflections Double Gyroid and Double Diamond Morphologies

Double Gyroid	$Ia\bar{3}d$	Double Diamond	$Pn\bar{3}m$
reflection	$\frac{q_{hkl}}{q_{211}}$	reflection	$\frac{q_{hkl}}{q_{110}}$
{211}	1.00	{110}	1.00
{220}	$\sqrt{\frac{4}{3}}$, 1.16	{111}	$\sqrt{\frac{3}{2}}$, 1.22
{321}	$\sqrt{\frac{7}{3}}$, 1.53	{200}	$\sqrt{2}$, 1.41
{400}	$\sqrt{\frac{8}{3}}$, 1.63	{211}	$\sqrt{3}$, 1.73
{420}	$\sqrt{\frac{10}{3}}$, 1.83	{220}	$\sqrt{4}$, 2.00
{332}	$\sqrt{\frac{11}{3}}$, 1.91	{221}	$\sqrt{\frac{9}{2}}$, 2.12
{422}	$\sqrt{4}$, 2.00	{310}	$\sqrt{5}$, 2.24
{431}	$\sqrt{\frac{13}{3}}$, 2.08	{311}	$\sqrt{\frac{11}{2}}$, 2.35
{521}	$\sqrt{5}$, 2.24	{222}	$\sqrt{6}$, 2.45
{440}	$\sqrt{\frac{16}{3}}$, 2.31	{321}	$\sqrt{7}$, 2.65
{532},{611}	$\sqrt{\frac{19}{3}}$, 2.52	{400}	$\sqrt{8}$, 2.83
{620}	$\sqrt{\frac{20}{3}}$, 2.58	{322}	$\sqrt{\frac{17}{2}}$, 2.91
{631}	$\sqrt{\frac{23}{3}}$, 2.77	{411}, {330}	$\sqrt{9}$, 3.00
{721}	$\sqrt{9}$, 3.00	{331}	$\sqrt{\frac{19}{2}}$, 3.08

4.1.2 Modeling of the DG and DD Morphologies

Level surface models are convenient to model 3-D periodic, interconnected microphase- separated structures (Lambert, Radzilowski, and Thomas, 1996). The level surfaces employed are simple trigonometric functions which maintain the symmetries of a given space group. Families of level surfaces F(x, y, z) can be constructed by variation of the constant, t = F(x, y, z). While level surfaces have neither constant mean curvature nor constant thickness, they can provide *connected* surfaces of appropriate symmetry and volume fraction. To construct a level surface we used the lowest order allowed Fourier component of a space group and chose a particular value of the constant t which controls the volume fraction contained within the connected network. For the structures of interest the following equations for G (space group $I4_132$, {110} Fourier component) and D (space group $Fd\bar{3}m$, {111} Fourier component) were used.

$$\text{single G: } \sin x \cos y + \sin y \cos z + \sin z \cos x = t \tag{4.10}$$

$$\text{single D: } \sin x \sin y \sin z + \sin x \cos y \cos z + \cos x \sin y \cos z + \cos x \cos y \sin z = t \tag{4.11}$$

The t = 0 level set for G approximates Schoen's G minimal surface (1970) and for D approximates Schwarz's D surface (1890).

By taking *pairs* of surfaces $F(x, y, z) = \pm t$ the double gyroid structure with super group $Ia\bar{3}d$ and the double diamond structure with super group $Pn\bar{3}m$, are realized. Of course, single gyroid and diamond structures can also be modeled. Simulations for different unit cell orientations, sample thicknesses, and slice locations of DG and DD within the unit cella were done on a Silicon Graphics Indigo 2 workstation using the software TEMsim developed by Hoffman (Hoffman and Hoffman). The simulations are based on the ray tracing technique in which a ray tracing algorithm is used for making 2-dimensional projections from 3-dimensional models of the candidate geometries described by IMDSs (Anderson, Bellare, Hoffman, Hoffman, Gunther, and Thomas, 1992). For example, in order to mathematically describe the IMDS of the DG structure, which is comprised of 2 triply periodic, tricontinuous networks embedded in a matrix, space was divided into 3 continuous regions by taking pairs of level surfaces. Each network phase had a volume fraction equal to half of the total minority volume fraction and the matrix had the volume fraction of the majority component. The matrix was modeled to yield the desired majority volume fraction, which was 0.66 for the 34 vol %S triblock. For DG surfaces, $t = \pm 1.0$ corresponded to a volume fraction of 0.66, whereas for DD surfaces, t

= 0.9 corresponded to a volume fraction of 0.67. Once a level surface was generated, it was sliced to a desired thickness defined by two parallel planes (hkl) oriented normal to a direction specified by the Miller indices [hkl]. Finally the two-dimensional projection along [hkl] was made using the ray tracing algorithm. This procedure is identical to microtoming a sample and examining it using TEM.

FFTs were made from the simulated TEM images. Approximately 32 x 32 unit cells were montaged together in a 1024 x 1024 pixel array. A program written by Lescanec, uses the 1024 x 1024 square input, multiplied by a Hanning window to reduce edge effects, performs the FFT, and outputs the data on a log-scale as a 2-dimensional image (Press, Flannery, Teukolsky, and Vetterling, 1988).

4.2 Imparting Orientation

As discussed in section 2.8.3, the elastic modulus of a single-crystalline material is a fourth rank tensor. Cubic materials, having the highest symmetry of the crystal classes and having only three independent elastic constants (as discussed in section 2.8.3), are still elastically anisotropic. Any given grain of material which is not inherently isotropic may have a different elastic reponses in different directions. The modulus of a polygranular or isotropic sample is the superposition of all of the moduli of different orientations of randomly oriented grains, such that the response of a given direction cannot be deconvoluted from the single measured value. Therefore, in order to sample the anisotropy of the modulus, oriented samples need to be produced.

Oriented or textured films were made by the roll-casting process. The roll-casting orientation technique was developed by Albalak in the Thomas laboratory (1993, 1994). High-quality, near-single crystal sphere, cylinder, and lamellar morphology films of SIS and SBS films of have been produced by rollcasting triblock copolymers of the respective compositions in the past (Albalak and Thomas, 1994; Albalak, Thomas, and Capel, 1997; Prasman and Thomas, 1998). This section reports on the roll casting apparatus and process, as well as the symmetries of oriented cylinder and lamellar morphologies.

4.2.1 Rollcasting Apparatus and Process

Figure 4.1 shows a schematic diagram of a roll-caster. Two parallel rollers, one made of of teflon, the other made of stainless steel, counter-rotate with a fixed frequency. Each roller is independently motor-driven at constant speed. Frequencies range from 5 rpm to 40 rpm, which correspond to shear rates of approximately 0.1 to 1.0 sec $^{-1}$, depending on the gap size. The rollers are separated by a gap, which can be set by a micrometer gauge, and usually ranges between 0.05 mm - 2 mm. This process has been used in this laboratory in the past to produce films of uniform thickness with highly oriented sphere, cylinder, and lamellar morphologies. The self-assembly of microdomains characteristic of block copolymers occurs in the presence of a flow field, thereby producing highly oriented films. The extensional flow component is a key factor in this process for orientation. Practical experience shows that the factors that prolong the order-disorder transition period of the polymer while in the flow field improve the degree and quality of orientation in the film. Hence, the more time the domains have to improve their order over a large area, the better oriented are the subsequent samples.

A concentrated polymer solution is prepared several days in advance of roll-casting. Typical solvents are toluene and cumene. Toluene, shown in figure 4.2a, is a non-preferential solvent for PS and PI but has the higher vapor pressure (boiling point: 111°C)

of the two solvents. Cumene, a slightly heavier but chemically similar molecule, shown in figure 4.2b is an even less-preferential solvent for PS and PI (Annighoefer and Gronski, 1983), and has a lower vapor pressure (boiling point: 152-154°C) than toluene. Therefore, roll-casting and the subsequent drying of the films take longer with cumene than with toluene. However, the cumene allows the molecules and domains more time to orient before reaching the order-disorder concentration. Either solvent can be used, depending on the preference of the user.

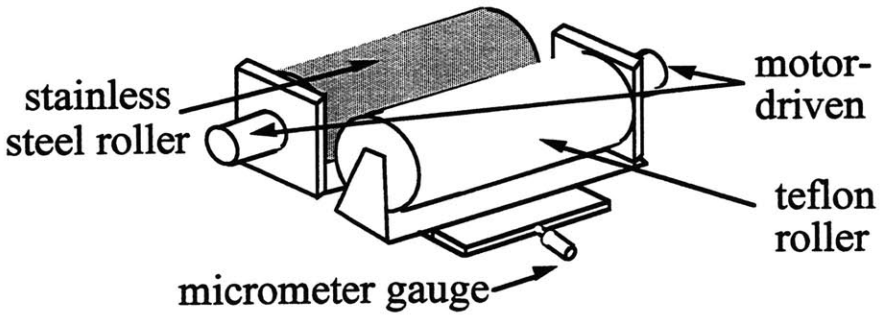

Figure 4.1 : Schematic of the rollcaster. The basic parts include two motor-drivien counter-rotating rollers, one of teflon, the other of stainless steel, and a micrometer gauge to set the gap distance between rollers.

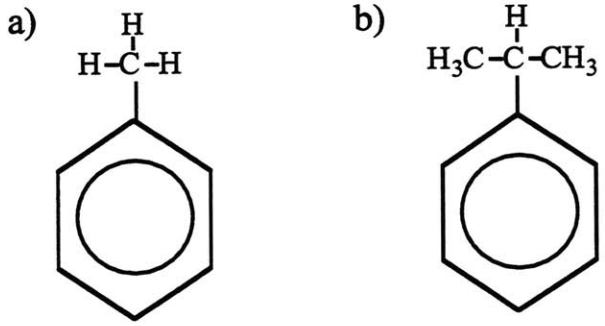

Figure 4.2: a) Toluene and b) Cumene

The length of dissolution time and amount of solvent to be used, are affected by several factors, such as the molecular weight and architecture of the polymer and the amount of polymer to be dissolved. Diblock or triblock polymer molecular weights up to ~80,000 g/mol typically require solution concentrations of 1g polymer to at least 2 ml solvent, which renders the solution with a warm-honey-like consistency. More concentrated solutions, i.e., with a molasses-like consistency, take longer for uniform mixing. More dilute solutions, i.e., with a vegetable oil-like consistency, require smaller

gap sizes both at start and at each subsequent addition in order to prevent the solution from dripping through the gap, and more iterations are needed. Usually 1-2 days dissolution time are sufficient for 10g of polymer or less, while 3-4 days are required for a sample of 20-30g. High molecular weight polymers, i.e., molecular weights > 200,000 g/mol, and complex molecules, such as stars, require solution concentrations of 1g polymer to 3-4 ml solvent, and 1-2 weeks dissolution time at room temperature. The use of either stirbars or heat are suggested in aiding the dissolution of large amounts of polymer.

The basic method of roll-casting a film using this technique is briefly illustrated in figure 4.3. The rollers are first set to the desired rpm and the gap distance to 0.05 mm. Then, a sufficient amount of solution is poured into the gap region to uniformly coat both rollers. A reservoir of solution is placed underneath the rollers, and a cover is used to enclose the area in order to create a solvent-rich atmosphere to slow evaporation of the solvent from the polymer solution under roll cast flow. As the solvent evaporates, the film eventually becomes tacky and gel-like and transfers to the stainless steel roller due to the higher surface tension. If films thicker than 0.3 mm are desired, then just after the film adheres to the steel roller, the gap region is increased by another 0.2-0.5 mm, and more solution is poured onto the rollers. This is repeated until the size of the gap reaches the desired thickness of the film.

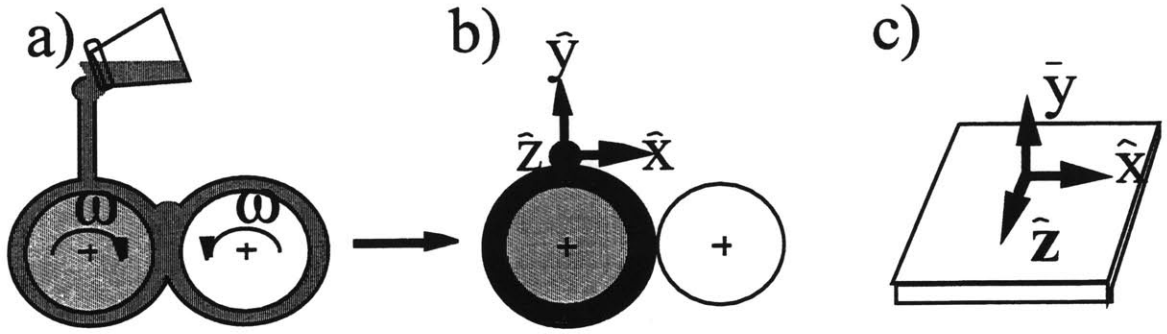

Figure 4.3: a) Roll-casting a film from solution. The rollers counter-rotate at the same angular velocity. As the solvent evaporates, the polymer film adheres to the steel roller, as in figure 2b. b&c) Definition of the rollcast axes; $\hat{x}$ is in the flow direction, $\hat{y}$ is normal to the film, and $\hat{z}$ is in the plane of the film along the neutral axis.

Once the final-thickness film transfers to the steel roller, the gap is increased to back the rollers away from one another, and both the evaporation shield and solvent reservior are removed. The steel roller with polymer is allowed to spin freely and uncovered for another 15-30 minutes to allow solvent to evaporate from the film to improve its mechanical

integrity. Then, the steel roller is stopped and a cut or depression across the surface is made using a bevelled wooden edge cut from the end of a cotton applicator or tongue depressor. As the film still has 5-10% residual solvent (Honeker, 1997), the film is left on the roller overnight to dry, so as to increase the mechanical integrity of the film. If removed right away, the soft, solvent-swollen film is susceptible to damage during removal and handling.

To remove the dried film from the steel roller, a non-solvent, such as methanol or ethanol is sprayed along the cut during and then between the polymer film and the steel surface in order to facilitate removal by reducing the surface tension that the polymer has for the roller surface. The finished film is removed from the roller and allowed to dry several minutes. Edge material can trimmed away subsequently with a razor blade.

The film is then flattened between two teflon sheets separated by a spacer, usually 3-4 layers of microscope slides, giving the film enough room to freely expand or contract, so as to allow residual stresses to be relieved without introducing new constraints and so as not to trap large air pockets. In this manner, the film is dried in vacuum for two days to remove residual solvent. It is important to note that if solvent is trapped within the film and taken to high temperature, bubbles will be created in the film. While still under vacuum, the temperature is then slowly ramped to the annealing temperature over a period of 2 days, so that the film softens and relaxes gradually and air pockets are not trapped underneath the film. The slow ramp-up also reduces the amount of temperature over-shoot exceeding the set-point temperature. Films are annealed for 1-3 weeks at $T > T_g^{PS}$. For SIS materials, 120°C is the typical annealing temperature, as annealing at higher temperature will run the risk of PI degradation. Antioxidant, e.g., Irganox, is added at amounts < 1 wt.% of the polymer to inhibit degradation. The length of annealing time depends on the intent of the annealing process. To improve long range order and rid of residual stresses incurred by the flow field, annealing for one week is sufficient. This is usually the case for cylinders and lamellae. To induce a phase transformation from cylinders to DG, annealing for either much longer times (2-4 weeks at 120°C for MW ~ 50 or 60K) or higher temperatures (T_{ODT} - 5°C for ~2-3 days) is necessary, depending on the area and thickness of the film, as well as the T_{ODT} of the polymer.

Currently, there are two rollcasters available in this laboratory. The first, which accomodates commercially available polymers i.e., large quantities, has rollers with a length of 20 cm, and diameters of 1.9 cm . This results in films with dimensions 20 cm x 6 cm. The thickness of the film can range between 0.5 mm to 2 mm. Thus, in order to make a roll-cast film on this apparatus, at least 6 grams of material are needed.

To accommodate situations when only a small amount (< 5g) of polymer is available, a mini roll-caster was constructed with two possible roll diameters of 1.0 cm (3/8 inch) or 1.6 cm (5/8 inch), roller length of 2.5 cm (1 inch), and gap distances 0.5 to 2 mm. With this set-up, films of dimensions 2.5 cm x 3 cm x 0.5 mm can be produced. This reduces the minimum materials requirements to 0.8 grams of polymer. In addition, heating capabilities have been incorporated into the design to allow for temperature studies. The rollers are heated by cartridge heaters just beneath the teflon and stainless steel sheaths. The temperature of the surface of each of the rollers is monitored by separate thermocouple probes. Likewise, the temperature of each of the rollers is adjusted separately by individual temperature controllers. The heaters can accommodate temperatures up to 300 °C. This option allows films to be rolled out at elevated temperatures. Figure 4.4 is a schematic of the mini rollcaster.

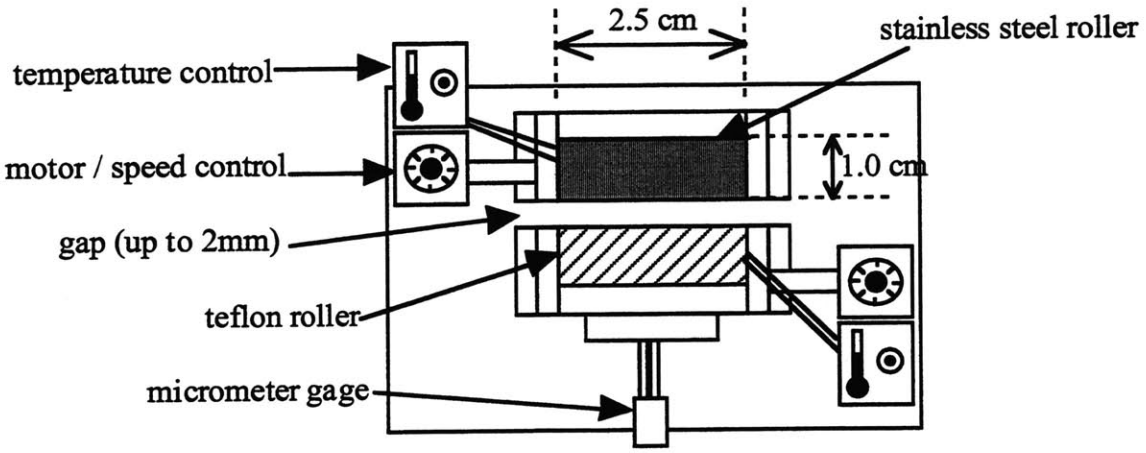

Figure 4.4: Schematic of the mini rollcaster, with heating capabilities. The rollers are 2.5 cm long and 1 cm in diameter.

Roller speeds on the larger rollcaster can range from 5 rpm to 40 rpm, with a suggested velocity at 9 rpm (Honeker, 1997). However, the higher the roller velocity, the more the polymer chains are stretched and the more distorted the domains become due to the applied flow field. Studies done on materials rolled at high velocity (40 rpm) have shown that annealing the films induces large dimensional changes in the domains caused by the relaxations of stretched molecules (Albalak, Thomas, and Capel, 1997).

Optimum roller velocities (for best film orientation) on the mini rollcaster have been found to be 22-23 revolutions per minute (rpm). The speed of the steel roller is set slightly faster than the teflon roller to promote adhesion to the steel roller; hence, the steel roller is set to 23 rpm and the teflon to 22 rpm.

4.2.2 Symmetry of Roll Cast Morphologies

During the roll-casting process the microdomains self-assemble in the presence of a flow field, which biases the structural symmetry. The resulting film will have a morphology which is the compromise between three factors: the symmetry which is imposed by the flow field, minimizing the interfacial area between the components, and minimizing chain stretching. Curie's principle states that under a large applied field the symmetries which persist in the resulting material will be those which are common to both the crystallographic point group of the sample and the symmetry group of the applied field. Curie's principle, however, formally applies to materials whose microstructure or domain structure is already formed. In roll-casting processes in which the microstructure is not already formed, the applied field can bias the orientation of the microstructure but it does not necessarily limit the resulting symmetry of the film to that common to the process.

The roll casting process theoretically produces films with symmetry $\frac{2}{m}\frac{2}{m}\frac{2}{m}$, or 2mm symmetry along each of the three axes normal to the roll cast film planes. This is shown in figures 4.5 and 4.6. Hexagonally packed cylinders have p6mm symmetry, and lamellae have pmhyu symmetry, both of which have at least 2mm symmetry. In the plane of the roll-cast film, it is found that cylinders and lamellae align themselves along the direction of the flow field, much like dipoles in an applied field. Because the lamellar symmetry and the symmetry of any of the planes of a roll cast film are the same, the packing and arrangement of the lamellae in each direction is straightforward, arranged 2mm to conform to the directions of flow. Most films of roll-cast-oriented lamellae have been found to lie perpendicular to the roll-cast plane but in the direction of flow, as shown in figure 4.6 b (Albalak, Thomas, and Capel, 1997),. However, under some conditions, the lamellae lie in the xz plane in the direction of flow (Albalak and Thomas, 1993). Cylinders have additional symmetry requirements which may or may not be accomodated. It is experimentally observed, however, that in the plane perpendicular to the direction of flow, cylinders have long range hexagonal p6mm arrangement with the (10) planes parallel to the xz plane, as shown in figure 4.6 a (Albalak, Thomas, and Capel, 1997; Honeker, 1997). Schulz et al. (Schulz, Bates, Almdal, and Mortensen, 1994) also noted that shear induces the (10) hexagonal plane parallel to the shear plane. It is this plane in which the chain stretching and packing requirements are satisfied and the supergroup symmetry of the morphology is evident.

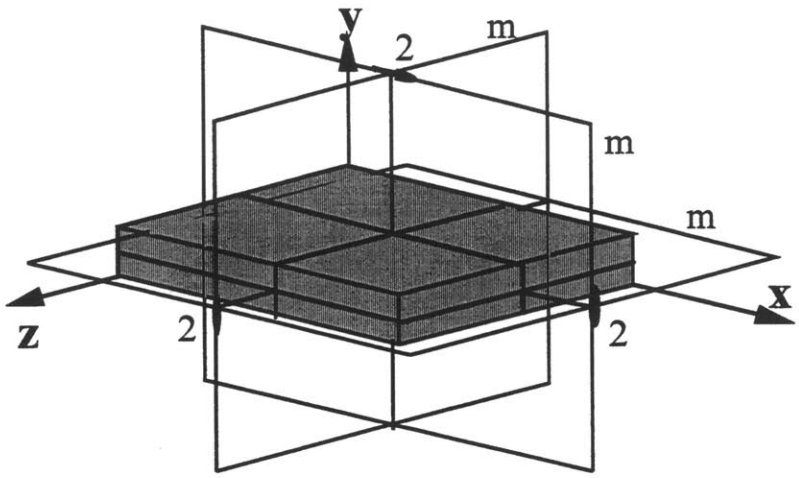

Figure 4.5: Theoretical symmetry of a roll cast film. Each face has 2mm plane symmetry, giving an overall $\frac{2}{m}\frac{2}{m}\frac{2}{m}$ point group symmetry.

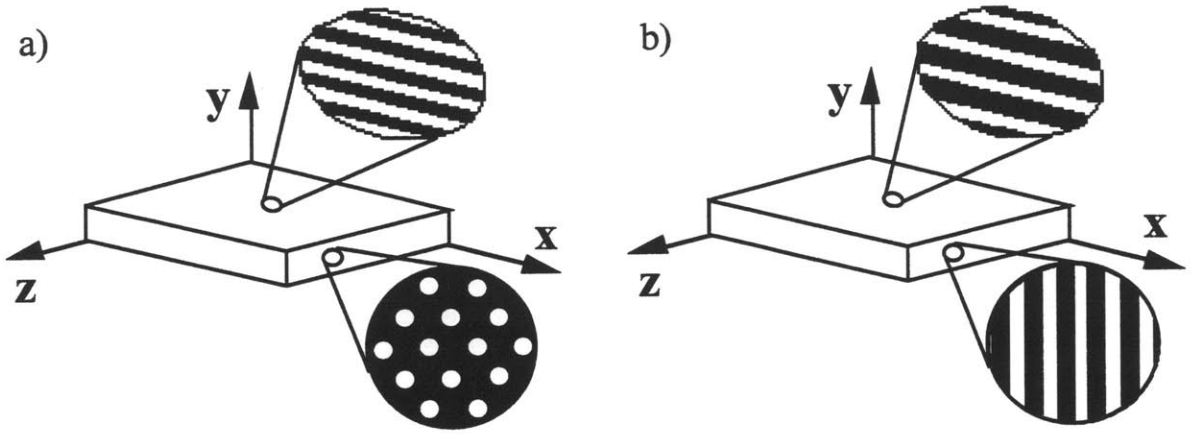

Figure 4.6: Schematic of the roll-cast morphology of cylinders and lamellae. The roll cast cylinders lie in the plane of the roll cast film, and the roll cast lamellae lie perpendicular to the plane of the film, in the direction of the roll cast direction.

4.3 Experimental Procedures for Mechanical Testing

Then methods used for experimental observation of the mechanical behavior of the DG, namely sample preparation, Brookhaven procedures, and high voltage crosslinking of stretched samples, are described in the following section.

4.3.1 Tensile Specimen Preparation

Tensile samples approximately 1.5 mm wide were cut from the 0.67 mm - 1 mm thick roll cast or static cast films. Samples were taped with the preferred orientation to a wooden block with lines drawn for guides. A razor blade was positioned over a line, and a hammer was used to drive the razor blade down, cutting through the rubbery material (two people are usually necessary: one to hold the razor blade in place, the other to hammer). This method was used instead of stamping from steel-ruled dies with an Arbor press (as described in Honeker's thesis (1997) because it was found to save material, and the orientation of the cut sample relative to the film could be better controlled for the smaller films produced by the mini-roll caster.

As the samples are stretched to high elongations the force of retraction increases, and at the same time the samples become thinner, thereby increasing the possibilities of slippage out of the grips. To prevent (minimize) such slippage, saw-toothed sample grips were machined, as shown in figure 4.7, for both the mini tensile tester and the Instron tensile tester. However, these teeth are points of stress concentration and samples have a tendency to break at or within the grips.

To minimize the effect of the stress concentrations, bevelled endpieces are attached to the ends of the sample. These end pieces are cut from strips of an abundant polymer, usually simple cast commercially available cylinder or lamellar SIS or SBS triblocks, with about the same width as the tensile samples. The endpieces are bevelled to provide a gradual slope to the sample and minimize the stress concentration of a step-function increase in thickness end piece.

Just a small amount of toluene is brushed onto the underside (the surface having larger area) of 4 endpieces, which are subsequently pressed onto the tops and bottoms of each end of the sample, as shown in figure 4.7. The toluene solvates both the polymer on the endpieces and the surface of the sample such that polymer chains from either surface interdiffuse; only a diffusion distance of the chain end-to-end distance, R_g, is needed for the two pieces to become welded. The sample then is allowed to dry several hours before testing.

The sample initial gauge length, L_o, is usually between 9 and 14 mm long.

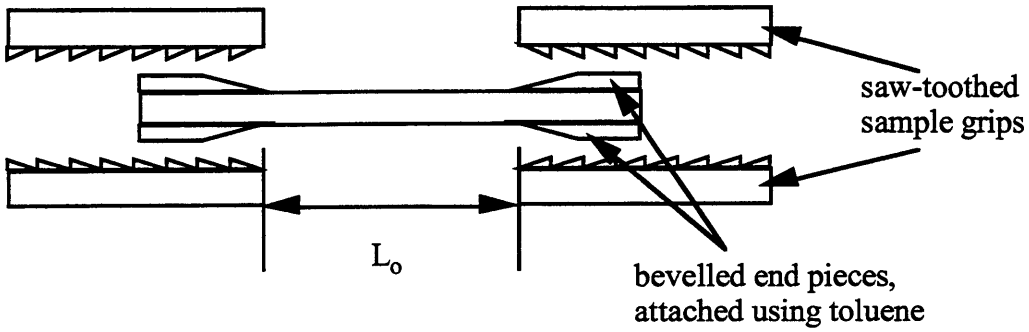

Figure 4.7: Schematic of the saw-toothed sample grips, and the sample to be stretched with the attached end pieces. L_o is measured as the length between the edges of the end pieces.

4.3.2 Deformation Stages

Two types of tensile testers were used. The Instron 4501 tester was used to gather the data used in compiling the engineering properties, while the Mini tester was used at Brookhaven for in-situ SAXS-deformation studies.

4.3.2.1 Instron Tester

An Instron 4501 deformation stage equipped with a 10N or 5kN load cell was used to gather the statistical tensile data, and the stress-strain curves were compared with those obtained on the strip chart recorder at Brookhaven. The software Instron Series IX was run on a PC which was interfaced to the 4500 Instron controller.

Experimental conditions similar to those at Brookhaven were used with the Instron in order to have a basis for comparison of the mechanical data. Samples 9-15 mm in gauge length were stretched to 600% and back at a constant crosshead velocity of 2.6 mm/min. Samples were held using the above-mentioned saw-toothed faces under 75 psi with compressed-air pneumatic grips. Sample gauge lengths were too small for use with the extensometer such that sample displacement was monitored by that of the crosshead. A sampling rate of 2 points/second was used in collecting data.

4.3.2.2 Mini Tensile Tester

A miniaturized tensile tester was designed by Dr. Christian Honeker, built at the MIT Nuclear Engineering Machine Shop, and modified by Dr. Carl Zimba. The mini tester was designed to fit onto the Klinger rail on x-ray beamline X12B at the NSLS at BNL for in-situ stretching experiments.

The stretcher consists of a stretching frame mounted onto a double tilt cradle. Figure 4.8 shows a schematic of the stretching frame. The crossheads move symmetrically

away from (or towards) the center line such that the center of the sample, which coincides with the location of the x-ray beam, is kept constant. Stepper motors advance the relative spacing between crossheads 1 inch every 1800 steps. The total length of travel possible with the stretcher is 80 mm. Limit switches at the edge of the stretcher frame and at the center line prevent the crossheads from colliding with either the stretcher frame or themselves.

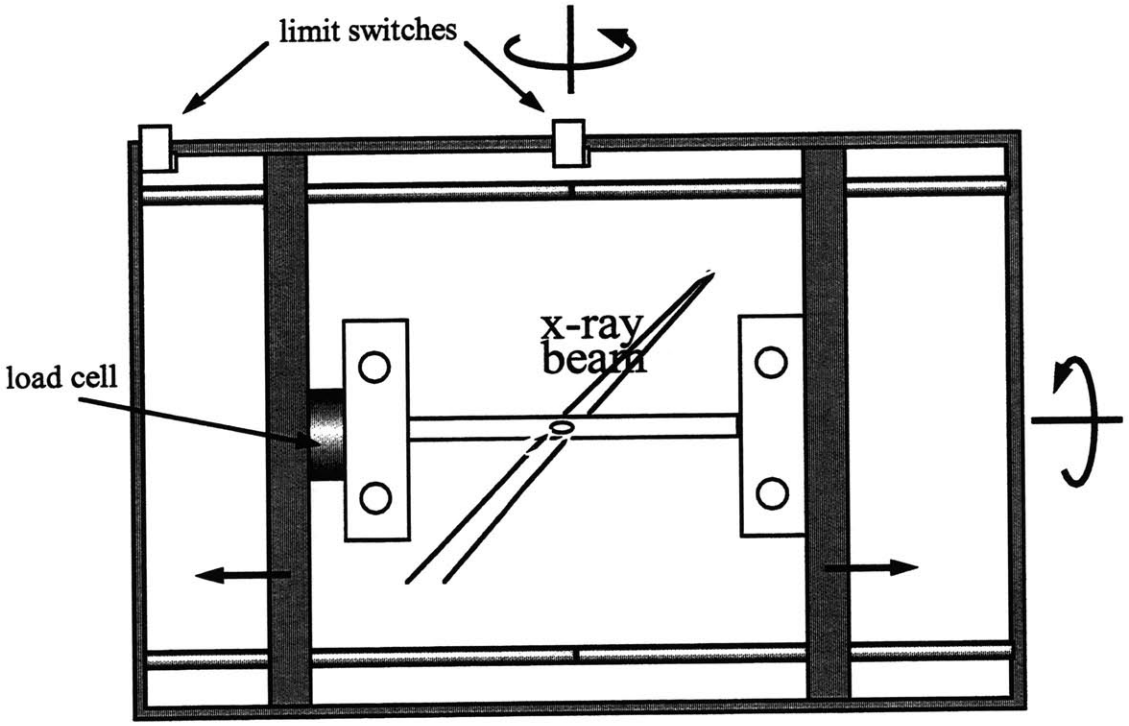

Figure 4.8: Schematic of the Mini tensile stretcher used on X12B for in-situ SAXS-deformation experiments.

A control box is used to control the speed of the stretching, as well as to monitor the displacement of the crosshead (via counts, or number of steps). The control box is connected to the stretcher and power supply through an umbilical, which enables the experimenter freedom of motion in or around the hutch.

Three main speed settings are available for stretching, with a range of speeds within each main setting. The slow, medium, and fast settings access crosshead velocities of 2.6 - 5.3 mm/min, 5.3 - 7.9 mm/min, and 7.9 - 10 mm/min, respectively. The settings are accessed by a switch (F, M, S), while speeds within each setting are accessed with a dial (0-60). Speeds higher than 10 mm/min are not recommended, as they cause the motors to sieze.

The Mini tester has rotational capabilities around the two axes in the plane of the tester to provide more flexibility when using textured materials (e.g., orienting the crystal axes with the x-ray beam). The rotation motor drivers are available on beamline X12B and rotate the stage at 66.67 steps per degree (6000 steps/90 degrees). Rotation angles are ± 60° around the axis of stretching and ± 10° around the axis normal to stretching.

Samples are set in grips using a modified vice with pins to fit the holes. Each end of the sample is sandwiched in between two plates, which are then held together using screws, as shown in figure 4.9a. Three Belleville washers are set inbetween the head of the screw and the surface of a grip to act as a spring (figure 4.9b). At high elongations, the samples become thinner and the Belleville washers expand to keep the sample fixed tightly. After the tensile stage is rotated to the horizontal position and the distance between crossheads adjusted to fit the length of the sample, the samples are mounted into the stretching device, being careful not to fold or twist the tensile sample.

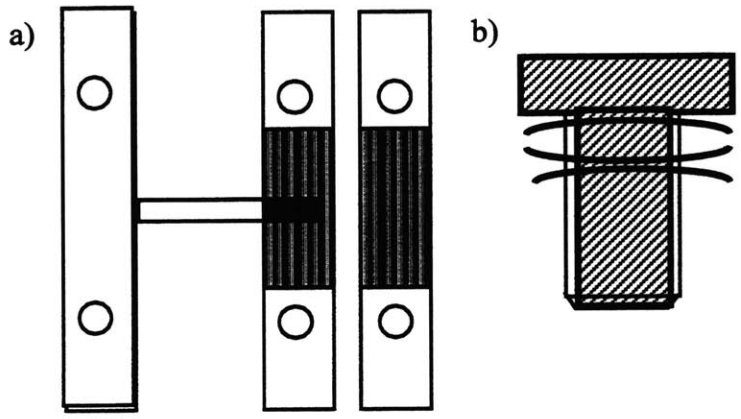

Figure 4.9: (a) Samples are mounted in between grip-sandwiches, held together by (b) screws with three Belleville washers acting as springs.

4.3.3 Synchrotron SAXS

As was mentioned in section 1.2, Synchrotron SAXS was employed to study deformation. The high flux enabled quick "snapshots" of diffraction to be taken in-situ during deformation, and the high energies enabled the first two closedly-spaced DG peaks ($q_2/q_1 = 1.15$) to be resolved.

4.3.3.1 Set-Up

Synchrotron small angle x-ray experiments were conducted at Brookhaven National Laboratory on beamline X12B using 1.549 Å x-rays (corresponding to the 8 keV Helium L_{III} electron x-ray atomic fine structure (EXAFS) absorption edge) and sample-to-detector

distances ranging from 247 cm to 260 cm. Table 6.1 lists the parameters of the various runs.

The Mini tensile stage with an attached 50 lb. load cell was used to deform tensile specimens at strain rates of 0.57 - 1.05 min^{-1}. In-situ SAXS patterns, along with simultaneous load-deformation curves, were taken as tensile specimens were loaded up to ~ 600 - 700% and unloaded to zero load. Scattering patterns were collected using a custom-built 2D detector with exposure times ranging from 5 s. to 10 min. The gas-delay line detector measures 10 cm x 10 cm and consists of a 508 x 496 mesh of wires with a 32-bit dynamic range of intensity and a maximum count rate of 6 x 10^5 counts per second. The beamline, its capabilities, and the detector are described in references (Capel, 1993) and (Capel, Smith, and Yu, 1995) and on the webpage http://crim12b.nsls.bnl.gov/x12b.htm. A schematic of the set-up for the deformation experiments is shown in figure 4.10.

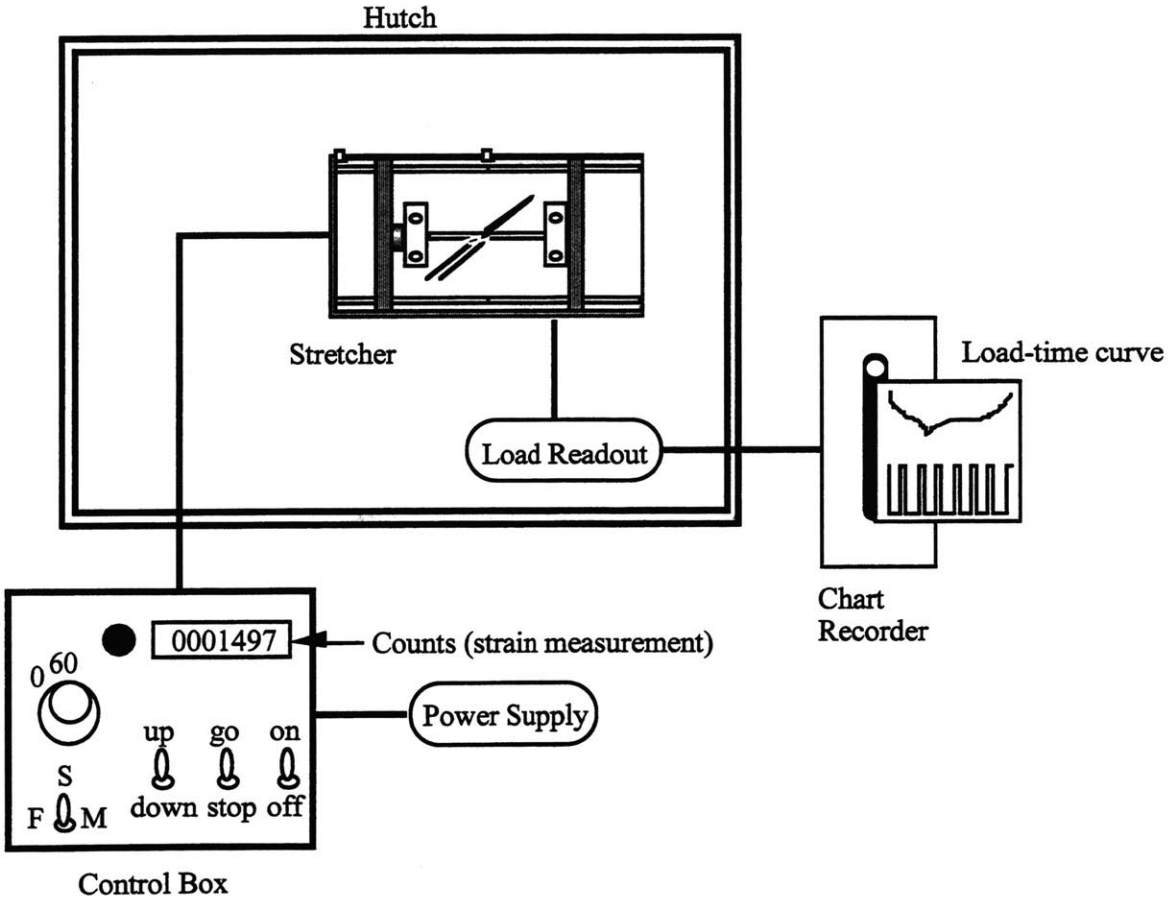

Figure 4.10. Schematic of the experimental set up at X12B, NSLS, BNL.

Table 4.2: Parameters of the runs at X12B.

run	wavelength (A)	SDD (cm)	#x,y pixels per 10cm	x, y beam center	calibrant
aug96	1.549	247	502, 470	262, 251	cholesterol myristate, duck tendon, sca32
sep96	1.549	260	503, 480	271, 257	sca32
mar97	1.549	217	502, 470	267, 255	sca32, dexco39
aug97	1.549	228	505, 483	267, 240	dexco39
apr98	1.549	245	502, 479	262, 238	dexco39
aug98	1.549	238	500, 480	281, 250	dexco39

4.3.3.2 Calibration

The duck tendon calibrant during the August 1996 run was first checked at a short SDD (149 cm) with cholesterol myristate, which has a characteristic spacing of 50.7 Å (Craven and DeTitta, 1976) and a dried and stained duck tendon. This was then cross-correlated a few days later at a long SDD (247 cm) with the duck tendon and the 32%S SIS cylinder sample (sca32), which was found to have d_{10} = 233 Å. Although it is widely known that the duck tendon spacing changes with time and with humidity (Bolduan and Bear, 1950), it was expected that in the few days of the August 1996 run the spacing did not change, especially since the tendon was very old (over 10 years), and since the beamline was climate controlled. In the March 1997 run, quiescent cast Dexco 39%S SIS was found to be a reliable calibrant since the material is hydrophobic and hence the characteristic spacing does not change with humidity. A stabilizing antioxidant was also added at the time of casting, which would minimize the crosslinking of the PI (crosslinking could possibly change the characteristic spacings). It is a lamellar sample (see section 4.4) with low polydispersity (1.03) such that its 2D SAXS pattern consists of very sharp, well-defined rings with an interplanar spacing of d_{001} = 140 Å. The Dexco 39%S is now used as the calibrant.

4.3.3.3 In-situ SAXS Experiments

Three main types of experiments were done at Brookhaven: dynamic stretches, static stretches with stress-relaxation, and rotation static stretches. Dynamic stretches are those in which short patterns are taken in-situ to monitor the qualitative nature of the patterns as a function of time. Static stretches with those in which the sample is stretched

to a given strain and held, while a long exposure pattern (usually 2-5 min) is taken while the stress is monitored on the strip chart. This experiment is used to generate the detailed, high-intensity, publication-quality diffraction patterns. Rotations or tilts around the force axis can also be done in conjunction with the static stretches to observe the diffraction behavior of deformed double gyroid at different angles.

Static stretches are done by stretching the sample to the desired strain by counts and taking a single 2-5 minute static pattern. Dynamic stretches and rotation series consist of multi-step processes which are simplified with scripts for computer control.

4.3.3.3.1 Dynamic Series

The computers can be controlled at Brookhaven to take data in up to four blocks of patterns of specified exposure times. Parameters for input are the number of patterns per block, the exposure time ("active dwell") of each pattern, and the pause ("still dwell") time between each pattern. A dynamic experiment was usually divided by exposure times. For example, a typical experiment of stretching a sample with initial gauge length of 1.3 mm to 600% elongation and back is the following:

Block #	Purpose	Active Dwell	Still Dwell	No. of Patterns
Block 1	stretching from 0% to 200%	15 s. on	1 s. off	40
Block 2	stretching from 200% to 600% (40 patterns) reverse unloading from 600% to 200% (40 patterns)	29 s. on	1 s. off	80
Block 3	unloading from 200% to 0 load	15 s. on	1 s. off	40
Block 4	fully unloaded static	2 min. on	1 s. off	1

The number of patterns in a given block is calculated by the following:

$$\#\text{ patterns} = \frac{\text{total length of travel (mm)}}{\text{crosshead speed}\left(\frac{\text{mm}}{\text{min}}\right)} \times \frac{60\,\frac{\text{s}}{\text{min}}}{(\text{total time per pattern (s)})}$$

And the average strain interval captured in each pattern of a block is calculated as

$$\text{strain interval} = \frac{\text{total strain traversed}}{\#\text{ patterns}}.$$

4.3.3.3.2 Rotation Series

A rotation series is a simple block in which a pattern is taken and the tensile stage is rotated by a pre-set interval. Parameters to specify are the exposure time and the value for angular rotation.

4.3.3.4 Analyzing SAXS patterns

The 2D SAXS patterns are viewed using a program "frnew" (earlier version) or "frwire" (later version). Useful tools under this menu are to obtain q or d values directly from the viewer or to view the integration path. The 2D data are also integrated into 1D intensity vs. q plots using a program "fi_gui" ("frame integrator, general user interface") written by Malcolm Capel for use with the x-ray patterns taken at X12B. Two main modes of integrations were done, which are described below and shown in figure 4.11. Other integration modes, as well as the data reduction programs and its user manuals can be found on the webpage http://crim12b.nsls.bnl.gov/x12b_downloads.html.

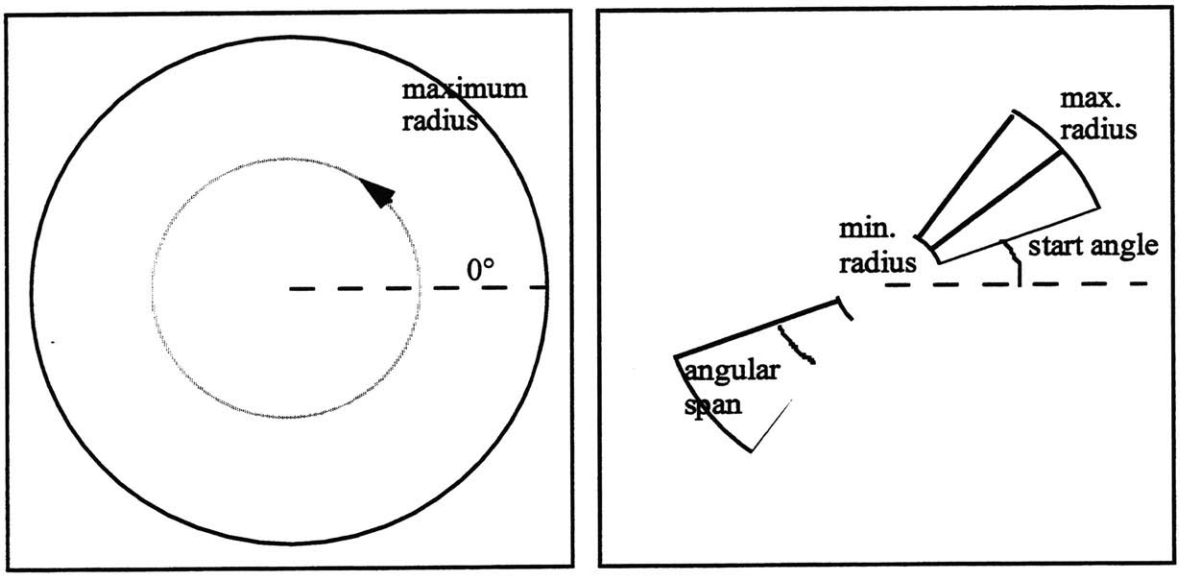

Figure 4.11: Schematic of the integration paths used to reduce the 2D SAXS patterns to 1D intensity vs. q plots.

circular integration, fixed q-intensity: azimuthally integrates over 360° in circles of fixed q value from the center to the user-specified maximum radius.

sectorial integration, fixed q-intensity: azimuthally integrates over a specified angular range in arcs of fixed q value. The user-defined parameters are the minimum and maximum radii, the start angle, angular span of integration, the

number of sectors over which to integrate, and the skipping angle between the start angle of each sector.

4.3.3.5 In-situ Load-Deformation Curves

A 50 lb load cell is attached between one of the sample grip holders and the crosshead bar. The load read-out is attached to a strip chart recorder, which then enables in-situ load-time curves to be taken simultaneous with the in-situ SAXS patterns. A voltage signal is sent to a second channel on the strip chart recorder when the sample shutters open such that the exact location of data collection can be monitored on the load-time curve.

The strip chart recorder is usually set to run at 1.25 cm/min (0.5 inch/min), 5 lb full scale. The load-time curve can then be converted into a load-deformation curve by setting the origin at zero counts and knowing the total number of crosshead counts both at maximum strain and at full unloading. Since both the crosshead and the strip chart paper move at a constant velocity, the number of counts elsewhere along the curve can be interpolated between the three points.

UnScannit 2.0 was used to digitize the load-counts (deformation) curve, which was subequently converted into stress-strain using sample dimensions and the conversion factor of 1800 counts per inch of relative crosshead movement.

4.3.4 In-Situ TEM (MIT High Voltage Lab)

To retain the high-strain deformation microstructure for real-space investigation by TEM, samples stretched to various extents were heavily crosslinked by irradiating with 200 Mrad (80 passes) of 2.6 MeV electrons using a Van deGraaf generator at the MIT High Voltage Lab with assistance from Kenneth Wright. The samples were stretched either on the mounting vice (also used to mount tensile samples at BNL) or on clamps. This treatment effectively raises the glass transition temperature of the rubbery block so that the deformed sample becomes fixed in its extended state. An estimate of the macroscopic strain retained was made by measuring the distances between lines initially drawn on the surface before stretching and irradiation. Sections were then prepared for and observed in TEM by the methods described in section 5.1.

4.4 References

Albalak, R. J. and E. L. Thomas (1993). "Microphase-Separation Of Block Copolymer Solutions In A Flow Field." Journal of Polymer Science Part B: Polymer Physics **31**: 37-46.

Albalak, R. J. and E. L. Thomas (1994). "Roll-Casting Of Block Copolymers And Of Block Copolymer-Homopolymer Blends." Journal of Polymer Science Part B: Polymer Physics **32**: 341-350.

Albalak, R. J., E. L. Thomas and M. S. Capel (1997). "Thermal Annealing Of Roll-Cast Triblock Copolymer Films." Polymer **38**: 3819.

Anderson, D. M., J. Bellare, J. T. Hoffman, D. Hoffman, J. Gunther and E. L. Thomas (1992). "Algorithms For The Computer Simulation Of Two-Dimensional Projections From Structures Determined By Dividing Surfaces." Journal of Colloid and Interface Science **148**(2): 398-414.

Annighoefer, F. and W. Gronski (1983). "Block Copolymers With Highly Oriented Lamellar Morphology." Makromolekulare Chemie Rapid Communications **4**: 123-127.

Bolduan, O. E. A. and R. S. Bear (1950). "Unidirectional Nature Of The Large Periodic Structure Of Collagen Fibrils." Journal of Polymer Science **5**(2): 159-168.

Capel, M. (1993). "X12b - A Facility For Time-Resolved X-Ray Diffraction For Biology And Macromolecular Systems At The Nsls." Synchrotron Radiation News **6**(2): 22-27.

Capel, M. C., G. C. Smith and B. Yu (1995). "One- And Two-Dimensional X-Ray Detector Systems At Nsls Beam Line X12b, For Time-Resolved And Static X-Ray-Diffraction Studies." Review of Scientific Instruments **66**(2): 2295-2299.

Craven, B. M. and G. T. DeTitta (1976). "Cholesteryl Myristate: Structures Of The Crystalline Solid And Mesophases." Journal of the Chemical Society Perkin Transactions II(7): 814-822.

Hahn, T., Ed. (1993). International Tables for Crystallography. Dordrecht, Holland, D. Reidel Publishing Company.

Hoffman, J. and D. Hoffman website: http://www.msri.org/Computing/jim/software/temsim/proj/.

Honeker, C. C. (1997). Large Strain Deformation Behavior of Oriented Triblock Copolymer Cylinders. PhD. thesis, Massachusetts Institute of Technology.

Lambert, C. A., L. H. Radzilowski and E. L. Thomas (1996). "Triply Periodic Level Surfaces As Models For Cubic Tricontinuous Block Copolymer Morphologies." Philosophical Transactions of the Royal Society of London A **354**: 2009-2023.

Prasman, E. and E. L. Thomas (1998). "High-Strain Tensile Deformation Of A Sphere-Forming Triblock Copolymer/Mineral Oil Blend." Journal of Polymer Science, Part B: Polymer Physics **36**: 1625-1636.

Press, W. H., B. P. Flannery, S. A. Teukolsky and W. T. Vetterling (1988). Numerical Recipes in C: The Art of Scientific Computing. New York, Cambridge University Press.

Schoen, A. H. (1970). Infinite periodic minimal surfaces without selfintersections, NASA.

Schulz, M. F., F. S. Bates, K. Almdal and K. Mortensen (1994). "Epitaxial Relationship For Hexagonal-To-Cubic Phase Transition In A Block Copolymer Mixture." Physical Review Letters **73**(1): 86-89.

Schwarz, H. A. (1890). Gesammelte Mathematische Abhandlungen. Berlin, Springer.

Chapter 5:
Acquiring Interconnected Cubic Triblock Copolymers

This chapter relates the efforts at acquiring interconnected cubic triblock copolymers having typical molecular weights and compositions of commercial thermoplastic elastomers, in quantities sufficient enough with which to make detailed and systematic measurements of mechanical and deformation behavior. The chapter begins with a survey of the appearance of the two interconnected cubic morphologies found in various block copolymer systems (section 4.1). The historical review is taken from Avgeroupoulos, Dair, Hadjichristidis, and Thomas, "The Tricontinuous Double Gyroid Cubic Phase in Triblock Copolymers of the ABA-Type", *Macromolecules*, **30**, 5634-5642 (1997), which was a collaborative effort between myself and Prof. Thomas with Prof. Nikos Hadjichristidis and his graduate student, Apostolos Avgeropoulos, of the anionic synthesis group of the University of Athens, Greece. It was thought that for the paper a historical review summarizing work done on the morphology of interconnected cubics was in order, and is subsequently included in this chapter as background information regarding interconnected cubic morphologies.

In a collaborative effort with the Hadjichristidis group at the University of Athens, Greece, PI-rich SIS polymers were synthesized by Avgeropoulos in January 1996 with compositions which were hoped to have an interconnected cubic morphology. It was requested that two polymers be made, with compositions of 32 and 34% PS. To my great joy, the 34%S SIS triblock was determined to have double gyroid morphology. However, since the search for cubics were first done on a laboratory scale, only two grams of each material were made - enough for molecular and structural characterization and preliminary mechanical tests, but more material of the same composition were necessary for comprehensive testing. A third triblock was synthesized in October 1996 by an easier synthesis route, but which yielded larger quantities of material. Section 4.2 describes the experimental procedures for characterizing morphologies, and section 4.3 presents the results for the University of Athens polymers.

Around the same time that we requested the third SIS triblock, we approached Dexco, a commercial supplier of SIS triblock copolymers, and suggested a collaborative effort between MIT and Dexco to produce SIS triblocks in composition ranges of the novel morphology, so as to provide sufficient amounts of DG SIS triblock. Three triblock copolymers were made as a result, and the morphological characterizations are given in section 4.4

5.1 History of Double Diamond and Double Gyroid Morphologies in Block Copolymers

Liquid crystal and surfactant (soft condensed matter) systems have shown in the past to have a rich morphology (Mitchell, Tiddy, Waring, Bostock, and McDonald, 1983), (Luzzati, Delacroix, Gulik, Gulik-Krzywicki, Mariani, and Vargas, 1997). Structures having $Pn\bar{3}m$ symmetry were observed in the past in liquid crystal and surfactant systems (Longley and McIntosh, 1983), (Charvolin and Sadoc, 1987). As block copolymers are also soft condensed matter systems, it was only a matter of time before similar phases were discovered in these systems.

In 1976, Aggarwal published a TEM image of an interconnected, highly ordered microphase separated structure without comment about the precise domain structure of the polystyrene (PS) and polyisoprene (PI) radial star block copolymer consisting of 30 wt % PS and having 15 arms (Aggarwal, 1976). The TEM micrograph showing the novel morphology was taken by J. Beecher. The particular sample was synthesized by Bi and Fetters (1975). For about 10 years, no further work occurred on this novel structure until Fetters and Thomas undertook a detailed collaborative study of the morphology of star diblock copolymers. In 1986, the Ordered Bicontinuous Double Diamond (OBDD) cubic morphology was reported as a new equilibrium microdomain structure in star block copolymers of PS and PI with 8, 12 and 18 arms, for a minority PS volume fraction of 0.27 (Alward, Kinning, Thomas, and Fetters, 1986), (Thomas, Alward, Kinning, Martin, Handlin, and Fetters, 1986).

The OBDD structure consists of two interpenetrating but non-intersecting networks of the minority component in a matrix of the majority. It should be kept in mind that at least some of the structures initially identified as OBDD (space group $Pn\bar{3}m$) may actually be DG (space group $Ia\bar{3}d$) This will be elaborated later. In the OBDD structure each network exhibits the symmetry of a diamond cubic lattice with each node displaying tetrahedral symmetry. Both the networks and the matrix are three-dimensionally continuous. The interface between the two components can be represented by a topologically connected IMDS (see section 2.3 for discussion on IMDS) (Thomas, Anderson, Henkee, and Hoffman, 1988). One striking characteristic of this OBDD morphology was the "wagon-wheel" like patterns frequently observed in the TEM images. Indeed the published micrograph in Aggarwal's review was very similar to the characteristic [111] projection of the OBDD, suggesting that the original radial arm copolymer exhibited this structure. In another study of star block copolymers with PS volume fraction of 0.27, it was found that a structural transition occurred from hexagonally packed cylinders to OBDD in star block copolymers depending on the number of arms

(Kinning, Thomas, Alward, Fetters, and Handlin, 1986). For stars with 2, 4, or 5 arms (a 2 arm star being a triblock) the morphology was hexagonally packed cylinders, while star blocks with 6, 8, 12, or 18 arms displayed an OBDD structure.

Another study observed an extensive study of 18-arm star block copolymers of PS and PI extended results to other compositions and showed that not only does the OBDD structure appeared for a PS outer block star copolymer with a composition of 0.27 and 0.32 volume fraction PS, but also when PI is the outer minority block, with a composition of 0.27 volume fraction PI (Herman, Kinning, Thomas, and Fetters, 1987).

Another study observed the new morphology in linear diblock copolymers, in the range between 0.62-0.66 for PS content (Hasegawa, Tanaka, Yamasaki, and Hashimoto, 1987). They reported that this novel structure appeared only on one side of the phase diagram, and described the basic unit of the minority component as a tetrapod composed of four short rod-like elements of the PI phase. These units are linked to form ordered, 3-dimensional networks, with the PS block filling the matrix. It was suggested this tetrapod network structure was most likely the OBDD structure of the star blocks described above. This morphology also appeared in a tri-component pentablock copolymer of the I-S-I-A-I type (I is polyisoprene, S is polystyrene and A is poly[(4-vinylbenzyl)dimethylamine]) where a single diamond lattice (space group symmetry $Fd\bar{3}m$) was considered as a possible model for the bicontinuous structure (Hasegawa, Sumitomo, Hashimoto, and Kawai, 1983).

Evidence of the OBDD morphology was also obtained in binary blends of an initially lamellar poly(styrene-b-isoprene) diblock copolymer and homopolymer polystyrene (hPS) of various molecular weights (Winey, Thomas, and Fetters, 1991). The microdomain size could be altered by changing the molecular weight of the homopolymer. The mean curvature of the IMDS and the area per junction (average surface area occupied by a block copolymer junction) increased when the hPS concentration was increased and or when the molecular weight of the hPS was decreased. The OBDD structure in the binary blends occurred for an overall PS volume fraction equivalent to that for the neat copolymers, namely 0.64-0.67 (Winey, Thomas, and Fetters, 1992). The dependence of this cubic structure on the diblock molecular weight in the blends was also studied (Spontak, Smith, and Ashraf, 1993). It should be pointed out that if the pure diblock formed the lamellar morphology, then in the blend the hPS resided in the matrix of the OBDD. If instead the pure diblock forms the cylindrical morphology, then the hPS resides inside the network region. Attempts to obtain the OBDD blend morphology with hPS in the matrix by using a diblock with cylindrical microdomains failed.

Results from a TEM study of linear triblock copolymer/ homopolymer blends composed of a cylinder-forming poly(styrene-b-butadiene-b-styrene) triblock and poly(vinylmethylether) homopolymer, showed that this system exhibited the OBDD morphology as well (Xie, Yang, and Jiang, 1993). The homopolymer PVME and the PS blocks of the copolymers mix together in the channels, while the PBd blocks of the copolymer occupy the matrix region. This cubic structure, generated in copolymer/homopolymer blends with total hard phase volume fraction equal to 0.3, was the first made using a triblock copolymer.

Mogi et al. found an ordered tricontinuous double-diamond (OTDD) structure during their study of the morphology of triblock copolymers of the ABC type, where A is PI, B is PS and C is poly(2-vinyl pyridine) (PVP) (Mogi, Kotsuji, Kaneko, Mori, Matsushita, and Noda, 1992), (Mogi, Mori, Matsushita, and Noda, 1992). The OTDD is similar to the OBDD structure for diblock copolymers, the difference being that in the OTDD case there are the two chemically distinct minority component networks formed by the two end blocks. In the TEM study of these samples images from two different projections of the structure (the [111] and the [001]) were shown. The volume fraction of PS at which OTDD was observed was between 0.48 to 0.66. Earlier work of such ABC triblocks had shown the existence of these peculiar and complex structures, but no further explanations were given (Matsushita, Choshi, Fujimoto, and Nagasawa, 1980), (Matsushita, Yamada, Hattori, Fujimoto, Sawada, Nagasawa, and Matsui, 1983), (Arai, Kotaka, Kitano, and Yoshimura, 1980), (Kudose and Kotaka, 1984), not only because the preparation of well-characterized samples was difficult, but also because the equilibrium morphologies were not systematically studied.

Noda et al. (Matsushita, Tamura, and Noda, 1994), (Mogi, Nomura, Kotsuji, Ohnishi, Matsushita, and Noda, 1994) also found the OTDD structure in styrene-isoprene-2-vinyl pyridine triblock copolymers of the ABC type which consist of the same components as in references (Mogi et al., 1992, 1992), but with a different block sequence. It was supposed that these triblocks would form symmetric equilibrium morphologies, when the A and C blocks had the same volume fraction and when A/B and B/C interfaces possess similar surface energies. Although the TEM image showed a clear bicontinuous morphology, the SAXS patterns exhibited broad shoulders and weak peaks, making indexing for the OTDD structure somewhat speculative.

During a study of diblock copolymer thermal behavior by Gobran (Gobran, 1990), an unusual microphase order-order transition was noted in a low molecular weight PS-PI diblock copolymer containing 34% PS. The sample formed a lamellar phase under normal casting and annealing (120° C) conditions, but when annealed at higher temperatures, the

characteristic diffraction for lamellae disappeared and new peaks appeared with the two prominent low-order reflections having $\frac{q_2}{q_1} \approx \frac{\sqrt{4}}{\sqrt{3}}$. TEM results of samples quenched from the high temperature phase revealed that the new morphology was three-dimensionally continuous and consisted of interpenetrating styrene and isoprene domains similar to those for the OBDD [23, 24]. However, a definitive structural assignment could not be made due to the limited quality of the TEM and SAXS data resulting from the restricted long range order of the microdomain morphology.

Subsequently, by combining high-resolution SAXS, computer image simulations, and TEM of well annealed specimens, the equilibrium high-temperature microphase was shown to be a bicontinuous cubic phase, but *not* the OBDD (Hajduk, Harper, Gruner, Honeker, Thomas, and Fetters, 1994). SAXS data from the new structure was most consistent with space group $Ia\bar{3}d$. TEM images showed clear 6-fold and 4-fold patterns which are quite similar to previously published images of the OBDD. However, simulated projections of a constant thickness model based on the gyroid minimal surface showed excellent agreement with the TEM data. This structure was initially termed gyroid*, where "*" is used to distinguish the morphology from the G (for gyroid) minimal surface (Schoen, 1970). The structure consists of two interpenetrating but non-intersecting networks as in the OBDD of the minority component in a matrix of the majority. The networks are three-dimensionally continuous and enantiomeric, with nodes having 3-fold symmetry. Due to the similarity to the double diamond structure, and admitting to the future possibility of the discovery of a single network structure, possibly already found (Hasegawa et al., 1983), we now prefer to call the interconnected network structure with $Ia\bar{3}d$ symmetry the *double* gyroid (DG). Simultaneously, Bates et al. (Förster, Khandpur, Zhao, Bates, Hamley, Ryan, and Bras, 1994) discovered an $Ia\bar{3}d$ morphology using SAXS and TEM in a 60/40 binary copolymer blend consisting of two intermediate segregated SI diblock copolymers of equal molecular weights but different compositions and in a shear oriented polystyrene-poly(2-vinyl pyridine) diblock copolymer (Schulz, Bates. Almdal, and Mortensen, 1994).

In spite of the difference in symmetry between the two interconnected-minority-block-network cubic phases, computer simulations of TEM images based on a parallel surface construct employing the G minimal surface as the base surface indicated that certain projections of the gyroid* (henceforth DG) resembled those for the OBDD (henceforth DD) morphology. In particular, when viewed along the [111] direction, both the DG and the DD structures can produce the "wagon wheel" (Alward, 1985) projection depending on the slice thickness. This, plus the fact that the ratio $\frac{q_2}{q_1}$ of the first two allowed reflections for

each of the space groups were reasonably close (for DD the ratio is $\frac{\sqrt{3}}{\sqrt{2}} = 1.225$, whereas for DG the ratio is $\frac{\sqrt{4}}{\sqrt{3}} = 1.155$) prompted a careful re-examination (Hajduk, Harper, Gruner, Honeker, Thomas, Fetters, 1995) of two polystyrene-polyisoprene starblock copolymer samples previously thought to possess the DD morphology (Alward et al., 1986), (Thomas et al., 1986, 1988). By employing an improved SAXS apparatus and longer annealing procedures, the scattering patterns showed four reflections for both starblock samples. After comparing the predicted and measured peak positions and intensities for a 0.27 volume fraction minority component for the constant thickness models of the DD and the DG structures, the conclusion was that the scattering results are most consistent with the $Ia\bar{3}d$ space group. After this study it was suggested that other copolymer and copolymer/homopolymer blend systems whose structures were previously identified only by TEM using the "wagon wheel" image as the characteristic signature of the OBDD may in fact have microdomain structures more consistent with the DG phase.

The ABC sample that was previously characterized as OTDD has been re-examined by Matsushita and found to be Ordered Tricontinuous Double Gyroid, where the two channels are PI and PVP and the matrix is PS (Matsushita, Suzuki, and Seki, 1998).

A recent study (Tselikas, Hadjichristidis, Lescanec, Honeker, Wohlgemuth, and Thomas, 1996) of the morphologies of miktoarm block copolymers with architecture of the type $(PS_M\text{-}PI_M)_n\text{-}(PS_M\text{-}PI_M)_n$ where M=20K, n=1,2 and the arm asymmetry parameter α=1, 2 or 4 (α is the ratio of the outer block molecular weight to that of the inner block) verified the DD structure for a star block with n=2 and α=4. TEM images exhibiting 6- and 4-fold symmetry and a continuous PS and PI microdomain geometry, together with optical measurements of approximately zero birefringence, suggested an interconnected cubic structure. SAXS data were inconclusive due to the insufficient peak resolution for this high molecular weight (400,000 g/mole) star copolymer. However, excellent matches of the TEM data with level surface models based on the DD structure were found for the [110] projection (which can be used to differentiate between the DD and DG structures), whereas matches to the DG structure were poor (Lambert, Radzilowski, and Thomas, 1996).

These miktoarm block copolymers with n=2 and α=4 were determined to be DD rather than DG. The star-block copolymer samples (with $n \geq 6$ arms) studied earlier by Alward were in fact DG, and not DD. Much of the data presented as DD before 1994 need to be re-examined. However, as for blends, theoretical calculations show that the Pn3m (DD) phase is favored when homopolymer is added (Matsen, 1995).

Nonetheless, the past morphology studies have gone to show that it is quite important to be able to distinguish DD from DG, using both TEM data as well as SAXS data.

5.2 Laboratory Scale SIS Materials (U. of Athens)

PI-rich SIS polymers were synthesized by Avgeropoulos at the University of Athens, Greece, with compositions that were hoped to have an interconnected cubic morphology. Two polymers were requested with compositions of 32% S and 34% S, and block molecular weights of 14/62/14 kg/mol and 16/62/16 kg/mol respectively. Symmetric triblocks were obtained by linking the half of the total living triblock with dimethyldichlorosilane, a lengthy procedure requiring many subsequent fractionations for purification. The two resulting polymers had compositions of 32 vol. % S and 34 vol. % S, and block molecular weights of 11/55/11 kg/mol and 13.6/46.4/13.6 kg/mol, respectively. A third triblock was requested later, and was made via sequential addition of monomers. This triblock had a 36 vol.% S composition with block molecular weights of 13.6/44/12 kg/mol. These triblocks are in the intermediate segregation regime with a calculated $\Delta N\chi$ from the critical $N\chi$ of about 40 (Owens. Gancarz, Koberstein, and Russell, 1989) (Mayes and Olvera do la Cruz, 1989) where N is the number of statistical segments and χ is the Flory-Huggins segment-segment interaction parameter.

In addition to the synthesis, Avergopoulos also carried out the molecular characterization of the polymers. The morphological characterizations were done by myself.

5.2.1 Synthesis and Chemical Characterization Procedures

All of the University of Athens triblocks were prepared by anionic polymerization using high vacuum techniques in evacuated, n-butyl lithium (n-BuLi) washed, benzene-rinsed glass vessels. The purification of styrene (Merck), isoprene (Fluka) and benzene (C_6H_6, Merck) to the standards required for anionic polymerization have been described elsewhere (Morton and Fetters, 1975) (Iatrou and Hadjichristidis, 1992, 1993). Tetrahydrofuran (THF, Merck) was stirred overnight over calcium hydride (CaH_2), distilled on the vacuum line to a sodium mirror and was left to react for 24 hours. This procedure was repeated until no degradation of the mirror was observed. Then, it was distilled into a flask containing a sodium mirror and traces of styrene. The appearance of a red color due to the formation of polystyrylsodium (PSNa) indicated the high purity of the THF. A middle fraction of THF was used. Dichlorodimethylsilane was fractionally distilled on the vacuum line and subdivided into ampoules. Sec-BuLi, prepared from sec-

butyl chloride and a lithium dispersion, was the initiator, and C_6H_6 the solvent for all polymerizations.

Fractionation was carried out by adding methanol to the stirred polymer solution (~0.5% w/v) in toluene at room temperature until turbidity was detected. The mixture was then heated and stirred gently until clear, transferred to a warm separatory funnel and allowed to equilibrate to room temperature overnight. This procedure was repeated until no precursors or undesirable products were shown to be present by Size Exclusion Chromatography (SEC).

SEC experiments were carried out at 30°C using a Waters Model 510 pump, Waters Model 410 differential refractometer and Waters Model 486 tunable absorbance detector. Three Phenomenex (type: phenogel 5 linear, pore size: 50 Å to 10^6 Å) columns were used. THF, distilled over CaH_2 and sodium, was the carrier solvent at a flow rate of 1 ml/min.

The weight-average molecular weight (M_w) of the final polymers was determined with a Chromatix KMX-6 low-angle laser photometer (LALLS). This instrument, equipped with a helium-neon laser, was operated at a wavelength of 633 nm. The refractive index increments, dn/dc, in THF at 25°C, were measured with a Chromatix KMX-16 refractometer.

The number-average molecular weight (M_n) was determined with a Wescan Model 230 membrane osmometer at 35°C. Toluene, distilled over CaH_2, was the solvent.

The M_w values were obtained from the $(KC/\Delta R_\theta)^{1/2}$ vs. C plots (ΔR_θ, excess Rayleigh ratio; K, combination of known optical constants; C, concentration) and the M_n values from the $(\Pi/C)^{1/2}$ vs. C plots (Π, osmotic pressure). In all cases, the correlation coefficient was better than 0.99.

^{1}H-NMR determination of the composition and the molecular microstructure of the materials was carried out in cadmium chloride ($CdCl_3$) at 30^0C using a Varian Unity Plus 300/54 instrument. For the polyisoprene block, the typical molecular microstructure characteristic of anionic polymerization of isoprene in benzene was observed to be 9 wt. % 3,4, 70 wt. % cis-1,4, and 21 wt. % trans-1,4).

Further details concerning the SEC, membrane osmometry, LALLS, and NMR measurements are given elsewhere (Iatrou and Hadjichristidis, 1992, 1993).

Polymer degradation after the annealing procedures was checked by dissolving a portion of each of the annealed samples in THF and re-running SEC. No detectable difference was observed, indicating no unreacted linking agent left after the fractionation procedure, and no high temperature branching of PI.

5.2.2 32%S and 34%S SIS Triblocks

The results of the synthesis and the chemical characteristics will be presented first, followed by the morphological assignment.

5.2.2.1 Synthesis by Linking Diblocks with Dichlorodimethylsilane

The synthesis and chemical characterization procedures for the 34% S triblock are reported in (Avgeropoulos, Dair, Hadjichristidis, and Thomas, 1997) and reproduced here for completeness. The 32% S triblock was synthesized and chemically characterized by the same procedures as the 34% S triblock, but this was not explicitly stated in the article. Two triblock copolymers, 32%S and 34%S SIS, (named for their attempted % PS composition), were synthesized by linking half of the total living triblock PSPILi with $Cl_2Si(CH_3)_2$ (dichlorodimethylsilane). The reaction is as follows:

$$\text{St} + \text{sec-Bu Li} \xrightarrow{C_6H_6} \text{PS LI} \qquad \text{(A)}$$

$$\text{PS LI} + \text{Is} \xrightarrow{C_6H_6} \text{PS PI Li} \qquad \text{(AB)}$$

$$\text{(small excess) PS PI Li} + (CH_3)_2\text{SI Cl}_2 \xrightarrow{C_6H_6} (\text{PS PI})_2\text{ Si }(CH_3)_2 + \text{PS PI Li}$$

Triblock copolymer of the ABA type

where St and Is are the the styrene and isoprene monomers, respectively, sec-BuLi is the butyl lithium initiator, and C_6H_6 is the solvent benzene.

The use of $Cl_2Si(CH_3)_2$ leads to a final product having two end blocks with exactly the same molecular weight. However, the completion of the reaction needs at least one month in order to ensure that all the chlorosilane had reacted with the living diblock. The progress of the reaction was monitored by removing samples from the reactor and analyzing them by SEC. When there was no distinguishable change in the ratio of the two peaks, the triblock was purified from the diblock by fractionation. The final polymers were a 31-32 wt.% PS and a 34-36 wt.% PS triblock. Two grams of each material resulted from the synthesis and 9 fractionations. Typical SEC chromatograms of the fractionated triblocks are given in Figures 5.1a and b, and the molecular characteristics are shown in Table 5.1.

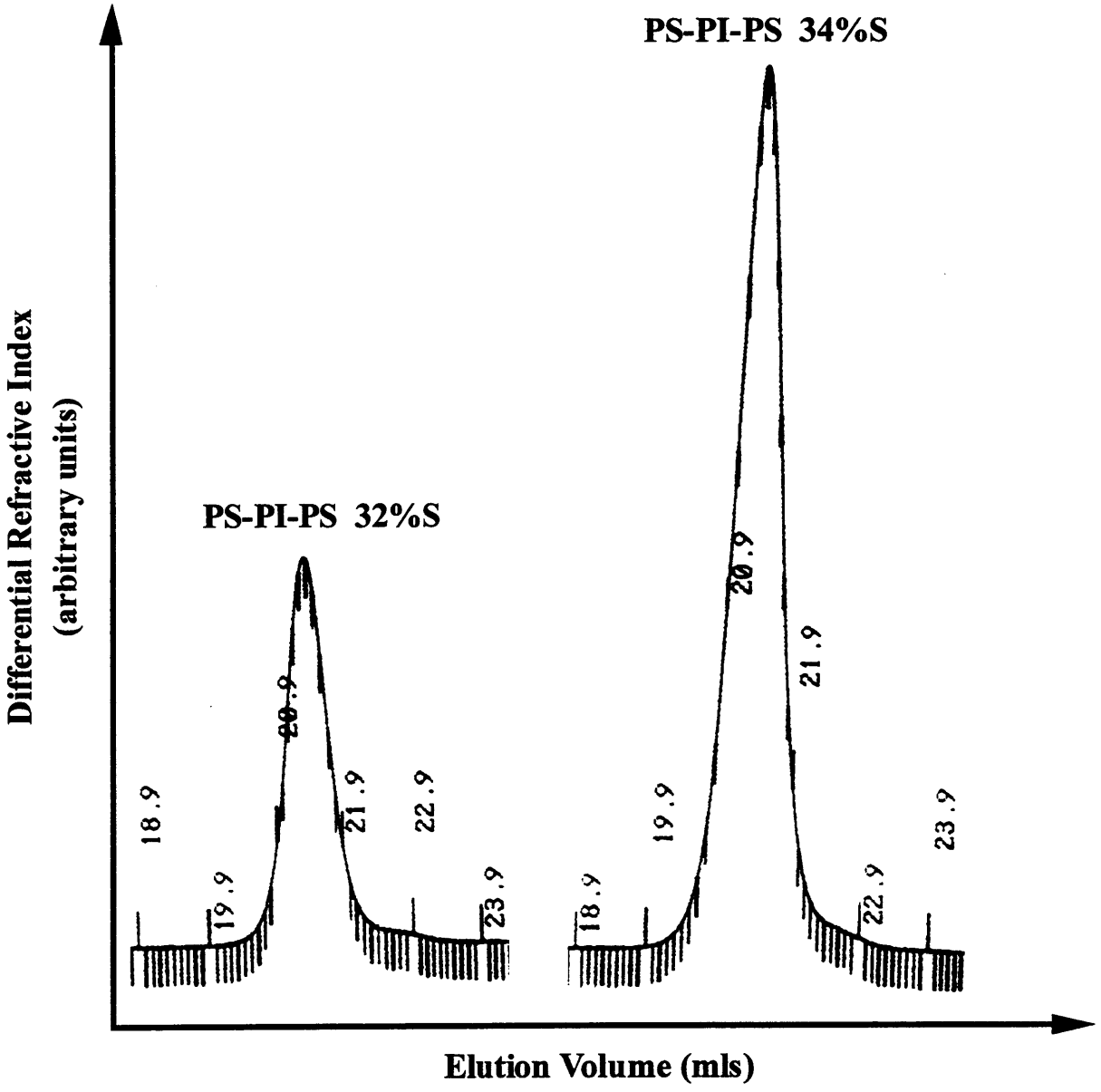

Figure 5.1: SEC chromatograms of the a) 32% S SIS and b) 34% S SIS triblock copolymers.

Table 5.1: Characteristics of the triblock copolymers. Molecular weights are as given from SEC/RI chromatograms.

Sample	Block M_w x 10^3	M_n x 10^3 (g/mol)	M_w x 10^3 (g/mol)	PDI	%PS (UV/SEC)	%PS (H-NMR)
32% S	11.0 / 55.0 / 11.0	74.5	77.5	1.04	32	31
34% S	13.6 / 46.4 / 13.6	70.8	73.6	1.04	36	34

5.2.2.2 Morphological Characterization

5.2.2.2.1 The 32%S SIS Triblock

Figure 5.2 shows the SAXS scattering data plot of ln [q^2*I(q)] vs. q, taken as a full circular azimuthal integration. The 32% PS polymer shows four distinct peaks in $\frac{q_n}{q_1}$ ratios of 1.00 ± 0.02 : 1.74 : 2.00 : 2.65, which are approximately 1 : $\sqrt{3}$: $\sqrt{4}$: $\sqrt{7}$, characteristic of a p6mm plane group . For block copolymers, the q-ratios correspond to the cylinder morphology.

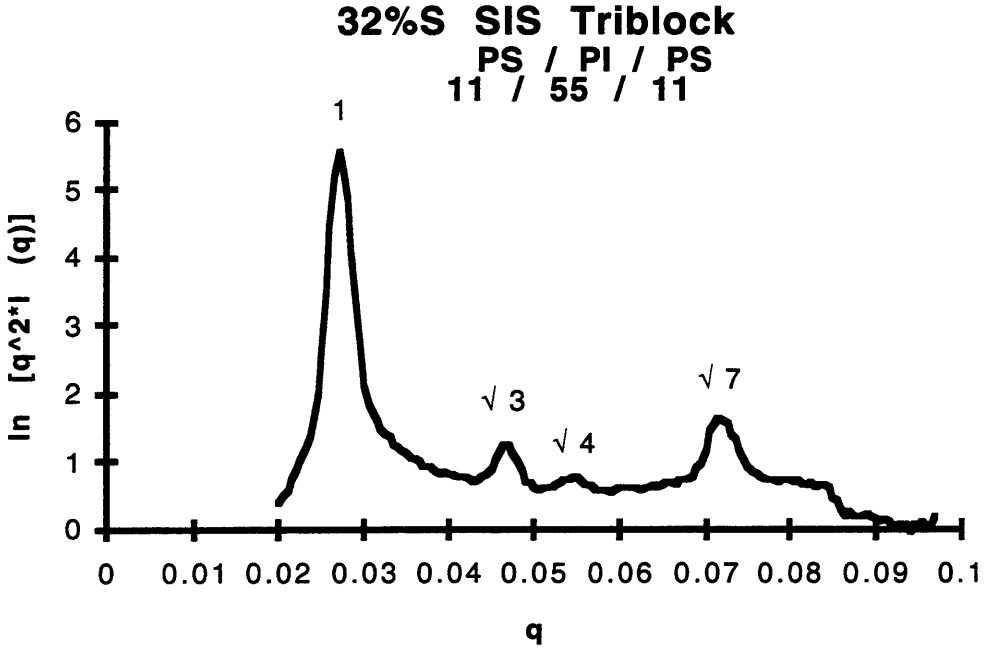

Figure 5.2: Small Angle X-ray Scattering pattern of the 32%S SIS (11K/55K/11K) triblock made by Apostolos and Hadjichristidis. The observed peaks occur in ratios of 1 : $\sqrt{3}$: $\sqrt{4}$: $\sqrt{7}$, indicating p6mm symmetry.

Selected bright-field TEM micrographs of the 32%S triblock are shown in figures 5.3a and b. The light regions are polystyrene and the dark regions are OsO_4-stained PI. There are two types of regions seen. The first, as shown in figure 5.3a, shows an "end-on" view of hexagonally packed PS cylinders in a PI matrix, and figure 5.3b shows a transverse view of the cylinders, revealing alternating lines of PS and PI.

From the combination of SAXS and TEM results, it was concluded that the morphology of the 32%S material is hexagonally packed cylinders. The first two peaks in the SAXS pattern correspond to the (10) and (11) reflections, respectively, which occur at

$q_{10} = 0.0268$ Å^{-1} and $q_{11} = 0.0470$ Å^{-1}. The characteristic interplanar spacing is $d_{10} = 234$ Å and the lattice parameter is a = 234 Å.

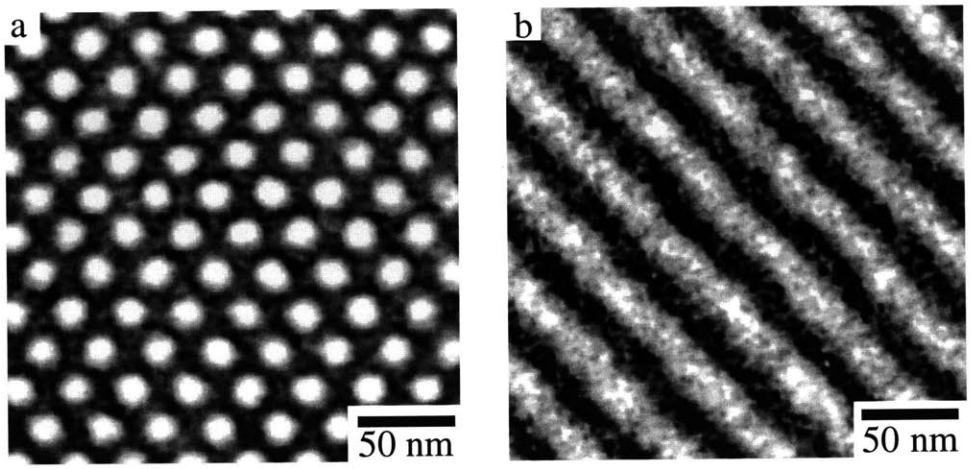

Figure 5.3: Bright-field TEM images of 32% S SIS triblock. a) An axial view of the hexagonally packed cylinders. b) A transverse view of the cylinders.

5.2.2.2.2 The 34%S SIS Triblock

Selected bright-field TEM micrographs of the 34%S SIS (13.6K/46.4K/13.6K) triblock are shown in figure 5.4. The TEM images do not resemble the classical block copolymer morphologies of spheres, cylinders, or lamellae, and suggest that the morphology has interconnected structures, with channels of PS and matrix of PI. The grains exhibit 6-fold, 4-fold, and 2-fold symmetric projections, characteristic for a microphase with cubic symmetry. The structural symmetry of the 34%S SIS was also studied through optical birefringence measurements. Materials exhibiting cubic symmetry show no birefringence because all second rank tensor properties (e.g., optical) of cubic crystals are isotropic. Non-cubic periodic microphases are optically anisotropic, and thus exhibit non-zero birefringences. Films of the triblock showed negligible birefringence, indicating that the materials are either homogeneous or cubic. From the TEM images and SAXS patterns, it can be seen that the sample is microphase separated, so the factor of homogeneity must be excluded. Hence, we are left with a cubic structure.

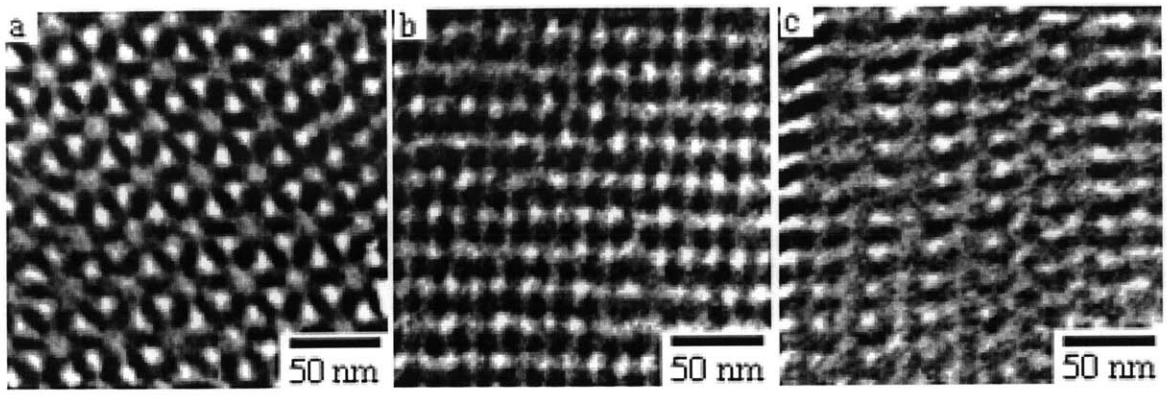

Figure 5.4: Bright-field TEM images of the 34% S SIS triblock. Grains exhibit a) 6-fold symmetry, b) 4-fold symmetry, and c) 2-fold symmetry.

Figure 5.5 shows the SAXS scattering data plot of the 34%S SIS (13.6K/46.4K/13.6K) triblock. Most noticeable are the first two peaks which are closely spaced but fully resolvable with a $\frac{q_2}{q_1}$ ratio of 1.162 ± 0.002. Higher order peaks occur at $\frac{q_n}{q_1}$ ratios of 1.54, 2.00 : ~2.3 : ~2.6 : 3.00.

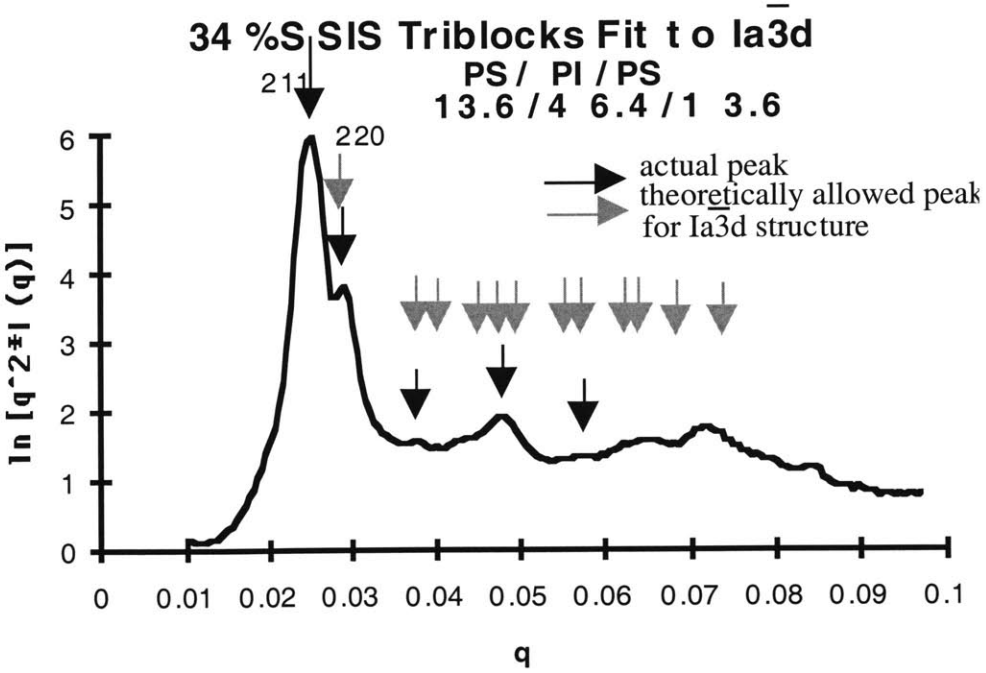

Figure 5.5: Small Angle X-ray scattering pattern of the 34%S SIS (13.K/46.4/13.6) triblock indexed to the Ia3d space group. The pattern is 2-D azimuthally integrated 360°. Ln [q^2*I(q)] (relative intensity) is plotted vs. q. The black arrows indicate the the actual peaks, while the grey arrows represent theoretically allowed peaks.

Considering the expected values of $\frac{q_2}{q_1}$ for various cubic space groups suggests $\frac{q_2}{q_1} = \frac{\sqrt{4}}{\sqrt{3}} = \frac{\sqrt{8}}{\sqrt{6}}$; thus the first two reflections are either (111) and (200) or (211) and (220).

Due to the lack of sharp, well-resolved reflections at larger q despite annealing treatments, further distinction by SAXS would only be possible via laborious modeling of the intensity of the reflections using an appropriately defined IMDS and volume fraction for each space group. Instead, the approach used here is to eliminate candidate space groups using observations from the experimental TEM images, and considerations given to the geometrical requirements and implications of the observed interconnected structures.

There are eight possible cubic space groups consistent with the first two reflections in a ratio of $\frac{\sqrt{4}}{\sqrt{3}}$. These are F23, $Fm\bar{3}$, $Pa\bar{3}$, F432, $F\bar{4}3m$, $I\bar{4}3d$, $Fm\bar{3}m$ and $Ia\bar{3}d$. Further distinction amongst these can be made using the projected symmetries found from TEM images for incident beam along the <111>, <100> and <110> directions. The <111> experimental image is shown in figure 4.4a; the symmetry is that of p6mm. Figure 4.4b shows the <100> experimental image of the triblock, which exhibits p4mm symmetry. Figure 4.4c shows the <110> experimental image, which has c2mm symmetry. Table 5.2 gives the set of eight possible cubic space groups consistent with the limited x-ray data and the plane group symmetry of their high symmetry projections. By noting the symmetry observed in TEM images and their corresponding power spectra, certain of these space groups which fail to display the required symmetry of their high symmetry projections can be eliminated. In this manner, the definite presence of the p6mm symmetry for the <111> wagon wheel projection eliminates all but groups $Fm\bar{3}m$ and $Ia\bar{3}d$. Similarly, the clear occurrence of p4mm symmetry for the <100> projection eliminates all but F432, $F\bar{4}3m$, $Fm\bar{3}m$ and $Ia\bar{3}d$. The c2mm symmetry of the <110> images projection eliminates all but $Fm\bar{3}$, F432, $Fm\bar{3}m$ and $Ia\bar{3}d$. Taken together, SAXS and the high symmetry TEM projections rule out 6 of the 8 possible groups leaving only $Fm\bar{3}m$ and $Ia\bar{3}d$.

A final constraint on the space group symmetry is the connectivity of the structure strongly suggested by the TEM data. Bicontinuous structures can be modeled using skeletal graphs. This was developed earlier in Section 3.4. The simplest tri-functional skeletal network known is that of the gyroid. A four-functional network can be made using nodes with tetrahedral symmetry. A six- functional model with Pm3m symmetry is also possible. The tri-functional double gyroid structure with $Ia\bar{3}d$ symmetry satisfies all the constraints and appears as the best model. The nodes of a 3D network in the $Fm\bar{3}m$ structure cannot both be linked by tri-functional segments and retain the symmetry.

Linking the nodes of $Fm\bar{3}m$ with tetrahedral functional segments results in a diamond structure, with change of the space group and subsequent loss of the $\frac{q_2}{q_1}$ ratio and required projections. Similarly, using hexafunctional nodes changes the structure to primitive cubic symmetry ($Pm\bar{3}m$) likewise with loss of the necessary SAXS peaks and high symmetry TEM projections. Thus there is only one suitable space group left, namely $Ia\bar{3}d$.

Table 5.2: High Symmetry Projections of Cubic Space Groups having $\frac{q_2}{q_1} = \frac{\sqrt{4}}{\sqrt{3}}$

Space Group	**<111>**	**<100>**	**<110>**
F23	p3	p2mm	c1m1
$Fm\bar{3}$	p6	p2mm	c2mm
$Pa\bar{3}$	p6	p2gm	p2gg
F432	p3m1	p4mm	c2mm
$F\bar{4}3m$	p31m	p4mm	c1m1
$I\bar{4}3d$	p31m	p4gm	c1m1
$Fm\bar{3}m$	p6mm	p4mm	c2mm
$Ia\bar{3}d$	p6mm	p4mm	c2mm

Transmission Electron Microscopy

Of note in the TEM images in figure 5.4 is the "wagon wheel pattern" found in the <111> experimental projection, which, as explained in the beginning of the chapter, has led to confusion in the past in the morphological identification of block copolymers with cubic structures, namely between the DD and DG morphologies. Although SAXS results eliminate the $Pn\bar{3}m$ space group, it would be instructive to confirm that the morphology is DG rather than DD. One approach is to perform a more quantitative evaluation of the TEM data on selected regions. Using the PS sphere-tilt method (as described in section 4.1.1.2), the average TEM section thickness was determined to be 710±10 Å. Various candidate structures then can be distinguished by quantitive determination of the local section thickness and by comparison of the images and optical diffraction patterns with the corresponding simulated projections and their Fast Fourier Transforms (FFT). However, for the purposes of this discussion, since the space group of the DD structure has been eliminated, TEM will only be used to observe the nature of the interconnectivity of the

structure. In addition, TEMsim will be employed as a verification tool to aid in the determination of the morphology.

Fischer and Koch (1987) have discovered another possible triply periodic IMDS compatible with the $Ia\bar{3}d$ space group. It is presently undetermined whether some surface related to the Fisher-Koch S surface would divide space into the volume fractions appropriate to our triblock sample, as well as produce simulated images that would correspond well with the TEM data. However, since the S surface has a higher genus per unit cell, it will be less likely to occur in physical systems due to an inherently higher surface area at a particular length scale, compared to structures based on Schoen's G surface.

Six-Fold Projection

Figures 5.6a-b show the TEM image and OT of the {111} projection of the PS-rich triblock. Figures 5.6c-d show the simulated TEM image and its FFT of a {111} projection of the DG structure, 1 unit cell thick, with a similar composition. Excellent matches to this projection and its FFT are attained for the DG level surface models $\geq$ 0.5 unit cell thick. Figures 5.6e-f are the simulated TEM image and its FFT of a {111} projection of a DD surface, 0.25 unit cell thick; such a projection and FFT is obtained for only a 0.25 unit cell thickness in the the DD level surface model.

The optical transform and FFTs of the DG and DD level surface models each have 12 prominent spots around the center beam, with an alternating pattern of a high-intensity spot next to a lower-intensity spot, the higher intensity spot being closer to the center than the lower-intensity spot, and the $\frac{q_2}{q_1}$ ratio equal to 1.16. From the OT of the TEM image of the PS-rich triblock, the ratio of peak-to-center distances between the second peak to the first peak is 1.14, with the first peak is stronger than the second.

For DD, the expected ratio between the first two peaks, $\frac{q_2}{q_1}$, is 1.225, which corresponds to $\frac{q_{111}}{q_{110}}$. However, since it is the {111} projection that is being considered, the {111} peaks in DD will not be seen. Some possible reflections for the {111} projection for the DD morpohology are the {110}, {211}, {220}, {321}, {330}, etc. In the FFT of the simulated TEM image the first peak has a stronger intensity than the second on a log(Intensity) scale, and the ratio of distances from the center between the second peak to the first peak is 1.16, which is equal to $\frac{\sqrt{4}}{\sqrt{3}}$ or $\frac{\sqrt{8}}{\sqrt{6}}$. Since the {111} peaks are not allowed in the {111} projection, the ratio of the second peak to the first must be $\frac{\sqrt{8}}{\sqrt{6}}$, which

corresponds also to $\frac{q_{211}}{q_{220}}$ in the double diamond morphology. The reflections for the FFT of the {111} projection through a thickness of 1/4 unit cell is indexed in figure 5.6f.

The simulated {111} projections and FFTs of both the DG and DD level surface models closely resemble the experimental data. Thus at first glance, neither the TEMSIM projections nor their FFTs allow us to determine whether the experimental image and optical transform resemble those of DD or DG. However, a comparison of the thicknesses used in generating the projections and FFTs and the achieveable microtome section thicknesses provide better bases upon which to make a decision.

The {111} projection and FFT of the DG shown in figures 5.6c-d can be achieved for any thicknesses $\geq$ 0.50 unit cell, while the projection and FFT of DD shown in figures 5.6e-f can only be achieved for a thickness of 1/4 unit cell. From small-angle x-ray scattering data, the first reflection corresponds to a d-spacing of d_1 = 240 Å. We can use the relation between d-spacing and lattice parameter for cubic structures,

$$d_{hkl} = \frac{a}{\sqrt{h^2 + k^2 + l^2}}$$

where d is the d-spacing, a is the lattice cell parameter, and h, k, and l are the Miller indices of the reflection. If the morphology is assumed to be DG, then $d_1 = d_{211}$ and a_{DG} = 620 Å. Looking down the <111> direction, the thickness of 1/2 unit DG cell would be $\frac{1}{2}\sqrt{3}\, a_{DG}$, or 540 Å; section thicknesses 540 Å or greater would give the observed projection and optical transform. Reasonable thicknesses for microtomed sections are 500-1500 Å, and hence it is possible that a DG sample could give the observed projections and optical transforms.

If the morphology is assumed to be DD, then $d_1 = d_{110}$ and a_{DD} = 360 Å. The thickness of 1/4 unit DD cell in the <111> direction would be $\frac{1}{4}\sqrt{3}\, a_{DD}$, or 160 Å. Section thicknesses of only 160 Å would give the observed projection and optical transform. It is highly unlikely to microtome a 1/4 unit DD cell in the <111> direction, and therefore, it is unlikely that the observed six-fold projection and optical transform belong to the DD morphology.

As the section thicknesses are increased, the FFT of the {111} projection of the DD changes from that in figure 3f and begins to resemble a 6-pointed star. In particular, for 1/4 cell, the {110} is weak, the {220} is strong, and the {330} is weak. As the section thickness increases the {220} weakens while the {110} and {330} get strong. Therefore, the FFT of the {111} projection of a DD section 500 - 1500 Å thick would resemble more a 6-pointed star than that shown in figure 5.6f.

Thus for the {111} projections, the PS-rich triblock exhibits characteristics which can be reproduced by both projections of DD and DG level surface models. However given the thicknesses required for the projections, the experimental data can be better reproduced by the DG model on a more practical level. The peaks in the optical transform can be indexed according to the DG model, the first being a {211} reflection and the second being a {220} reflection.

Four-Fold Projection

Figures 5.7a-b show the TEM images and OT of the 4-fold projection. The TEM image exhibits p4mm symmetry, as does the diffraction pattern. As with the six-fold projection, the 4-fold projections of the DD and DG are similar in nature (both having p4mm symmetry) such that differentiation of the two morphologies based on the 4-fold is ambiguous and can be yet again a source of confusion between the two morphologies.

Two-Fold Projection

A sharper difference between the two morphologies lies in the 2-fold projections, in particular, the {110} projections of the DD compared to the DG. The {110} projections of DD and DG have p2mm and c2mm plane group symmetries, respectively, which leads to major differences in the corresponding images and Fourier transforms as well. Figures 5.8a-b show the experimental TEM image and optical transform of the PS-rich sample, which both exhibit c2mm symmetry. The ratio of what would be q_{220} to what would be q_{211} in the experimental optical transform gives 1.18. At first glance, the morphologies under consideration to which this ratio is consistent is somewhat equivocal, as the projection can be off the tilt axis for [110]. (It should be mentioned that a {110}-type reflection can be seen in the [110] projection, as a $(1\bar{1}0)$ peak is perpendicular to the [110] direction.) Quantitatively, the ratio 1.18 can represent either $\frac{q_{220}}{q_{211}} = 1.155$ for DG, or $\frac{q_{111}}{q_{110}} = 1.225$ for DD.

Figures 5.8c-d show the simulated projections and indexed FFTs for a 1-unit-cell-thick DG {110} projection, respectively. It should be noted that this projection can be achieved for unit cell thicknesses ≥ 1 unit cell, due to the existence of the 2-fold screw axes in the DG structure. Both the experimental TEM image and optical transform look qualitatively similar to the {110} TEMsim projection and FFT of the level surface model of DG, respectively.

The simulated projection and indexed FFT for a 1-unit-cell-thick DD {110} projection are shown in figures 5.8e-f. This projection and FFT can be achieved for unit cell thicknesses ≥ 1/4 unit cell. Qualitatively, neither the projection nor the FFT bear any

qualitative resemblance to the either the experimental TEM image or its optical transform, respectively. This and the fact that the {110} projection of the DD structure has p2mm symmetry rather than c2mm symmetry make it quite obvious that the experimental image is not the {110} projection of DD. Therefore, a DD projection with c2mm symmetry was sought. Although not every 2-fold for the DD was surveyed with TEMsim, those that were explored (the {110}, {112}, {113}, {114}, and {115}) were the most likely candidates to have been identified as 2-folds in the TEM. None of the 2-fold DD projections are convincing matches to the experimental TEM image, but the projection which bears the closest resemblance to the experimental TEM image and to having c2mm symmetry was that of the [113]. Figures 5.8g-h show a 1 unit-cell-thick {113} projection of DD and its FFT. This projection and FFT can be obtained for section thicknesses ≥ 1/2 unit cell. The FFT clearly does not resemble the optical transform of the experimental TEM image. In light of the shady resemblance between the 2-fold TEMsim projections of the DD and the experimental image, as well as the incongruous transforms, we can conclude with certainty that the 2-fold projection of the PI-rich triblock is not DD.

The 2-fold was the most elucidative cubic symmetry projection in identifying the morphology. The striking resemblance between the experimental 2-fold TEM image and the {110} TEMsim projection of the level surface model of the DG, as well as the congruency between the experimental optical transform and the FFT of the TEMsim image, lead us to conclude that the experimentally observed 2-fold is commensurate with the DG morphology.

A comparison of the experimental TEM images with the computer generated projections and the corresponding optical transforms with FFTs of the {111}, {001}, and particularly the {110} projection show that the morphology obtained in the PS-rich triblock compares well with a level surface model of the DG cubic structure.

Thus, from a combination of SAXS, TEM, and geometrical considerations, there is only one suitable space group and interconnected network structure that well satisfies all of our data for each of the two ABA triblocks: the tri-functional double gyroid structure with $Ia\bar{3}d$ symmetry. The first two peaks in the SAXS pattern correspond to the (211) and (220) reflections which occur at $q_{211} = 0.0247$ Å^{-1} and $q_{220} = 0.0285$ Å^{-1}, respectively. The corresponding (211) interplanar spacing is $d_{211} = 254$ Å, and the lattice parameter of the DG unit cell is a = 624 Å. As mentioned in section 3.5, the length of a DG strut is $L = \frac{a\sqrt{2}}{4} = 220$ Å, and the diameter $= \frac{L}{3} = 74$ Å.

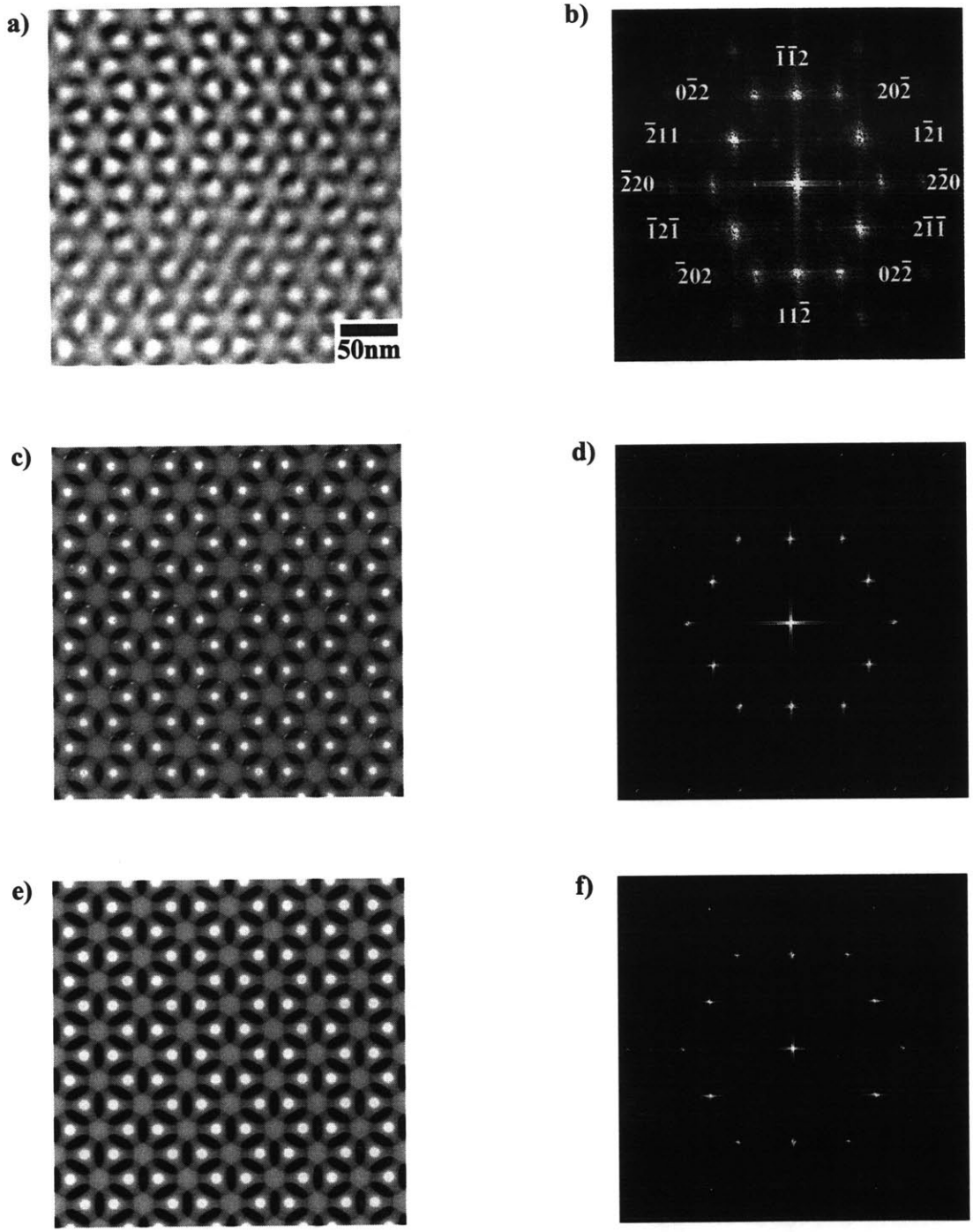

Figure 5.6: a) Bright−field TEM image of a 6−fold projection of the 34%S SIS cast from toluene. The light regions are PS and the dark regions are PI stained with OsO_4. b) Optical diffraction pattern taken from the same image. c). Simulated [111] projection of the DG level surface: s_p = +/− 1.0; 1.0 unit cell thick. d). FFT of the simulated DG [110] projection. e). Simulated [111] projection of the DD level surface, PI−rich; s_p = +/− 0.8; 0.25 unit cell thick. f). FFT of the simulated D [111] projection

a)

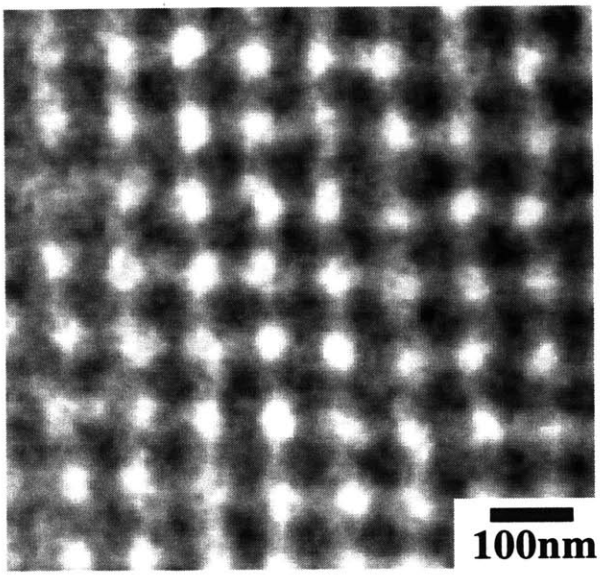

b)

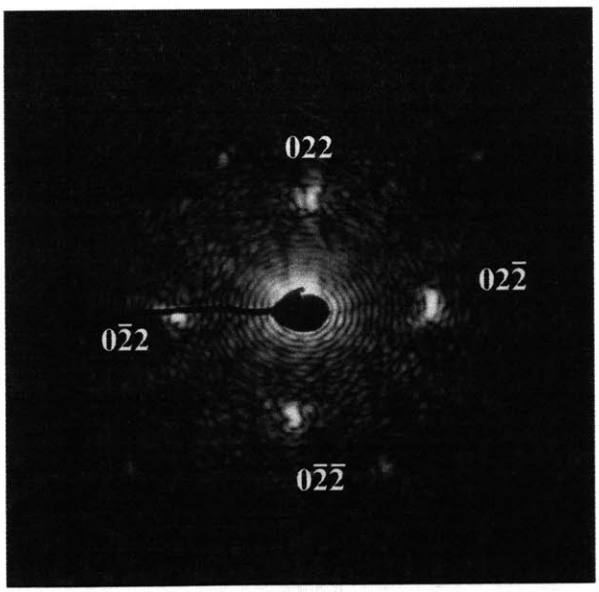

Figure 5.7: a) Bright−field TEM image of a 4−fold projection of the 34%S SIS cast from toluene. The light regions are PS and the dark regions are PI stained with OsO_4. b) Optical diffraction pattern taken from the same image.

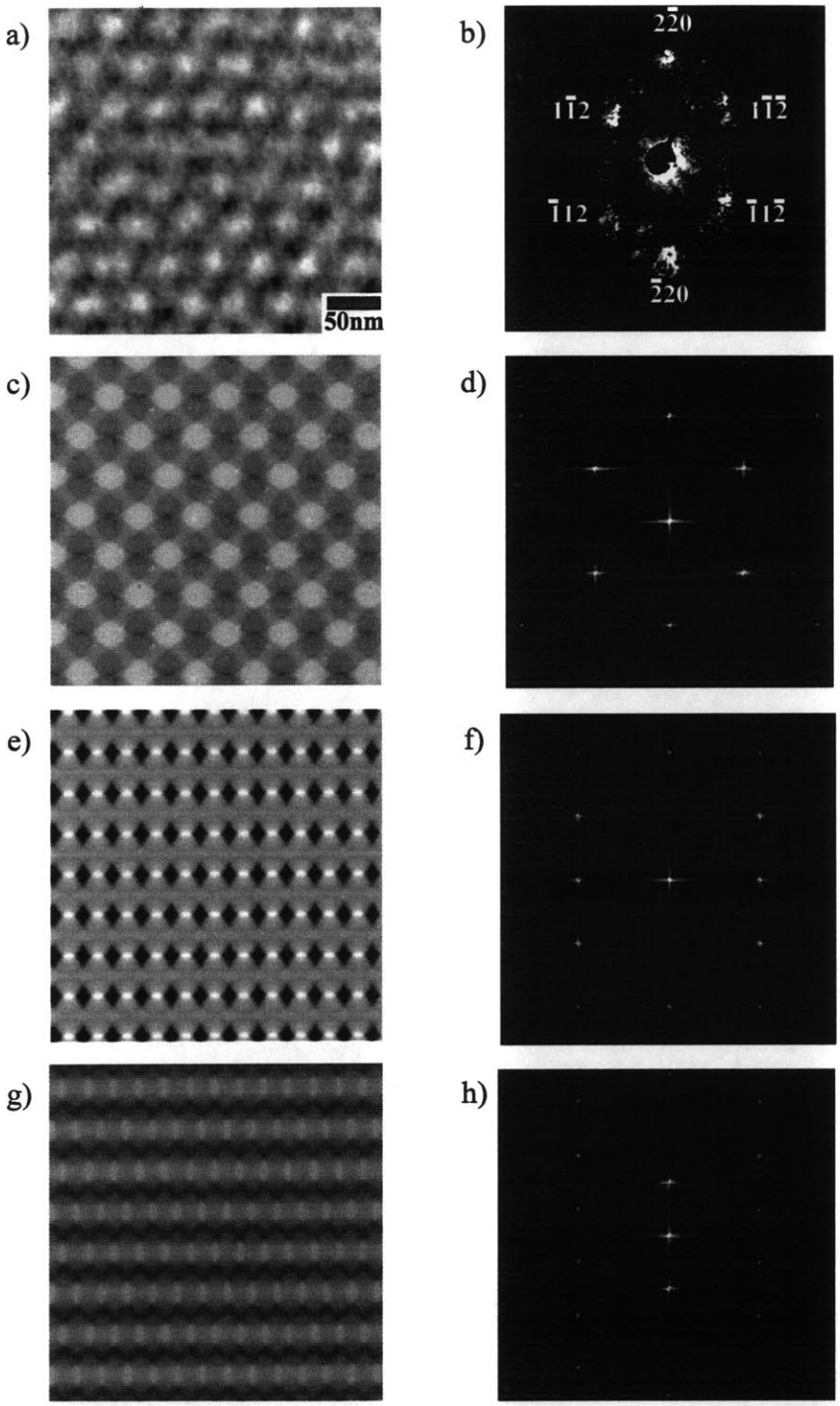

Figure 5.8: a) Bright−field TEM image of a 2−fold projection of the 34%S SIS cast from toluene. The light regions are PS and the dark regions are PI stained with OsO_4. b) Optical diffraction pattern taken from the same image. c). Simulated [110] projection of the DG level surface: s_p = +/− 1.0; 1.0 unit cell thick. d). FFT of the simulated DG [110] projection. e). Simulated [110] projection of the DD level surface, PI−rich; s_p = +/− 0.8; 1.0 unit cell thick. f). FFT of the simulated D [110] projection. g). Simulated [113] projection of the DD level surface, PI−rich; s_p = +/− 0.8; 0.5 unit cell thick. h) FFT of the simulated D [113] projection.

5.2.3 The 36% SIS

For the purposes of mechanical testing, additional material was synthesized with 34 vol.% styrene, i.e., with the DG composition. It was also stated that the triblock not necessarily have to be *exactly* symmetric, and the triblock was subsequently synthesized by sequential addition of monomers with a final composition of 36% S. Although with this process, exact symmetry of the molecule is not achieved, the final triblock is produced in three days and no fractionation is needed.

5.2.3.1 Synthesis by Sequential Addition of Monomers

The 36% S SIS triblock was synthesized by sequential addition of monomers. The reaction used is the following:

$$\mathbf{St + sec\text{-}Bu\ Li \xrightarrow{C_6H_6} PS\ LI} \qquad \mathbf{(A)}$$

$$\mathbf{PS\ LI + Is \xrightarrow{C_6H_6} PS\ PI\ Li} \qquad \mathbf{(AB)}$$

$$\mathbf{PS\ PI\ Li + St \xrightarrow[of\ THF]{small\ amount} \underset{Triblock\ copolymer\ of\ the\ ABA\ type}{PS\ PI\ PS}}$$

In order to increase the initiation rate of the styrene towards the PILi macroinitiator, a small amount of THF (less than 0.5 ml) was added. No change in the microstructure of the PI block occurs from the small amount of THF used, since THF is added after the complete polymerization of the isoprene. The only disadvantage of this method is that the two PS blocks may not have precisely the same molecular weight.

The final polymer was a 36 wt.% PS triblock with block molecular weights of 13.6K/44.4K/12K. Twenty grams of polymer resulted from the synthesis. The SEC chromatogram of the triblock is given in figure 4.9. The molecular characteristics of the triblock is shown in table 5.3

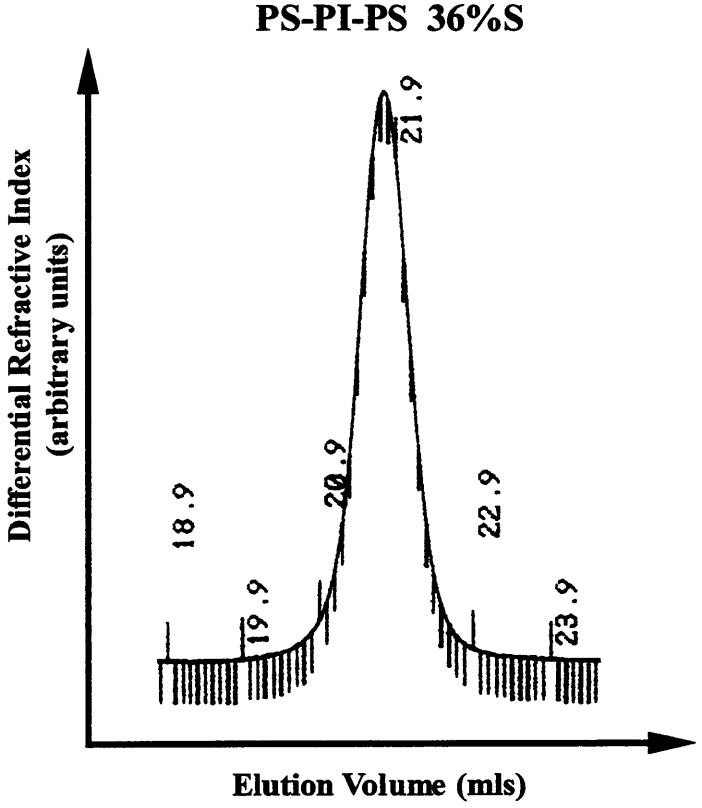

Figure 5.9: SEC chromatogram of the 36% PS SIS triblock copolymer made by sequential addition of monomers.

Table 5.3: Molecular characteristics of the polymer made by sequential addition

Sample	Block M_w x 10^3	M_w x 10^3 (g/mol)	PDI	%PS (UV/SEC)
36% S	13.4/44.4/12	69.8	1.03	36

5.2.3.2 Morphological Characterization

The SAXS scattering pattern of the 36% PS SIS triblock copolymer made by sequential addition of monomers is shown in figure 4.10. Peaks occur in $\frac{q_n}{q_1}$ ratios of 1.00 : 1.16 : 1.54 : 1.84 : 2.30 : 2.54, which according to Table 4.1b, can be indexed to Ia3d. (The highest order peaks are harder to index, because closely spaced reflections may cause peaks to overlap and either cause them to broaden or to peak in intensity at a q intermediate of two allowed.)

The previous sections have described in detail how the morphology of the 34%S SIS polymer was determined to be the tri-functional double gyroid structure with $Ia\bar{3}d$

symmetry. The SAXS, TEM, and geometrical considerations unambigously lead to this conclusion. To avoid an unnecessary and lengthy repetition of the same arguments to this third triblock copolymer, an alternative route to determining its morphology is taken. Given that the polymer whose space group is Ia3d has a topologically interconnected DG morphologically, it is likely that another polymer, with a nearly equivalent composition and molecular weight, such as the 36%S SIS whose space group is also Ia3d, has the same morphology, that of the DG.

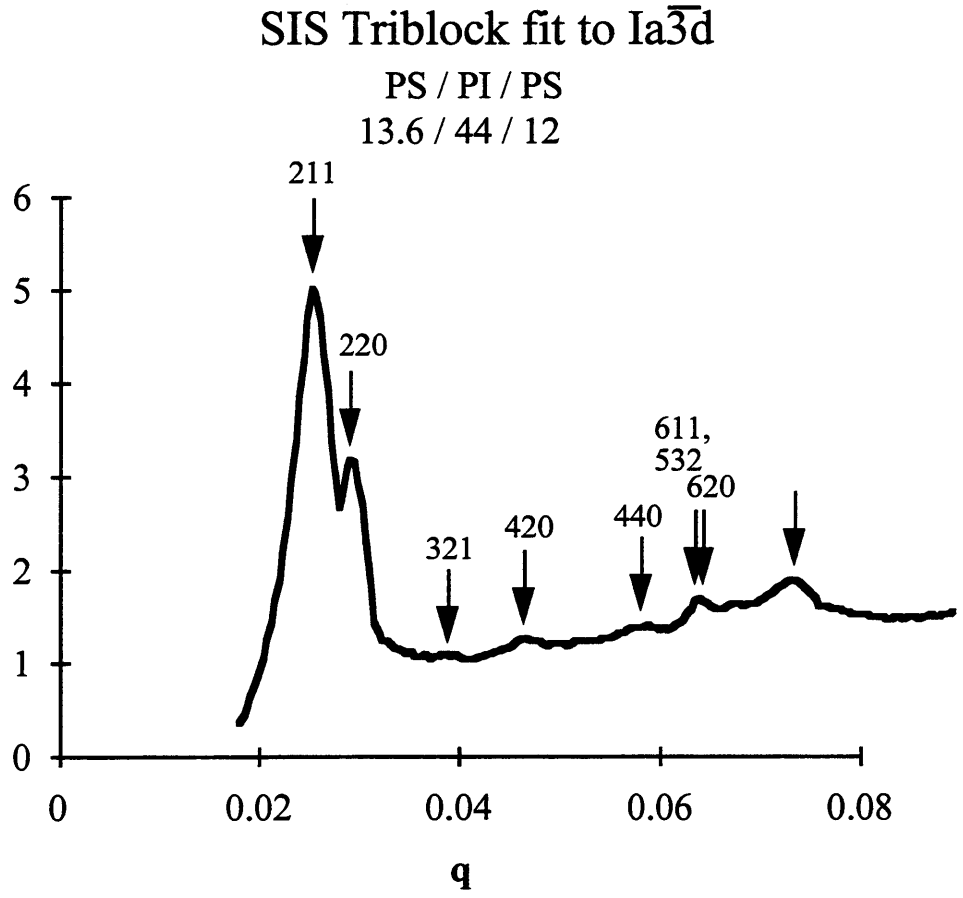

Figure 5.10: Plot of the azimuthally integrated ln [q^2 * I(q)] vs. q for the 36% S 13.6/44/12 kg/mol SIS triblock. The arrows indicate the allowed reflections for the Ia3d space group.

The first two peaks in the SAXS pattern correspond to the (211) and (220) reflections which occur at q_{211} = 0.0255 $Å^{-1}$ and q_{220} = 0.0295 $Å^{-1}$, respectively. The corresponding

(211) interplanar spacing is d_{211} = 246 Å, and the lattice parameter of the DG unit cell is a = 604 Å.

Summary of the U. of Athens Triblocks

In collaboration with the Hadjichristidis group at the University of Athens, Greece, three polymers were made by Avgeropoulos in an attempt to isolate and obtain an interconnected cubic morphology in triblock copolymers. Of the three polymers made, two exhibited exhibited a cubic morphology. The samples, molecular weights, synthesis route, and resulting morphology are given in Table 5.4.

Table 5.4: Characteristics of the polymers synthesized by Avgeropoulos of the Hadjichristidis group at the University of Athens, Greece. χN values were calculated according to (Owens et al., 1989)

Sample ID	Block Mol. Wt.	χN	Synthesis Route	Amount Made
32%S	11/55/11	65	linking by chlorosilane	2g
34%S	13.6/46.4/13.6	63	linking by chlorosilane	2g
36%S	13.6/44.4/12	60	sequential addition of monomers	20g

Sample ID	Morphology	Characteristic Peak	Characteristic Spacing	Lattice Parameter
32%S	cylinders	$q_{10} = 0.0270$ Å^{-1}	$d_{10} = 233$ Å	a = 233 Å
34%S	DG	$q_{211} = 0.0247$ Å^{-1}	$d_{211} = 254$ Å	a = 623 Å
36%S	DG	$q_{211} = 0.0255$ Å^{-1}	$d_{211} = 246$ Å	a = 604 Å

5.3 Industrial Scale SIS Triblocks (Dexco)

In July, 1996, we contacted Dr. Brian Walther, a collaborator from the Dexco Company, an industrial producer of SIS triblock copolymers. We told Dr. Walther of our work on the mechanical properties of interconnected cubic morphologies in block copolymers and of our discovery of a DG triblock. We proposed to him that MIT and Dexco form a collaboration for Dexco to industrially synthesize triblocks of various molecular weights with compositions in the predicted DG composition range, so that we could adequately process them using roll-casting for characterization studies into the mechanical behavior. This collaboration between our group and Dexco would then open possibilities to produce a material or product with novel mechanical properties. In addition, Dexco could later have access to and capitalize on the results and be one of the first suppliers of DG triblocks or producers of the first DG triblock applications. Brian Walther used Dexco pilot lines and made for us three SIS triblock copolymers in September, 1996. The three samples made and characteristics are given in table 5.5. This section reports on the morphology of each of the polymers, static cast from toluene, as found through SAXS and TEM.

Table 5.5: Dexco polymers and their characteristics

	Sample	**Molecular Weight**	**Polydispersity**
6725-51	39 wt% S SIS	73,300	1.03
6725-49	35 wt% S SIS	124,000	1.03
6725-50	33.8 wt% S SIS	166,000	1.03

Dexco 39%S SIS

Figure 5.11 shows the 2-dimensional azimuthal integration of the small angle x-ray scattering data plot of ln $[q^2 * I(q)]$ vs q of Dexco sample 6725-51, 39.3 weight % S SIS polymer. The peaks are in ratios of $\frac{q_n}{q_1}$ of 1 : 2 : 3 (weak) : 4 : 5, consistent with a lamellar morphology. The third reflection is suppressed due to a zero in the structure factor for block copolymer compositions close to $\frac{1}{3}$ (Skoulios, 1973). The (100) domain spacing corresponding to the first peak (long period of the lamellae) is 266 A.

Figure 5.12 shows a typical bright-field TEM micrograph, with PS as the bright regions and PI as the osmium-stained dark regions. The alternating thin layers of PS and thick layers of PI suggest a lamellar morphology. The PS layers are 1/3 of the long period of the lamellar spacing and 1/2 of the PI layers.

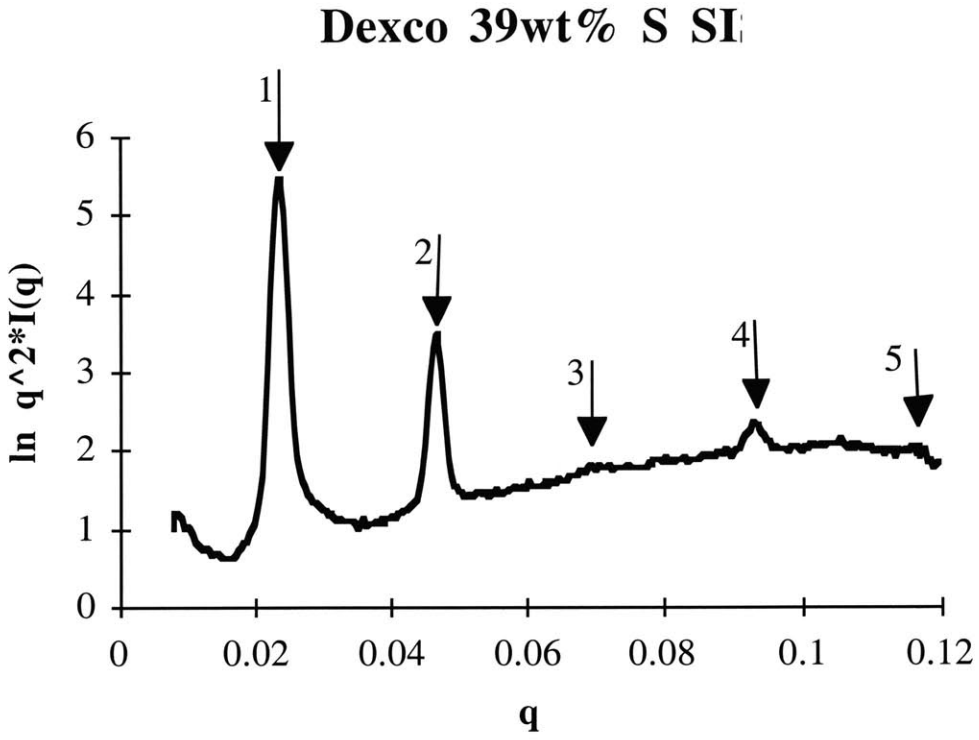

Figure 5.11: Small angle x-ray scattering data for Dexco sample 6725-51, 39.3 weight % S SIS polymer. The observed peaks occur in ratios of 1:2:3:4:5, consistent with a lamellar morphology.

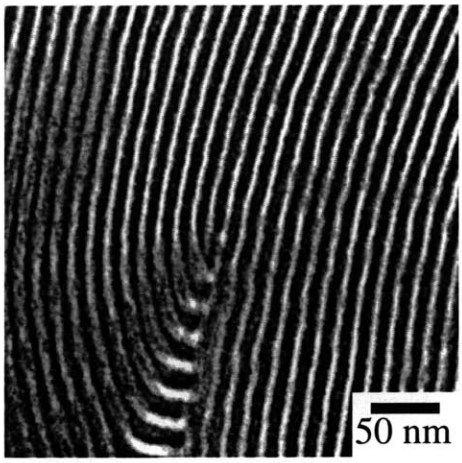

Figure 5.12: Bright field TEM image of Dexco sample 6725-51, 39.3 weight % S SIS polymer. The light regions are PS and the dark regions are PI.

Dexco 35%S SIS

Figures 5.13a-c show the bright field TEM micrographs of Dexco 6725-49, 35.0% S SIS polymer. Figure 5.13a shows different grains of cylinders, the stripes being a view normal to the cylinder axis, and the hexagonally-packed array of dots being an axial view down the cylinder axis. Existing concurrently in the same sample are regions with cubic morphology, as exhibited by regions of 6-fold symmetry (figure 5.13b), 4-fold symmetry (figure 5.13c), and 2-fold symmetry (figure 5.13d).

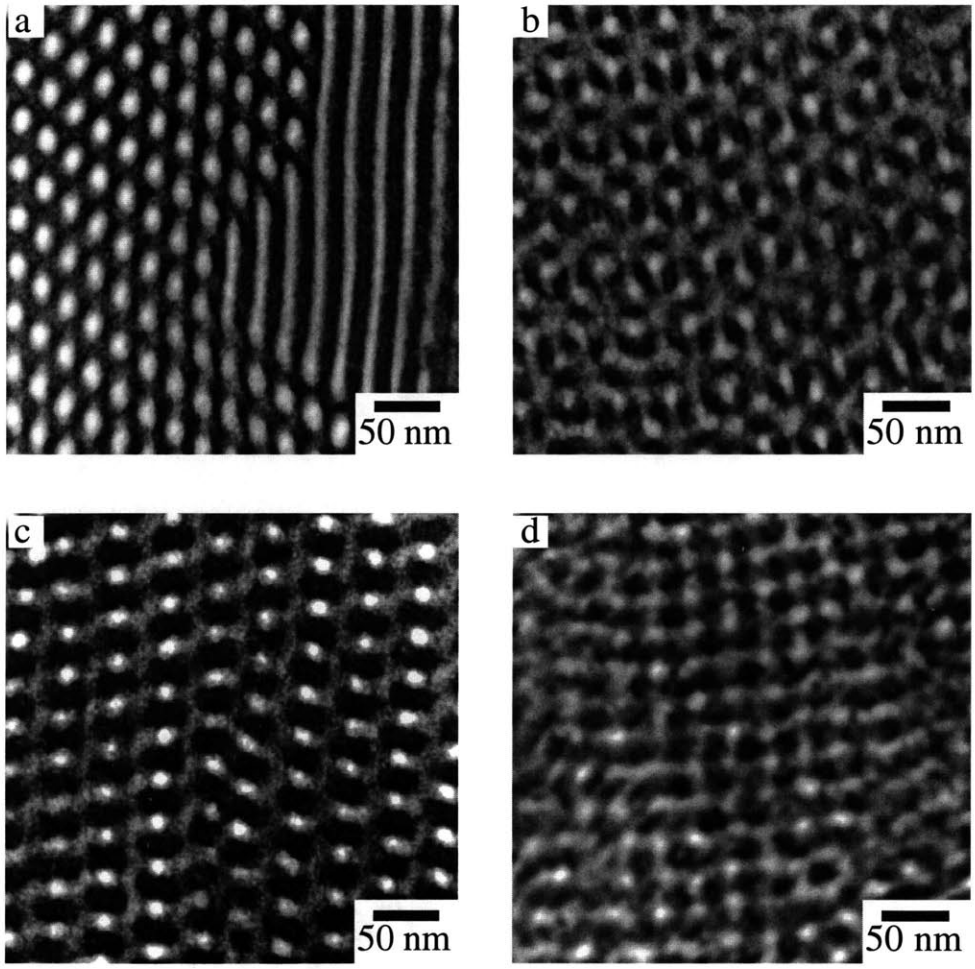

Figure 5.13: TEM images of Dexco sample 6725-49, 35.0% S SIS. a) View characteristic of cylinder morphology - the left hand side depicts the cylinders end-on, showing the hexagonally packed rods, and the right hand side depicts the side view of the cylinders. In addition to the cylinder microdomain morphology, there exist regions exhibiting b) 6-fold symmetry, c) 4-fold symmetry, and d) 2-fold symmetry, characteristic of a cubic morphology. From experience with other polymers which show the DG morphology, these domains are likely to be DG.

These views, in particular the 2-fold shown in figure 5.13d, are characterisic of the double gyroid microdomain morphology. Judging from an overall survey of the sample using TEM, perhaps 30-40% of the sample is DG.

Figure 5.14 shows the two-dimensional azimuthal integration small angle x-ray scattering plot of ln [q^2 * I(q] vs q. The expected ratios $\frac{q_n}{q_1}$ for cylinders and for gyroid are given in Table 1. The experimentally observed peaks in a 20-degree angular integration range are in ratios of $\frac{q_n}{q_1}$ of 1.00:1.83: 2.00: 2.68: 3.00. These ratios are very close to (but not exactly) those of the allowed reflection ratios for cylinders (see table 4.1a). The $\sqrt{3}$ peak is shifted to higher q from that of the allowed cylinder reflection, perhaps due to the overlap of the $\sqrt{4}$ peaks, or more likely due to the overlap with an allowed DG reflection, such as that of the (420) of DG, which has the ratio of 1.83 or the (332) reflection, which has the ratio of 1.91. The $\sqrt{7}$ peak is quite broad and its peak position was difficult to assign. Both cylinders and DG have a $\sqrt{7}$ peak (the (21) reflection for cylinders, and the (541) reflection for DG). The domain spacing of the first peak, d_{10}, is 357 Å.

Considering the TEM and SAXS results, the morphology of the polymer is bi-phasic cylinders and double gyroid.

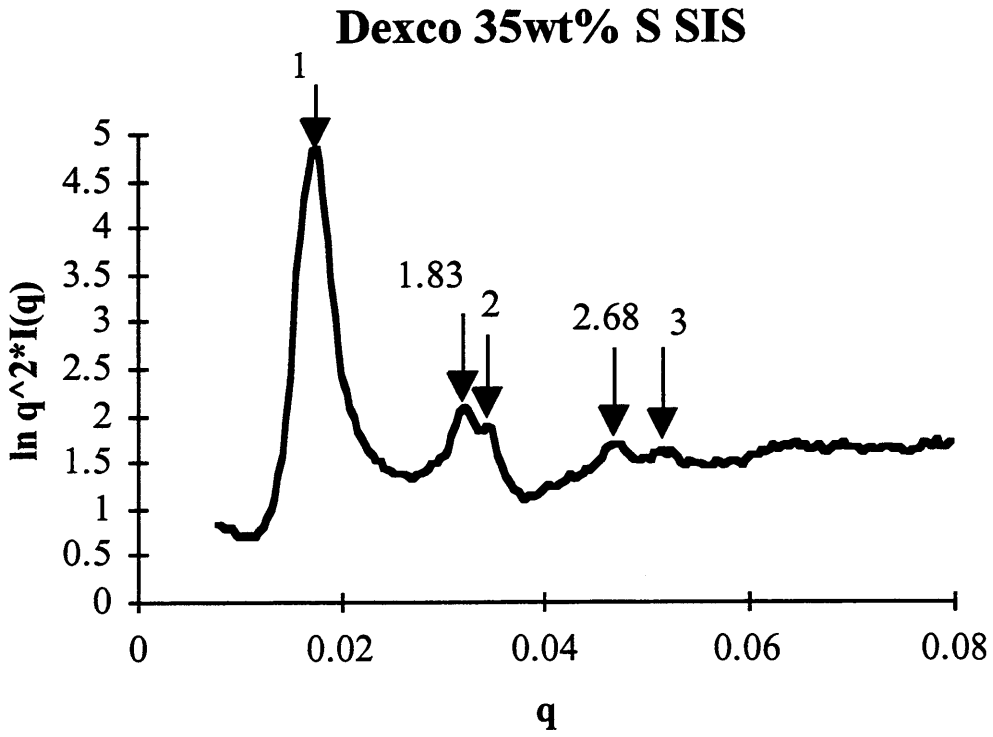

Dexco 33.8% SIS

Figures 5.15a-b are typical bright field TEM micrographs of Dexco 6725-50, 33.8% S SIS polymer (molecular weight 166,000), showing cylindrical morphology. Figure 4.15a shows an end-on view of hexagonally packed cylinders, and figure 5.15b shows the side view of cylinders. The sample does not show very large grains in TEM, and presumably because of the very high molecular weight which hinders the mobility.

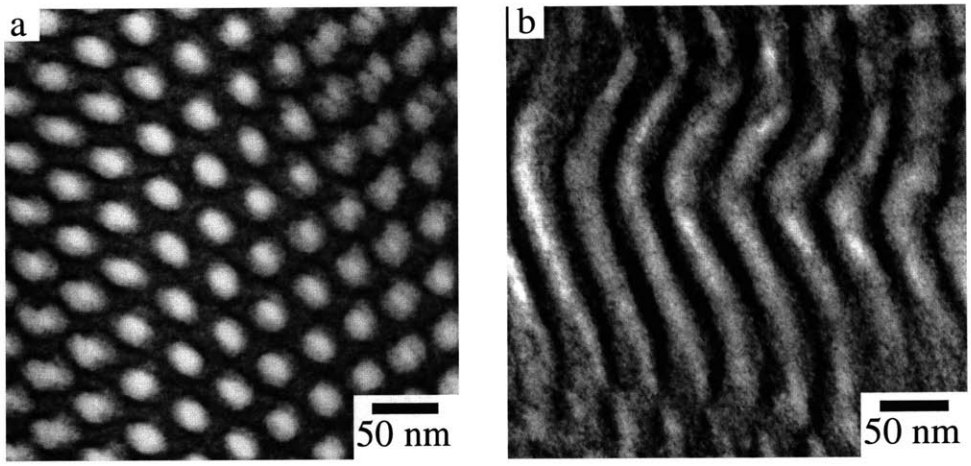

Figure 5.15: TEM micrographs of Dexco , 33.8 wt% S. a) hexagonal packing of PS cylinders, and b) transverse view of the cylinders.

Figure 5.16 shows the two-dimensional azimuthal integration small angle x-ray scattering plot of ln $[q^2 * I(q]$ vs q. The integrated intensity versus q plot shows very broad peaks, with nominal q-ratios of 1, 1.68, and 2.68, characteristic of cylinders. The domain spacing of the (10) peak, d_{10} , is 409 Å. The broad peaks are due to the small grains and short-range order. In light of both SAXS and TEM, the morphology is cylinders.

Conclusions

Table 5.6 summarizes the morphologies of the three Dexco triblocks. Regardless of whether the double gyroid morphology is suppressed in favor of cylinders due to kinetic effects or due to thermodynamic effects, the problems arise in both cases from the high molecular weight. In the thermodynamic case, higher molecular weights result in higher χN. According to Mean Field calculations, the double gyroid phase becomes unstable at high χN, achieving, instead, the cylinder morphology for increasing molecular weight. In the kinetic case, higher molecular weights result in kinetically

unstable at high χN, achieving, instead, the cylinder morphology for increasing molecular weight. In the kinetic case, higher molecular weights result in kinetically constrained chains and would require long annealing periods to obtain the desired double gyroid morphology. Thus molecular weights of both Dexco 35 wt%S SIS and Dexco 33.8 wt%S SIS are too high to achieve completely double gyroid morphology.

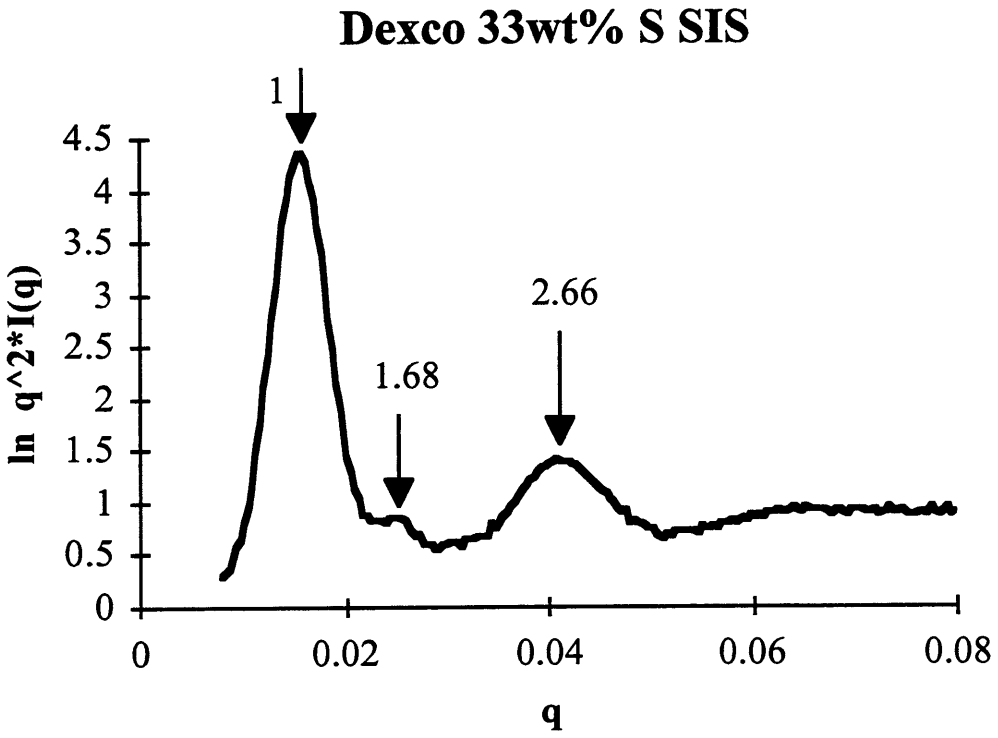

Figure 5.16: SAXS pattern of Dexco 6725-50, 33.8% S SIS.

Table 5.6: Morphologies of the Different Molecular Weight SIS Triblocks with Composition ~34-35%S. χN values were calculated according to (Owens et al., 1989)

Polymer	**Mol. Wt.**	**χN**	**Morphology**
Greek 34% S	73,600	81	double gyroid
Dexco 35% S	124,000	136	cylinders + double gyroid (mainly cylinders)
Dexco 33.8% S	166,000	184	cylinders

5.4 Morphology Results and Discussion

The polymers synthesized by Dexco and by the Hadjichristidis group make an interesting series for observing the morphology as a function of molecular weight. Figure 5.17 shows the XN for the polymers (at 120°C) as a function of composition, with the observed morphology specified.

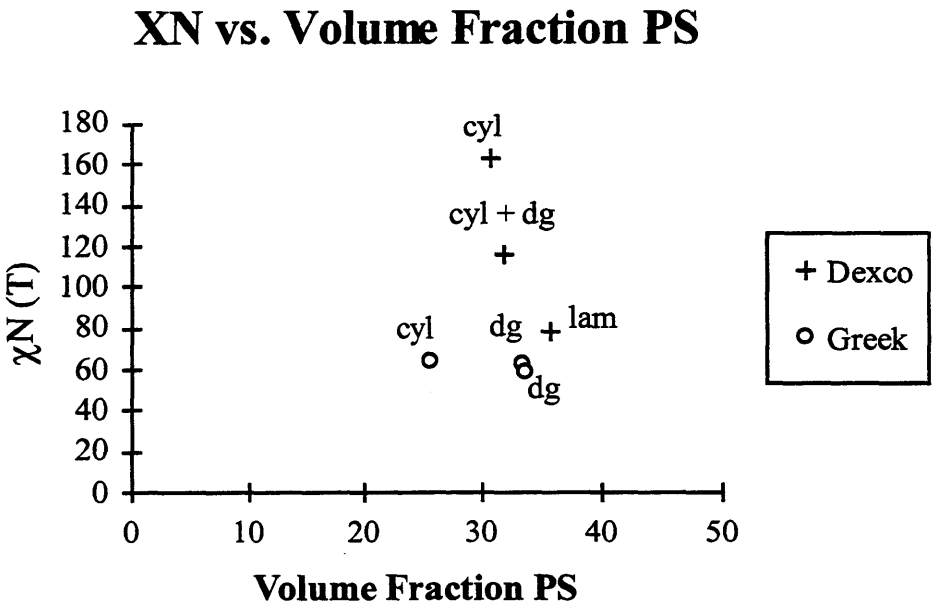

Figure 5.17: χN vs. volume fraction PS for SIS triblocks synthesized by Dexco and the Hadjichristidis group in U. of Athens.

The morphology of the U. of Athens 34wt%S SIS, MW = 73,600 is double gyroid (Avgeropoulos et al., 1997). Based on TEM and SAXS data, the polymer is very well-ordered, forming large grains ~2 μm in diameter, after static casting from toluene and annealing at 120°C for 2 weeks. The Dexco 35 wt%S SIS, MW = 124,000 polymer was shown in figures 3a-c. Throughout the film, there are regions of cylinders and of double gyroid, cylinders predominating, with grains ~1-2 μm. The Dexco 33.8 wt%S SIS, MW = 166,000 polymer was shown in figures 5a-c. Throughout the film, there are grains of cylinders ~1-2 μm large, indicating good order.

The trend seems to be that as the molecular weight is increased, the morphology goes from double gyroid to cylinders. The question arises, is the disappearance of the double gyroid phase a kinetic effect or a thermodynamic effect? For example, there are two possible explanations for the co-existence of double gyroid and cylinders in the Dexco 35 wt%S SIS. The first is that the molecular weight is high and thus the kinetic mobility is

low, resulting in simple casting into cylinders at ambient temperatures and slowly annealing to double gyroid at elevated temperatures. If this is the case, the transition from cylinders to gyroid is a nucleation and growth process, as evidenced by patches of DG amongst the cylinder grains.

A second explanation for the co-existence of the two phases is that morphology for the χN of this polymer is at the cylinder-gyroid boundary such that the two phases do co-exist at equilibrium for the annealing temperature. Matsen and Bates (Matsen and Bates, 1996) used Mean-Field calculations to generate a diblock copolymer phase diagram for a PS-PI system. Although these phase diagrams have not yet been calculated for triblock copolymers, the phase diagrams for diblocks provide some insight into the expected phase behavior for triblocks. The theoretical phase diagram shows that the double gyroid phase is a weak- to intermediate-segregation phase in a small composition window, which disappears at large χN. Therefore, according to this phase diagram, as the molecular weight increases, double gyroid becomes an unstable phase. The 35 wt%S SIS may be at the cylinder-gyroid boundary such that the two phases do co-exist at equilibrium.

The Dexco 33.8 wt%S SIS, MW = 166,000, has the composition for double gyroid, yet the morphology of the simple-cast, annealed films are cylinders. Again, this could be due to kinetics, where the polymer is too high in molecular weight such that the chains are kinetically constrained to transit the morphology to double gyroid under the annealing conditions. However, this does not seem likely, as there is good order in the cylinders, which indicates that there was enough kinetic mobility to form fairly large grains. The thermodynamic explanation for the morphology is that the high molecular weight, and hence χN of this polymer pushes the morphology into the cylinder regime.

Of course, the resulting morphologies could as well be due to the combination of kinetic and thermodynamic factors. The Dexco polymers 6725-50 and 6725-51 will be used for further studies into the phase behavior.

Solution Behavior/ ODT

For roll casting, previous Dexco polymers (Dexco Vector 4211-D, MW 97K, 30 wt% S) have been typically dissolved in toluene or cumene at a (1g polymer / 2ml solvent) concentration. The 35wt% S SIS was dissolved in cumene (1g polymer / 2.5 mL cumene) to achieve a viscosity suitable for roll-casting. SAXS patterns of the annealed roll-cast polymer indicated lamellae. Since the symmetries of the flow field in roll-casting is commensurate with those of either cylinders or lamellae, the as-cast morphology of roll-casted polymer is not readily double gyroid. It seems that the usual annealing treatment of 5 days at 120°C does not change the morphology much and the films remain lamellar. It is

inferred that due to the high molecular weight of the polymer, the chains are kinetically constrained.

The 33.8 wt% S SIS was dissolved in cumene and toluene at room temperature in a 1w/4v concentration, but solvation took well over a month to dissolve. The original purpose in roll casting these samples was for studies into the mechanical behavior of double gyroid materials. As so, the polymer was not roll-cast, because the simple-cast morphology seemed to be cylinders and because solvation in cumene was relatively slow.

5.5 Mineral Oil Blends

Blends were made by adding mineral oil to a lamellar triblock to suppress the styrene content enough to achieve the double gyroid morphology. The triblock copolymer used was Dexco Vector 4411-D, which is an 18k-44k-18k SIS with 45 wt.% styrene and total molecular weight of 80k, and a lamellar morphology. The mineral oil used was Penreco Drakeol 500, which, according to the manufacturer, contains 67.5% carbons as paraffins, 32.5% carbons as napthenes, and 0% carbons as aromatics. The fact that the oil has no aromatics is significant in that the oil swelling of the styrene microphase-separated domains is minimized against the swelling of the diene. Three such mineral oil blends were made such that the total styrene content was in the composition range for double gyroid.

The morphology was verified via SAXS but not via TEM. It comes with the experience of characterizing the morphologies of the aforementioned block copolymers, that SAXS is sufficiently reliable at distinguishing between the microdomain morphologies that block copolymers form. It does so by distinguishing the space group of the microphase separated morphology. As each morphology has a characteristic space group and hence a distinct SAXS pattern, we can reliably determine the morphology by SAXS alone. This also gives us the advantage of not needing to introduce mineral oil, which is a volatile, into the vacuum column of the TEM.

Figure 5.18 shows the SAXS patterns of the mineral oil blended materials, both as-cast, and lightly annealed at 120°C under vacuum. The peaks in the 18 wt.% mineral oil (36.9 wt.% styrene) samples, both annealed and unannealed, are in a ratio of 1 : 1.15 : 1.53 : 2.01 : 2.25 : 2.52 : 2.86, which are consistent with the ratios for the (211), (200), (321), (420), (422), (521), and (532) reflections of Ia3d. Hence, it can be concluded with a high degree of confidence that the morphology of the 18 wt.% mineral oil blend is DG. The unannealed sample also exhibits peaks in the correct ratios for DG, although it is less ordered than the annealed sample.

Furthermore, the SAXS patterns for the 20 wt. % mineral oil (36 wt.% styrene) can also be matched to those for DG. This is in contrast to the 22 wt.% mineral oil (35.1 wt.% styrene) sample, which has a cylinder morphology in the unannealed state and lamellar morphology when annealed. The results are summarized in Table 5.7.

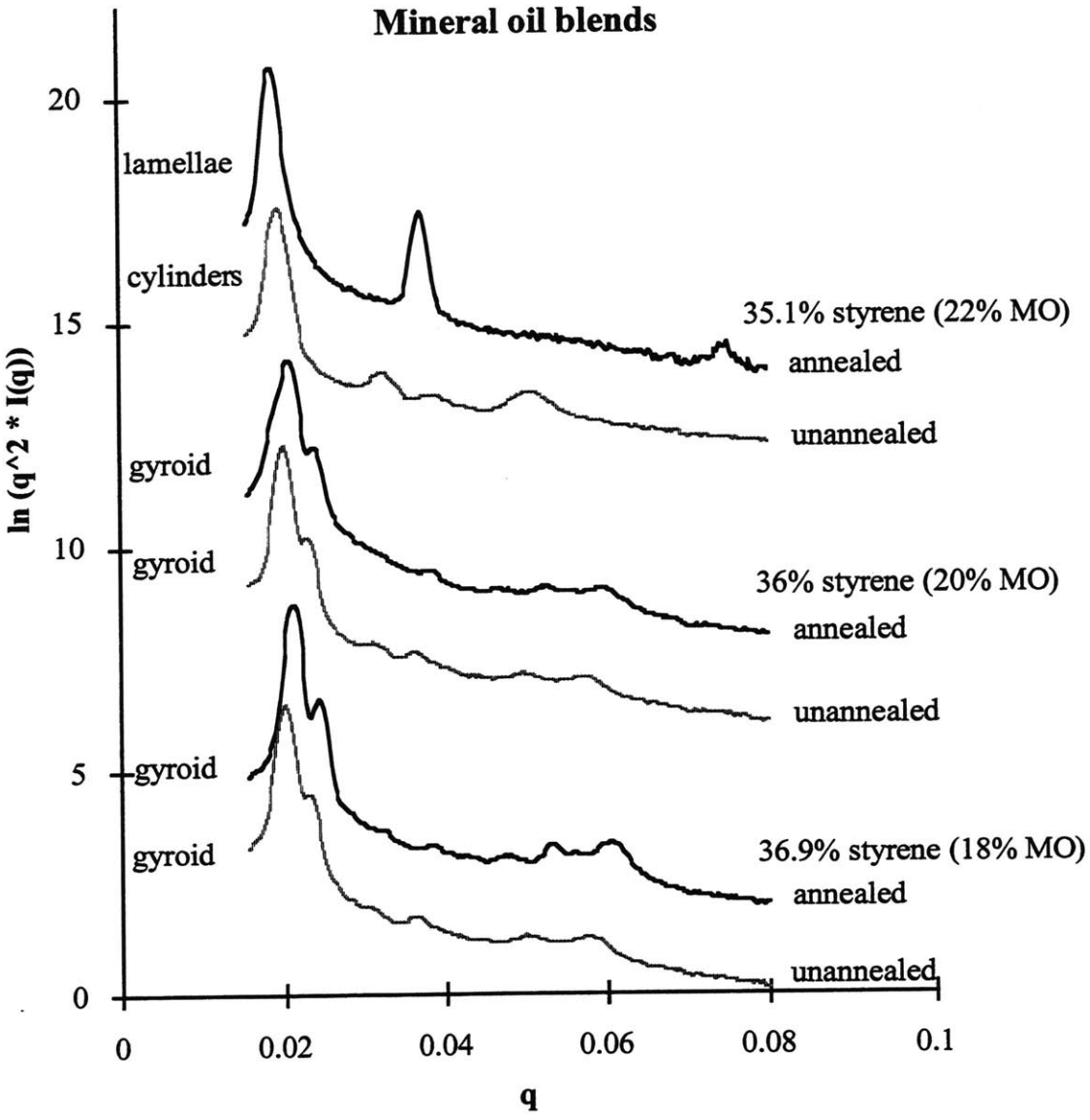

Figure 5.17: SAXS scattering data for SIS-mineral oil blends

Table 5.7: 18/44/18 SIS Mineral Oil Blends

Wt. % MO	Total wt. % S		Morphology	d spacing
18	36.9	annealed	DG	$d_{211} = 298$
		unannealed	DG	$d_{211} = 314$
20	36.0	annealed	DG	$d_{211} = 305$
		unannealed	DG	$d_{211} = 316$
22	35.1	annealed	lamellae	d_{001}=338
		unannealed	cylinders	d_{001}=325

The rationale for the use of mineral oils to achieve the DG morphology is primarly the lower cost of mineral oil. Mineral oil is a cheaper filler and this can reduce the material cost significantly, especially in large scale operations. The presence of mineral oil enhances the mobility of the chains and since the chains have more chances to correct themselves, larger grains can be achieved. The main drawback is the volatility of mineral oils. If samples are annealed in a vacuum oven for extended periods of time, then the mineral oil evaporates and the morphology changes back towards that of the mother triblock copolymer.

The use of mineral oil is also interesting from a scientific point of view. The addition of mineral oil changes the number of entanglements in the diene phase and thereby enhances mobility of the chains. The reduced entanglement density leads to a reduction in stress that the polymer can bear at high elongations. Furthermore, when the polymer is stretched, the polymer chains can apply an osmotic pressure on the mineral oil and force it out of the diene domains into the grain boundaries, which may facilitate grain boundary motion or slip between the planes.

5.6 References

Aggarwal, S. L. (1976). "Structure And Properties Of Block Polymers And Multiphase Polymer Systems: An Overview Of Present Status And Future Potential." Polymer **17**: 938-956.

Alward, D. B. (1985). A morphological study of a series of multiarmed star block copolymers of polyisoprene and polystyrene. Ph. D. thesis thesis, University of Massachusetts.

Alward, D. B., D. J. Kinning, E. L. Thomas and L. J. Fetters (1986). "Effect Of Arm Number And Arm Molecular Weight On The Solid-State Morphology Of Poly(Styrene-Isoprene) Star Block Copolymers." Macromolecules **19**: 215-224.

Arai, K., T. Kotaka, Y. Kitano and K. Yoshimura (1980). "Poly(Styrene-B-Butadiene-B-4-Vinylpyridine) Three-Block Polymers. Synthesis, Characterization, Morphology, And Mechanical Properties." Macromolecules **13**: 1670-1678.

Avgeropoulos, A., B. J. Dair, N. Hadjichristidis and E. L. Thomas (1997). "The Tricontinuous Double Gyroid Cubic Phase In Triblock Copolymers Of The Aba-Type." Macromolecules **30**: 5634-5642.

Bi, L.-K. and L. J. Fetters (1975). "Domain Morphology Of Star Block Copolymer Of Ps And Pi." Macromolecules **8**(1): 90-92.

Charvolin, J. and J. F. Sadoc (1987). "Periodic Systems Of Frustrated Fluid Films And <<Bicontinuous>> Cubic Structures In Liquid Crystals." Journal de Physique France **48**: 1559-1569.

Fischer, W. and E. Koch (1987). "On 3-Periodic Minimal Surfaces." Zeitschrift für Kristallographie **179**: 31-52.

Förster, S., A. K. Khandpur, J. Zhao, F. S. Bates, I. W. Hamley, A. J. Ryan and W. Bras (1994). "Complex Phase Behavior Of Polyisoprene-Polystyrene Diblock Copolymers Near The Order-Disorder Transition." Macromolecules **27**: 6922-6935.

Gobran, D. A. (1990). Phase Separation and Morphology of Diblock and Segmented Block Copolymers. Ph. D. thesis, University of Massachusetts.

Hajduk, D. A., P. E. Harper, S. M. Gruner, C. C. Honeker, G. Kim, E. L. Thomas and L. J. Fetters (1994). "The Gyroid: A New Equilibrium Morphology In Weakly Segregated Diblock Copolymers." Macromolecules **27**: 4063-4075.

Hajduk, D. A., P. E. Harper, S. M. Gruner, C. C. Honeker, E. L. Thomas and L. J. Fetters (1995). "A Reevaluation Of Bicontinuous Cubic Phases In Starblock Copolymers." Macromolecules **28**: 2570-2573.

Hasegawa, H., T. Sumitomo, T. Hashimoto and H. Kawai (1983). . 32nd Polymer Symposium of the Society of Polymer Science, Japan, Polymer Preprints Japan.

Hasegawa, H., H. Tanaka, K. Yamasaki and T. Hashimoto (1987). "Bicontinuous Microdomain Morphology Of Block Copolymers. 1. Tetrapod-Network Structure Of Polystyrene-Polyisoprene Diblock Polymer." Macromolecules **20**: 1651-1662.

Herman, D. S., D. J. Kinning, E. L. Thomas and L. J. Fetters (1987). "A Compositional Study Of The Morphology Of 18-Armed Poly(Styrene-Isoprene) Star Block Copolymers." Macromolecules **20**: 2940-2942.

Iatrou, H. and N. Hadjichristidis (1992). "Synthesis Of A Model 3-Miktoarm Star Terpolymer." Macromolecules **25**: 4649-4651.

Iatrou, H. and N. Hadjichristidis (1993). "Synthesis And Characterization Of Model 4-Miktoarm Star Co- And Quaterpolymers." Macromolecules **26**: 2479-2484.

Kinning, D. J., E. L. Thomas, D. B. Alward, L. J. Fetters and D. L. J. Handlin (1986). "Sharpness Of The Functionality Induced Structural Transition In Poly(Styrene-Isoprene) Star Block Copolymers." Macromolecules **19**: 1288-1290.

Kudose, I. and T. Kotaka (1984). "Morphological And Viscoelastic Properties Of Poly(Styrene-B-Butadiene-B-4-Vinylpyridine) Three-Block Polymers Of The Abc Type." Macromolecules **17**: 2325-2332.

Lambert, C. A., L. H. Radzilowski and E. L. Thomas (1996). "Triply Periodic Level Surfaces As Models For Cubic Tricontinuous Block Copolymer Morphologies." Philosophical Transactions of the Royal Society of London A **354**: 2009-2023.

Longley, W. and T. J. McIntosh (1983). "A Bicontinuous Tetrahedral Structure In A Liquid-Crystalline Lipid." Nature **303**: 612-614.

Luzzati, V., H. Delacroix, A. Gulik, T. Gulik-Krzywicki, P. Mariani and R. Vargas (1997). "The Cubic Phases Of Lipids" in Lipid Polymorphism and Membrane Properties. R. M. Epand. New York, NY, Academic Press. **44:** 3-24.

Matsen, M. W. (1995). "Phase Behavior Of Block Copolymer/Homopolymer Blends." Macromolecules **28**: 5765-5773.

Matsen, M. W. and F. S. Bates (1996). "Unifying Weak- And Strong-Segregation Block Copolymer Theories." Macromolecules **29**(4): 1091-1098.

Matsushita, Y., H. Choshi, T. Fujimoto and N. Nagasawa (1980). "Preparation And Morphological Properties Of A Triblock Copolymer Of Abc Type." Macromolecules **13**: 1053-1058.

Matsushita, Y., J. Suzuki and M. Seki (1998). "Surfaces Of Tricontinuous Structure Formed By An Abc Triblock Copolymer In Bulk." Physica B. Condensed Matter **248**: 238.

Matsushita, Y., M. Tamura and I. Noda (1994). "Tricontinuous Double-Diamond Structure Formed By A Styrene-Isoprene-2-Vinylpyridine Triblock Copolymer." Macromolecules **27**: 3680-3682.

Matsushita, Y., K. Yamada, T. Hattori, T. Fujimoto, Y. Sawada, M. Nagasawa and C. Matsui (1983). "Morphologies Of Abc-Type Triblock Copolymers With Different Compositions." Macro. **16**: 10-13.

Mayes, A. M. and M. Olvera de la Cruz (1989). "Microphase Separation In Multiblock Copolymer Melts." Journal of Chemical Physics **91**(11): 7228-7235.

Mitchell, D. J., G. J. T. Tiddy, L. Waring, T. Bostock and M. P. McDonald (1983). "Phase Behavior Of Polyoxyethylene Surfactants With Water." Journal of the Chemical Society, Faraday Transactions 1 **79**: 975-1000.

Mogi, Y., H. Kotsuji, Y. Kaneko, K. Mori, Y. Matsushita and I. Noda (1992). "Preparation And Morphology Of Triblock Copolymers Of The Abc Type." Macro. **25**: 5408-5411.

Mogi, Y., K. Mori, Y. Matsushita and I. Noda (1992). "Tricontinuous Morphology Of Triblock Copolymers Of The Abc Type." Macromolecules **25**: 5412-5415.

Mogi, Y., M. Nomura, H. Kotsuji, K. Ohnishi, Y. Matsushita and I. Noda (1994). "Superlattice Structures In Morphologies Of The Abc Triblock Copolymers." Macromolecules **27**: 6755-6760.

Morton, M. and L. J. Fetters (1975). "Anionic Polymerization Of Vinyl Monomers." Rubber Chemistry and Technology **48**: 359-409.

Owens, J. N., I. S. Gancarz, J. T. Koberstein and T. P. Russell (1989). "Investigation Of The Microphase Separation Transition In Low Molecular Weight Diblock Copolymers." Macro. **22**: 3380-3387.

Schoen, A. H. (1970). Infinite periodic minimal surfaces without selfintersections, NASA.

Schulz, M. F., F. S. Bates, K. Almdal and K. Mortensen (1994). "Epitaxial Relationship For Hexagonal-To-Cubic Phase Transition In A Block Copolymer Mixture." Physical Review Letters **73**(1): 86-89.

Skoulios, A. E. (1973). "Organization And Structural Problems In Block And Graft Copolymers" in Block and Graft Copolymers: Proceedings of the 19th Sagamore Army Materials Research Conference. J. J. Burke and V. Weiss. Syracuse, Syracuse University Press: 121-139.

Spontak, R. J., S. D. Smith and A. Ashraf (1993). "Dependence Of The Obdd Morphology On Diblock Copolymer Molecular Weight In Copolymer/Homopolymer Blends." Macro. **26**: 956-962.

Thomas, E. L., D. B. Alward, D. J. Kinning, D. C. Martin, D. L. Handlin Jr. and L. J. Fetters (1986). "Ordered Bicontinuous Double-Diamond Structure Of Star Block Copolymers: A New Equilibrium Microdomain Morphology." Macromolecules **19**: 2197-2202.

Thomas, E. L., D. M. Anderson, C. S. Henkee and D. Hoffman (1988). "Periodic Area-Minimizing Surfaces In Block Copolymers." Nature **334**(6184): 598-601.

Tselikas, Y., N. Hadjichristidis, R. L. Lescanec, C. C. Honeker, M. Wohlgemuth and E. L. Thomas (1996). "Architecturally-Induced Tricontinuous Cubic Morphology In Compositionally Symmetric Miktoarm Starblock Copolymers." Macromolecules **29**: 3390-3396.

Winey, K. I., E. L. Thomas and L. J. Fetters (1991). "Ordered Morphologies In Binary Blends Of Diblock Copolymer And Hompolymer And Characterization Of Their Intermaterial Dividing Surfaces." Journal of Chemical Physics **95**(12): 9367-9375.

Winey, K. I., E. L. Thomas and L. J. Fetters (1992). "The Ordered Bicontinuous Double-Diamond Morphology In Diblock Copolymer/Homopolymer Blends." Macromolecules **25**: 422-428.

Xie, R., B. Yang and B. Jiang (1993). "The Ordered Bicontinuous Double Diamond Morphology In Triblock Copolymer / Homopolymer Blends." Macromolecules **26**: 7097.

Chapter 6: Morphology of Rollcast Polymers with Composition in the DG Range

This chapter reports on the morphology of roll cast SIS polymers having composition within those for the DG morphology. Samples of the 34 SIS and the 36 SIS were roll cast from cumene on the mini-roll caster in the same manner as described in section 6.1. Although the rollcasting flow field is not commensurate with the symmetries of the tricontinuous cubic structure, the process was chosen nonetheless to orient the polymers with equilibrium DG morphology. The immediate roll cast morphology might rather be cylinders or lamellae and not necessarily DG. However, it was thought that annealing would provide a kinetic pathway for the non-equilibrium cylinders or lamellae to transform towards DG.

Schulz et al. had found that shearing a diblock copolymer blend with an overall volume fraction of PS of 0.37 (ϕ_{PS} = 0.37) resulted in a shear-oriented cylinder morphology, but that the DG phase emerged upon heating (below T_{ODT}) without shear. This method of growing the equilibrium morphology from a non-equilibrium one through annealing has been dubbed "epitaxial growth" (Schulz, Bates, Almdal, and Mortensen, 1994). It was hoped that DG could be produced with the adaptation of this method to first roll-cast orient the material macroscopically and then to phase transform the film to DG. The morphology of the as-roll cast films is presented in section 6.2.1. Epitaxial growth and epitaxial relationships will be discussed in a literature review in section 6.2.2. The morphology of the roll-cast annealed films is given in section 6.3.

6.1 As-Roll Cast Morphologies

6.1.1 As-Roll Cast Morphology of 34 SIS

Figure 6.1 shows the 2D SAXS pattern (logarithmic scaling of intensity) of the as-roll cast film of the 34 SIS, made via linking of symmetric diblocks with dichlorosilane, and dried under vacuum for one day at ambient temperature. The pattern was taken with the beam through the film thickness direction (y), with the roll cast direction (x) being vertical.

Figure 6.2 shows two-dimensional azimuthal integrations of the SAXS pattern. As a function of q, I(q) * q is plotted (rather than q^2*I(q) for isotropic materials) as a modified Lorentz correction for an oriented material. The dotted line (top) is the full azimuthal integration, and the solid line (below) is the integration over a 10° arc around the equator. Peaks occur at ratios of $\frac{q_n}{q_1}$ of 1.00 : 1.74 : 1.97 : 2.73, indicative of a cylindrical

morphology. The first equatorial peak corresponding to the (10) cylinder planes occurs at $q_{10} = 0.0265$ Å^{-1}. This value is approximately equal to the (10) spacing of the quiescent cast SIS 32 cylinder sample, where $q_{10} = 0.0268$ Å^{-1}. Since the samples are very close in molecular weight (MW_{32} = 77,000 and MW_{34} = 74,000), the fact that the cylinders have about the same spacing indicates that there is little, if any, strain in the cylinders in the roll cast film.

The Bragg peaks along the equator of the pattern in figure 6.1 indicate that the cylinders are preferentially oriented in the vertical direction, which is along the roll-cast direction. The cylindrical morphology likely occurs due to the imposed symmetry of the roll-casting process. Other studies have also shown that under a shear field the DG phase is suppressed in favor of cylinders or lamellae (Schulz et al., 1994; Hajduk, Ho, Hillmyer, Bates, and Almdal, 1998).

Close inspection of the 2D SAXS pattern in figure 6.2 reveals very weak off-equatorial scattering, occuring at q = 0.0250 Å^{-1}, which is approximately equal to the value of q_{211} of the quiescent-cast SIS 34 DG. The off-equatorial scatterings occur at 50±5° from the equator. These off-equatorial components do not belong to the oriented cylinder phase (which should produce scattering only along the equator), but rather it is surmised that they are harbingers of another phase to come and belong to a precursor of the DG.

6.1.2 As-Roll Cast Morphology of 36 SIS

Figure 6.3 shows the 2D SAXS pattern for the roll cast but unannealed 36 SIS polymer (which was synthesized by the sequential addition of monomer). This sample was left for ~5 days with its residual solvent before being dried completely under vacuum. Again, the pattern was taken with the beam through the film thickness direction (y), with the roll cast direction (x) being vertical. The most prominent features in are the equatorial peaks, which occur at q = 0.0265, 0.0527, and 0.797 Å^{-1}. The q ratios are 1.00 : 1.99 : 3.00, characteristic of a layered structure having the first domain spacing of 237 Å. Figure 6.4 shows the 2D azimuthal angle integration, both full and through a 10° arc around the equator, of the pattern in figure 6.3. The 10° integration about the equator strongly suggests lamellae, with the overwhelming presence of the 1:2:3 reflections (and the lack of equatorial $\sqrt{3}$ and $\sqrt{7}$ peaks).

In the full 2D azimuthal integration in figure 6.4, broad and weak scattering occurs at $\frac{q_n}{q_1} \sim = 1.65$ and at 2.63, but the exact peak locations are difficult to assign. This

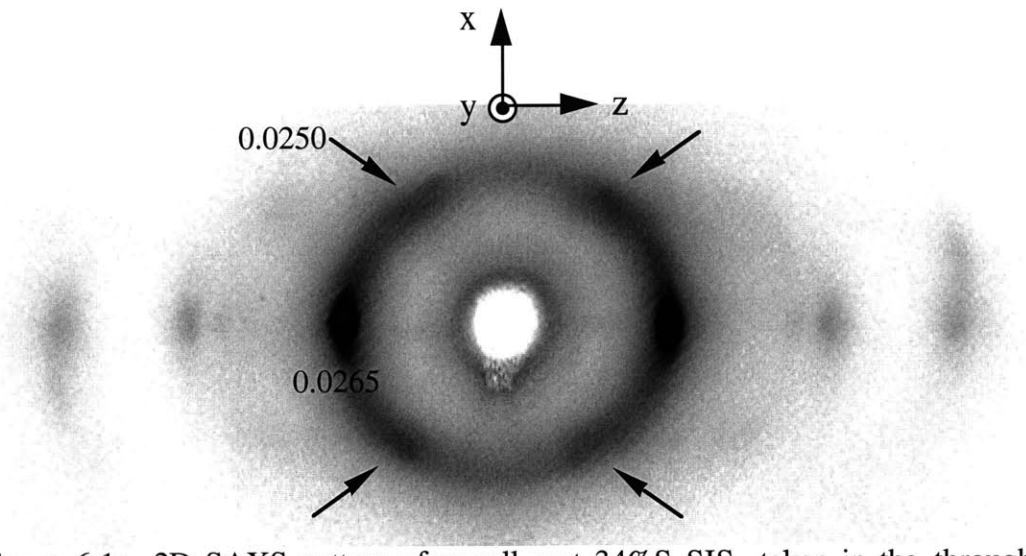

Figure 6.1: 2D SAXS pattern of as-roll cast 34%S SIS, taken in the through-thickness (y) direction. The roll cast direction (x) is in the vertical. The arrows indicate diffuse off-equatorial scattering.

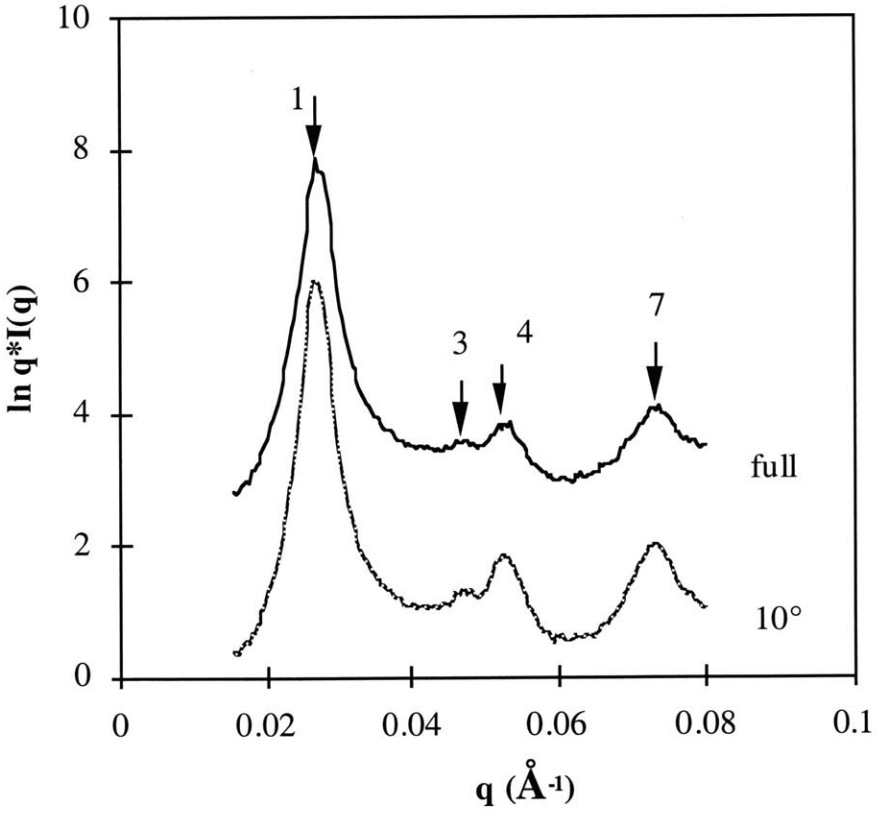

Figure 6.2: 2D azimuthal integrations of the SAXS pattern in figure 6.1. The top graph is a full azimuthal integration and the lower graph is a 10° integration around the equator.

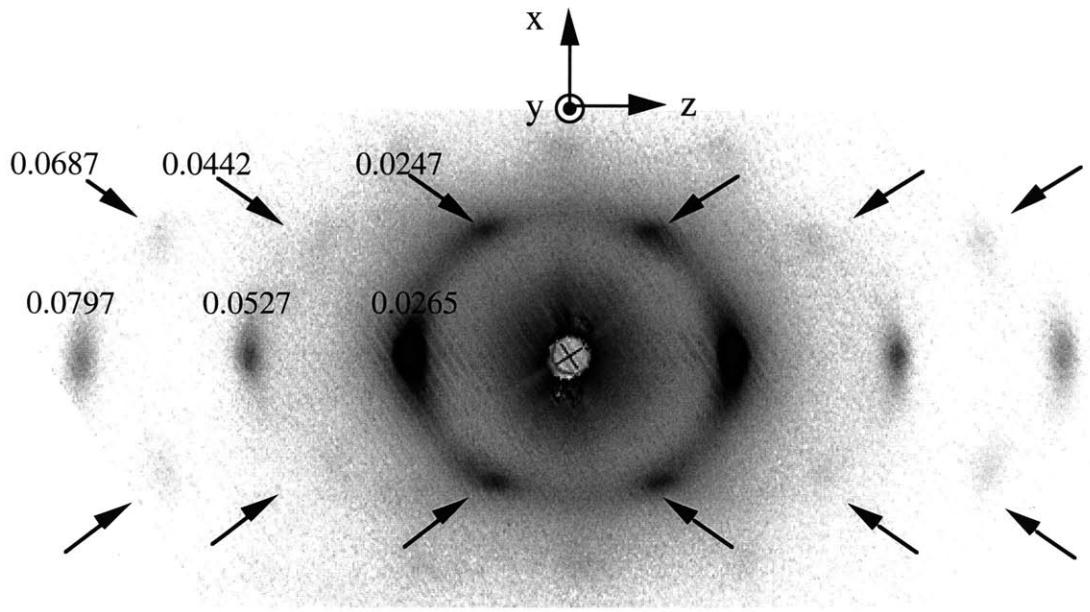

Figure 6.3: 2D SAXS pattern for 36 SIS, roll cast unannealed. The pattern was taken with the beam through the film (y); shown here the roll cast flow direction (x) is vertical. The arrows indicate the diffuse off-equatorial scattering.

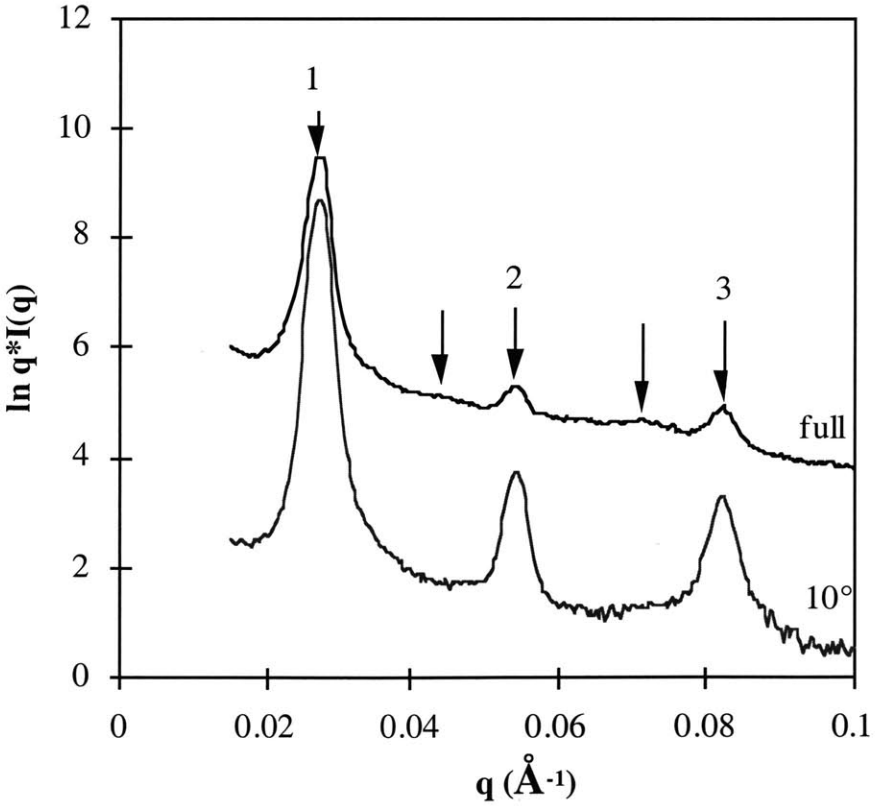

Figure 6.4: 2D azimuthal integration of the roll cast unannealed sample 36 SIS pattern shown in figure 6.7. The top (solid) line is the full integration, and the lower (dotted) line is a 10° integration around the equator.

TEM images show the existence of lamellae even in the annealed sample (see section 6.3.2). Therefore, it is suggested by both the SAXS of the unnannealed sample and the TEM of the annealed sample that the morphology of the roll cast unannealed film is lamellae.

Both of the 2D SAXS patterns in figures 6.2 and 6.4 shows off-equatorial scattering, indicating the existence of a morphology more than just oriented cylinders and lamellae, respectively. These off-equatorial species may arise from the disposition of the polymer to transform towards the equilibrium DG phase.

In the case of the 36 SIS, the unannealed film shows more off-equatorial species with higher intensities than the 34 SIS unannealed film, and comparisons of the azimuthal integrations show that the off-equatorial species have a different q-value than those of the equatorial lamellar spots. These differences between the two films may arise from the difference in roll cast morphology between two. As will be discussed in section 6.2.2, cylinders transform directly to DG, while lamellae transform to an intermediate phase first.

Rançon and Charvolin observed in lyotropic liquid crystal hexaethylene glycol mono-n-dodecyl ether (C12EO6) / water systems that at concentrations in which the cubic $Ia\bar{3}d$ phase is observed at low temperatures, just below the fluid isotropic-to-lamellar transition temperature the pattern of the high-temperature lamellar phase has diffuse off-equatorial components, which grow in intensity as the cubic $Ia\bar{3}d$ phase is approached. The diffuse off-equatorial scattering in the lamellar pattern, as indicated by the arrows in figure 6.5 (reproduced from (Rançon and Charvolin, 1988)) is only observed in samples which have a low-temperature cubic $Ia\bar{3}d$ phase.

Rançon and Charvolin interpreted the off-equatorial diffuse scattering as fluctuations within the lamellar phase in setting up the transition between lamellae and DG. They suggested that the fluctuations are not directly related to the DG phase, but rather to an intermediate metastable hexagonal phase, either of cylinders having short-range hexagonal organization or of an "inverted hexagonal phase" (1988). The mechanism that they proposed for the transition through the metastable intermediate phase is discussed further in section 5.3.2.2 on the lamellar-to-DG transition.

The equilibrium morphology of both the 34 and the 36 SIS polymers is DG (quiescent cast samples; see section 4.3), and the off-equatorial scattering of the 34 and 36 SIS polymers in figures 6.1 and 6.3 bears great resemblance to that seen in figure 6.5 by Rançon and Charvolin. Although the roll-cast morphology is not directly DG but rather predominanly cylinders and lamellae, the existence of off-equatorial scattering, as seen in figures 6.1 and 6.3, is indicative of a predisposition of the cylinders and lamellae to transform towards a more equlibrium DG phase for the composition of the polymer. It

may perhaps also be the case that the roll cast lamellae undergo a transition to a metastable phase before transforming into DG. The comparative strengths of off-equatorial peaks may indicate that 1) lamellae are less stable compared to the intermediate or the DG phase in the vicinity of the transformation, or 2) the cylinder-to-DG transformation kinetics are slower than that of the lamellae-to-intermediate/DG transformation.

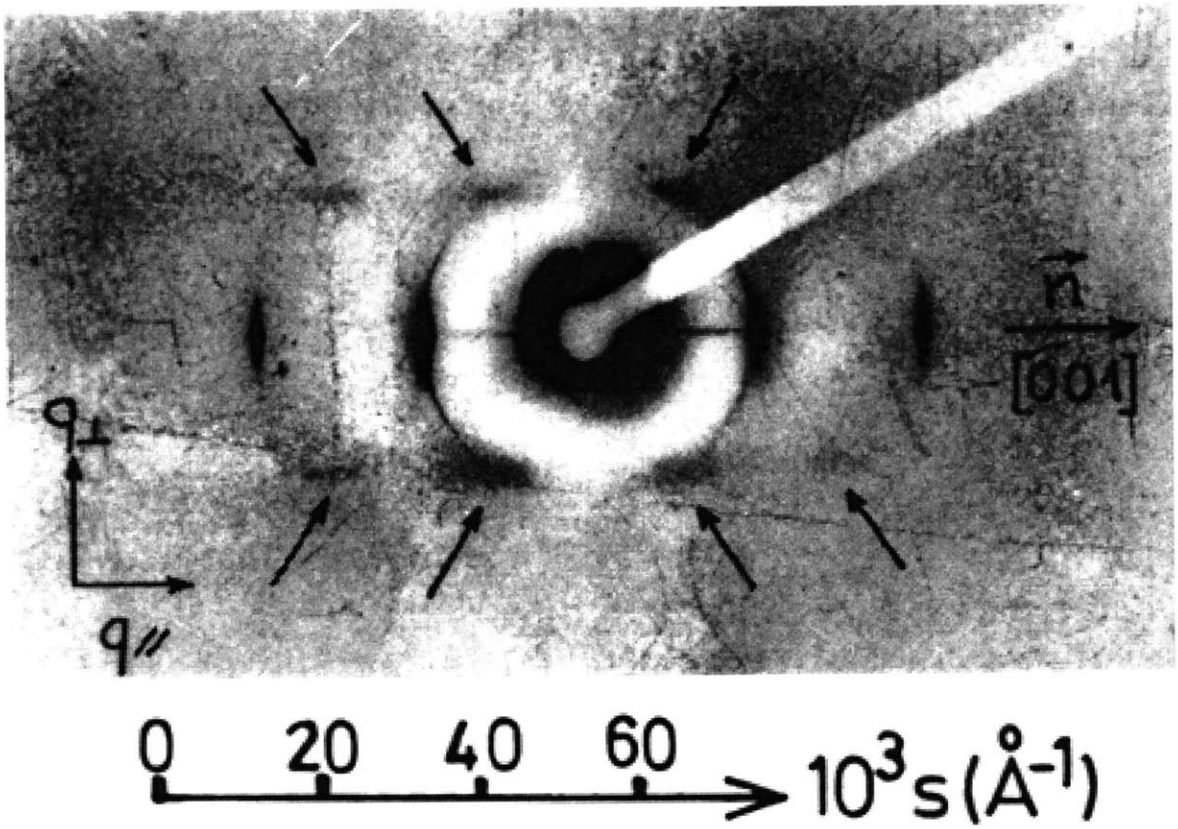

Figure 6.5: (reproduced from (Rançon and Charvolin, 1988)) SAXS pattern of a sample containing 62% C12OE6 in water. The sample is monocrystalline lamellar at high temperatures and bicontinuous cubic Ia$\bar{3}$d (DG) at low temperatures. This pattern shows scattering of the lamellar phase just above the lamellar-to-cubic transition temperature, with the lamellae perpendicular to the plane of the page. The arrows indicate the off-equatorial diffuse scattering

6.2 Background on Epitaxy and Transition Mechanisms

The original purpose of roll casting DG samples was to produce an oriented film of DG. However, the roll-casting process imposes symmetry constraints on the resulting film. The flow field is commensurate with that of cylinders and lamellae but not directly with DG such that roll cast 34%S SIS films are cylinders while roll cast 36%S SIS films are lamellar. As previously mentioned, the optimistic intention was to then to phase transform the flow-field-imposed morphology into that of the equilibrium morphology. Indeed diffuse scattering in both the roll cast cylinder and lamellar phases indicated fluctuations within the cylinder and lamellar phases and a predisposition toward the equilibrium DG phase.

Formally the word "epitaxy" refers to the oriented intergrowth of two crystalline phases, whereby the surface and nature of the lattice of one induces a preferred orientation of the other (Considine, 1983). "Epitaxy" in macromolecular systems was used by the lipid/surfactant community to describe the growth of a new phase from an existing phase by passing through an order-order transition (Rançon and Charvolin, 1988). Recent literature studies demonstrated that "epitaxial relationships" existed between cylinders, DG, and lamellae, and that order-order transitions could be induced via temperature. The relationships are described as "epitaxial", because the new phases grew with specific orientations relative to the planes of the "old" phase, and the interplanar spacings of the phases were conserved. The transitions considered are in soft condensed matter systems and are expected to have similar mechanisms of transformation and epitaxial growth (Schulz et al., 1994; Matsen, 1998). Although the literature reports these transitions in highly kinetically mobile systems (eg. surfactant/lipid/water systems and low molecular weight diblock copolymer systems), we speculated that these mechanisms could also be valid with the higher molecular weight roll cast triblocks (~80 kg/mol), which, although are less kinetically mobile, are also soft condensed matter systems. Therefore, for insight into the morphology of the roll cast films, the epitaxial relationships and transitions in the lipid/surfactant/water systems and and low molecular weight diblock systems which developed within the same time period as these roll casting and phase transformation experiments will be reviewed next.

6.2.1 Lamellar, DG, and Cylinder Epitaxial Relationships

Rançon and Charvolin (1988) examined polymorphic surfactant/water systems (lyotropic liquid crystals) and established from polarizing optical microscopy, SAXS, and SANS the following epitaxial relations between the planes of lamellae, the $Ia\bar{3}d$ 3D interconnected cubic phase (i.e., DG), and cylinders:

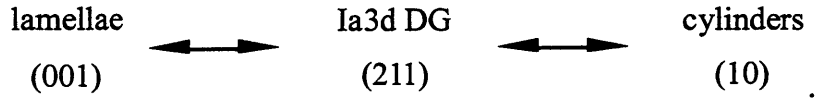

Shown schematically in figure 6.6a are the 3D representations of the three morphologies oriented correctly relative to one another based on the observed epitaxial relationships. Not only were the {001} lamellar, {211} DG, and {10} cylinder planes found to lie in the same orientation, but also their spacings were found to be the same.

As mentioned in section 3.4, Rançon and Charvolin (1988) also determined in lyotropic liquid crystal - water systems of type I (see figure 3.2; the struts consist the hydrocarbon tails with the head groups at the surface of the struts) that the {211} planes are the those with the highest density of matter in the $Ia\bar{3}d$ 3D interconnected phase. These highest density planes correspond to the {001} planes of lamellae and {10} planes of cylinders, which are their respective planes of highest density. This was consistent with the observations made of freeze-fracture planes and facets of bubbles trapped in monocrystals of the $Ia\bar{3}d$ 3D interconnected phase (DG). In particular, Delacroix et al. found in the same type of lyotropic liquid crystal system that fracture of DG occurs preferentially along the {211} planes, then along {110} planes, and lastly along {100} planes. The {211} fracture planes were very flat and more uniform with less cross-over into higher and lower planes than in either the {110} or the {100} planes, indicating that the {211} planes are the planes of highest density in the $Ia\bar{3}d$ 3D interconnected phase (Delacroix, Mariani, and Bulik-Krzywicki, 1990; Delacroix, Gulik-Krzywicki, Mariani, and Risler, 1993). Sotta found that bubbles in a monocrystal of this same lyotropic liquid crystal system facet with {211}-type planes (see figure 3.4), which are also found to be the planes having the largest inter-reticular spacing and of lowest surface energy. Hashimoto et al. (1997), found in block copolymer systems that DG also freeze-fractures preferentially along the {211} planes in a blend of SI diblock copolymer and homopolystyrene systems having 66 wt% total PS.

For DG which consist of struts of surfactant (having the higher density) surrounded by water (having the lower density), the planes of highest density material are those of the {211} planes. In a case such as the I-rich SIS triblock copolymers used in this thesis, the "highest density planes" would correspond to those of highest PS density. Figure 6.6b is a skeletal graph representation showing the lamellar planes and their relation to the dense {211} DG planes and to the dense {10} cylinder planes.

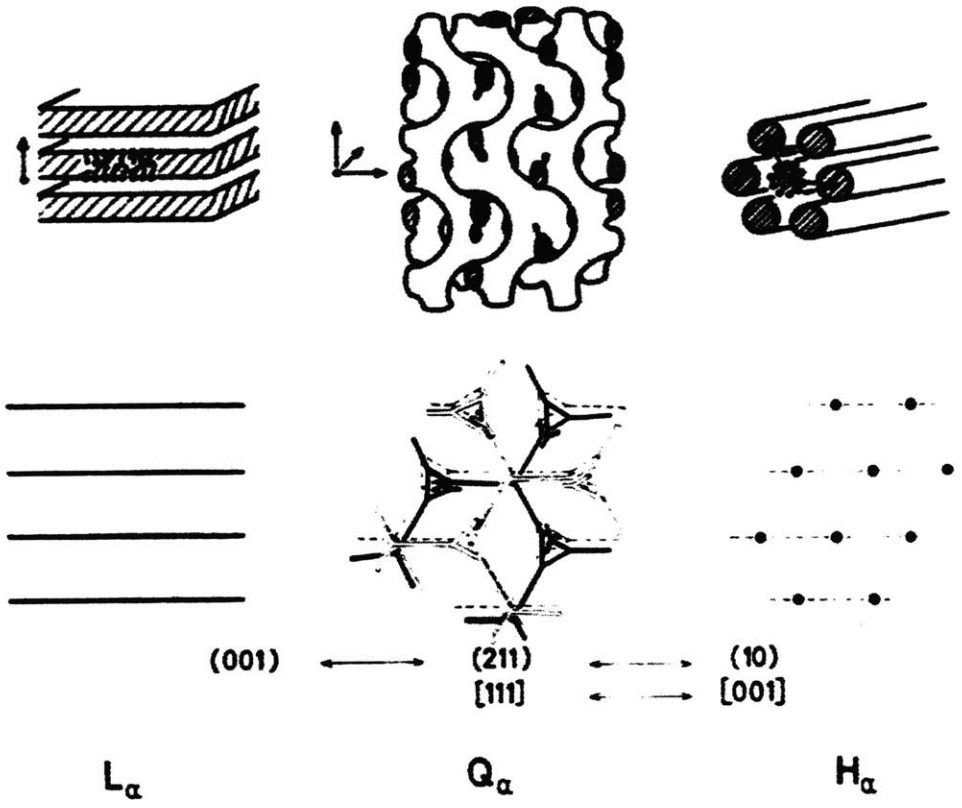

Figure 6.6: a) 3-D perspective representations of lamellae (L_α), DG (Q_α), and cylinders (H_α), and their correct orientations relative to one another. b): The bottom figure shows the planes of lamellae, DG, and cylinders in which epitaxial relations between the phases are observed. (Both figures are adapted from (Rançon and Charvolin, 1988)).

6.2.2 Transition Mechanisms

A study of epitaxial transformations in surfactant/water systems shows that the cylinder-to-DG and lamellae-to-DG transitions are first order via a nucleation and growth mechanism (Charvolin and Sadoc, 1990; Clerc, Laggner, Levelut, and Rapp, 1995). In block copolymer systems, the fact that the boundaries between the two phases can be seen (Förster, Khandpur, Zhao, Bates, Hamley, Ryan, and Bras, 1994; Hajduk, Tepe, Takenouchi, Tirrel, Bates, almdal, and Mortensen, 1998) also suggests a nucleation and growth mechanism in these materials. (Nucleation and growth mechanisms of disorder-to-order transitions in block copolymer systems were first seen by Hashimoto (Hashimoto and Sakamoto, 1995).)

Although both the cylinder-to-DG transformation and the lamellae-to-DG transformation occur via nucleation and growth, the exact paths and mechanisms of each are quite different. The transitions of both will be detailed in the subsequent sections.

6.2.2.1 DG ↔ Cylinder Transitions

6.2.2.1.1 Surfactant Systems

Rançon and Charvolin studied the interconnected Ia$\bar{3}$d (DG)-to-cylinder transformation in the $C_{12}OE_6$ / water system (1988). They found that the cylinder axes, or the <001> hexagonal directions, grew along the <111> direction of the cubic cells (the direction containing 3-fold symmetry axes). Hence, one cubic monocrystal lead to 4 monocrystals of cylinders oriented along the four tetrahedral <111> directions already present in the monocrystal of the cubic phase. Cylinders grew at all the places of the threefold DG axes; and that the same spacing was measured between the three-fold DG axes ($\bar{3}$, 3_1, and 3_2) as between the cylinders of the hexagonal phase; i.e., $d_{100,\,cyl} = d_{211,\,dg}$. They proposed the mechanism that the cylinders undergo deformations "correlated from cylinder to cylinder" which signifies that cylinders rupture and connect to other cylinders.

Clerc et al. (Clerc, Levelut, and Sadoc, 1991) studied the reverse transition, that of cylinder-to-Ia$\bar{3}$d cubic (DG), in the same material system. They found that the <111> DG direction preferentially grew along the cylinder axes, and that the cylinder/DG interface occured between a {211} DG plane and a {10} cylinder plane.

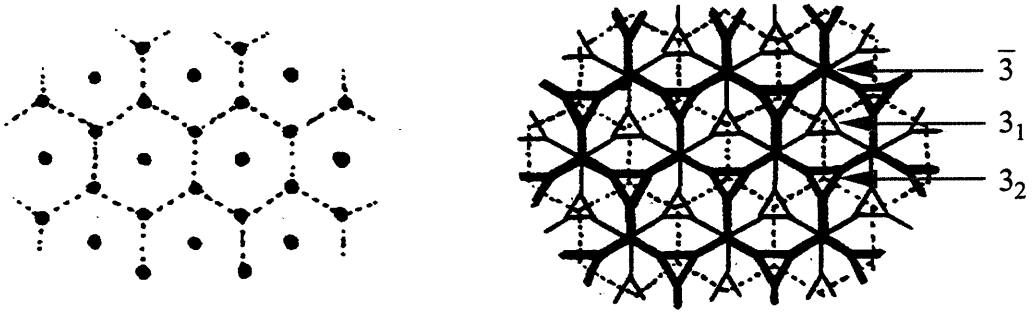

Figure 6.7: Schematic of the mechanism for the cylinder-to-DG transition, as viewed down the cylinder axis (left) and the [111] DG axis (right), adapted from (Clerc, Levelut, and Sadoc, 1991). The solitary cylinders in the left figure will transform into the $\bar{3}$ DG axes from the surrounding 6 cylinders. The 3_1, 3_2, and $\bar{3}$ axes are labelled in the DG figure on the right. In the mechanism proposed by Clerc et al., each 3-fold screw axis is formed as a consequence of being connected to three $\bar{3}$ axes.

(Clerc, Levelut, and Sadoc, 1991) hypothesized that the cylinder-to-DG transition transformed two-out-of-three cylinders into 3_1 and 3_2 helices, and the remaining one-out-of-three is changed into a $\bar{3}$ axis. The $\bar{3}$ axis consists of three-fold nodes laying perpendicular to the cylinder axes but stacked along the [111] DG direction; it forms from

the surrounding six cylinders, which connect three-by-three into nodes, shifted along the [111] axis. They hypothesized that formation of the $\bar{3}$ axis is sufficient to transform all of the cylinders into the DG structure, as the helices are formed as a consequence of a cylinder being connected to three $\bar{3}$ axes. Figure 6.7 shows a schematic of their proposed mechanism.

6.2.2.1.2 Block Copolymer Systems

Epitaxial growth of DG from cylinders also has been found to be possible in block copolymer systems (Förster et al., 1994; Schulz et al., 1994). Schulz et al. observed the cylinder-to-DG phase transition in a PS-PVP diblock copolymer blend having an overall ϕ_{PS} = 0.37 and total molecular weight of approximately 20,000 g/mol. Shearing the polymer at 140°C produced an aligned cylinder phase. At 150°C an order-order transition (OOT) was observed via an increase in G' in dynamic mechanical thermal analysis (DMTA) measurements. Through SAXS and TEM, they identified the high temperature phase to be DG. They observed epitaxial relationships between cylinders and DG through SANS of the shear-oriented cylinder state before and after heating above the order-order transition temperature, T_{OOT}. Although Schulz et al. mis-identify the epitaxial relationships, Förster et al. later correctly identified the relationships as $\{01\}_{cyl} \rightarrow \{211\}_{dg}$ and $\{11\}_{cyl} \rightarrow \{220\}_{dg}$, in accord with those observed by the surfactant community (Rançon and Charvolin, 1988; Clerc, Levelut, and Sadoc, 1991).

Forster (1994) provided TEM evidence for coherent lattice matching between cylinders and DG and found that the cylinder/DG interface was extremely stable. They found that in a DG-to-cylinder transition the cylinder phase readily orients under shear, but the near-liquid-like viscoelastic properties of the cylinder phase produced a "lubricated flow" condition such that isolated DG domains could not feel the shear field. Therefore it is difficult either to orient homogeneously a bulk cubic specimen (which forms cylinders under shear) or to produce a uniform cylinder specimen from the cubic specimen.

6.2.2.1.3 Theoretical Calculations of Cylinder-to-DG Transitions in Block Copolymer Systems

Theoretical calculations (mean field calculations by (Matsen and Schick, 1994), theory of anisotropic fluctuations by (Laradji, Shi, Desai, and Noolandi, 1997), and self-consistent field theory (SCFT) by (Matsen, 1998) predicted an epitaxial relationship between the DG <111> direction and the hexagonally packed cylinder axis. Matsen used self-consistent field theory (SCFT) to map out cylinder-to-DG and DG-to-cylinder transitions (1998), either of which are initiated by thermal fluctuations or by defects in the

microstructure. The cylinder-to-DG transition, reproduced in figure 6.8, is initiated by the formation of a five-functional junction, a trifunctional node transverse to the cylinder axes, connected to a cylinder running through the center of the node), by which the cylinder pinches off, leaving a trifuctional node. The two energetically unfavorable cylinder ends would then form junctions to other cylinders, creating more ends, and thereby propagating the transformation.

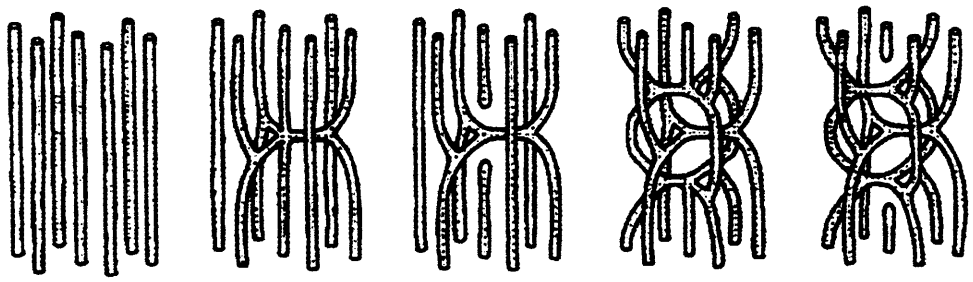

Figure 6.8: from (Matsen, 1998). Schematic of cylinders transforming to DG. The transition is initiated when a 5-functional node forms, consisting of a planar trifunctional node with a cylinder running through it. The cylinder pinches off and the ends form trifunctional nodes with other cylinders, thereby propagating the transition.

Vigild et al. (Vigild, Almdal, Mortensen, Hamley, Fairclough, and Ryan, 1998) studied the phase behavior and transition kinetics of a blend of two poly(ethylene-alt-propylene)-poly(dimethylsiloxane) (PEP-PDMS) diblock copolymers using SANS and in-situ DMA. The blend consisted of a 1:3 ratio of a 10,600 MW diblock with $\phi_{PEP} = 0.65$ (lamellar morphology) and a 11,700 MW diblock with $\phi_{PEP} = 0.70$ (cylinder morphology), having an overall composition $\phi_{PEP} = 0.69$. They observed that in the transition from a high temperature cylinder phase to a lower temperature DG phase, the spacings of the {10} cylinder planes match those of the {211} DG planes, supporting the now widely observed epitaxy between the cylinder and DG phases. The in-situ DMA experiments included the simultaneous application of small amplitude ($\gamma = 1\%$), low frequency ($\omega = 1$ rad/s) oscillatory shear during SANS observation. They found in the initial stages of cylinder-to-DG transition that the rheological characteristics changed dramatically while the SANS patterns did not change much at all. According to the SANS patterns the characteristic time for the cylinder-to-DG transformation was 1.5 hours, while full formation takes ~1 hour longer.

Matsen noted that in his SCFT model of the cylinder-to-DG growth process, many mistakes were made, some being corrected and others left as defects in the microstructure.

From Mariani et al.'s theory of DG-to-cylinder transition mechanisms, it seems that a transition from cylinder to DG is a much more involved process because it transforms a phase of lower symmetry to that of higher symmetry (Mariani, Amaral, saturni, and Delacroix, 1994) . Therefore, the creation of a *single* crystal DG from cylinders may be difficut, in that many defects may also be formed.

6.2.2.2 Lamellar-to-DG Transition

6.2.2.2.1 Surfactant Systems

Of the two types transitions (cylinder-to-DG and lamellar-to-DG), the lamellar-to-DG transition is the more complex. Initial studies by the surfactant community indicate that the transition from lamellae to DG occurs via a transition to an intermediate metastable hexagonal phase (Rançon and Charvolin, 1988; Charvolin and Sadoc, 1990). Rançon and Charvolin (1988) found that the transformation from lamellae to $Ia\bar{3}d$ 3D interconnected phase involves the break-up of the lamellae into locally hexagonally-packed arrays, which were presumed, but never confirmed, to be cylinders. From this presumption they hypothesized that the lamellar-to-DG and cylinder-to-DG transformations underwent similar processes. They saw that x-ray diffraction patterns (shown in figure 6.9) of lamellar monocyrstal samples cooled from the fluid isotropic phase exhibited Bragg reflections along the equator, characteristic of the lamellae. However, they saw additional "diffuse scattering" (shown by the arrows in figure 6.9) which became apparent only a few degrees below the isotropic/lamellar phase and increased in intensity as the temperature was lowered toward the lamellar-to-DG transition. This "diffuse scattering" was only observed in samples which were able to undergo lamellar to DG transformations and were not associated with the cubic structure. In fact, upon very slow cooling it was at times possible to get scattering patterns with 6-fold symmetry with scattering vectors occuring in ratios of $1:\sqrt{3}:\sqrt{4}$. When such 6-fold patterns were observed, they only appeared transiently These observations indicated the existence of a metastable phase with characteristics of a hexagonal phase en route from lamellae to DG.

The diffuse off-equatorial scatterings were interpreted as cylindrical fluctuations within the lamellar phase. As the sample was cooled, the lamellar spacing decreased, supporting their view of fragmentation of the lamellar layers as water penetrated the bilayers and the lamellar spacing contracted. Rançon and Charvolin concluded that the lamellar phase did not transform directly to the DG phase, but rather, went through local cylindrical fluctuations first. Their preliminary hypothesis was that the lamellar-to-DG and

the cylinder-to-DG transitions undergo similar processes such that the problem is essentially reduced to transforming the cylinders into the DG phase.

(Insight from the block copolymer systems give reason to believe that the intermediate phase was not that of cylinders, but rather that of a perforated layer (PL) phase, which will be discussed more in the next section. In this PL phase the minority lamellar layers become perforated by the majority phase which then use these channels to connect together the layers of the majority phase. A schematic is given in figure 6.10. The perforations could be packed hexagonally, thereby giving rise to the 6-fold symmetry of the scattering pattern.)

Charvolin discussed the reasons for the intermediate phase in the L-to-DG transition in the framework of classical nucleation and growth theory (Charvolin, 1990). The nucleation of a new phase within another is determined not only by the free energy differences between the two phases, $\Delta f_{transition}$, at that particular temperature, but also by the magnitude of the grain boundary energies between the two phases, σ. For small particles, the grain boundary energies play the dominant role in preventing the nucleation (σ*area > $\Delta f_{transition}$*volume), while larger particles are stabilized because of the volume energy gain of the transition from the thermodynamically unstable to the stable phase ($\Delta f_{transition}$*volume > σ*area). Charvolin predicted that the hexagonal intermediate phase can be formed directly from fluctuations of the lamellar phase, but the cubic phase requires distortions and mass transfer. There being no flat lines in the cubic phase as there are in the lamellar phase, the lamellae/cubic boundary energy, $\sigma_{L/DG}$, is much higher than that of the lamellae/hexagonal intermediate, $\sigma_{L/Hex}$. Thus the transformation of the lamellae may first go through the easier hexagonal intermediate phase. This approach was later called upon by Hajduk et al. (Hajduk et al., 1998) to interpret intermediate phases in block copolymer systems.

(Clerc, Levelut, and Sadoc, 1991) hypothesized that during the lamellar-to-DG transition, each lamellae became perforated with holes through which the other phase penetrates. Connections formed up and down between each second lamellae to form one of the three-dimensional DG networks, as shown in figure 6.9. This mechanism inherently includes an intermediate stage where the lamellae become perforated sheets.

Imai et al. (Imai, Kato, and Schneider, 1997) used SANS to explore the kinetics of the cylinder-to-cubic and lamellar-to-cubic transitions in a non-ionic surfactant/water system. They found that the cylinders transform directly to the cubic phase via the successive formation of planar trifunctional nodes, whereas lamellae transform to the cubic phase via the formation of a channel of water between two layers of surfactant lamellae.

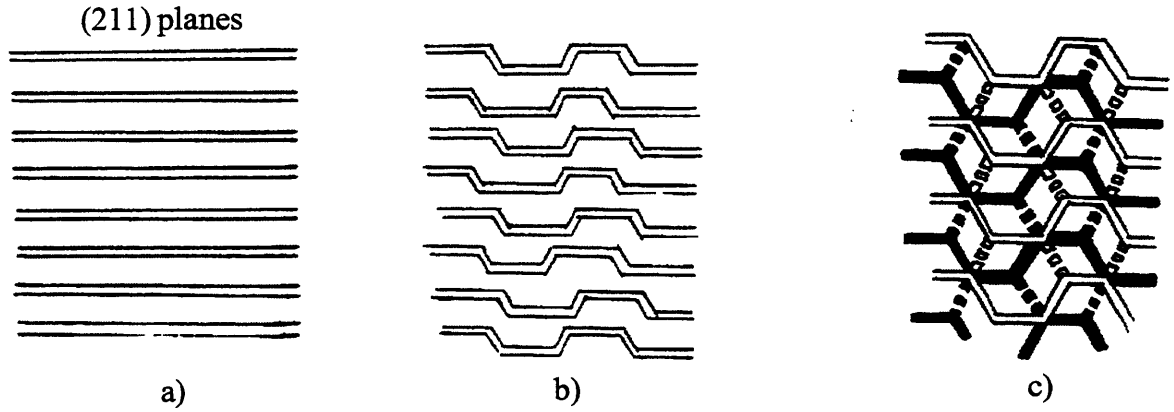

Figure 6.9: Schematic of the model by (Clerc et al., 1991) for transition of lamellae to DG, as seen from the side. The [{001} lamellar planes transforming to the {211} DG planes. Viewing is along the <100> lamellar direction and the <111> DG direction. a) The lamellae planes become perforated and form hexagonally connected rods laying in the plane of the lamellae. b) The planar hexagons now twist. c) Every second lamellae form connections up and down to become one of the DG networks. From [Clerc, 1991 #1714].

6.2.2.2.2 The Role of the Perforated Layer Phase in the Lamellar-to-DG Transition in Block Copolymer Systems

In addition to the DG phase, other complex phases have been discovered in block copolymer systems which occur in a composition window between that of cylinders and lamellae. Examples include the lamellar-catenoid (LC) (Thomas, Anderson, Henkee, and Hoffman, 1988), perforated layer (PL) and modulated layer (ML) phases (Hamley, Koppi, Rosedale, Bates, Almdal, and Mortensen, 1993; Förster et al., 1994; Hamley Gehlsen, Khandpur, Koppi, Rosedale, Schulz, Bates, Almdal, and Mortensen., 1994; Khandpur, Forster, Bates, Hamley, Ryan, Bras, Almdal, and Mortensen, 1995; Schulz, Khandpur, Bates, Almdal, Mortensen, Hajduk, and Gruner, 1996; Zhao, Majumdar, Schulz, Bates, Almdal, Mortensen, Hajduk, and Gruner, 1996; Hajduk, Takenouchi, Hillmyer, Bates, Vigild, and Almdal, 1997; Hajduk et al., 1998). On closer inspection, the lamellar-catenoid phase and the perforated layer phase are identical. (It will subsequently be referred as PL, in light of the number of references to be reviewed here which use "PL" in reference to the phase.) Both the PL and ML phases were found to have R3m symmetry.

The PL phase consists of layers of the minority component between layers of the majority component. The minority layers are perforated by channels of the majority component. A schematic representation is shown in figure 6.10b. The ML phase consists of modulations or fluctuations in the lamellar sheets, as shown in figure 6.10a.

Although it was originally thought that these additional complex phases were equilibrium ones, subsequent studies and simulations showed them to only be metastable phases (Hajduk et al., 1997)(Qi and Wang, 1997). Simulations of the L-DG-CYL phase transitions showed that the ML phase developed into the PL phase, and thus the ML is a precursor to the PL phase (Qi and Wang, 1997). This explanation is also supported by the fact that the two belong to the same space group.

Even though the DG is a thermodynamically more stable phase, the grain boundary energies and differences in the geometries of the lamellar and cubic phases cause the lamellar-to-DG transition to pass through an intermediate phase.

Although the early work on the transformation of L-to-DG in liquid crystal systems assumed the involvement of an intermediate metastable hexagonal phase, subsequent work on these block copolymer systems suggest that the intermediate phase is a hexagonally-packed perforated lamellar (HPL) phase, which is the PL phase with hexagonal packing of the layers.

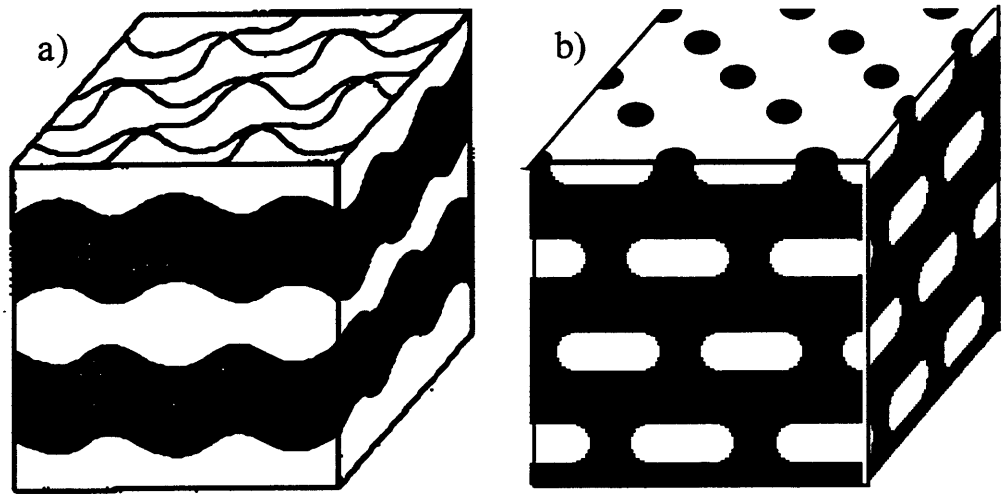

Figure 6.10: a) The modulated layer (ML) phase. b) The perforated layer (PL) phase. Here, the perforated layers are packed in an ABAB arrangement.

Hajduk et al. (1998) argued that the L-to-DG transition passes through an intermediate state, the PL phase. Using SAXS, SANS, DMA, and TEM to investigate the L-to-PL, PL-to-DG, and DG-to-L transitions, they unconvincingly reason that the PL phase distinguishes itself from the L phase in scattering experiments by the breadth of its radial and azimuthal peaks. However, simultaneous rheological experiments indicated a transition with a sharp increase in G'. It is questionable why they did not consider the scattering data to indicate a misorientation of the existing lamellae. Their TEM micrographs

were also unconvincing evidence of a distinction of the PL phase from either L or DG. The PL micrographs seem to be lamellae and cylinders in various orientations. Although they did not show their micrographs of co-existing PL and DG, they admitted that it was hard to distinguish PL from DG because of the "epitaxially related" PL and DG structures.

Their evidence for epitaxial relationships between phases was questionable. TEM micrographs of co-existing L and DG phases were separated by a layer several lamellar spacings wide, consisting of a poorly ordered material. Hence, epitaxy is questionable. Throughout the paper, the existence of tilt grain boundares, distorted lattice spacings, and disparity between lattice spacings of nucleating structures was discussed. However, these very elements weakened their argument of epitaxial growth in the transitions.

In a study on the blend of (PEP-PDMS) diblock copolymers with an overall composition ϕ_{PEP} = 0.69, Vigild et al. (1998) observed three order-order transitions according to DMA. Using rheology and SANS, they conjecture dthe phases to be in the following order from low to high temperature: L, HPL, DG, and hexagonally-packed cylinders. Their in-situ rheology and SANS experiments also showed that HPL was not an equlibrium phase but rather a long-lived, dynamically-accessed metastable phase in the transition from L to DG. They found that the equatorial peaks of the HPL transformed into those of DG. However, the off-equatorial HPL peaks were not epitaxially related to the off-equatorial DG peaks because the two types occur at different angles to the equator. Based on these observations, they conjectured that the HPL-to-DG transition occured epitaxially only to the extent that the HPL layers transformed into the {211} DG planes. The elements giving rise to characteristic HPL scattering deteriorated before the structural elements of the DG phase grew.

Preliminary work by Matsen using SCFT to model the L-to-DG transition has shown that this transition is much more complex than the C-to-DG transition and involves some type of metastable pathways.

6.2.2.3 The Perforated Layer Phase

Unlike the PL phase which is a metastable phase, the ML phase is thought to be a transitionary state towards PL. Hence, a separate discussion of the ML phase is inappropriate and this will be included in this section on the PL phase.

Hajduk et al. (1997) found that the long-range hexagonal arrangement of the perforations in the perforated layer in block copolymer morphologies was induced by a shear or flow field. In previous studies where the PL phase had been induced via a shear field, a distinct hexagonal scattering pattern could be seen in SANS and SAXS. In unsheared material, either solvent-cast or melt pressed, it could be determined that the

layers lied preferentially in the plane of the film. However, the perforations had only short range order and the packing was clearly not hexagonal. The SAXS patterns of the unsheared PL phase were indistinguishable from those of the L phase, except for an increase in widths of the first two peaks (without any additional peaks). TEM micrographs of unsheared PL also showed that the geometry of the packing of the layers was irregular (Schulz et al., 1996). This is contrary to the observations in $C_{12}OE_6$/water systems by Rançon and Charvolin (1988), who saw that upon very slow cooling, it was at times possible to get monocrystalline scattering patterns of a metastable hexagonal phase. (However I don't understand that if this were supposed to be HPL, then the hexagonal perforations should have its own distinct scattering signal, separate from that of the layers. Understandably, if Rançon and Charvolin were looking directly onto the hexagonal perforations, then they wouldn't have a signal corresponding to the layered phase. However, the powder pattern of this metastable phase show rings at q-ratios of $1:\sqrt{3}:\sqrt{4}$.)

Hajduk et al. (1997) observed that the PL phase transformed to DG under prolonged annealing, and concluded that the PL phase was therefore a metastable phase. They believed that at certain compositions, DG could be an equilibrium phase at higher degrees of segregation than previously believed. It was also thought (Förster et al., 1994; Hajduk et al., 1997) that the HPL structure facilitated the L-to-DG transition because the HPL phase is made up of the same trifuctional structural elements as the DG phase and planar as the L phase.

The DG phase was found to persist even when cooled below the temperature at which L is stable, i.e., DG can be undercooled . However, it was found that full reversibility of the L-PL transition occured only in samples that were in the lamellar-"complex phase" window. They also found that the PL-to-DG transformation was much slower as the molecular weight of the species increased. Hence, in very high molecular weight systems the DG phase could be kinetically suppressed and the PL phase could persist.

These experimental observations have been complemented by theories that predict the existence and structure of metastable phases in the L-to-DG transition.

Yeung et al. (Yeung, Shi, Noolandi, and Desai, 1996) used the theory of anisotropic fluctuations to predict the scattering functions of a fluctuation having approximate hexagonal symmetry of the lamellar phase. They found that the structure had layer undulations with an in-layer periodicity 10% larger than the interlayer spacing.

Laradji et al. (Laradji et al., 1997, 1997) used a theory of anisotropic fluctuations about the mean-field solution to the self-consistent field theory to predict the stability of phase behavior of the complex phases between lamellae and cylinders in diblock copolymer

melts. This theory for copolymer melts is analogous to the theory of energy bands in solids. The theory predicted that the HPL phase was not an equilibrium phase but rather a result of unstable fluctuations of the L phase transforming to the C phase. They interpreted these predictions in light of experimental evidence and asserted that the HPL phase was an intermediate structure. They also found in the reverse (C-to-L) transition that the unstable fluctuations of cylinders lead directly to the lamellar phase, i.e, absence of PL. Therefore, it could be concluded that the L-to-C transition is non-reversible.

However, their same calculations have also found the DG phase to be unstable, even in weakly segregated regimes ($11.14 \leq XN \leq 12$, where $XN=11.14$ is the triple point for cylinders, DG, and lamellae). In order to account for experimental evidence that DG is an equilibrium phase, they admitted that higher order fluctuations, that were not included in their calculations, may be able to stabilize the DG phase. They asserted that the predicted instability of the DG phase was consistent with the experimental phase diagrams, e.g., Bates (Förster et al., 1994; Khandpur et al., 1995; Schulz et al., 1996; Zhao et al., 1996), indicating that DG was only observed as an equilibrium phase in weakly segregated systems.

Qi and Wang (1997) used a time-dependent Ginzburg-Landau approach to predict the intermediate phases and the transition pathways between the classical phases, omitting the DG phase, and considering barrierless transitions with global changes in microstructure , i.e., not nucleation and growth. In the L-to-C transition, their simulations predicted that a phase resembling PL corresponding to saddle points in the free energy. Hence, a "pseudostable" intermediate state in the L-to-C transition was predicted. Their simulations also found in the PL an in-layer period which is 1.15 times the interlayer spacing.

Qi and Wang (1997) also predicted the stability and mechanism of formation of the PL phase, as well as the nature of the layers. Their Ginzburg-Landau simulations indicated that structures arising from fluctuations of the L phase have a periodicity of two layers, meaning an ABAB stacking as opposed to an ABC stacking. This indicates that either an hcp-based or a bcc-based PL phase can form. They noted that the predicted scattering pattern from the bcc-based PL phase matched that experimentally seen by Forster et al. (1994) when the latter sheared a PS-PI diblock having a composition within the complex phase window. Förster et al. saw that this pattern transform into that of the $Ia\bar{3}d$ (10 spot) pattern upon annealing. Qi and Wang predicted that because a cubic phase underlies both the DG phase and the bcc-based PL structure, the G phase most likely transformed from the bcc-based PL structure, and that shear aided in selecting one of the degenerate PL phases.

Matsen (Matsen and Schick, 1994, 1994) used a mean field theory to predict stable phases and found that DG was a stable phase in compositions between L and C. He also found that catenoid lamellar had nearly the same free energy as DGand that the catenoid lamellar ABAB stacking was more favorable.

Although these theories predicted fluctuations of the stable classical phases to initiate the complex phases, most experimental evidence pointed to a nucleation and growth mechanism of transformation. The evidence for this is shown by the coexistence of domains of both morphologies in samples that have not completed the transformation (Hajduk, Harper, Gruner, Honeker, Kim, Thomas, and Fetters, 1994; Hajduk et al., 1998)

6.2.2.4 Kinetics Studies

Vigild et al. (1998) use SANS and in-situ DMA to study the phase behavior and transition kinetics of a blend of two poly(ethylene-alt-propylene)-poly(dimethylsiloxane) (PEP-PDMS) diblock copolymers. having an overall composition $\phi_{PEP} = 0.69$. With application of small amplitude ($\gamma = 1\%$), low frequency ($\omega = 1$ rad/s) oscillatory shear in in-situ SANS experiments, they find that the rheological characteristics change dramatically while the patterns do not change much at all in the initial stages of cylinder-to-DG transition. According to the SANS patterns the characteristic time for transformation of the DG phase from the C phase is 1.5 hours, while full formation takes ~1 hour longer, and the characteristic time transformation of the DG phase from the HPL phase is 3 hours, with full formation taking several hours longer.

It was also found that the DG phase could be undercooled, but the L phase from which it transforms cannot be superheated (Hajduk et al., 1997; Vigild et al., 1998). The HPL phase was found to be a long-lived, persistant metastable phase facilitating the lamellar-to-DG transition, with the kinetics of the transition being slower with higher molecular weight samples.

Although neither Hajduk et al.'s (1998) identification of PL nor their evidences for epitaxial transitions between the L, PL, and DG phases is convincing, their theory on the mechanism of tranformation between the phases was more reasonable. They hypothesized the L-to-DG phase transformation to pass through a metastable PL phase with the kinetics of the transformation being one of nucleation and growth. They asserted that their experimental evidence was consistent with the tranformation pathways depicted in figure 6.11. Upon heating, L transforms first to PL and then to DG. Upon cooling, DG transforms directly back to L.

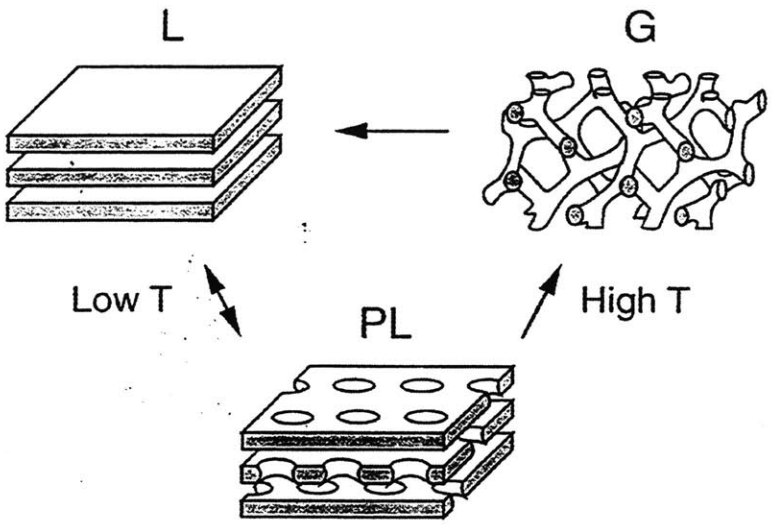

Figure 6.11: From (Hajduk et al., 1998). Schematic of the pathways for L ↔ DG transitions.

Using classical nucleation theory and considering the opposing forces between reducing bulk free energies while increasing surface energies to explain the presence of the PL phase in the L-to-DG transition, they speculated that the difference in plane spacings gave rise to a distortion or strain at the L/DG grain boundaries. Hence a surface energy, σ, existed which could hinder the nucleation of another phase within the metastable phase. In addition, the mass re-organization and the associated deformations would also hinder the nucleation or formation of DG in supercooled L phase. They argued that the surface energy of the L/PL interface was smaller than that of either the L/G or the PL/G interface, $\sigma_{L/PL} < (\sigma_{L/G} \approx \sigma_{PL/G})$, presumably because of the planar nature of the PL phase. The free energy of transformation from L to PL or DG, $\Delta f_{L\rightarrow PL} \approx \Delta f_{L\rightarrow DG}$, is large because L is superheated above the point where it is stable, while that from PL to DG, $\Delta f_{PL\rightarrow DG}$, is small. Therefore, the transition from L to PL is predicted to be fast (as seen in their experiments), but the transition from PL to DG is very slow such that the PL could remain as a long-lived metastable phase.

6.3 Roll Cast Annealed Morphology

From the literature studies, it can be concluded that cylinder-to-DG transformations occur directly, whereas the lamellar-to-DG transformations occur via an intermediate perforated layer phase. As the 34%S SIS roll casts first into cylinder, phase transformation can occur to the DG directly, and mechanical properties studies can be conducted on an oriented DG phase. However, the 36%S SIS roll casts first into lamellae, which upon annealing, could transform into the long-lived metastable PL phase. If this is the case, then it may be necessary to omit the roll cast 36%S SIS samples from the deformation studies of the equilibrium DG phase.

6.3.1 Roll Cast Annealed 36%S SIS (Having Lamellar Precursor)

Figure 6.12 shows the 2D SAXS pattern of the roll cast annealed 36%S SIS material, whose precursor is oriented lamellae. The ratios of the observed peaks normalized with respect to the first equatorial peak, $\frac{q_n}{q_1}$, are labelled on the pattern. The majority of the peaks are not in agreement with those of DG (see table 4.1a and b). In fact, the second layer line has peaks in ratios 1.00 : 1.71 : 2.62, in aggreement with hexagonal packing. The third layer line has some peaks which could be attributed to DG, namely the $\frac{q_n}{q_1}$ = 1.65 and 2.39 peaks, but not the 1.32 peak.. If the second layer line were to reflect a structure elongated in the direction of flow, then the observed peaks could also be assigned to the hexagonal structure. However, if this were the case, then why the elongation is not reflected in second line cannot be explained. The inability of the reflections to be fit to Ia3d DG and the strong correlation of the second layer line to a hexagonal packing suggest that the structure is not DG but perhaps rather that of HPL or a mixture of DG and HPL. Indeed, as was discussed in the previous section, the transition of lamellae to DG occurs proceeds via the intermediate PL phase. Hajduk et al (reference) conjectured that the PL phase may have hexagonal packing of the perforated layers when sheared, as is the case in the roll casting flow field, which could explain the observed hexagonal reflections in figure 6.12. TEM through the roll cast film (in the shear plane) shows that the roll cast 36%S SIS material consists of lamellar-like stripes. It may be the case that the roll cast 36%S SIS samples are kinetically confined to the metastable, long-lived HPL phase. Nonetheless, because of the ambiguity of the phase, these samples will not be used in the analysis of the deformation of DG. Its complete phase assignment and deformation behavior are left as future work and continuation of the project, although much of the SAXS and TEM work on deformed samples has been completed.

6.3.2 Roll Cast Annealed 34%S SIS (Having Cylinder Precursor)

Figures 6.13 show the thru-film view (in the shearing plane) of roll cast 34%S SIS annealed for 2-3 weeks at 120°C, labelled with the ratios of the observed peaks normalized with respect to the first equatorial peak, $\frac{q_n}{q_1}$, with q_1 being the outer peak of the equatorial doublet (the neglect of the first peak in the doublet will be taken up in the upcoming section). As a result of its cylinder precursor, the annealed structure most likely transforms directly into DG, rather than to a long-lived metastable phase as reported by the literature and explained in the previous section. The q ratio values of most of the peaks are in agreement with those of DG, and none of the peaks have ratios consistent with a hexagonal lattice (compare with tables 4.1a and b). In addition, TEM in different directions (x, y, and z) show interconnected structures. These pieces of information making a compelling case for a DG morphology, so the structure will be considered more in the context of DG. The equatorial doublet, however, is not characteristic of the double gyroid morphology, and will be addressed next.

6.3.3 Equatorial Doublet

Figure 6.14 shows the q*I(q) vs. q azimuthal integration of figure 6.13 spanning 20° about the equator. The doublet seen on the equator occurs in a ratio of 1.00 : 1.11, which is not consistent with DG. The second peak is more intense than the first and occurs at q = 0.0246 Å^{-1}, approximately the same as that of the (10) cylinder reflection of the unannealed sample and that of the (211) of the simple cast DG of the *same* polymer, indicating that the second peak is the one more relevant to the DG structure. The first peak occurs at q = 0.0222 Å^{-1}, which is not a position previously encountered. The first peak occurs at a q-value not previously encountered in these samples.

As a control, a commercial SIS polymer having a cylinder morphology was roll cast on the mini roll caster with the same parameters as the roll cast U. of Athens materials. The quiescent cast cylinder sample has q_{10} = 0.0223 Å. Figure 6.15 shows the 2D SAXS pattern from a 30 wt% S SIS triblock with total molecular weight of 102 kg/mol. Note that peaks occur mainly along the equator, as is characteristic of a roll cast cylinder sample with axes along the vertical.

Doublets were also seen in these films of this roll cast polymer. The second, more intense peak of the doublet corresponds to the (10) peak of the quiescent cast cylinder sample, while the first peak occurs at a q value not encountered in a quiescent-cast sample. Higher order harmonics of peaks only along the equator occur at ratios of $\sqrt{3}$ and $\sqrt{7}$, characteristic of the hexagonal symmetry of oriented cylinders, if ratioed with respect to the

second peak of the doublet. No significant ratios occur if the higher harmonics are taken with respect to the first peak.

Honeker also notes in his thesis (Ch. 7) this inner first doublet in the thru-film view of some roll cast sample of the same 30 wt% S SIS triblock copolymer, and ignores it in his stretches because its origin could not be explained (Honeker, 1997). Vigild et al. (1998) also see in a sheared diblock blend material (having a supposed oriented HPL morphology) an inner doublet for which they could not account.

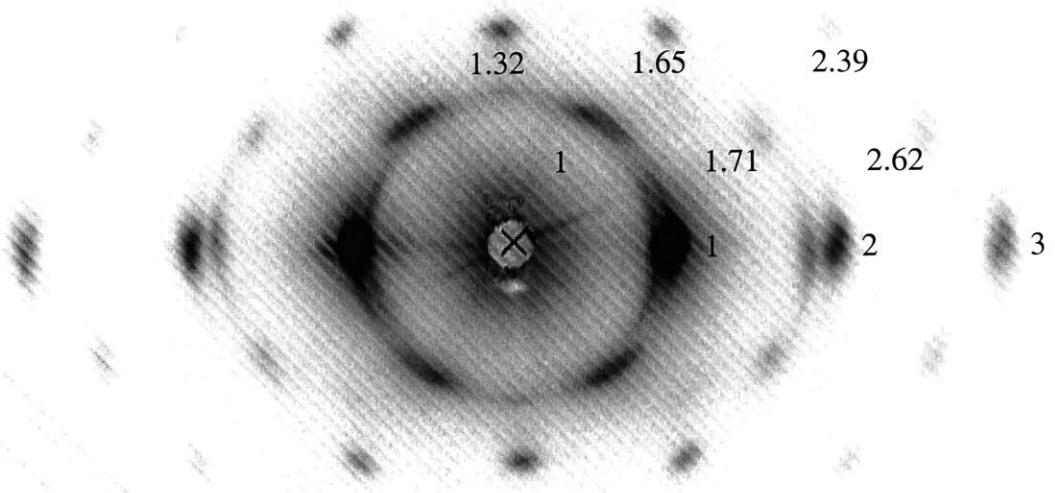

Figure 6.12: 2D SAXS pattern of roll cast annealed 36%S SIS. The q-ratios are normalized with respect to the value of the outer peak (higher q) of the equatorial doublet. The reasons for choosing the outer peak will be discussed in section 5.2.4.2.1.

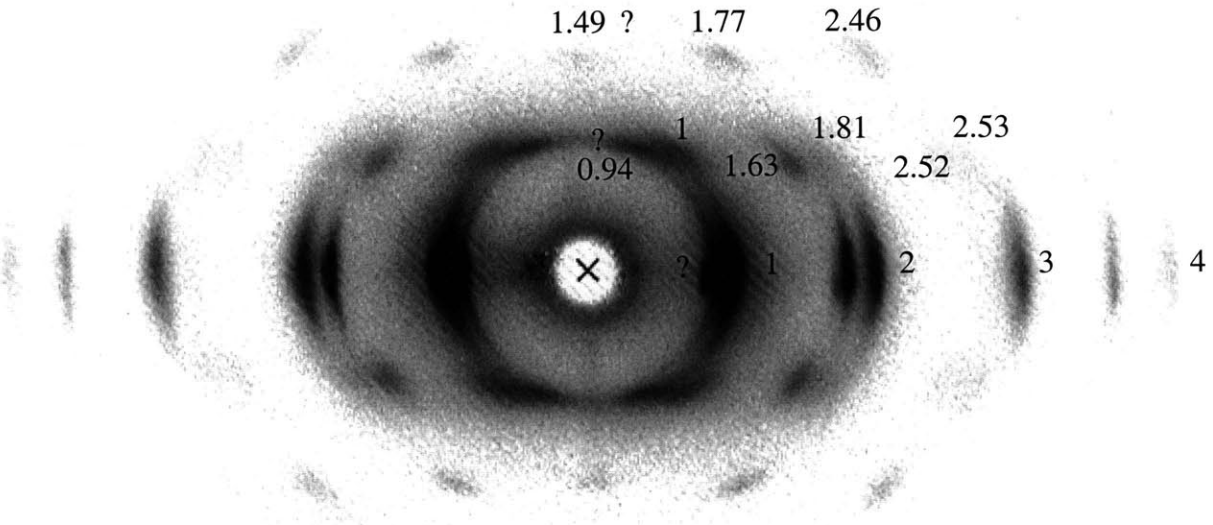

Figure 6.13: The 2D SAXS pattern of roll cast annealed 34%S SIS, labelled with the q-ratios normalized to the outer peak of the equatorial doublet.

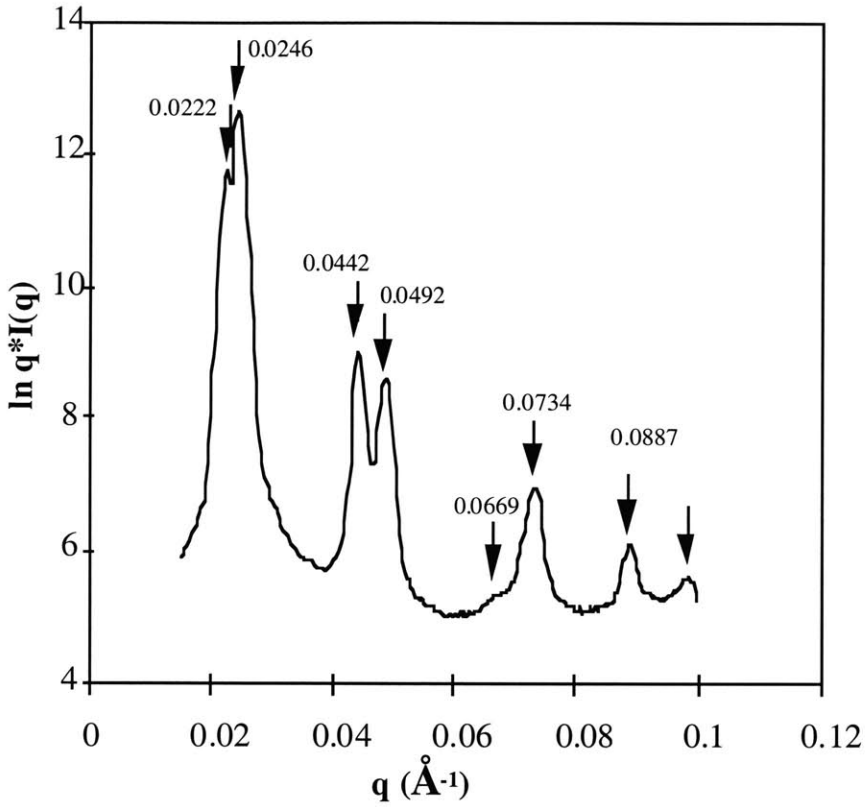

Figure 6.14: Integrated SAXS pattern of the roll cast 34%S SIS annealed 2 weeks at 120°C. The ln q*I(q) vs. q azimuthal integration is taken over 20° about the equator of figure 6.13b.

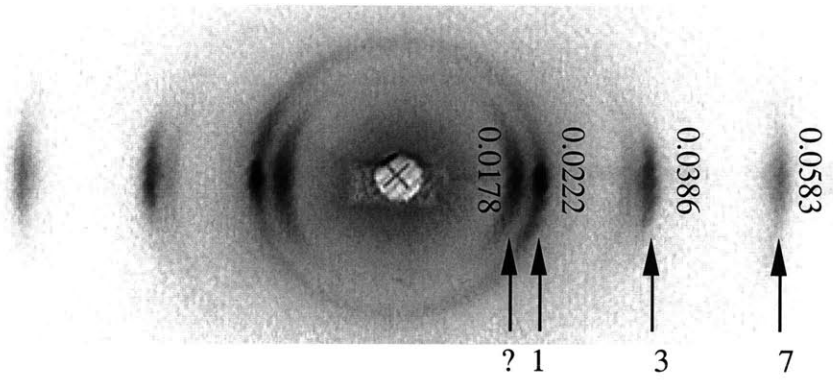

Figure 6.15: 2D SAXS pattern of Dexco 4211, 30 wt%S SIS with block molecular weights 15-72-15 kg/mol. The polymer was roll cast on the mini-roll caster with the same parameters as for all of the roll cast polymers used in this thesis and annealed at 120°C for 2 weeks. The ring along the second peak indicates that there are some grains not oriented along the roll cast direction.

In light of these observations on roll cast cylinders here, in Honeker's thesis, and on other work on sheared block copolymers, the first peak of the equatorial doublet (and its higher order harmonics) seems to have origins outside of the inherent morphological structure of the polymer and will be disregarded in the analyses of the roll cast annealed 34%S SIS samples.

6.3.4 Indexing Orientation of Roll Cast 34%S SIS

Figures 6.16 b-d show the typical 2D SAXS pattern of a roll cast annealed 34%S SIS film, viewed through the film, down the neutral axis, and down the roll cast axis, respectively, with the q values for the peaks labelled. Figure 6.18 a shows the orientations of the patterns relative to the roll cast and film axes.

The pattern viewed through the film shown in figure 6.16b has the x-ray beam oriented perpendicular to the plane of shear (the x-z plane). Of the three, this orientation shows the richest Bragg features. The equator has 3-4 orders of reflections, and the pattern has two additional layer lines parallel to the equator. Both of these indicate high order within the plane of shear.

Figure 6.16c shows the 2D SAXS pattern down the neutral axis of the film with the flow direction along the horizontal. There are six Bragg reflections at nearly the same q values. The off-meridional peaks occur at 35° from the flow axis, or 55° from the meridian. The existence of Bragg peaks (as opposed to streaks) indicates ordering in the short range, but the lack of higher order harmonics indicates that there is not as much long range order as in the plane of shear.

Figure 6.16d shows the 2D SAXS pattern down the roll cast axis. The pattern mainly consists of arcs, but has higher order harmonics along the equator. The arcing of the Bragg peaks indicates that there is a mosaicity of grains around the roll cast axis, which reveals that a roll cast film of material having quiescent-cast DG morphology is not single-crystalline. Subsequent efforts at acquiring samples and SAXS patterns having better order were unsuccessful. However in shear-aligned block copolymer systems mosaicity around the shear axis was also observed, even in the best cases (Förster et al., 1994; Schulz et al., 1994; Zhao et al., 1996).

At first glance it may seem unfortunate that there exists a mosaicity in the roll cast film around the [111] axis for the sake of the anisotropic mechanical properties of DG. However, as mentioned in section 2.8.4, planar 3-fold symmetry renders the mechanical properties isotropic in the plane. Therefore, mosaicity in the plane does not further complicate the interpretation of the mechanical properties.

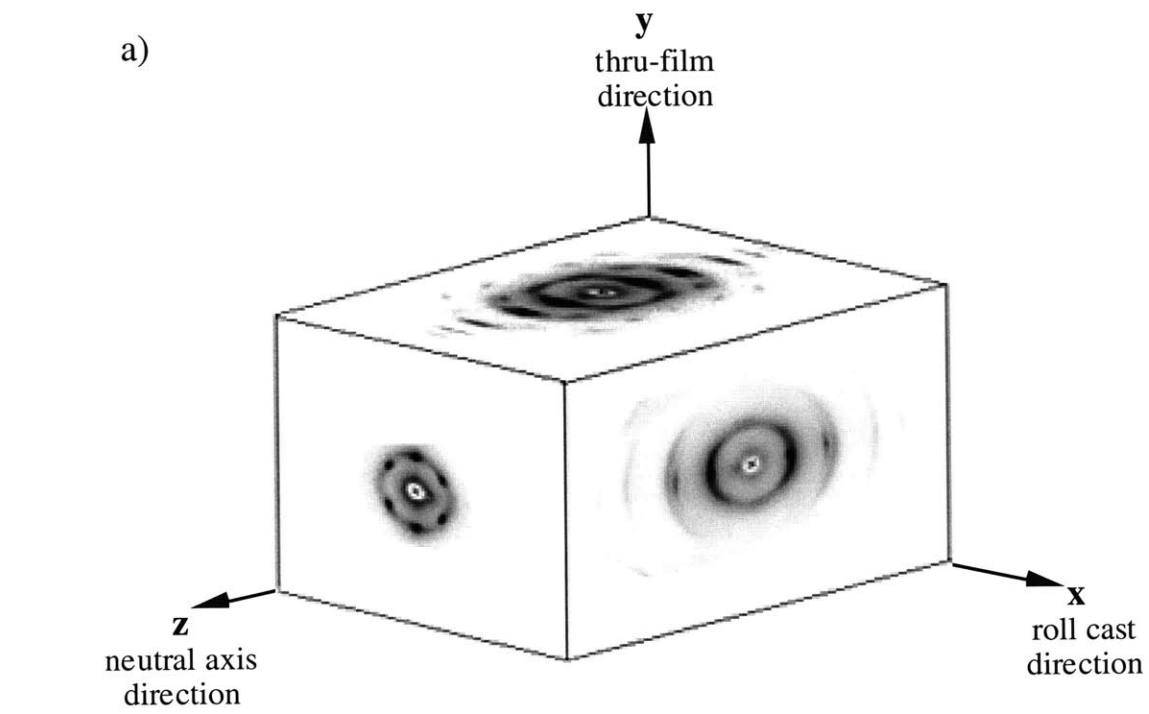

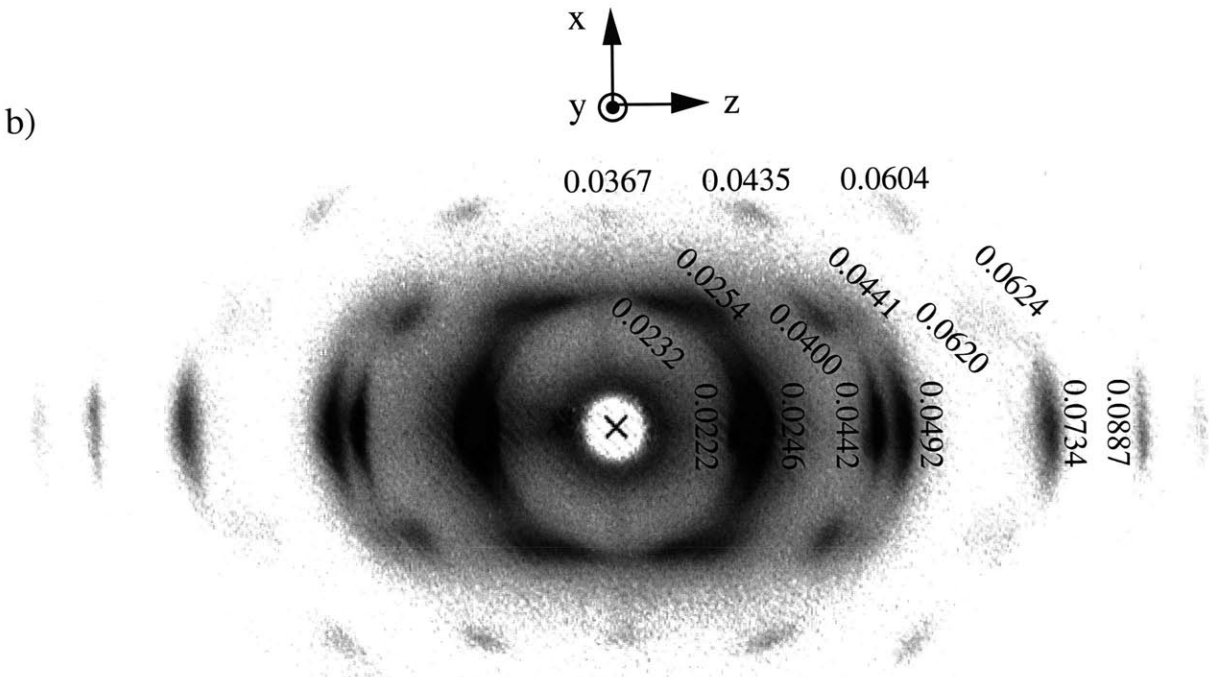

Figures 6.16: a) 2D SAXS patterns of roll cast DG relative to the axes of the film. The box shows the orientations of the patterns relative to each other and to the roll cast axes. b) 2D SAXS pattern with the beam oriented through the roll cast film, with the roll cast axis along the vertical. The q values of the peaks are labelled.

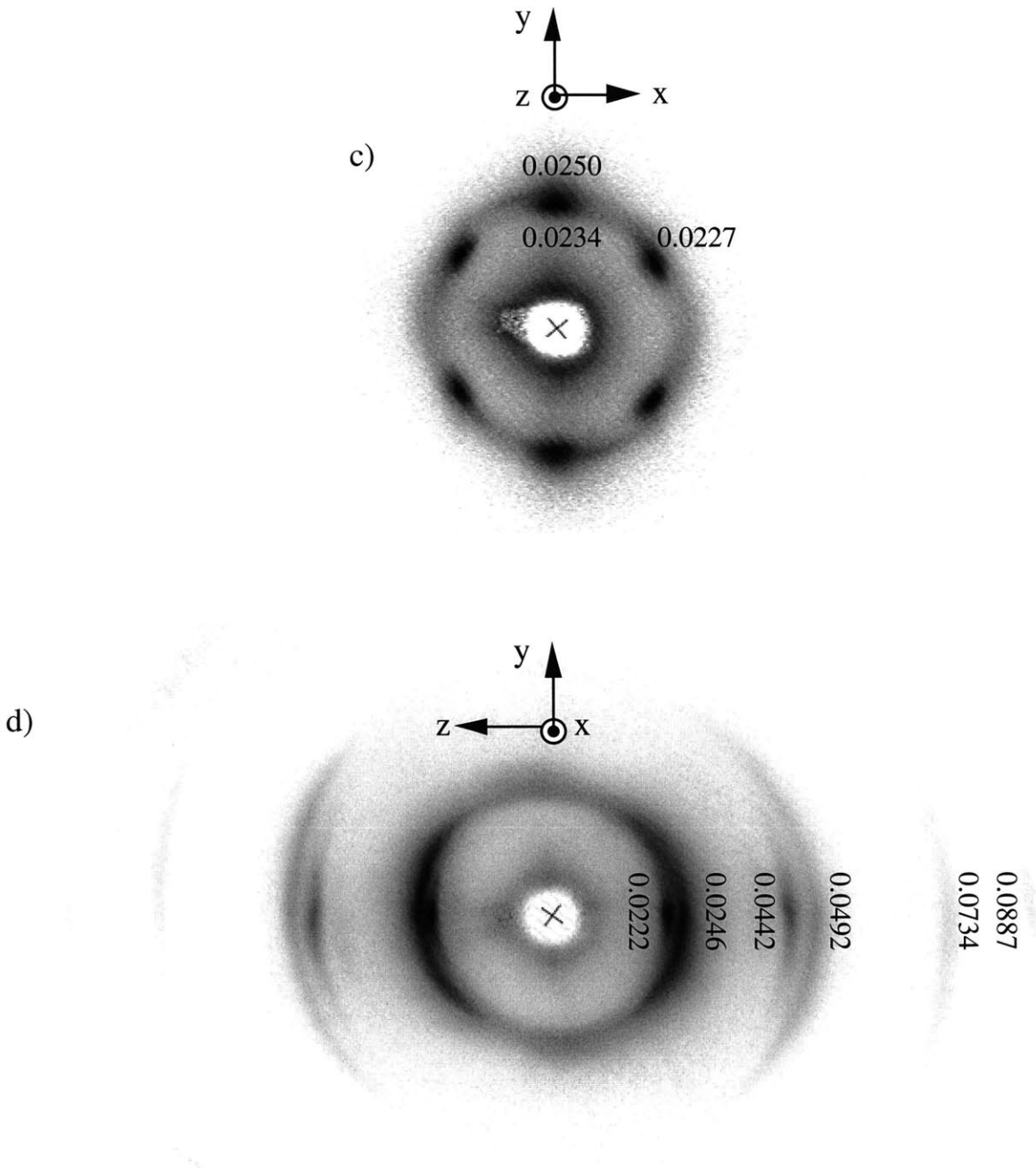

Figure 6.16: c) 2D SAXS pattern of a roll cast film with the beam oriented along the neutral axis. d) 2D SAXS pattern down the roll cast axis. The q values of the peaks in both patterns are labelled.

6.3.5 TEM of Roll Cast Annealed 34%S SIS

Figure 6.17a shows the TEM image of roll cast annealed 34%S SIS, viewing the planes parallel to the plane of the film with the roll cast direction vertical. This figure is the real-space correspondence to the SAXS pattern shown in figure 6.16b. The electron beam is oriented down the same axis as the x-ray beam in figure 6.16b, with the roll cast axis vertical in both. The SAXS pattern of the sample from which figure 6.17a was taken is shown in figure 6.16b. The optical transform and digital fast Fourier transform of the TEM image in 6.17a are shown in figures 6.16c-d. In essence both the SAXS pattern and the transforms are diffraction patterns of the real space structures. Note that the main or strongest features of the SAXS pattern are present in the transforms, indicating that the TEM image is indeed the real-space view of the 2D SAXS pattern in figure 6.16b. The weaker features of the SAXS pattern might not appear in the transforms for two reasons. First, the optical transforms are recorded on Polaroid film such that intensities are shown on a linear scale, thereby biasing the strongest reflections; the intensities of 2D SAXS patterns are logarithmic in scale, such that weaker reflections can be seen. Secondly, SAXS integrates through the real three-dimensional sample volume such that diffraction from long range order is recorded. Only two-dimensional TEM projections through 500 Å - thick films and much smaller cross-sectional areas of the sample (1 μm in TEM images versus 1 mm in SAXS) are used for optical and Fourier transforms, such that any longer-range order and/or texturing may not be observable by the transforms.

The TEM image shows that different grains exist in the plane of the roll cast film. The grains are much longer in the roll cast direction than transverse -- from left to right, about 4 grains can be distinguished, whereas the grains continue past the top and bottom of the image. Judging from the projections of the different grains, misorientation occurs predominantly around the roll cast axis rather than in the plane of the page; i.e., grain boundaries separate grains of DG having different projections (being rotated about the roll cast axis), as opposed to grains of the same projections having different tilts (which would hence be rotated about an axis normal to the plane of the page). Along the bottom left of the micrograph, two twinned {110} grains meet. The image also shows that the [111] helices, or the PS domains having the highest PS connectivity, are oriented along the roll cast direction.

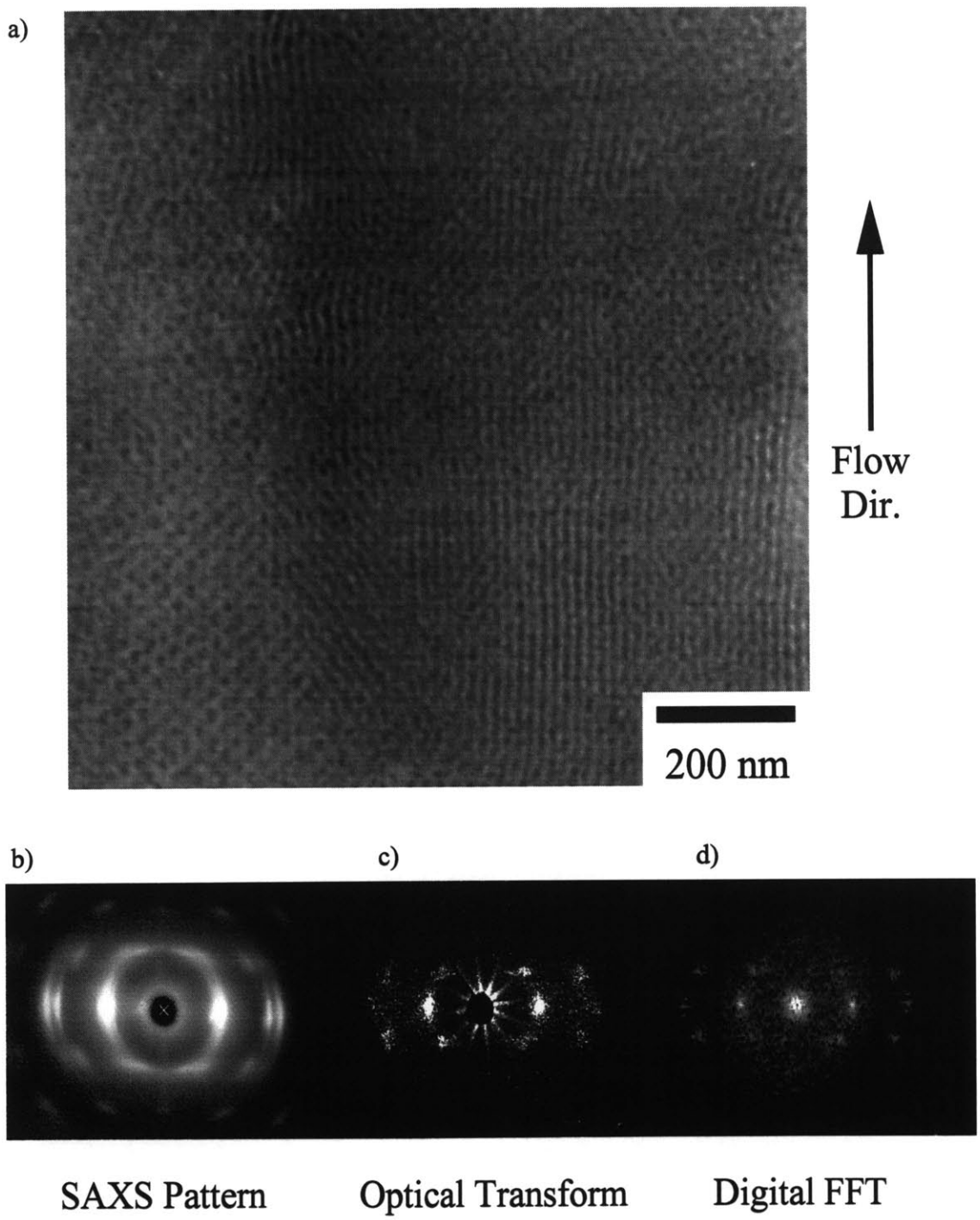

Figure 6.17: a) TEM image in the plane of a roll cast annealed 34%S SIS film. b) SAXS pattern of a sample. c) Optical transform of the TEM image shown in figure 6.17a. d) Fast Fourier Transform of the image in 6.17a.

Simple-cast films have DG as equilibrium morphology such that an oriented form of the DG was the first morphology considered for the roll-cast annealed structure. Since the cylinders are aligned with the roll-cast direction and since the cylinder axes are observed to have an epitaxial relationship with <111> directions of the DG, a <111> is expected to be aligned along the roll cast direction. The roll cast direction is now designated the [111], as opposed to another of its eight <111>-type directions. In addition, the q value of the first peak is 0.0246, which is approximately the same as that of the simple cast {112} value (0.0247). It is with the intention to satisfactorily explain these two major observations that a model for the orientation and indexing is sought.

In a cubic system the indices of a plane are the same as those describing the direction normal to it, schematized in figure 6.18. Because the shear plane (shown in figure 6.16b) also contains the [111] direction, the normal to the plane is also perpendicular to the [111] direction. The indices of the plane (hkl) and of its normal [hkl] can then be sought according to the principle that [111]•[hkl] = 0, or that [111]•(hkl) = 0. The choices are $(\bar{1}10)$, $(1\bar{1}0)$, or $(11\bar{2})$ and subsequent permutations of the indices.

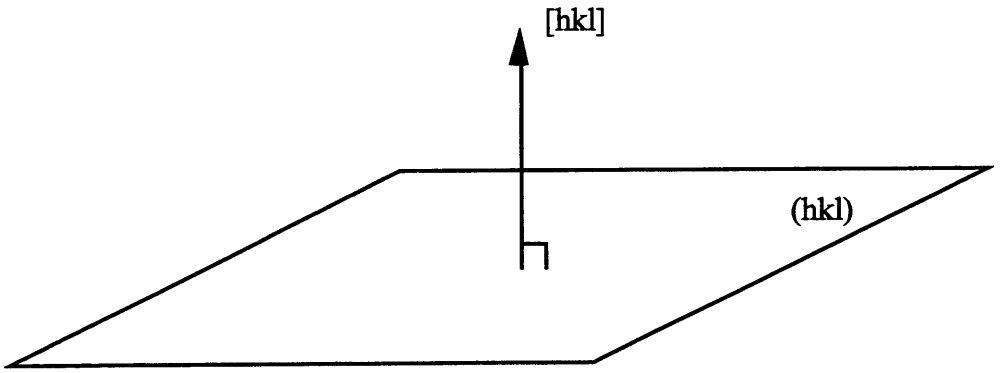

Figure 6.18: In the cubic system, the indices of the plane are the same as those describing the normal to the plane.

TEMsim was used to make the {110} and {112} projections of level set models of DG with volume fractions 34% PS and 66% PI, as shown in figures 6.19. The {110} projection is found to have c2mm symmetry, while the {112} has p2gm symmetry. The indexed FFTs of both projections are shown in figures 5.21 a-b.

The 2D SAXS pattern in figure 6.16b seems to be composed of layer lines. Attempted layer lines drawn at various angles through the pattern (not shown) indicated the best fit to be layer lines vertical and horizontal relative to the pattern, shown in figure 6.21. Qualitatively the in-plane SAXS pattern seems to bear greater resemblance to that of the {110} projection than the {112} projection. The possibilities and consequences of both of

these orientations will be discussed in light of the experimental scattering and mechanical properties observations.

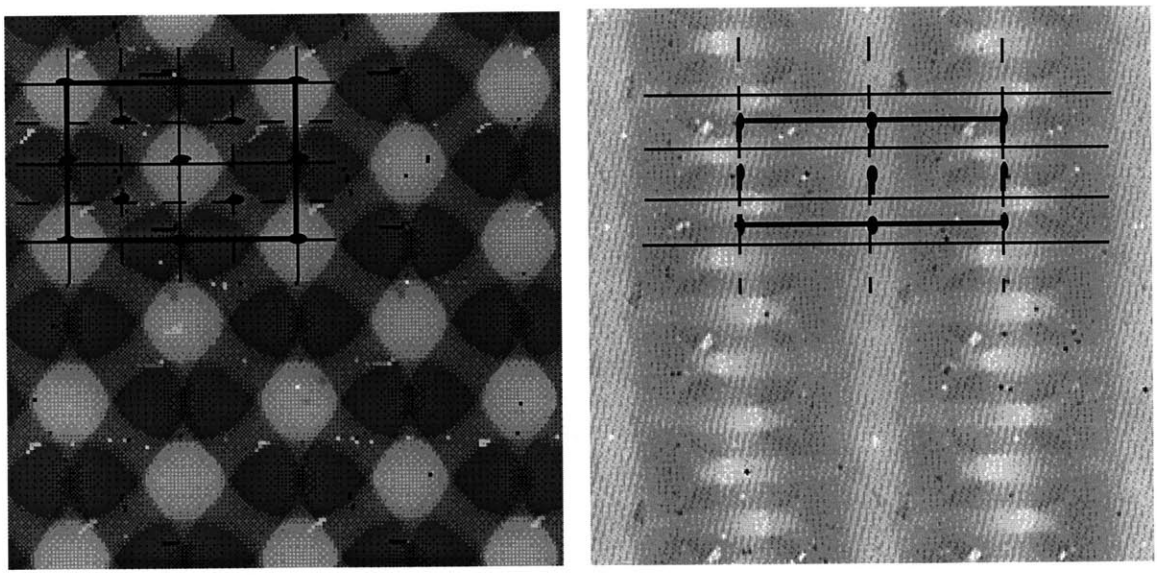

a) b)

Figure 6.19: TEMsim projections of the level set model of DG with s_p = ± 1.0, corresponding to 34% PS by volume, in the a) {110} and b) {112} projections. The solid lines delineate mirror planes, the dashed lines denote glide planes, and the bold lines outline the edges of the unit cells. The black lens-shapes indicate 2-fold rotational axes.

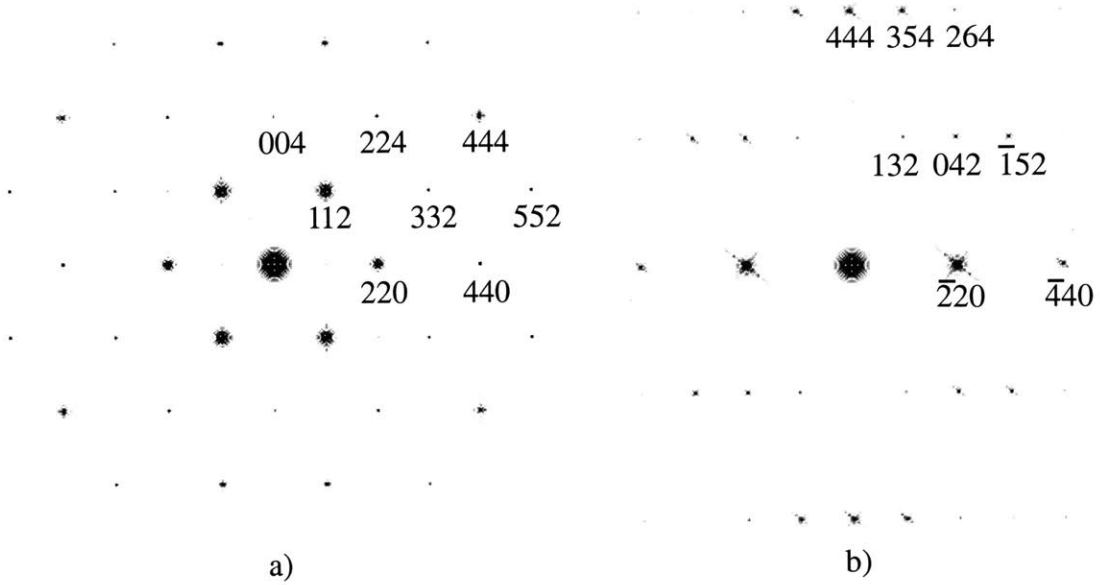

a) b)

Figure 6.20: The FFTs of a) the {110} and b) the {112} projections shown in figures 6.19a and b, respectively.

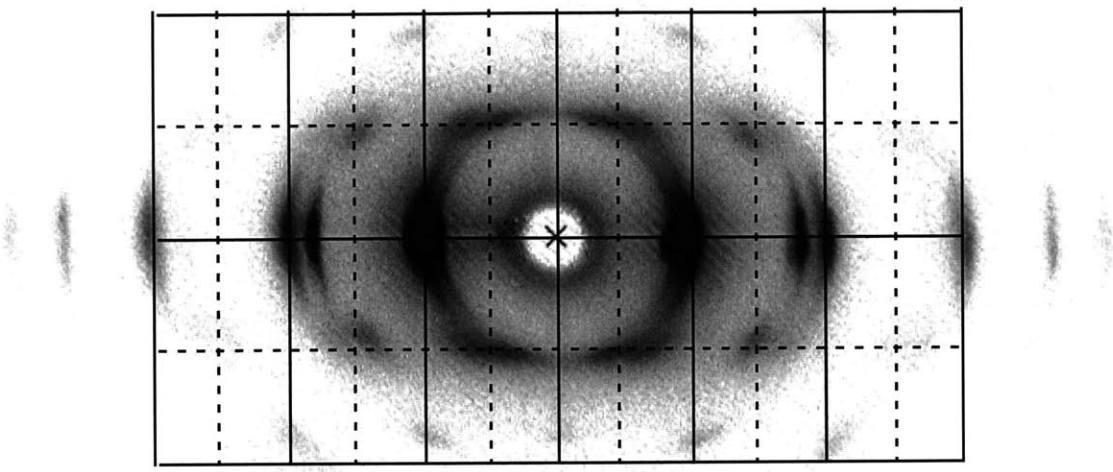

Figure 6.21: 2D SAXS pattern with layer lines superimposed.

{110} projection

If the observed scattering pattern in the shear plane is indeed the (110) projection in the orientation shown in figure 6.16b, then comparison of the the ratio of the horizontal to vertical layer lines in both the FFT (1.4) and the experimental pattern (1.3) indicates that the scattering objects are elongated in the roll-cast direction. Although the sample was annealed above T_g^{PS} for two weeks, it is possible that the sample had some residual strain in the flow direction.

The first peak on the equator would correspond to the (220) peak, and the corresponding planes are standing up perpendicular to the plane of the paper in the direction of the roll cast axis. The inter-layer spacings of these proposed (220) planes are larger than that of the simple cast DG, which would mean that roll-casting the polymer causes these planes to expand in the lateral direction relative to the roll-cast axis. Since there is possible residual elongation strain in the roll cast direction and since the Poisson's ratio for these types of materials is non-negative, expanded planes in the transverse direction are unlikely.

In the {110} projection the first peak along the roll-cast direction corresponds to the (004) reflection, which would make the [001] direction lie along the roll-cast axis. However, this consequence does not agree with other observations. As was mentioned in section 5.3.1.1, the cylinder axis aligns along the roll cast axis, which, as seen by others, is epitaxially related to the [111] direction of DG, the direction of highest PS continuity. In addition, the stress-strain behavior of the roll-cast direction (see chapter 7) exhibits necking behavior, which is characteristic of high-continuity PS domains along the stretching direction. The <001> direction of the DG, however, consist of large, loose helices (4_1 and 4_3 screw axes) with no direct PS connectivity and could not account for the necking

4_3 screw axes) with no direct PS connectivity and could not account for the necking behavior. Therefore, it is unlikely that the [001] direction could be along the roll-cast direction.

These reasons, mainly the last, are compelling evidence against a single {110} projection with a <001> direction along the roll cast axis.

{112} projection

With this projection the roll-cast direction would be placed along the [111], which is in agreement with the mechanical behavior observations and the fact that this direction grew from the cylinder axes. However the FFT of the {112} projection does not bear much qualitative resemblance to the observed roll-cast scattering pattern through the film. The former has p2mm symmetry and the ratio of meridional to equatorial layer lines is much larger (2.4 for the fft of the {112} projection, 1.3 for the observed scattering pattern). The first equatorial peak would correspond to the (220) reflection, but as discussed above, the q-value of the equatorial peak on the roll cast pattern (through the film) does not match that of the simple cast q_{220} but rather that of q_{211}. In light of the discrepancies, the observed scattering pattern is most unlikely to be that of a {112}.

Twinned {110} projection

The preceding discussions showed that the observed scattering pattern in the shear plane could not be indexed to either the {110} or the {112} projections. The {110} projection, although qualitatively was similar to the observed scattering pattern, was found to be inadequate because it predicted the <001> direction to be along the roll-cast direction of the {110} projection. It was observed that the roll cast direction grew from the cylinder axis, which has been observed to be epitaxially related to the <111> DG directions, and that the roll cast direction is along a mechanically robust direction. Both are compelling evidence that a <111> DG direction lies along the roll cast direction.

It may be possible that the [111] direction is forced to lie in the roll-cast direction. If the {110} pattern were forced to have a <111> lie in the roll cast direction, the result would be as in figure 6.22a, where the {211} peaks lie on the equator and both {211} and {220} forming the first layer line. This pattern is skewed and only has primitive symmetry around the roll cast axis. However, because the roll casting process induces 2-fold symmetry in the film along all three axes, the structure whose pattern can be created by rotating figure 6.20a by 180° around the roll cast axis is equally probable. The reciprocal space pattern of the degenerate structure is shown in figure 6.22b. The resulting pattern of the two {110} planes twinned about the <111> axis is shown in figure 6.23.

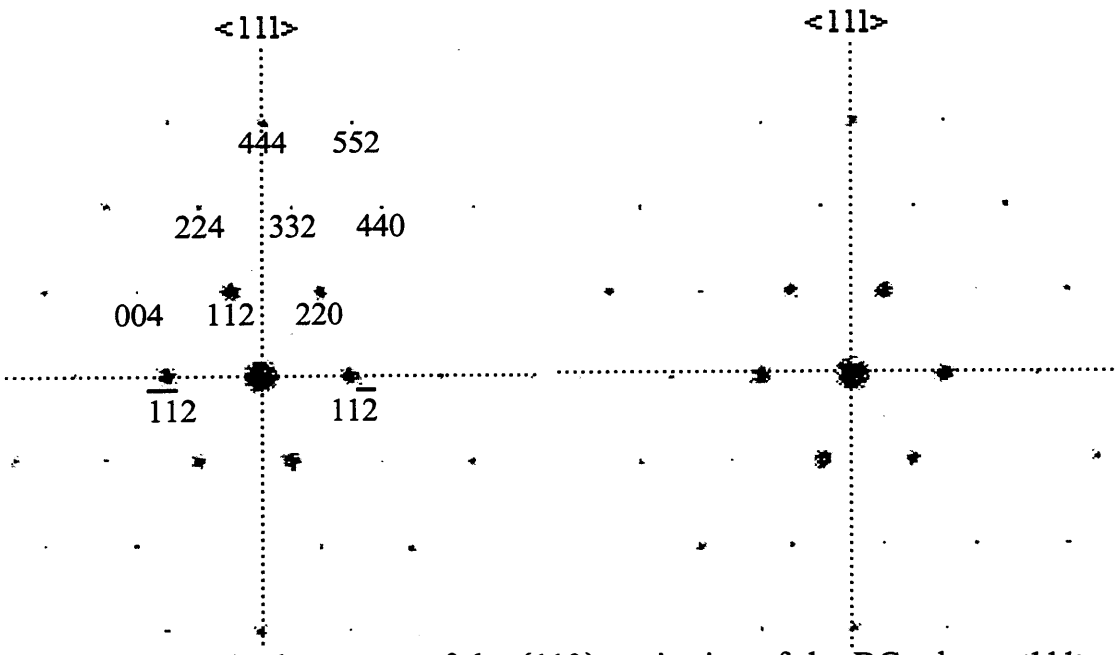

Figure 6.22: a) The pattern of the {110} projection of the DG where <111> direction lies along the roll cast axis. b) The 180° rotation of that in figure 6.22a about the [111] axis, which forms with equal probability.

The pattern of the twinned {110} planes about the [111] axis bears striking qualitative resemblance to the observed scattering pattern in figure 6.16b. The [112] and [220] peaks of the twinned pattern on the horizontal layer lines in figure 6.23 are in close enough proximity such that misorientation of the grains could cause broadening of the peaks enough for them to touch, thereby creating the appearance of one single Bragg streak. Indeed, this explanation is consistent with observed pattern, which seems to have Bragg streaks along the horizontal layer lines. In addition, the [111] direction is along the roll cast direction, in accordance with epitaxial and mechanical properties observations. Furthermore, the twinned model predicts that the first equatorial peak is a {112} reflection, in accordance with the observed first equatorial peak having a q-value equal to the simple cast q_{211} of the same sample.

Although in most of the cylinder films roll cast in our laboratory, the {10} cylinder planes are parallel to the plane of the film (which is parallel to the plane of shear) (Albalak, Thomas, and Capel, 1997; Honeker, 1997), the epitaxial relationships between cylinders and DG dictate that in these roll cast samples the {10} cylinder planes are perpendicular to the plane of the film, with the axes of the cylinders in the direction of flow.

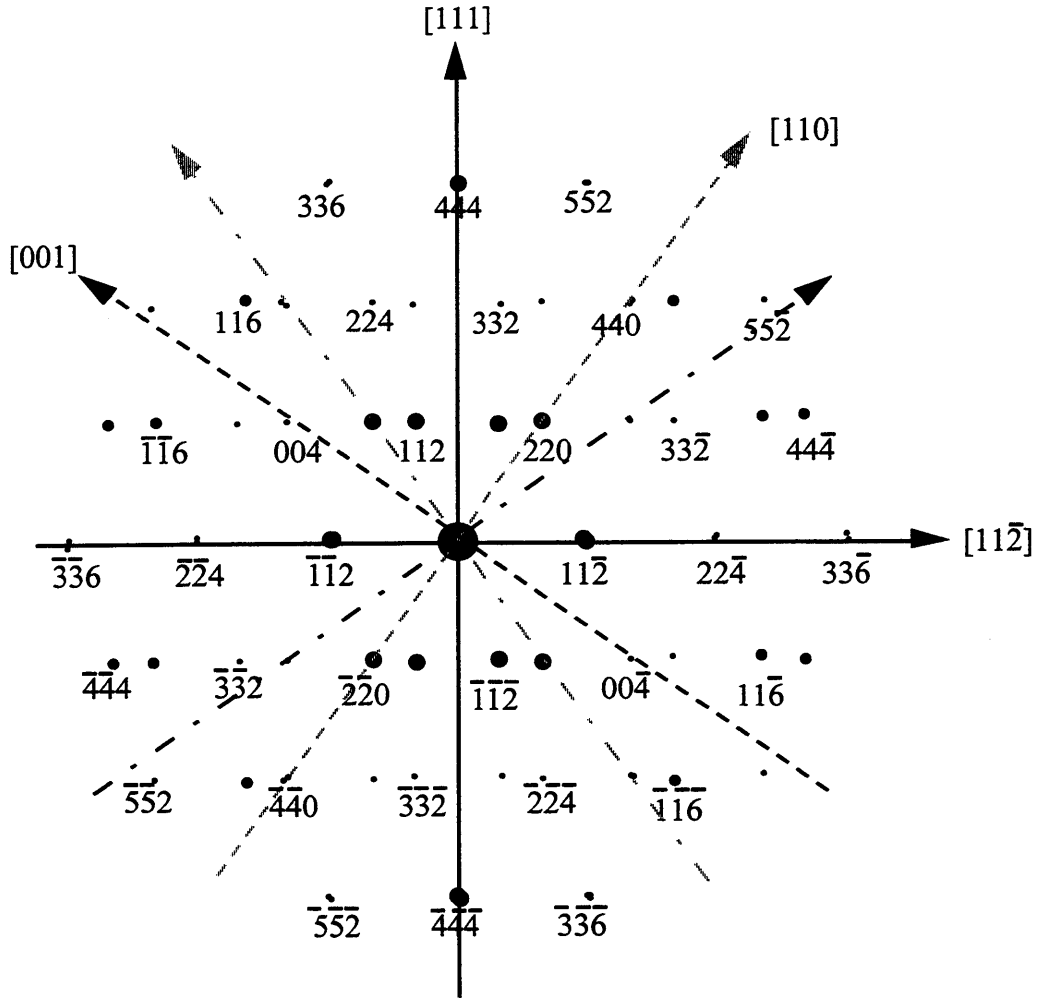

Figure 6.23: Scattering pattern of two {110} planes twinned about the [111] axis with indexing of only one of the lattices indexed. The dashed black line indicates the original {110} and {001} axes of the lattice which is indexed, while the dashed grey line indicates the axes of the lattice which is not indexed.

It is most likely that the observed scattering pattern through the roll cast film is that of twinned {110} planes in the plane of the roll cast film about the [111] axis, which is oriented along the roll cast flow direction. Most of the observed peaks and the nature of the scattering patterns in the three roll cast directions can be explained by this indexing (disregarding the inner peak of the equatorial doublet, a phenomenon also seen in other sheared systems).

6.4 References

Albalak, R. J., E. L. Thomas and M. S. Capel (1997). "Thermal Annealing Of Roll-Cast Triblock Copolymer Films." Polymer **38**: 3819.

Charvolin, J. (1990). "Crystals Of Fluid Films." Contemporary Physics **31**(1): 1-17.

Charvolin, J. and J. F. Sadoc (1990). "Structures Built By Amphiphiles And Frustrated Fluid Films." Colloque de Physique **C7**(23): C7-83-C7-96.

Clerc, M., P. Laggner, A.-M. Levelut and G. Rapp (1995). "Rates Of Phase Transformations Between Mesophases Formed By A Non-Ionic Surfactant In Water: A Time-Resolved X-Ray Diffraction Study." Journal de Physique II (France) **5**: 901-917.

Clerc, M., A. M. Levelut and J. F. Sadoc (1991). "Transitions Between Mesophases Involving Cubic Phases In The Surfactant-Water Systems. Epitaxial Relations And Their Consequences In A Geometrical Framework." Journal of Physics II (France) **1**: 1263.

Considine, D. M., Ed. (1983). Van Nostrand's Scientific Encyclopedia. New York, Van Nostrand Reinhold Co. Inc.

Delacroix, H., T. Gulik-Krzywicki, P. Mariani and J.-L. Risler (1993). "Freeze-Fracture Electron Microscopy Of Lyotropic Lipid Systems. Quantitative Analysis Of Cubic Phases Of Space Group Ia3d (Q230)." Liquid Crystals **15**: 605-625.

Delacroix, H., P. Mariani And T. Gulik-Krzywicki (1990). "Image Analysis Of Freeze-Fractures Lipid-Water Cubic Phases Of Space Group Ia3d." Colloque de Physique **C7**(23): C7-119-C7-129.

Förster, S., A. K. Khandpur, J. Zhao, F. S. Bates, I. W. Hamley, A. J. Ryan and W. Bras (1994). "Complex Phase Behavior Of Polyisoprene-Polystyrene Diblock Copolymers Near The Order-Disorder Transition." Macromolecules **27**: 6922-6935.

Hajduk, D., H. Takenouchi, M. A. Hillmyer, F. S. Bates, M. E. Vigild and K. Almdal (1997). "Stability Of The Perforated Layer (Pl) Phase In Diblock Copolymer Melts." Macromolecules **30**: 3788-3795.

Hajduk, D. A., P. E. Harper, S. M. Gruner, C. C. Honeker, G. Kim, E. L. Thomas and L. J. Fetters (1994). "The Gyroid: A New Equilibrium Morphology In Weakly Segregated Diblock Copolymers." Macromolecules **27**: 4063-4075.

Hajduk, D. A., R.-M. Ho, M. A. Hillmyer, F. S. Bates and K. Almdal (1998). "Transition Mechanisms For Complex Ordered Phases In Block Copolymer Melts." Journal of Physical Chemistry B **102**: 1356-1363.

Hajduk, D. A., T. Tepe, H. Takenouchi, M. Tirrell, F. S. Bates, K. Almdal and K. Mortensen (1998). "Shear-Induced Ordering Kinetics Of A Triblock Copolymer Melt." Journal of Chemical Physics **108**: 1-8.

Hamley, I. W., M. D. Gehlsen, A. K. Khandpur, K. A. Koppi, J. Rosedale, M. F. Schulz, F. S. Bates, K. Almdal And K. Mortensen (1994). "Complex Layered Phases In Asymmetric Diblock Copolymers." Journal de Physique France II **4**(12): 2161-2186.

Hamley, I. W., K. A. Koppi, J. H. Rosedale, F. S. Bates, K. Almdal and K. Mortenson (1993). "Hexagonal mesophases between lamellae and cylinders in a diblock copolymer melt." Macromolecules **26**: 5959-5970.

Hashimoto, T. and N. Sakamoto (1995). "Nucleation And Anisotropic Growth Of Lamellar Microdomains In Block Copolymers." Macromolecules **28**: 4779-4781.

Hashimoto, T., K. Tsutsumi and Y. Funaki (1997). "Nanoprocessing Based On Bicontinuous Microdomains Of Block Copolymers: Nanochannels Coated With Metals." Langmuir **13**: 6869-6872.

Honeker, C. C. (1997). Large Strain Deformation Behavior of Oriented Triblock Copolymer Cylinders. PhD. thesis, Massachusetts Institute of Technology.

Imai, M., T. Kato and D. Schneider (1997). "Fluctuations And Growth Of A Cubic Network Observed In A Nonionic Surfactant System." Journal of Chemical Physics **106**: 9362-9371.

Khandpur, A. K., S. Förster, F. S. Bates, I. W. Hamley, A. J. Ryan, W. Bras, K. Almdal and K. Mortensen (1995). "Polyisoprene-Polystyrene Diblock Copolymer Phase Diagram Near The Order-Disorder Transition." Macromolecules **28**: 8795-8806.

Laradji, M., A.-C. Shi, R. C. Desai and J. Noolandi (1997). "Stability Of Ordered Phases In Weakly Segregated Diblock Copolymer Systems." Physical Review Letters **78**: 2577-2580.

Laradji, M., A.-C. Shi, J. Noolandi and R. C. Desai (1997). "Stability Of Ordered Phases In Diblock Copolymer Melts." Macromolecules **30**: 3242-3255.

Mariani, P., L. Q. Amaral, L. Saturni And H. Delacroix (1994). "Hexagonal-Cubic Phase Transitions In Lipid Containing Systems: Epitaxial Relationships And Cylinder Growth." Journal of Physics II (France) **4**: 1393-1416.

Matsen, M. W. (1998). "Cylinder-To-Gyroid Epitaxial Transitions In Complex Polymeric Liquids." Physical Review Letters **20**: 4470-4473.

Matsen, M. W. and M. Schick (1994). "Microphase Separation In Starblock Copolymer Melts." Macromolecules **27**: 6761-6767.

Matsen, M. W. and M. Schick (1994). "Stable And Unstable Phases Of A Diblock Copolymer Melt." Physical Review Letters **72**(16): 2660-2663.

Qi, S. and Z.-G. Wang (1997). "Kinetics Of Phase Transitions In Weakly Segregated Block Copolymers: Pseudostable And Transient States." Physical Review E **55**: 1682-1697.

Qi, S. and Z.-G. Wang (1997). "On The Nature Of The Perforated Layer Phase In Undiluted Diblock Copolymers." Macromolecules **30**: 4491-4497.

Rançon, Y. and J. Charvolin (1988). "Epitaxial Relationships During Phase Transformations In A Lyotropic Liquid Crystal." Journal of Physical Chemistry **92**: 2646-2651.

Rançon, Y. and J. Charvolin (1988). "Fluctuations And Phase Transformations In A Lyotropic Liquid Crystal." Journal of Physical Chemistry **92**: 6339-6344.

Schulz, M. F., F. S. Bates, K. Almdal and K. Mortensen (1994). "Epitaxial Relationship For Hexagonal-To-Cubic Phase Transition In A Block Copolymer Mixture." Physical Review Letters **73**(1): 86-89.

Schulz, M. F., A. K. Khandpur, F. S. Bates, K. Almdal, K. Mortensen, D. A. Hajduk and S. M. Gruner (1996). "Phase Behavior Of Polystyrene-Poly(2-Vinylpyridine) Diblock Copolymers." Macromolecules **29**: 2857-2867.

Thomas, E. L., D. M. Anderson, C. S. Henkee and D. Hoffman (1988). "Periodic Area-Minimizing Surfaces In Block Copolymers." Nature **334**(6184): 598-601.

Vigild, M. E., K. Almdal, K. Mortensen, I. W. Hamley, J. P. A. Fairclough and A. J. Ryan (1998). "Tranformations To And From The Gyroid Phase In A Diblock Copolymer." Macromolecules **31**: 5702-5716.

Yeung, C., A.-C. Shi, J. Noolandi and R. Desai (1996). "Anisotropic Fluctuations In Ordered Copolymer Phases." Macromolecular Theory and Simulations **5**: 291-298.

Zhao, J., B. Majumdar, M. F. Schulz, F. S. Bates, K. Almdal, K. Mortensen, D. A. Hajduk and S. M. Gruner (1996). "Phase Behavior Of Pure Diblocks And Binary Diblock Blends Of Poly(Ethylene)-Poly(Ethylethylene)." Macromolecules **29**: 1204-12015.

Chapter 7: Mechanical Properties of the DG Phase

This chapter presents the mechanical properties of the DG phase. Section 7.1 reports the engineering properties of the simple cast and roll cast DG samples, along with the procedures used to determine or assign the values. Section 7.2 provides a review of the basic concepts relevant to block copolymer mechanical properties, first through a survey of the early works on block copolymer mechanics, and then through a discussion of the relevant concepts. Section 7.3 then compares the polygranular isotropic DG stress-strain behavior with those of the classical morphologies to better realize the potential for this novel phase. Synchrotron SAXS and TEM studies of deformation will then be presented. Section 7.4 goes in-depth into the properties and deformation behavior of oriented samples to explore the anisotropy of the DG. Both the [111] direction properties (in the flow direction), transverse direction properties, and SAXS and TEM analyses of deformation in both directions will be discussed.

7.1 Engineering Properties

Section 7.1.1 presents the stress-strain curves and values of relevant engineering mechanical properties, and section 7.1.2 details the procedures used to determine or assign their values. From the 2D SAXS pattern taken down the roll cast axis, mosaicity around the roll cast axis is evident, such that the transverse direction is not precisely associated with a single-crystalline $[11\bar{2}]$ direction. Fortunately, as mentioned in section 2.8.4 on the criteria for elastic isotropy, 3-fold rotational symmetry about an axis normal to a given plane is sufficient to render the modulus in that plane isotropic. Thus the modulus transverse to the [111] axis is isotropic and the issue of mosaicity does not limit the the mechanical properties within the {111} plane. However, because of mosaicity of the grains (such that a given direction has a spread of granular orientations), properties in directions transverse to the [111] axis in the {111} plane, namely the $[11\bar{2}]$ along the neutral axis, will be better referred to as "transverse" properties.

7.1.1 Tables and Values

Figure 7.1 shows representative stress-strain curves of oriented DG stretched in the [111] and transverse directions, and of isotropic DG. Table 7.1 summarizes the tensile mechanical properties of the DG phase in the SIS system with ~34 volume % PS (sample SIS 34). Table 7.1a shows the relevant tensile properties upon stretching, and table 7.1b shows the relevant tensile properties upon unloading from 600% strain and subsequent

stretching. Note that the properties of the isotropic stretch are everywhere intermediate between those of the [111] and transverse stretches.

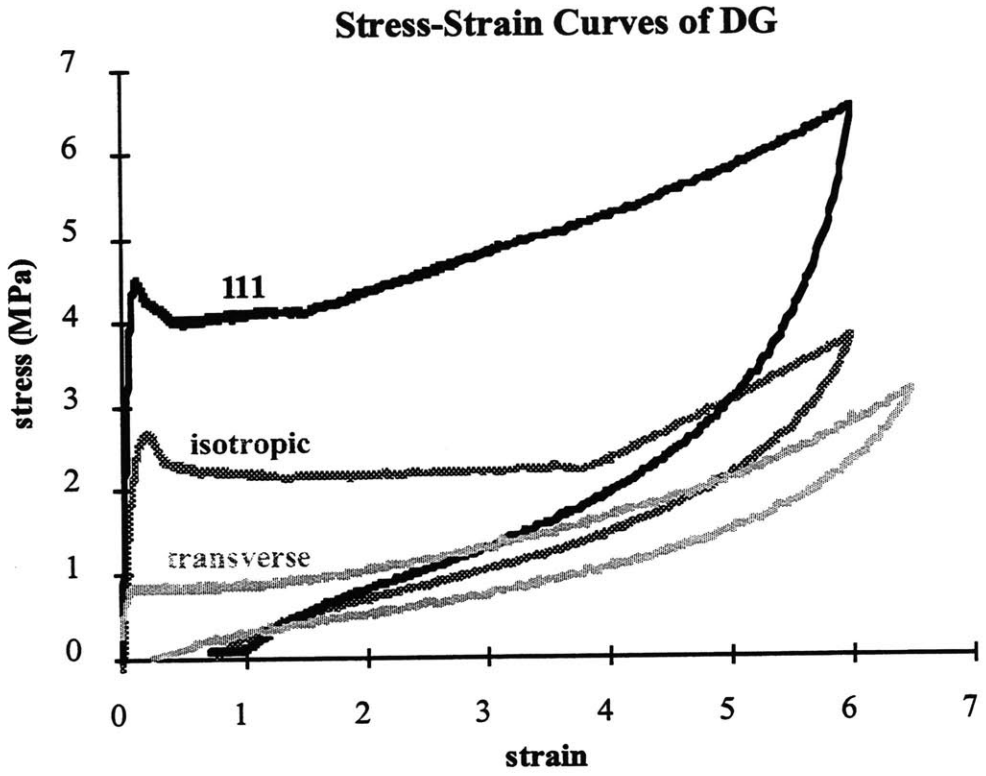

Figure 7.1: Overlayed stress-strain curves of oriented DG stretched in the [111] and transverse directions, as well as a stress-strain curve for polygranular isotropic DG.

Table 7.1a: Mechanical Properties of the Double Gyroid
(values averaged over 5 samples)

Stretch Direction	Initial Modulus (MPa)	Necking Behavior?	Yield Stress (MPa)	Yield Strain
isotropic	29 ± 5	yes	2.6 ± 0.5	0.20 ± 0.02
[111]	48 ± 9	yes	3.4 ± 0.7	0.15 ± 0.04
transverse	9.6 ± 3.2	no	0.74 ± 0.09	0.09 ± 0.03

Table 7.1b: Mechanical Properties of the Double Gyroid
After Stretching to 600% Strain
(values averaged over 5 samples)

Stretch Direction	Residual strain	Hysteresis	Mullins Effect	Microscopic Recovery?	Macroscopic Recovery?
isotropic	0.74 ± 0.06	0.50 ± 0.03	medium	full	full
[111]	0.93 ± 0.04	0.66 ± 0.02	strong	full	full
transverse	0.18 ± 0.08	0.41 ± 0.04	low	full	full

7.1.2 Definition of Properties and Procedures for Assigning Values

Initial Modulus

The initial modulus is the very inital slope at the origin of the stress-strain curve. The modulus along the [111] direction was found to be approximately 50 MPa, while the modulus along the transverse direction was found to be approximately 10, rendering the anisotropy factor $\frac{E_{\|}}{E_{\perp}} = 5$.

Necking Behavior

Necking behavior is defined as "a maximum load followed by nonuniform deformation" (McClintock and Argon, 1966) (for a good discussion on this topic, see McClintock and Argon (1966) and Ward (1975)). Whether a sample exhibited necking was primarily determined by whether the stress-strain behavior exhibits a maximum followed by a drop. Figure 7.2 shows the stress-strain curve of a sample which necks. When the stress-strain evidence for this criteria was ambiguous, the specimen was observed visually for evidence of a physical neck -- a sample which necks may also develop a decreased cross-sectional area in a localized length of the sample, as shown in figure 7.3 If there was no evidence for either of these criteria, it was determined that the sample did not undergo necking phenomenon.

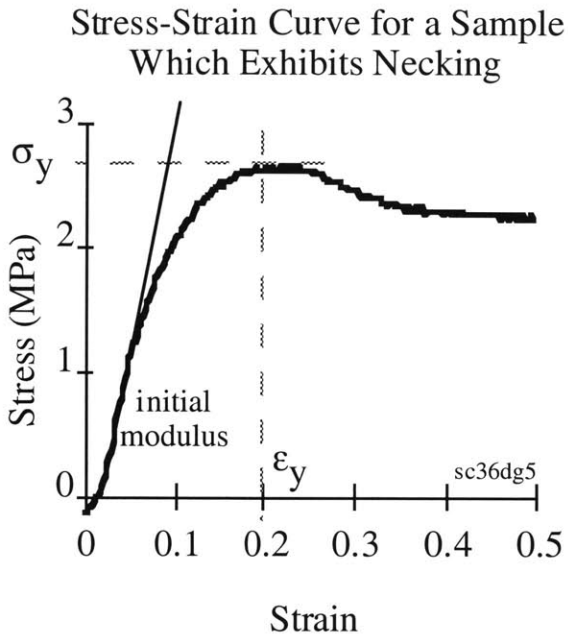

Figure 7.2: Stress-strain curve for a isotropic sample which exhibits necking, and the values for which the yield stress and strain are reported.

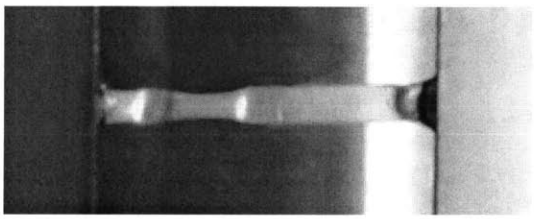

Figure 7.3: Photo of a real sample undergoing necking. The gauge length of the sample shown is ~16 mm.

Yield Stress and Yield Strain

Yielding is the general phenomenon of excessive "plastic" or "permanent" deformation, which is a generalized term referring to any deformation which is not recovered upon immediate unloading. In a sample which exhibits necking, the yield stress was taken as the maximum value of stress before load drop, and the yield strain was taken as the first value of strain where the stress reached the maximum. Figure 7.2 is a schematic showing the values taken for yield stress and strain for a sample which necks.

In a sample which does not exhibit necking, the yield point, or the point at which plastic deformation begins, is usually ambiguous. These samples generally deform elastically with an initial constant modulus, undergo a transition, and then deform with a lower, but constant slope. In such cases the yield stress and strain are found by the

following method, which is illustrated in figure 7.4. The line of initial modulus and the second constant slope are extended towards each other. The point at which they cross is deemed the yield strain. The actual stress corresponding to this stress is reported as the yield stress. It should be noted that a yield strain defined in this manner is inherently lower than that yield strains found in samples which neck. By this definition, the yield strains of samples which necked would be found by the intersection of the initial modulus line and the "constant slope" line (which is parallel to the x-axis at the stress level of maximum load), rather than as the first value having the second "constant slope".

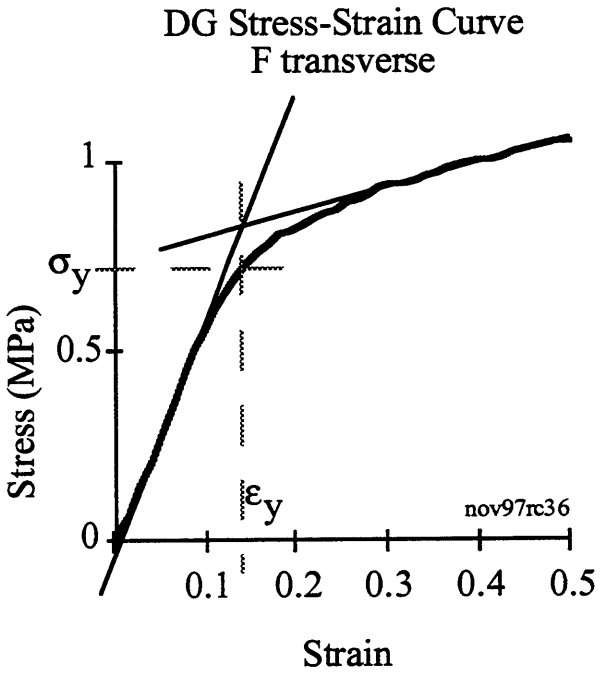

Figure 7.4: Stress strain curve for a sample which does not exhibit necking, and the values for which the yield stress and strain are reported.

Residual Strain

Residual strain is the strain which remains or is not recovered when the sample is initially fully unloaded. The value was determined to be the strain remaining at the point when the value of stress reached zero upon unloading from high strains.

It should be mentioned that the samples continue to relax after unloading and any residual strain in these samples are fully recoverable upon annealing above T_g. The values reported for "residual strain" are those for the strain which remain upon *immediate* unloading.

Hysteresis

The hysteresis is the fraction of energy put into the system which was not recovered upon immediate unloading; it is the fraction of energy put into the system which was either dissipated as plastic deformation work, or absorbed into the system (temporarily, until either long times or high temperature annealing). Hysteresis of a loading-unloading process is an indication of the relative elastic vs. plastic processes which are activated during deformation.

The hysteresis was found by first printing out a hardcopy of the stress-strain curve, and then weighing on a balance the area enveloped by the loading-unloading curves, and normalizing by the area underneath the loading curve. Figure 7.5 shows a loading-unloading stress-strain curve divided into areas A and B. The area A+B is the total energy put into the system to stretch it to the given strain, B is the energy recovered during unloading (indicative of the elastic or recoverable energy), and A is the energy dissipated by the load-unload cycle (indicative of the energy of plastic deformation). The hysteresis is the ratio of the areas A / (A+B).

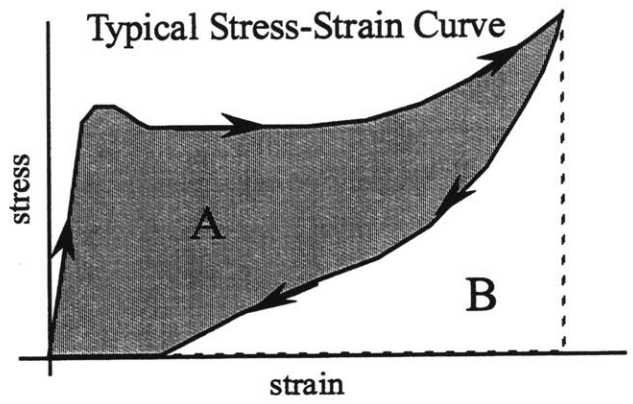

Figure 7.5: Schematic of a load-unload stress-strain curve. The hysteresis is found by the ratio of the areas A / (A+B).

The Mullins Effect

When thermoplastic elastomer tensile samples are stretched to a strain below that for ultimate failure, unloaded, and then immediately restretched, they exhibit a general phenomenon whereby the stress-strain behavior between the very first loading and all subsequent loadings are not the same. The second loading curve generally follows the shape of the unloading curve, the modulus of the first loading is usually much higher than that of the subsequent loadings, and any yielding which occurs in the first loading is not seen in the subsequent loadings. Figure 7.6 shows an example of this phenomenon.

The strength of the Mullins effect was qualitatively assigned a value "strong", "medium", or "weak" depending on the degree of deviation of the second stretch from the first.

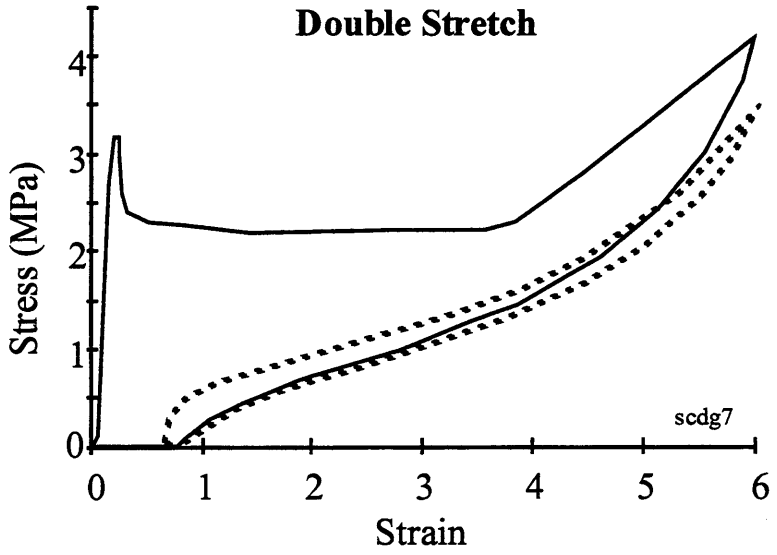

Figure 7.6: Schematic of a stress-strain curve on the first stretch (bold line) and on a subsequent stretch (dotted line).

Microscopic Recovery

Microscopic recovery refers to whether or not the long range order and oriented texture has been restored to a stretched sample after annealing above T_g. It was qualified based on comparisons of SAXS patterns of a given sample before stretching and after stretching and annealing. All of the samples studied showed full recovery, such that long range order was restored (as seen by the number of higher order harmonics) and all original Bragg peaks returned to the same q's.

Macroscopic Recovery

Macroscopic recovery refers to the propensity for recovery of its macroscopic sample dimensions after stretching and annealing. Sample dimensions were measured after stretching and annealing and compared to those taken before stretching. All samples stretched in the various directions were found to completely recover their macroscopic dimensions after annealing above T_g.

7.2 General Mechanical Properties of Triblock Copolymers

This section presents some general concepts in triblock copolymer mechanical properties. In section 7.2.1 a review of the earliest studies of mechanical properties of triblock copolymers will be presented, because many of the fundamental concepts were developed in those first studies. In section 7.2.2 these fundamental concepts will then be discussed in light of the mechanical properties of the DG (presented in the section).

7.2.1 Background on the Early Studies

A good historical account of the developments of triblock copolymers is given in Holden and Legge (1996) and Molau (1970). This section gives a brief account of the early mechanical properties studies and the concepts which developed as a result.

In essence, block copolymers were developed mainly for their mechanical properties. Triblock copolymers resulted from a research effort at the Shell Oil Company to remedy the propensity of polybutadiene and polyisoprene to flow. Polystyrene end blocks were chemically attached to one, and then to both, ends of the polydiene chains. Unlike their Newtonian polydiene homopolymers, these new triblock copolymers were found to exhibit non-Newtonian behavior in that their viscosities tended toward infinity as shear rate approached zero (Holden, Bishop, and Legge, 1969). In addition, these triblock copolymers exhibited tensile properties akin to gum vulcanizates. To explain these observations, domain theory was then developed. Domain theory states that below the glass transition temperature of PS, the PS hard domains agglomerate and act as crosslinks for the polydiene. As was mentioned in section 2.5, these materials are composites in that the PS and the polydiene phases still retain some of the character of their respective homopolymers. In particular, the material as a whole exhibits two glass transition temperatures characteristic of the two phases (Hendus, Illers, and Ropte,1966; Kraus Childers, and Gruver, 1967; Beecher, Marker, Bradford, Aggarwal, 1969; Holden, Bishop, and Legge, 1969).

One of the earliest mechanical properties studies of these triblock copolymers compared the tensile behavior of simple cast (i.e., unoriented, polygranular isotropic) films to vulcanized natural rubber (Bailey, Bishop, Hendricks, Holder, and Legge, 1966). A Kraton 101 (28 wt%S SBS, but 27 wt% SB diblock) material was found to have higher tensile strengths at all strains than the gum vulcanizate. It was later postulated that the higher tensile strengths of the triblock copolymer arose from two possible mechanisms: 1) the chains in the network redistribute uneven stresses via slippage of highly elongated chains, or 2) the hard filler-like particles absorb the energy released after PI chains have ruptured and re-distribute stresses, thereby preventing catastrophic failure after diene chains

have ruptured (Holden, Bishop, and Legge, 1969). Morton (1983) later showed that crosslinking the PI had no effect on the modulus of the system, which pointed to the second of the above-mentioned mechanisms, and that the strength of the material lay in the PS domains.

In another early investigation, Childers et al. (1967) studied the mechanical properties of about 10 triblock copolymers having total molecular weights of 100 kg/mol but varying in PS content. They did not, however, specify the methods or solvents (if any) used to process the polymers into tensile specimens, so that long range order, morphology, and orientation cannot be inferred. (It should be mentioned, however, that it was typical of industrial studies of the time that tensile samples were cut from sheets of compression-molded polymer, thereby having biaxial orientation.) Nonetheless, in comparing 10/80/10, 15/70/15, and 25/50/25 SBS copolymers, they found that the triblocks with low PS content were similar to gum vulcanizates, and increasing PS content caused ultimate failure at lower strains, but at higher stresses. Although never mentioned, it was implied that these low PS triblocks had discontinuous PS domains. It can now be inferred from their compositions that these polymers had spherical PS domains, such that the triblock copolymers were similar to crosslinked vulcanizates in nature and in mechanical behavior. Childers et al. (1967) found that the stress-strain curves of higher PS content triblocks exhibited a "knee" which developed into a distinct yield point in the 25/50/25 SBS. In this 25/50/25 SBS they noticed that yielding was subsequently followed by cold drawing, and then rubber-like behavior. They discovered that the polymers had a "permanent set" or residual strain when unloaded, the magnitude of which increased with increasing styrene content and amount of stretch. This study was also one of the first observations of a hysteresis or "Mullins" effect for polymers which neck. They postulated that as PS content is increased, the equilibrium structure of the PS domains became continuous, which accounted for the yielding and plastic flow properties of the 25/50/25. This hypothesis was one of the first to propose that the PS domains can form structures other than spheres (or, in another way, that the spheres coalesce into more continuous PS structures). They further interpreted the rubbery behavior upon increasing stress beyond plastic flow and drawing as being due to these PS domains becoming discontinuous units; however, no real-space investigations via electron microscopy were made into the morphologies of these materials

Holden et al. (1969) reported on the mechanical properties of several SBS triblock copolymers. Tensile samples were prepared from compression-molded sheets of polymer, and therefore contained biaxial orientation. One significant finding was that for constant PS content, tensile properties (ie, modulus and ultimate tensile strength) did not change with increasing molecular weight in a given SDS (so far as the PS was high enough in

molecular weight to form phase-separated domains). Holden et al. also discussed the effect of PS content on mechanical behavior of the triblocks. In particular, they observed the following characteristics of the polymers with increasing PS content:

Polymer	Stress-Strain Behavior
13%S SBS:	like undercured vulcanizate
27.5%S SBS:	like conventional vulcanizate
30-53%S SBS:	yield followed by drawing, then elastic extension
65%S SBS:	high yield stress followed by short draw and immediate break
80%S SBS:	no draw - breaks at approximately the same elongation as bulk PS

They interpreted the high values of modulus for polymers with PS content greater than 33% to be due to the "existence of a continuous PS phase" and that upon elongation these PS domains break. They assigned the rubbery behavior after drawing to be due to a continuous diene phase, which can only occur if the PS phase becomes discrete. It may be inferred that their notion of a continuous PS phase was probably not that of the bicontinuous DG phase, but rather that of the more classical morphologies having phases less discrete than spheres. From the two trends observed in these block copolymers, it can be inferred that block copolymers derive their strength from 1) the PS domains which act as the crosslinks of the diene phase, and 2) the PS content, and is independent of molecular weight insofar as the triblock can microphase separate. Also, this study was another which hypothesized that the PS domains could form structures other than spheres.

Brunwin et al. (1969) were the first to have taken x-ray patterns of highly extended samples. WAXS was used to investigate the source of the upturn in the stress-strain curve of a 40%S SBS sample at high elongations. They found that high elongations induced orientation, but not crystallization, of the polybutadiene chains and postulated that the restoring force for stretched samples to return toward their original length lies in the entropy of the diene phase. They also found that stretched samples, when placed in boiling water (ie, above Tg), recovered completely. From this they inferred that flow of the diene phase did not occur at high elongations and that the slow recovery at room temperature was due to "hindered segmental mobility". From stress-optical measurements they postulated that the PS blocks do not become rubber-like below 70° C; therefore, the loss of modulus and strength with increasing temperature are due to the increased mobility of the PS domains rather than to the softening of the PS blocks. They too noticed the Mullins/ stress-softening effect and that a residual strain remains when the sample is unloaded. They

attributed these two effects to the destruction of a continuous PS phase. Brunwin et al. were also the first to notice a difference in the stress-strain behavior of 52 wt%S SBS samples cast from different solvents, which they attributed to differences in arrangement of the PS domains (i.e., morphology). They also found that the SBS polymers underwent creep, being more pronounced at higher temperatures, but that the samples retracted to within 40% of their original length upon unloading. From this they postulated that the creep was due to the delayed segmental mobility of the chains rather than from permanent flow.

Beecher, Marker, Bradford, and Aggarwal (1969) studied the mechanical behavior of both compression molded (biaxially oriented) and solution cast (polygranular isotropic) SBS (Kraton 101, 28 wt%S SBS, but 27 wt% SB diblock). They studied the effect of casting solvents on the mechanical behavior of solution-cast samples, based on a previous study which suggested that the mechanical behavior of films cast from a tetrahydrofuran/methyl ethyl ketone (THF/MEK) mixture were different from those cast from a benzene/heptane mixture (Livigni, Marker, Shkapenko, Aggarwal,1967). Samples were cast from a THF/MEK mixture (solvents for both PS and PI or PB), a benzene/heptane solution (solvents for both PS and PI or PB), and carbon tetrachloride (a mutual solvent for two phases). DSC measurements suggested that samples cast from THF/MEK were highly phase separated, while those cast from CCl_4 were phase mixed, and those cast from benzene/heptane were intermediately phase separated. The stress-strain behavior of the highly phase separated samples cast from THF/MEK showed necking and drawing behavior and a stress-softening/Mullins effect on subsequent stretches, both of which were attributed to PS structures having been broken upon the first drawing. However, they found that whatever change in the structure occured upon the first stretch was reversible upon annealing at high temperature. The stress-strain curves from the somewhat-phase-separated benzene/heptane-cast films showed no yielding nor a region of cold drawing (i.e., rubbery behavior). Samples cast from CCl_4 showed mechanical properties characteristic of a leathery polymer close to its damping maximum (i.e., a more homogeneous, phase mixed material). It could hence be inferred that the mechanically robust elastic-plastic behavior of the block copolymers was due to the degree of phase separation.

The Beecher et al. (1969) study was also the first with TEM of SBS samples in both the stretched and unstretched states. Ultrathin (500-800 Å thick) solution-cast and compression-molded films were first stretched and then stained with OsO4 to provide contrast in the microscope. Beecher et al. interpreted their micrographs with spheres as the basic structural unit, with or without interconnections between the spheres (even though

today we expect the morphology of a 28 wt% S SBS sample to be PS cylinders in a PB matrix). Because of this difference, their interpretations of the micrographs of the stretched specimens may be somewhat suspicious. They suggested that with increasing stress the connected PS domains break up into elliptical domains, which further deform either by ductile rupture or by pullout of the PS chains. Nonetheless, this work pioneered the concept of TEM of deformed specimens as direct insight into the deformation mechanisms.

Possible tensile deformation mechanisms in block copolymer morphologies include 1) ductile failure in the PS domains, 2) brittle failure in the PS domains, or 3) elastic failure in the PB or PI center blocks (Quirk and Morton, 1996). Overwhelming evidence of the first mechanism was provided by three studies (Smith et al., 1969; Smith, 1970; and Morton 1983), which will be reviewed next.

Smith and Dickie (1969) studied the tensile behavior of compression-molded Kraton 101 and attributed the difference between the first stretch and subsequent stretches to "plastic" deformation of the PS domains upon the first stretch. They clarified that the use of the term "plastic" or "ductile" deformation referred to the extension of a hard material beyond the yield point. They mentioned that "as is well known" such deformation is often completely recoverable either at long times or high temperatures, but refrained from postulating molecular mechanisms for such plastic deformation. They mentioned that the residual strain of the slow-recovering PS domains would keep the rubber in tension such that the stresses are lower upon the second stretch. Smith (1970) later proposed that, as with crazing, PS can exhibit ductility on a microscopic scale, such as within the microdomains found in block copolymer morphologies. The mechanisms that he indicated by which a stretched and unloaded specimen could recover its original domain configuration after any PS domains had ruptured were due to the internal stresses of the PB matrix. He notes that at room temperature, such a recovery process is quite slow.

Morton (1983) reported his experimental observations on factors governing triblock copolymer behavior. He found that after the degree of phase separation, the T_g of the end blocks influence the tensile strength the most. He too observed that the amount of residual strain of stretched samples increased with increasing styrene content and strain to which the sample was stretched, which supported the existing theory that the stress is absorbed via distortion of the PS domains (Morton, McGrath, and Juliano, 1969; Smith and Dickie 1969). Even further evidence for such a mechanism was provided by comparing the stress-strain behavior of poly-α-methylstyrene-polyisoprene-poly-α-methylstyrene (mSImS) triblocks with the SIS analogs. He found that the mSImS triblocks, whose

endblocks have a higher T_g than PS, exhibited a higher modulus and higher stresses at all elongations, presumably due to the higher forces necessary to deform the hard domains.

These early studies brought forth many of the basic concepts of block copolymer mechanical behavior and important observations. A summary of these ideas as well as an inspection of some of the mechanical properties of DG will now be presented in light of the ideas introduced above.

7.2.2 Mechanical Properties of DG Triblock Copolymers: Discussion

DG SIS block copolymers are of similar constitution and have structures of similar length scales as the classical morphologies reviewed in section 7.2.1. The behavior of these nanocomposites can then be categorized as either properties due to the general block copolymer constitution or to behavior characteristic of the morphology. In this section the observations and behavior of DG attributable to general block copolymer mechanics will be discussed with respect to the fundamental concepts presented in section 7.2.1.

Yielding

In a generalized stress-strain curve, a material deforms elastically until it undergoes yield, or "plastic deformation". As was discussed by Smith and Dickie (1969), "plastic" deformation refers to the stretching of a hard material beyond yield. In polymeric materials, plastic deformation may occur by such mechanisms as necking, crazing, shear-banding, brittle failure, and/or molecular re-orientation of chains. (Several theories exist on the molecular origin of yielding in polymers, but the issue of it being a free-volume effect or a glass-transition effect is beyond the scope of this thesis.) In the samples stretched in the [111] and in the isotropic sample, yielding occurs by formation of a neck. As was postulated by Smith (1970) yielding is probably due to the ductility of the continous PS domains.

Load Drops in Tension

There are two phenomena which can produce load drops in tension, one being purely mechanical or geometric in origin, and one with a material basis. In tension, if the strain hardening rate is low and the plastic resistance is high, then the load will drop upon yielding. This geometric phenomenon is associated with loading in tension only, and as such, would be eliminated by using a compression geometry. The material phenomenon is associated with yielding of an aged glassy polymer and occurs regardless of testing geometry. An initially high force is necessary to either create "free" volume for molecular mobility or to initiate plastic flow. These samples are annealed/aged for 2 weeks above Tg

before being tested such that either stretching or compressing will invoke the material response. Since all of the samples are stretched in tension, the material response and any mechanical response will be overlapped without distinction.

Sharp Yield vs. Distributed Yield

Polygranular / isotropic DG samples and the oriented samples stretched in the [111] exibit sharp yield points, both in the stress-strain curves and as can be discerned in the sample during stretch (see figure 7.1 or 7.2). In contrast, the samples stretched in the transverse direction exhibit less of a distinctive yield point (figure 7.4) and they appear to deform uniformly to the eye. A sharp yield as exhibited on the stress-strain curve is indicative that all elements within a volume or subvolume yield simultaneously. A stress-strain curve which exhibits "no yield" or distributed yield (one which gradually changes slopes such that a distinct yield point cannot be identified) is indicative that there are highly variable stress concentrations in the sample due to different orientations and/or grain structures. In these distributed-yield samples, yielding is very local -- the fraction of volume undergoing yield at a given macroscopic strain is very small such that a distinct yield point for that element will not be seen. This contrast in yield characteristics already points to a different mechanism of deformation between the [111] and transverse directions. TEM of deformed samples, as will be presented later, can give more insight into the mechanisms of deformation in the two directions.

Necking

Necking behavior, as was mentioned in section 7.1.2, is defined as "a maximum load followed by nonuniform deformation" (McClintock and Argon, 1966; Ward 1975). A sample which necks may be observed to have a decreased cross-sectional area in a localized length of the sample, as shown in figure 7.3.

Geometrical Phenomenon

For a generalized material, a neck forms when the strain localizes either at an area with an inhomogeneity or an area where there is a fluctuation in sample properties such that the local yield stress is lowered. The sample cross-sectional area in such a region is effectively smaller than the rest of the sample, resulting in stress across this area greater than in the surrounding areas. A region with lowered yield stress will yield at a lower load and deform faster than the surrounding regions, thereby creating a localization in the strain.

If the material in the neck does not undergo strain hardening, then this region will subsequently deform at a faster rate than the unnecked regions (because it has a higher stress), and the sample eventually breaks in two. However, if the area in the neck

sufficiently strain hardens, then the stress required to deform this strain-hardened area becomes higher than the stress currently in the sample, and the neck is stabilized.

Material Phenomenon

For block copolymer morphologies, necking is a phenomenon associated with continous PS domains, as the phenomenon is absent in samples in which PS is discrete (e.g., spheres) but is most prominent in samples in which the tensile stretching axis is oriented along continuous PS domains. Necking, then, can be identified with the initiation of flow in the PS domains.

In the DG materials, both polygranular/isotropic samples and oriented samples stretched in the [111] direction sufficiently strain harden and exhibit a stablized neck, as can be observed both visually and by the plateau region in the stress-strain curve after the initial drop in load of yielding. The upturn of the stress-strain curve after the neck has propagated through the entire gauge length is another indication that the samples strain harden. Oriented samples stretched in the transverse direction show distributed yield (as noted above) and therefore do not neck.

Strain Hardening

In some polymers, strain-hardening leads to the phenomenon of cold drawing in conjunction with necking. Strain hardening in polymers can arise from 2 sources: 1) strain-induced crystallization, and 2) an increase in the stiffness along the stress direction as the material orients along the stress axis.

Strain-induced crystallization requires great stereoregularity along with molecular mobility for the reorganization of the chains. Upon elongation, either cis- or trans-polyisoprene can crystallize if they occur in sufficient block lengths. However, in the anionically polymerized PI in these DG samples (as well as in other block copolymer morphologies), the chain microstructure gives rise to a mixture of both cis and trans isomers (70% cis, 20% trans, 10% 3,4 and 1,2) (Avgeropoulos, Dair, Hadjichristidis, and Thomas, 1997), but not in any considerable block length to allow either the cis- or the trans- to cause crystallization upon elongation. (Fetters: private communication). Thus, in these samples, strain hardening cannot not due to the strain-induced crystallization.

Rather, then, the stabilized neck is due to the increase in stiffness of the oriented material which requires higher stresses to deform. In the cold drawing process, a neck forms within the cross-sectional area containing an instability at a stress necessary to cause flow in the PS and to align PS and PI chains in the small volume. The material in the neck elongates to the composite's natural draw ratio. Because of the molecular orientation of both the PS and the PI chains, the necked material has a higher stiffness than the unnecked

material, and a further increase in the strain of the strain-hardened material (beyond the natural draw ratio) requires a much higher stress than is present in the necked material. Therefore as the strain is increased further, unoriented chains on the shoulder of the neck become aligned at the same macroscopic level of stress and are drawn into the neck. The cold drawing phenomenon is exhibited in the stress-strain curve by a plateau region (after the load-drop due to neck formation), which terminates at a strain indicative of the natural draw ratio of the material.

Once the neck has propagated far enough to engulf the entire gauge length (i.e., after all of the polymer within the gauge length has been stretched to the natural draw ratio of the composite) further deformation of aligned chains is only achieved by one of three mechanisms. Deformation can occur by pulling on or breaking entanglements in the diene phase, by further molecular orientation in either (or both) of the PS or PI domains, or at the extreme, by deformation of the C-C bonds and angles inbetween. All of these mechanisms require increasingly higher and higher stress, which exhibits itself as an upturn in the stress-strain curve.

Plasticity of the PS domains

Bulk PS crazes when stretched in tension. A craze is the area of deformed material around the area of a crack continaing 50% oriented or elongated polymer "fibrils" and 50% void volume. Kambour (1964; Kambour and Holik, 1969; Beahan, Bevis, and Hull, 1971,1973; Kambour and Russell, 1971. These fibrils are cylindrical in shape and contain highly elongated chains. The natural draw ratio of PS craze fibrils in air is about $\lambda = 4$ (Lauterwasser and Kramer, 1979; Donald, Kramer, and Bubeck, 1982), and the diameter of a fibril is about 4-10 nm, with an average value of 6 nm (Brown and Kramer, 1981; Donald et al., 1981, 1981).

The struts of the DG nanocomposites studied here, having diameters of ~7 nm (70 Å), are on the length scale of a craze fibril such that normal crazing or shear banding mechanisms of the PS domains cannot occur. Rather, the PS struts themselves, which are surrounded with rubbery PI, will not mimic that of bulk PS, but rather, be more viscoelastic in character and sample the same plasticity as sampled by the PS in craze fibrils.

In addition, the molecular weight of the end PS blocks (14 kg/mol) are much less than the entanglement molecular weight of PS (35 kg/mol). At 600% strain, pullout of the PS chains may occur, especially if the behavior of the PS domains is viscoelastic and the PS chains are now susceptible to flow. Under certain conditions, some struts may draw down to become separate pieces.

Mullins Effect, Hysteresis, and Residual Strain

As with the classical morphologies, Mullin's or stress softening effect, hysteresis, and residual strain are observed in the stretches of these samples in different directions. These effects were first attributed to the breakage of the continous PS domains (Brunwin , Fischer, and Henderson, 1969; Fischer and Henderson, 1969; Fujimura, Hashimoto, and Kawai, 1978; Holden and Legge 1996). However, voiding and flow, which were not initially considered, both provide explanations for the sample not returning to its original dimensions. In addition, the factors of microyielding and plasticity of viscoelastic PS domains were not considered. These latter mechanisms do not create permanent flow, but rather cause slow recovery. Each of these possibilities will be now considered.

Voiding

In the SAXS patterns of stretched samples, streaks occur both above and below the equator, but not through the equator, indicating that voiding does not occur in the samples, even when stretched to 600% strain. (It should be mentioned, though, that in some stretches where the sample width becomes smaller than the beam at high strains, streaking will occur through the center from scattering off the edge of the sample. Streaks through the center do not occur in samples in which samples are wider than the beam at all strains.)

Flow

Unrecoverable residual strain is characteristic of uncrosslinked or unentangled polymers in the rubbery regime, of systems which have undergone permanent deformation (crazing, shear banding, voiding), or of systems which have undergone irreversible processes. However, with the samples that we study here, any residual strain is recoverable upon annealing above Tg, indicating that the samples did not undergo flow.

Viscoelasticity

In some instances, plastic deformation is a consequence of anelasticity or of long-time-scale viscoelasticity, but is not permanent. At long times or high temperatures, the plastic deformation may be found to be recoverable. In the materials studied here, the samples both microscopically and macroscopically return to their original states upon annealing. The SAXS patterns after annealing are almost identical to the pattern at start; long range order was restored (as seen by the number of higher order harmonics) and all original Bragg peaks returned to the same q's. These facts indicate that the microscopic structure of the interpenetrating networks has complete memory and is recoverable. In addition, samples return to their original dimensions when annealed, indicating full macroscopic recovery. Any pullout of the chains in the plastically deformed PS domains,

which are not entangled (MW < MWe), can diffuse back to an equivalent state such that the PS domains have the equilibrium dimensions as dictated by the surrounding PI.

It can then be inferred that the entangled PI chains provide the retractive force and memory for unloading. Due to these internal stresses of the PI matrix, a stretched and unloaded specimen can recover its original dimensions and initial domain configuration after any PS domains have ruptured. This recovery mechanism was first postulated by Smith (1970).

The viscoelastic properties can also explain the Mullins effect and hysteresis. The entangled PI chains provide the retractive force and memory for unloading, but as was mentioned by Smith and Dickie (1969), the residual strain of the slow-recovering PS domains keep the rubber in tension. This causes a lowering of the stresses upon the second stretch. It should be mentioned, that this complete recovery is not a general phenomenon of materials, but rather a special property of these triblock copolymer elastomers. It was even noticed in the early studies that upon annealing, the samples recover their original dimensions (Brunwin, Fischer, and Henderson, 1969; Smith and Dickie, 1969). This implies that the samples are viscoelastic. Although the times scales for complete recovery are long, they can be accelerated with temperature similar to the time-temperature superposition principle. (Time-temperature superposition principles and techniques, however, cannot be applied formally to these types of samples. The technique involves a reference temperature related to the Tg of the polymer, but these triblock copolymer composites have two, rather than one Tg.) Indeed some early research was done to fit shift factors to the time-temperature viscoelastic behavior (Smith and Dickie, 1969; Smith, 1970; Holden, Bishop, and Legge, 1969).

The Mullins effect, hysteresis, and residual strain were noticed to be more pronounced at higher styrene contents in the classical morphologies of cylinders and lamellae. The strengths of these effects are another way of determining or obtaining insight into the continuity of the original PS connectivity in a given direction, and of the amount of irreversible work (i.e., work not recovered immediately upon unloading) that was done during the initial stretch.

Ramifications for Future Applications

It can then be concluded in these materials, that within a given composition window for a given morphology, that as long as 1) the PS chains are high enough in molecular weight for phase separation and 2) the diene material is above the entanglement molecular weight Me, then the mechanical properties doesn't change much by increasing further the molecular weight. Indeed, very high molecular weights (>100-120 kg/mol) will become

rather difficult to process, as viscosity increases by $M^{3.4}$. As was mentioned in Morton (1983), flow properties involve moving phases through one another, which in turn involves the heat of mixing, such

In DG materials, consideration to the upper limit of molecular weight should not only be given to the viscosity, but also to the stability of the DG phase at high molecular weights (and hence high XN). It was shown in section 5.4 that even at molecular weights of 124,000 g/mol, the DG was losing stability, as the morphology was bi-phasic DG and cylinders, with the predominant phase being cylinders. Phase stability studies to determine the molecular weight boundaries of the material are required, if molecular weights higher than ~80 kg/mol are required.

It is inevitable in DG materials that one of the deformation mechanisms is chain pullout and drawing down of the PS domains. Since Me of PS is about 17-18k (measured from DMA loss compliance) (Ferry, 1980), molecular weights of 100,000 - 120,000 are necessary for the PS phase to be entangled. Therefore, with the molecular weights available for DG, the PS chains will not be entangled.

7.3 Deformation Behavior of Polycrystalline Isotropic DG

Now that the basic concepts of block copolymer mechanical properties has been discussed, it will be interesting to compare the morphological response of the DG with that of the classical morphologies. We first compare DG stress-strain data with data from the 3 classical microdomain structures where all samples have an overall isotropic microstructure. The information thus gathered will then provide impetus for studying oriented systems in order to learn more about the details of the deformation.

7.3.1 Stress-Strain Behavior of DG Relative to the Classical Morphologies

By changing the relative amounts of the components in the block copolymer, different microdomain morphologies can be achieved. The mechanical behavior of thermoplastic elastomer triblocks with the classical microdomain morphologies of spheres (Beecher et al., 1969; Inoue, Moritani, Hashimoto, and Kawai, 1971; Richards and Welsh, 1995; Brandt and Ruland, 1996; Prasman and Thomas, 1998) cylinders (Pedemonte Turturro, and Dondero, 1974; Odell and Keller, 1977; Tarasov, Tsvankin, and Godovsky, 1978; Hadziioannou, Mathis, and Skoulios, 1979; Honeker and Thomas, 1996; Honeker, 1997), and lamellae (Fujimura, Hashimoto, and Kawai, 1978; Thomas and Albalak, in preparation; Seguela and Prud'homme, 1981) have been investigated extensively. These morphologies have discontinuous, 1-dimensionally continuous, and 2-dimensionally continuous glassy reinforcing phases, respectively, embedded in a rubbery matrix. To date there have been only two preliminary conference reports concerning the large strain deformation behavior of the DG microdomain structure (Dair, Prasman, Capel, and Thomas, 1997; Dair, Thomas, Avgeropoulos, Hadjichristidis, and Capel, 1998). However, a previous small-strain dynamic mechanical analysis (DMA) study of thermoplastic elastomeric glassy-rubbery multiarm stars with randomly oriented domains (Alward, 1985; Kinning, Thomas, Alward, Fetters, and Handlin, 1986) showed that the room temperature storage modulus of a 6-arm star with an equilibrium 3-dimensionally bicontinuous morphology, later shown to be DG Hajduk et al. (1995), was ~10X higher than the that of the 5 arm star, which has an equilibrium cylinder morphology, but both having the same overall composition (30 volume% glassy phase). In addition, Sakurai et al. (Sakurai, Sakamoto, Shibayama, and Nomura, 1993) investigated the mechanical properties of a 56 wt% S SBS (B=polybutadiene) triblock with a chaotic bicontinuous microdomain morphology and found yielding accompanied by necking.

The simplest deformation studies are those on solution-cast isotropic polygranular materials. The stress-strain behavior of the different morphologies will be discussed first to compare the behavior of DG to the classical morphologies.

Figure 7.7a and b show the stress-strain curve of polygranular isotropic double gyroid morphology along with curves from isotropic thermoplastic SIS elastomer samples of the classical microdomain morphologies. All samples were prepared using the same procedures. Figure 7.7a shows the curves to 600% strain, and figure 7.7b is an enlargement of the curves to 100% strain. The different morphologies are realized by changing the triblock composition and occur at lower and higher volume fraction minority phase than the DG.

It is interesting to note that the isotropic DG sample exhibits necking as can be discerned visually and through the shape of the stress-strain curve, but the cylinder and even the lamellar samples do not. In figure 7.7a, the DG stress-strain curve necks and draws, characteristic of continous PS domains throughout. The stress-strain curve of the cylinder sample is reminiscent of an elastomer and exhibits no distinct yield point. The DG morphology has enhanced modulus and yield strength over that of the cylindrical morphology, even though the compositions are quite comparable. This result agrees with the preliminary results of Alward et al. (1985), where a star-block copolymer having an ordered bicontinous structure (now believed to be DG) exhibited yielding and necking behavior and had higher tensile strengths at all stresses above those of a triblock having cylinder morphology (as shown in figure 2.6).

Most surprising, however, was that the lamellar morphology does not exhibit necking. The lamellar stress-strain curve indicates that this sample has a more distinct yield point than either the cylinders or spheres, and of the four morphologies, the lamellae does have the highest modulus due to the increased PS content. However, both the stress-strain curve and visual inspection reproducibly indicate that the lamellar samples do not undergo necking and drawing phenomenon. It will be later discussed that *oriented* samples stretched in the plane of lamellae exibit necking.

In the literature most studies on lamellae have been on samples which were processed to have preferred orientation, whether uniaxial or biaxial (Childers and Kraus,1967; Holden and Bishop, 1969; Fujimura, Hashimoto, and Kawai, 1978; Hashimoto, Fujimura, Saijo, Kawai, Diamant, and Shen, 1979), and thereby exhibit necking and drawing. Séguéla and Prud'homme (1981) Seguela and Prud'homme (1981) asserts that SBS and SIS triblocks with styrene contents between 30-60 wt% exhibit necking, but the papers used to reference them either did not show necking (Pedemonte and Alfonso, 1975) on simple-cast 30%S SBS; Fischer et al. (1969) on simple cast 40 wt% S SBS) or had preferred orientation (Hashimoto et al., 1979) and indirectly (Fujimura , Hashimoto, and Kawai , 1978), both of which show necking stress-strain behavior in spin-cast 48%S SBS).

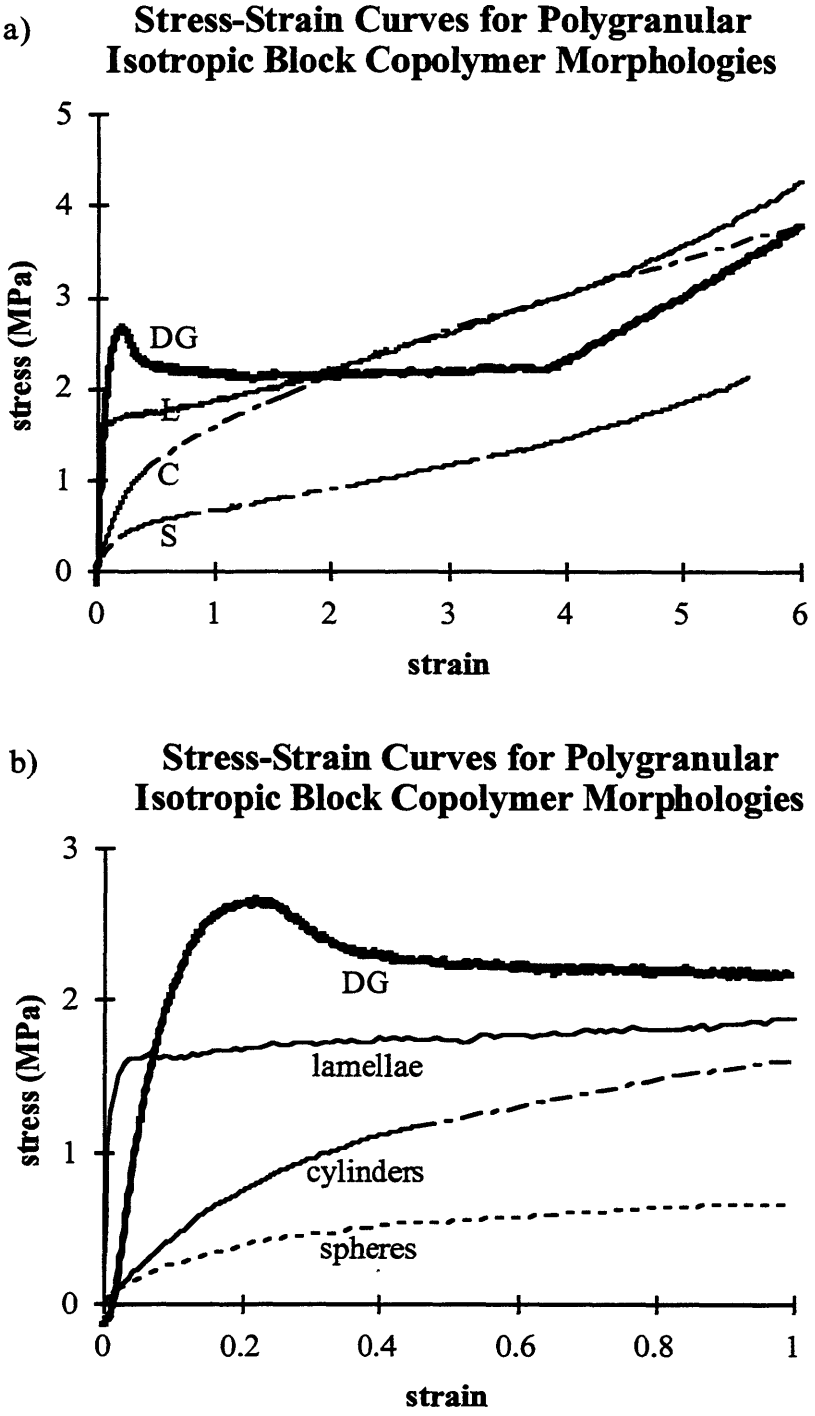

Figure 7.7: Stress-strain curves of isotropic DG (bold), overlayed with the classical morphologies of spheres (18% S SIS, block molecular weights 11.5 / 105 / 11.5 kg/mol, denoted "S"), cylinders (30% S, block molecular weights 14.5 / 68 / 14.5 kg/mold, denoted "C"), and lamellae (45% S SIS, block molecular weights 18 / 44 / 18 kg/mol, denoted "L"). The polymers are commercially available from the Dexco company. a) Stress-strain behavior to 600% strain. b) Stress-strain behavior to 100% strain. The curves of the classical morphologies were kindly provided by C. C. Honeker.

In fact, necking seems to be absent in stress-strain curves reported in studies of simple-cast lamellar-composition samples. Henderson et al. (1968) and Fischer and Henderson (1969) report on behavior of SIS polymers cast from toluene, MEK, and heptane. The stress-strain curve of the lamellar sample in figure 7.6 above mimics that of the toluene-cast samples having 40, 49, and 52%S (i.e., no necking behavior is observed).

As expected, the modulus of the morphologies increases with increasing PS content as can be discerned from the slopes of the initial deformation, and as expected, the lamellae have the highest modulus. Therefore, the necking - non-necking behavior of the stress-strain curves is not due to the PS content (as the morphologies with PS contents above and below that of DG both do not exibit necking). Rather, the necking behavior, which is indicative of continous PS phases, is an effect of the morphology only.

As mentioned earlier, Childers and Kraus (1967) studied the mechanical properties of about 10 triblock copolymers. Of the compositions he studied were a 34 wt% S and a 36 wt% S SBS. To my knowledge, this was the only mechanical properties study using polymers having compositions for DG (a morphology then unknown). Unfortunately neither the equilibrium (simple cast) morphologies nor the stress-strain properties of these two polymers were investigated -- the 34 wt% S was used in stress-relaxation studies only, and the 36% S was used in mineral-oil-extended studies only.

7.3.2 Deformation Behavior of Polygranular Isotropic DG via SAXS

The synchrotron SAXS investigation of the deformation behavior of polygranular isotropic DG cast from toluene is presented in this section. Most other work on isotropic samples has been on lamellae Hendus, Illers, and Ropte, 1966; Hashimoto et al. (1979; Seguela and Prud'homme 1981), and some on spheres (Inoue, Hashimoto, and Kawai, 1971; Richards and Welsh, 1995).

Figure 7.8 shows a typical stress-strain curve of quiescent cast, isotropic double gyroid, with accompanying SAXS patterns at different points along the deformation. The mechanical properties are listed in Table 7.1. The tensile modulus is approximately 30 MPa. Yield occurs at approximately 20% strain and approximately 2.6 MPa, accompanied by formation of a distinct neck. The hysteresis in the stress-strain curve is approximately 50%, and a Mullins effect is observed. As mentioned in section 7.2, these features suggest either a slow recovery of the plastically deformed PS domains.

Yielding

The SAXS pattern before the deformation begins is shown in figure 7.8 and consists of an isotropic ring pattern of the double gyroid with the characteristic {211} - {220} doublet. Upon loading, the higher order rings fade, and the remaining inner-most diffraction peaks become elliptical from the strain. At ~15% strain, necking occurs, as indicated by the drop in the stress-strain curve, by visual detection of a reduced area, and by the abrupt change in the nature of the scattering pattern; the characteristic isotropic rings are replaced by a pair of streaks elongated along the normal to the stretching direction. Upon further elongation the ring completely disappears and only the streaks remain. At nominal strains higher than this the pattern does not change until the neck has propagated across the entire gauge length of the sample. Once the neck has encompassed the entire gauge length, the strain in the yielded material begins to increase. The streaks in the SAXS pattern become somewhat sharper and more elongated, but the nature of the pattern does not change.

The pattern at yield shown in figure 7.8 captures the event right before the abrupt change from rings to streaks and shows the superimposed ring of yet unyielded material on the horizontal streaks.. To further investigate the yielding process in the isotropic samples, a sample was stretched in the mini tensile stretcher until a neck formed (~15% strain) and was allowed to propagate until the nominal strain in the sample was about 50%. Figure 7.9 shows the SAXS patterns along the transition from unnecked material to the necked material. Note that in the unnecked region, the sample pattern still consists of circles, but as the necked region is approached, there are fewer higher order rings in the pattern, and the rings have become elliptical. The ellipses are characteristic of a small strain in the sample volume which is not large enough to cause yielding. In dynamic stretches it is also noticed that before necking the rings become elliptical, but at the moment when a neck is formed in another part of the sample, the rings in unyielded areas become once again circular as the strain in the unyielded area has been relieved through localized deformation.

As was mentioned in section 7.2, necking is a general characteristic of samples which have continuous PS domains in the direction of stretch. Figure 7.9 show that in the region of the material where the unnecked material transitions to necked material, the lobe pattern forms while the rings are still there, the rings fade out in conjunction with the lobe pattern developing. This indicates that there are regions of yielded material co-existing with regions of unyielded material. Areas which are oriented with high PS connectivity along the tensile direction will yield first, giving rise to distributed yield. The neck is also drawing unyielded material into the yielded portion such that in the transition, both types of materials give their characteristic scattering pattern.

An analysis of the elliptical {211} ring at yield in figures 7.8 and 7.9 indicates that just before necking the sample has deformed +4.3 ± 0.7% along the tensile direction and -2.2 ± 0.4% in the transverse direction. It is noted that the local strain to yield is different from the yield strain defined by the strain at maximum load. The Poisson's ratio is calculated to be $\nu = -\frac{\varepsilon_{transverse}}{\varepsilon_{axial}} = 0.5$, that of an ideal rubber. The Poisson's ratio for the pure materials are $\nu_{PI} = 0.5$ and $\nu_{PS} = 0.33$ (both values from (McClintock and Argon, 1966)). The calculated Poisson ratio within the sample indicates that up until yield of the polygranular DG, the rubbery material is carrying the deformation.

Seguela and Prud'homme (1981) studied with SAXS the deformation behavior of a simple-cast hydrogenated SBS triblock copolymer with 29 wt% S, which they found to have randomly oriented lamellar microdomains. They measured the variation of the width and thickness of along the length of a neck-transition specimen and found that the yielding process is carried by the extension and contraction of the rubbery phase.

Strain in the Necked Region

The strain in the necked region can be estimated several ways. The first is through measurements of the dimensions of the physical neck by the relation $\varepsilon = \frac{\Delta L}{L_o} = \frac{A_o}{A}$. However, as the samples usually have initial cross-sections of 1-2 mm x 1-2 mm, the dimensions of the neck are very difficult to measure accurately given the rubbery compressible nature of the samples between the faces of a micrometer.

The other measure of the strain in the neck is that value at which the stress begins to rise after the plateau. The strain in the neck is characteristic of the polymer's natural draw ratio and only when all of the sample has the same value of strain will the stress once again rise in the sample. When the neck has propagated across the entire gauge length, the strain is the same at all points and macroscopic elongation of the sample results in an increase in strain uniformly across the sample. Therefore the strain at which the stress begins to rise after the plateau is the strain which is characteristic of the neck. From figure 7.1 the stress of the isotropic sample begins to rise at a strain of about 375%.

Streaks in the Lobe Pattern

The streaks in the lobe pattern were measured for a characteristic spacing, from the origin to the layer line. At yield the streak measured q = 0.0054 from the origin, which corresponds to d_{yield} = 1200 Å. Compared to the characteristic d of the simple cast DG,

$\varepsilon = \frac{d_{yield}}{d_{211}} - 1 = 360\%$, which is about the strain as measured from the stress-strain curve. The strain was then determined from the streak "spacing" for the pattern corresponding to the sample at 600% strain as measured by the counts on the mini stretcher. The streak measured to be $q = 0.0035$ from the origin, which corresponds to $d_{600\%\varepsilon} = 1800$ Å, such that $\varepsilon = \frac{d_{600\%\,\varepsilon}}{d_{211}} - 1 = 710\%$, about the macroscopically measured strain. It should be mentioned, however, that the values of the streaks to the origin are estimated and such low values of q are subject to large errors, since a pixel difference at or near q~0.0035 could result in a 40% difference in strains and near q~0.0055 could result in a 20% difference in strains. However, it seems that there may be a correlation of the streak "spacing" to the amount of strain in the "(211) planes" of a yielded sample.

Unloading

Figure 7.8 shows that upon unloading, elliptical rings return, starting at approximately 300% strain. Upon fully unloading, the sample shown has a nominal 70% residual strain, but measurements from the elliptical ring pattern indicates that there remains +40% strain in the axial direction and -15% strain in the transverse direction. The disparity is likely due to the relaxation between the time when the nominal strain at zero load was measured and the time when the SAXS pattern was taken. The pattern of the stretched sample reannealed for 5 days at 120% is identical to the original, with long rang order restored, as indicated by the higher order rings. The spacing of the first ring, $q_1 = 0.0247$, is identical to that at start. Even more significant is that the dimensions of the stretched and reannealed sample return to those of the original pre-stretched state. This indicates that any mode of large strain deformation is fully reversible upon annealing at high T.

Deformation Mechanism

The necking phenomenon, along with the drastic change in the SAXS pattern within the necked region indicate that the PS domains deform, also postulated by Seguela and Prud'homme (1981) in a deformation study of unoriented lamellar microdomains. Their SAXS patterns suggest non-affine deformation of the grains and hence plastic deformation occuring in the neck region associated with disruption of the continuous PS domains, but at high deformations, the grains orient by rotation of the lamellar stacking axis, achieved by shearing of the layers, but without a rotation of the layers themselves. Hashimoto et al. (1979) and Fujimura et al. (1978) observed with TEM that lamellae form chevron structures at low strains, but that these structures break up into a chaotic morphology of discrete PS domains. In the DG samples discussed above, the complete

microscopic and macroscopic recovery after annealing above the T_g indicates that breakup into discrete domains probably does not occur, but rather plastic deformation and then drawing of the PS domains.

TEM of stretched isotropic samples were not done because of the difficulty of interpretation, as DG is a complex structure in the *un*deformed state.

Need for Orientation

Hendus et al. (1966) also showed TEM evidence of alignment of lamellar domains in stretched simple cast 38%S SBS films. Their SAXS patterns show rings at start, and then the lobe pattern for samples stretched to necking, returning to an ellipse upon full retraction. The general behavior of the SAXS patterns upon stretching and unloading are similar to that of DG. The behavior of isotropic samples do not provide much information regarding the deformation mechanisms of the morphology, save for orientation of planes toward the stress axis at large strains. Each grain in the randomly oriented sample has a different response to the applied stress. Because the deformation behavior of an isotropic sample is a superposition of different orientations, and because the SAXS patterns consist of rings and or streaks, little information about the response of the morphology can be obtained about the deformation. Samples in which the morphology is oriented, however, would allow the behavior of the morphology in a particular direction to be examined.

Deformation of Isotropic DG
Accompanying SAXS Views

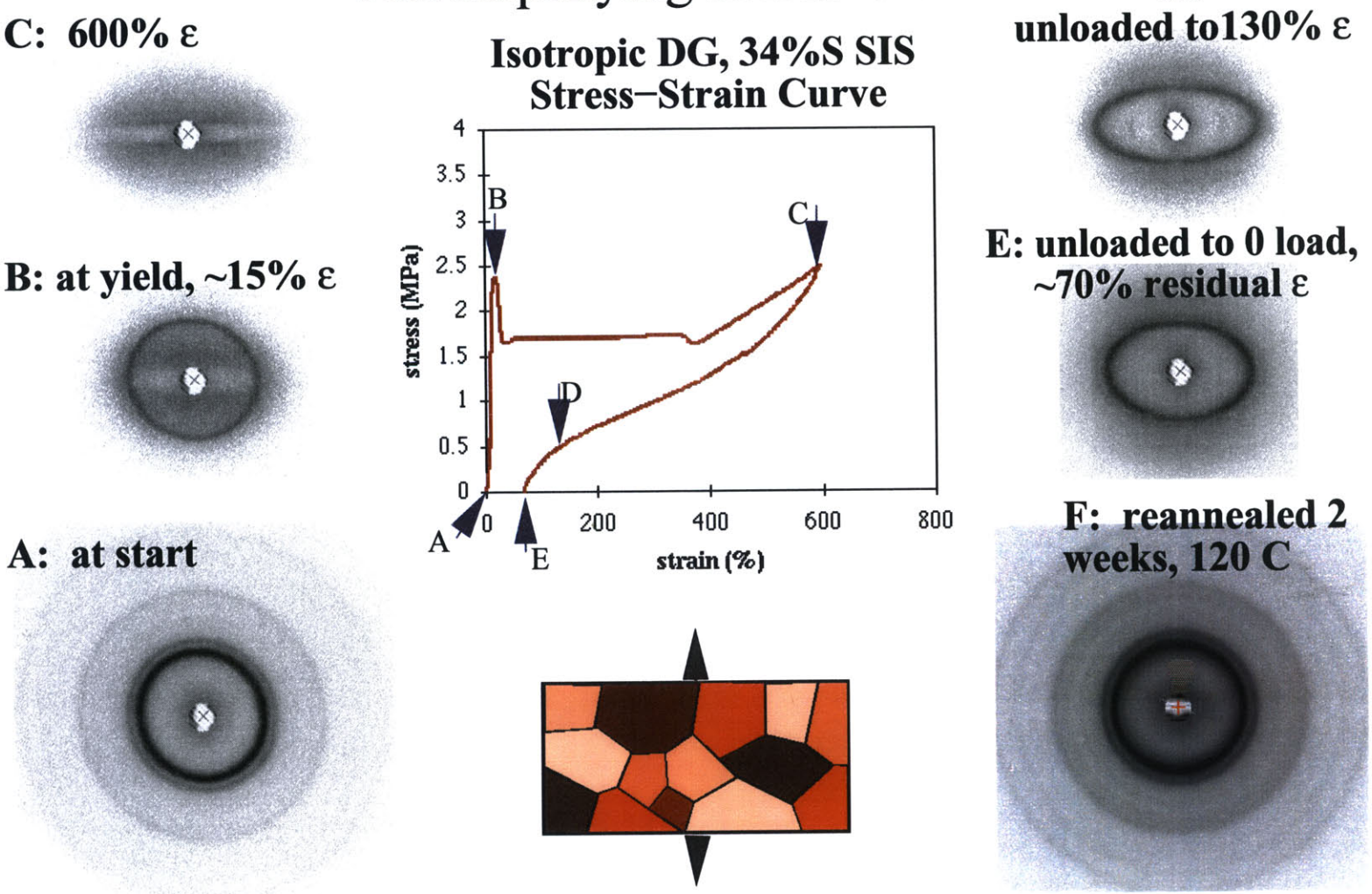

Figure 7.8: Stress–strain curve of an isotropic/polygranular 34%S SIS DG (center), with accompanying SAXS patterns.

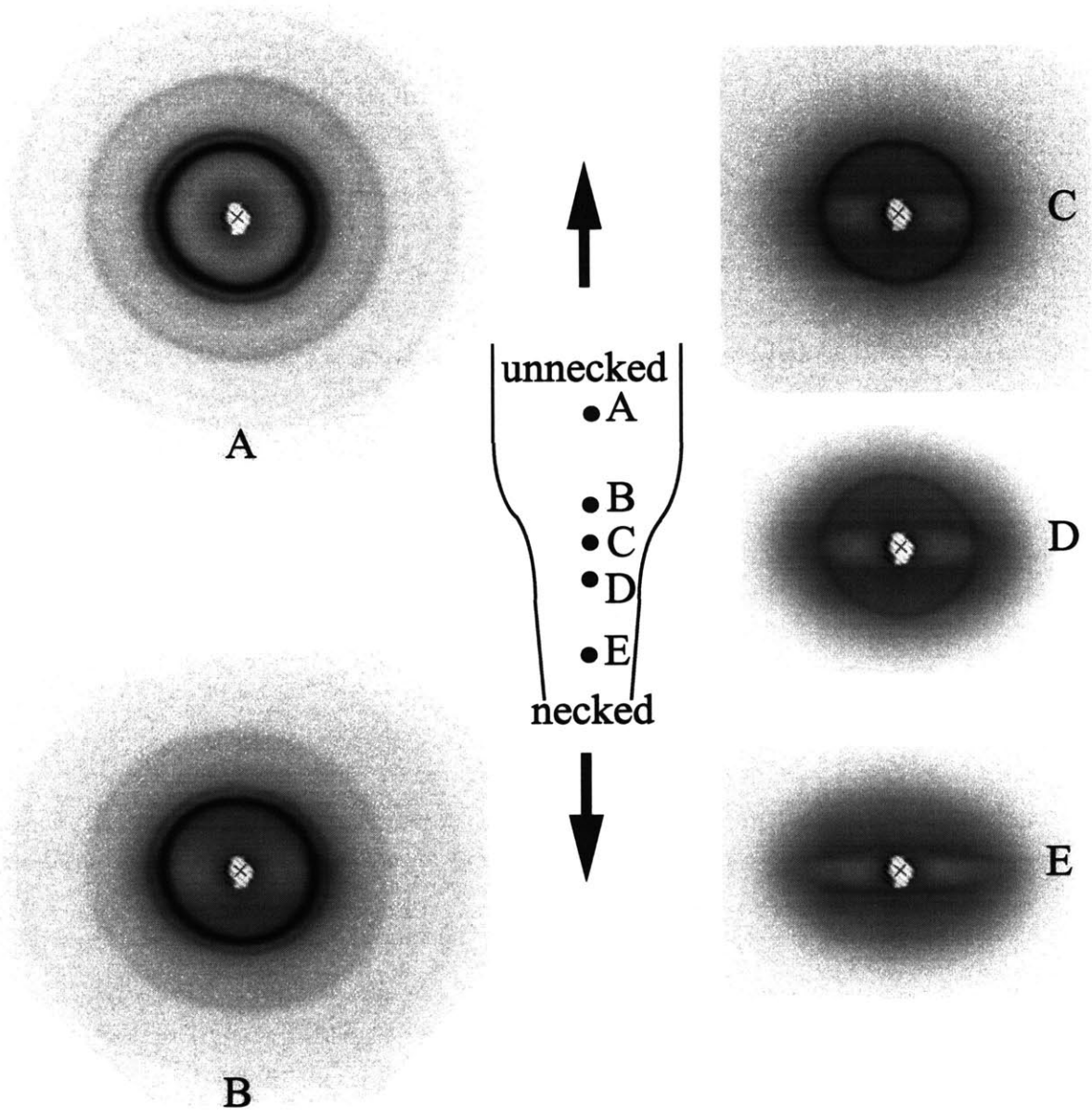

Figure 7.9: An isotropic 34%S SIS DG sample loaded to 40% total strain capturing the necking transition (schematic shown center), with SAXS patterns of different points along the neck transition. Point A is closest to unnecked material, while point E is in the necked region where the local strain is approximately 300–375%.

7.4 Orientation

Keller and associates were pioneers of studying the orientation and deformation behavior of block copolymers, mainly with cylinder morphologies, globally oriented via extrusion (Keller, Pedemonte, and Willmouth (1970); Folkes, Keller, and Scalisi (1973)). Odell and Keller (1977) used SAXS, TEM, and birefringence to study the deformation behavior of these oriented cylinders both parallel and perpendicular to the cylinder axes. They found the factor of anisotropy between stretching parallel and perpendicular to the cylinder axis to be 100. They found that stretching parallel to the direction of the cylinder axis resulted in necking at 3% nominal strain and drawing, wth the material in the neck having 80% strain. Using TEM they presented evidence for discontinuity or breakup of the cylinders, showing rodlets 70-110 nm in length. They also found that deformation perpendicular to the cylinder axis was affine up to 20% strain.

Tarasov, Tsvankin, and Godovsky (1978) were the first to study the large strain deformation of oriented cylinders via SAXS. They oriented their cylinders via press molding and subsequently stretched them both parallel and perpendicular to the cylinder axis. They interpreted their SAXS patterns in terms of break-up of the cylinders when stretched in the direction parallel to the axes, and deformation of the cylinders into chevron-like structures when stretched perpendicular to the axes.

Pakula, Saijo, Kawai, and Hashimoto (1985) also studied deformation of press-mold-oriented cylinders both parallel and perpendicular to the axes using 1D SAXS. Their interpretation, though questionable from their reconstruction of 2D SAXS patterns from 1D data, stated that stretching oriented cylinders both parallel and perpendicular to the axes resulted in the same "universal high deformation state" of broken cylinders in a chevron structure.

Honeker (1997) made in-depth studies of the deformation mechanism of roll-cast-oriented cylinders stretched perpendicular to the cylinder axes using a combination of in-situ synchrotron SAXS and TEM. He interprets the deformation to be cooperative bending of the PS rods into chevrons with characteristic length scales of microns, in order to rotate their long axis toward the stretch axis.

Only one study (to date) has been done on the deformation mechanisms and behavior of oriented lamellae. Albalak, Cohen, Dair, and Thomas (1999) have also used in-situ synchrotron SAXS and TEM to study roll-cast-oriented lamellae deformed both perpendicular and parallel to the lamellar layers. They too find that stretching parallel to the layers results in break-up of the continuous PS layers at high elongations, and stretching perpendicular to the layers results in bending of the layers into chevron-type structures.

It is with these results that the deformation behavior of the DG stretched in the different directions will be interpreted. It is fortunate that high resolution synchrotron SAXS and TEM can be coupled, such that a clear picture of the deformation mechanisms and changes in morphology can be tracked as a function of strain.

7.5 Deformation of Oriented DG in the [111] Direction

The mechanical properties are listed in table 7.1. The tensile modulus along [111] is approximately 50 MPa, considerably higher than the isotropic case. Yield occurs at approximately 15% strain and approximately 3.4 MPa, accompanied by formation of a distinct neck as in the case of isotropic DG. The hysteresis in the stress-strain curve is approximately 65%, higher than that of the isotropic sample, and a strong Mullins effect is observed. As mentioned previously in section 7.2, these features suggest either a slow recovery of the plastically deformed and elongated PS domains and grains or that the PS networks break when stretched beyond the yield point.

7.5.1 Geometry of the [111] Direction

To better understand the deformation of the [111] direction, the detailed geometry of the DG structure will first be discussed. Figure 7.10a shows a cross-sectional area normal to the [111] direction (i.e., the (111) plane) of the DG. The area outlined by the hexagon is the base of the cell in this plane, such that a prism built on such a base would encompass the same volume as that of the cubic unit cell based on the usual set of {100}-type planes. The DG consists of two screw axes and one inversion axis per unit translational unit in the (111) plane. The 3_1 and 3_2 screw axes contribute to the reinforcing mechanical properties of the DG in the [111] direction, but the $\bar{3}$ axes do not.

Figure 7.10b shows side views of the DG [111] prisms having the hexagonal base shown in figure 7.10a. The DG prism spans 6 struts in the [111] direction and is $\sqrt{3}$ a high (where "a" is the DG lattice parameter), which is the fundamental translation along this direction. The total volume encompassed in the prism is a^3, i.e., the same as that of a unit cube shown in figure 2.2. On the corners of the prism sit 3_1 and 3_2 screw axes (of alternating handedness), which form tight helices (likened to a stretched-out spring), each consisting of 6 struts, each strut angled at 35° from the [111] axis, but connected to one another along the [111] direction. Running through the center of the DG prism (as shown in figure 7.10b) is the $\bar{3}$ axis, which consists of 4 nodes (alternating between the two networks) stacked in the [111]. The nodal planes are perpendicular to the [111] axis and are not connected along the [111] direction; in fact, each node moves along the [111] direction according to the 3_1 or 3_2 helices to which they are connected when the material is

deformed in the [111] direction and are not themselves stretched by the tensile stress. Hence the $\bar{3}$ axes do not contribute to the reinforcement of the [111] direction.

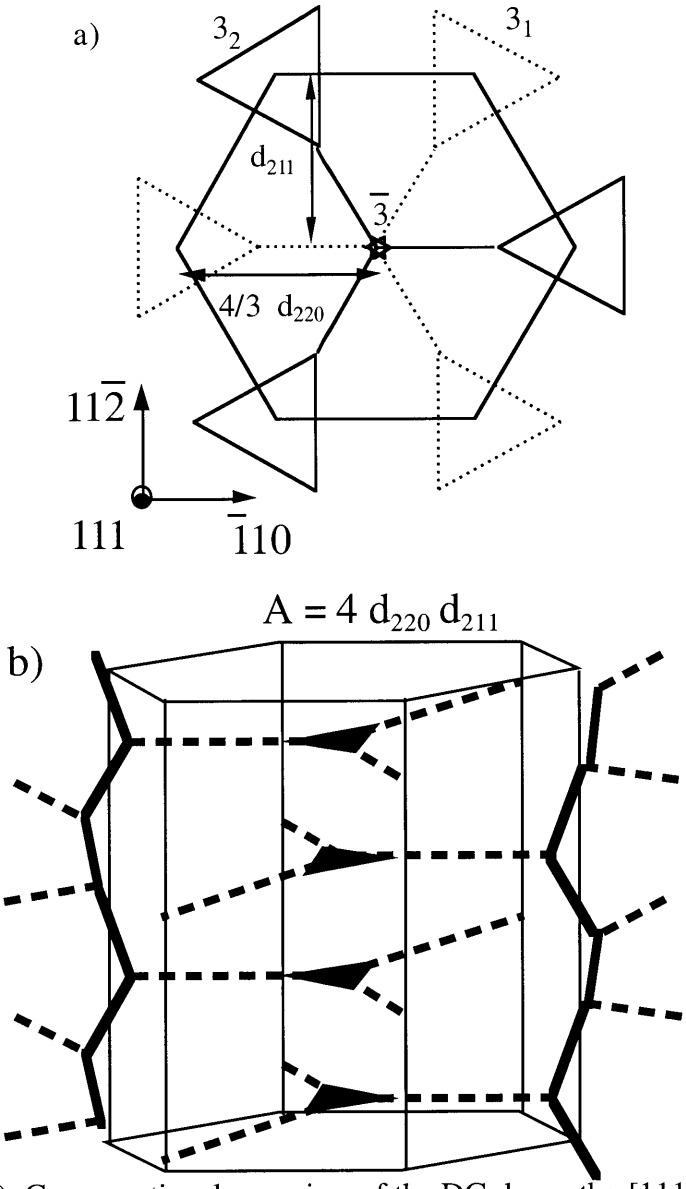

Figure 7.10: a) Cross-sectional area view of the DG down the [111] direction. b) Perspective view of the prism of the DG phase with the hexagonal base shown in figure 7.10a. The bolded lines indicate struts which contribute to the [111] modulus, and the dashed lines indicate struts which do not. The area of the base is $4\, d_{\bar{2}20}\, d_{11\bar{2}}$.

Understanding the mechanical response in the flow direction of this interpenetrating nanocomposite can be done with attention to the stiff, strong glassy networks which dominate over the soft elastomeric component and control the initial tensile modulus and the flow stress of the material. Examination of the skeletal graph (Schoen, 1970)(Grosse-

Brauckmann, 1997) of the double gyroid structure shows that the axes of the PS struts are everywhere oriented along <110> type directions. For loading along the [111] direction the most compact, direct continuous path of PS has 6 strut segments over a lattice repeat of $\sqrt{3}a$, all struts are ~35° from [111] forming equal numbers of tight 3_1 or 3_2 helices. The structure has $\sqrt{3}$ of these helical PS paths per a^2 (where a is the unit cell parameter of the DG).

7.5.2 In-situ SAXS of Deformation Along the [111] Direction

The roll cast oriented DG was deformed and the response of the microdomain morphology to the applied deformation observed by in situ X-ray scattering and by TEM of the deformed samples. Figure 7.11 shows the stress-strain curve and accompanying SAXS patterns of different points along the curve. The indexing of the SAXS pattern at zero strain is given in section 6.3.

To explore the transition from unyielded to necked material further, a sample was stretched in the [111] direction to a nominal strain of 50%, whereby the neck had formed and had progressed across part of the gauge length. Figure 7.12 shows the SAXS patterns along the transition from the unyielded to the yielded regions. The SAXS patterns show that up to yield (~15%) the deformation causes a loss of the higher order Bragg peaks with the equatorial peaks broadened and shifted (to higher q). Just before yield, the {211} equatorial "peak" moves out from q = 0.0247 (at start) to q = 0.0252, corresponding to a compressive strain of ~2% in the transverse direction. Because there are no peaks on the meridian along the axis of stretch, the strain in the axial direction cannot be calculated. At yield, the characteristic Bragg peaks have disappeared and have been replaced by a pair of streaks elongated along the normal to the stretching direction.

With still further elongation up to 600% the streaks become somewhat sharper and more elongated, as shown in figure 7.11. Although the streaks move closer toward the equator as the strain in the yielded region is increased (after the neck has propagated across the gauge length of the sample), there does not seem to be a correlation between the q of the streak with the macroscopic strain in the sample. In the isotropic stretch, the streaks could be correlated with the strain in the sample as strain in the{211} spacings. Because there are no {211} meridional peaks in the oriented sample at start, it might well be the case that the streaks in the [111] stretch are associated with a different structure than {211} planes.

Upon unloading several well-defined Bragg peaks return with the two equatorial (211) reflections particularly strong, and the off-equatorial {211} and {220} type reflections streaked. From the q-values of the {211} equatorial peaks which have returned, the calculated lateral strain of the unloaded sample is -26% (compressive). The sample

width-to-thickness ratio is approximately 1:1 to 1:1.5, such that plane stress can be assumed in the samples. Assuming a rubbery material, the tensile extensional ratio, λ, can then be calculated from the lateral compressive ratio, $\frac{1}{\sqrt{\lambda}}$, from which the strain $\varepsilon = \lambda - 1$ can be derived. The SAXS-calculated 80% residual tensile strain in the unloaded sample is in agreement with the observed macroscopic residual strain. The SAXS pattern of the unloaded sample after 5 days annealing at 120°C is nearly identical to the original, indicating that the interpenetrating PS networks are not permanently destroyed, even after loading to 600%. The spacing of the {211} peak of the annealed sample is the same as that before deformation indicating that the network heals on the microscopic scale. Annealing a deformed sample also returns the macroscopic dimensions of the sample to those at start, which indicates that if struts were plastically deformed below the natural draw ratio of PS, then annealing allowed the PS to achieve the rubbery regime and to relax to the original configurations. If struts had broken either by chain scission or pullout, then annealing allowed interdiffusion enough to return the domains to their original dimensions.

When immediately unloaded, DG stretched to 600% in the [111] direction has on average 100% residual strain (permanent set), higher than that of a conventional gum vulcanizate (permanent set ~10%, after Senyek (1986)) because the deformed viscoelastic PS domains prevent full immediate recovery. Two types of plastically deformed species can exist: PS domains are stretched in the tensile direction and some of the PS struts which are at an angle to the stretch direction and have collapsed under Poisson stress effects (in a manner similar to a hinge). Recovery from deformation is time-dependent such that the initial strain continues to relax toward zero strain.

Deformation of DG, F || [111]
Accompanying SAXS Views

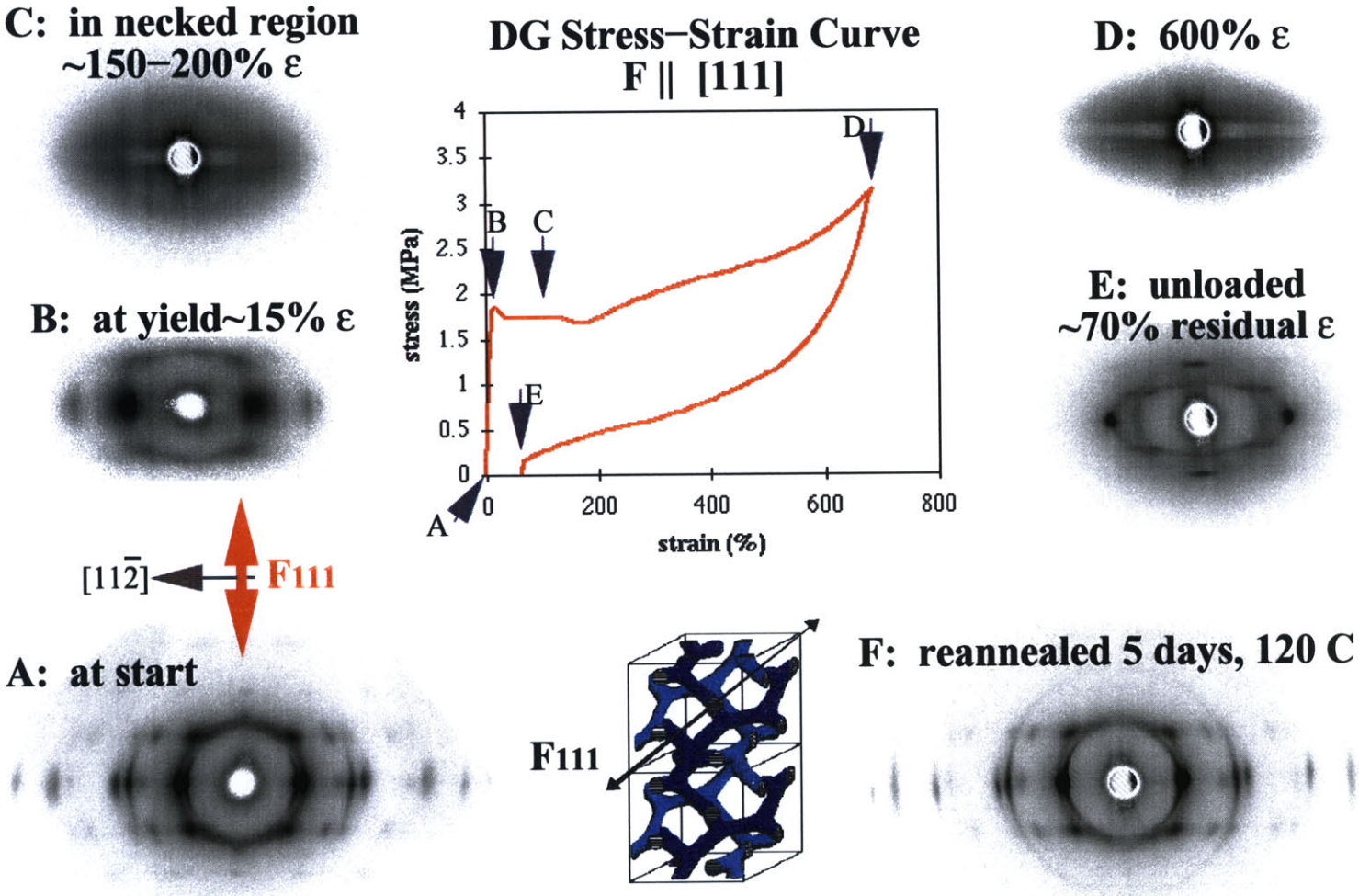

Figure 7.11: Stress–strain curve of roll cast annealed 34%S SIS DG stretched in the [111] direction (center) with accompanying SAXS patterns along the stress–strain curve..

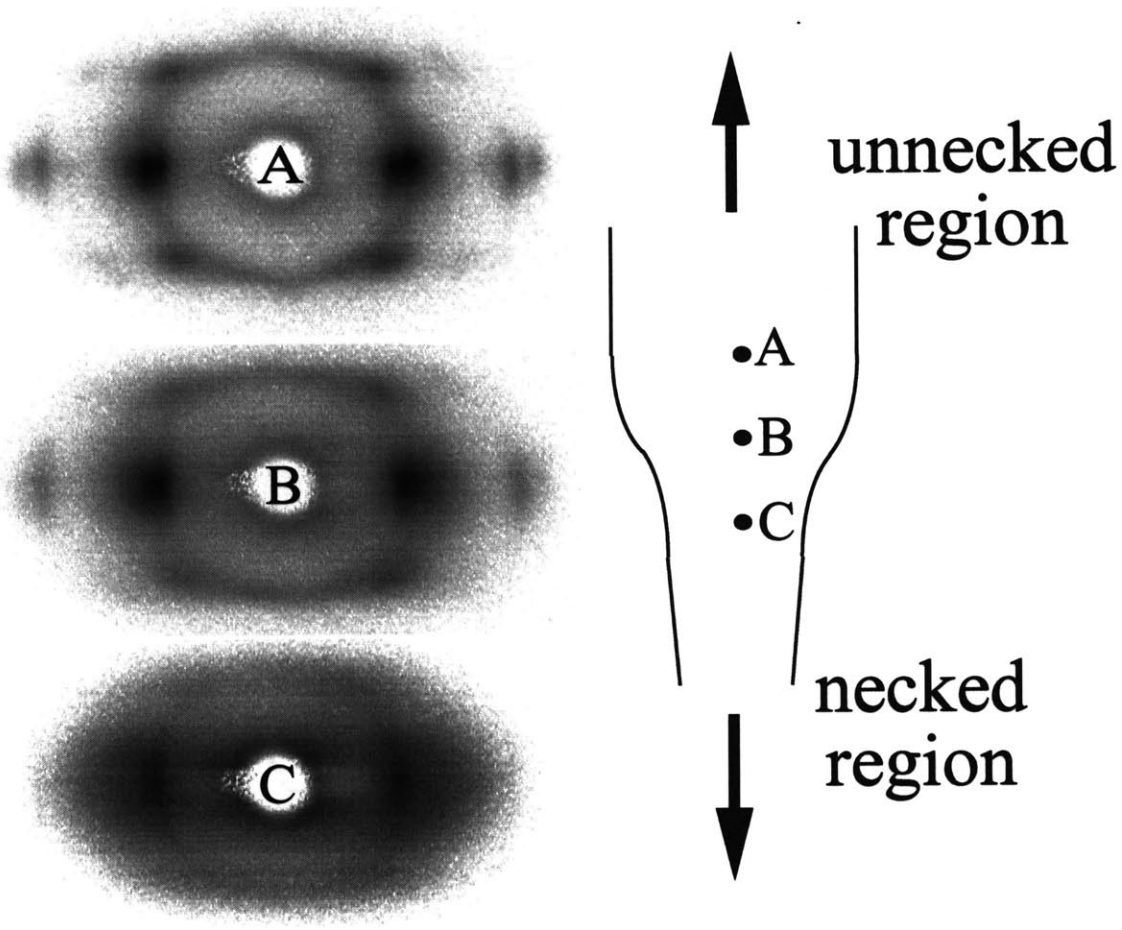

Figure 7.12: A roll cast annealed 34%S SIS DG stretched in the [111] direction loaded to 50% total strain capturing the necking transition (schematic shown center), with SAXS patterns of different points along the neck transition. Point A is closest to unnecked region, while point C is in the necked region where the local strain is approximately 200%.

7.5.3 TEM of DG Deformed in the [111] Direciton

Additional insight into the deformation process is available from TEM images of the stretched and crosslinked samples, shown in figure 7.13. At yield three types of regions are evident: 1) regions undergoing yield, as exemplified by the rows of bright periodically spaced PS regions in the direction of elongation, 2) regions where PS struts are oriented in several directions, 3) regions not yet yielded. Initial deformation may be taken up by rotation of the grains and by elastic bending of the PS struts. Subsequent deformation may occur by plastic bending of the struts, similar to opening a hinge. Sample necking may cause some portions of the polystyrene helices along the [111] direction to start to microneck and draw, with strut breakage occuring as well. The applied stress field along the [111] direction and Poisson induced transverse stresses act to twist disconnected struts in different directions from their original arrangement.

The TEM image of DG deformed in the [111] arrested at 300% strain shows relatively low image contrast at far left or far right without many distintive features. This can be interpreted as due to elongated PS networks in the PI matrix, causing the overall projected image to appear more uniform. Closer inspection of these areas reveal elongated strands of the PS. In addition, there are regions which have obvious PS and PI domains which appear to consist of broken struts angled at different directions to the force axis. The upper left hand side of the figure shows features suggestive of randomization of the PS strut directions. When a continous PS [111] domain breaks, it may untwist or re-orient itself such that a dangling strut becomes visible on the image plane.

Upon unloading the PI chains generate retractive forces to bring the PS networks back into their original positions. The TEM image of DG unloaded after being stretched to 600% shows that the material regains most of its original undeformed DG character, but some of the PS domains remain disconnected. The original DG structure as well as the macroscopic dimensions are completely restored after high temperature annealing. These are the conditions when plastically elongated PS chains in the struts have the kinetic mobility to relax to its random configurations. In addition lowering the area of the intermaterial dividing surface between the components and the recovery of the average end-to-end chain distances requires that interconnections and original structure of broken struts be reformed. Breakage of any PS domains occurs through pullout and/or scission, but either of these processes must be reversible such that annealing enables healing through diffusion

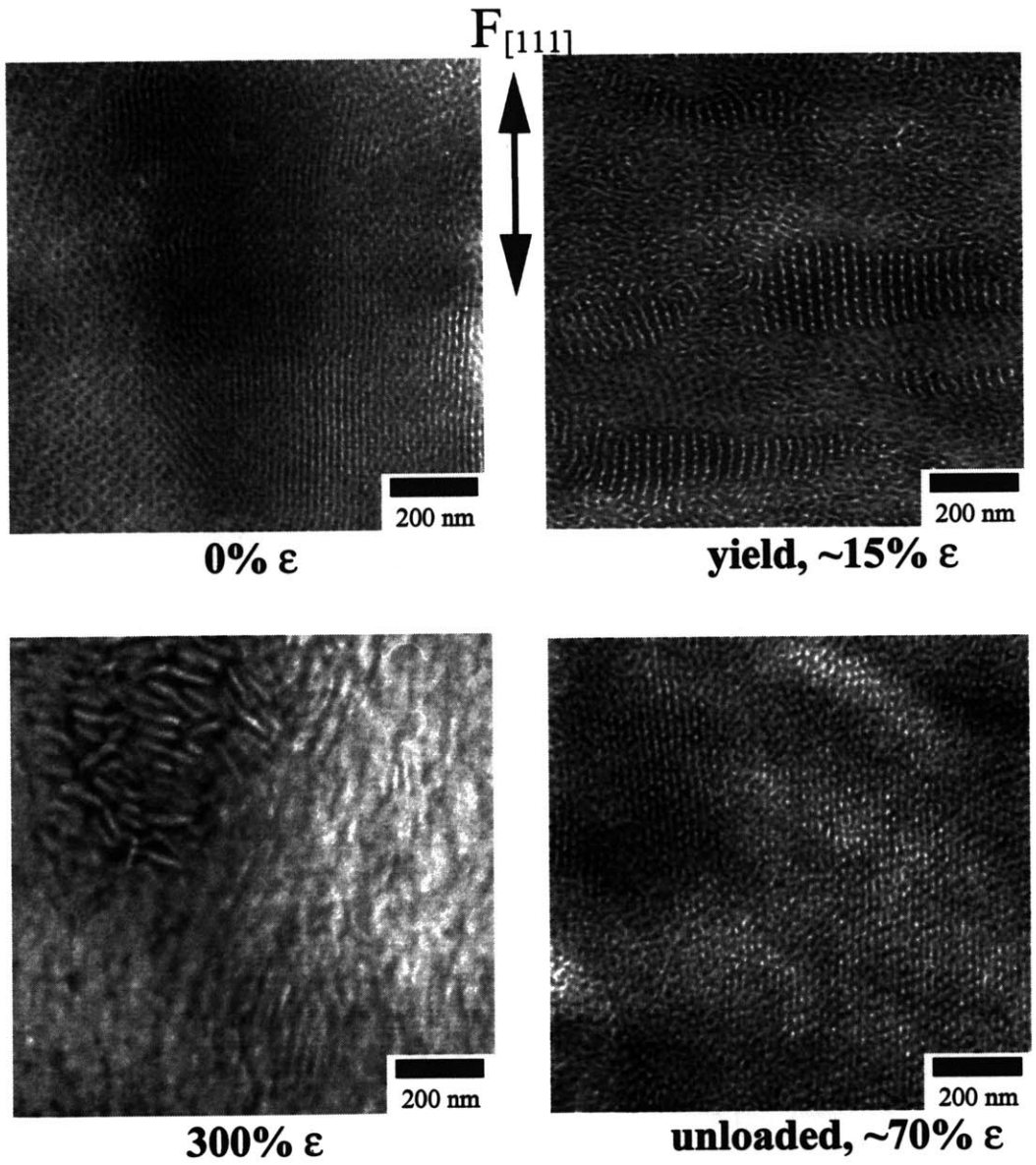

Figure 7.13: TEM micrographs of the DG stretched in the [111] direction at various levels of strain. The roll cast direction as well as the [111] is along the vertical.. Samples are viewed through the film (in the [110] direction).

7.5.4 Stress Relaxation of the [111] Direction

Figure 7.14a shows an imposed strain-time history for a sample stretched in the [111] direction for relaxation during loading and unloading, and figure 7.14b shows the stress-time response. Leathery polymers in general stress-relax because of the time-dependent response to the applied stimuli. If a sample were perfectly rubbery or perfectly glassy, then their responses to the applied stimuli are immediate, and no stress relaxation is expected. However, in the SIS samples studied here, the PI phase (a rubber) and the PS phase (a glassy polymer) combine on length scales such that the composite, and more likely the PS, is a leather.

Upon loading to any strain, the stress relaxes as the viscoelastic PS domains respond to the applied force. Loading strains of 100% and 600% were imposed, to sample a strain within the necked region and a strain after the neck has propagated across the sample. It was noticed during loading to nominal strains where the neck had not yet propagated across the entire gauge length, that stress was relieved by drawing unnecked material into the neck, thereby decreasing the strain of the material within the neck. It may be deduced that the amount of energy expended to draw unnecked material to the adjacent necked region is at least compensated by the amount of strain energy gained by relieving the stress in the necked region; presumably aligning grains, PS domains, and chains and yielding the material requires less energy than straining the aligned and yielded sample.

Unloading strains of 250%, 100%, and 65% were imposed. It was observed (but not shown here) on unloading that the stress continues to decrease when the strain is stopped and held fixed at 400% and 300% strain. This indicates that the some of the stress is relieved upon unloading, but overall the rate of unloading is below the rate of recovery when stopped at either 300% or 400% strain. When the sample is unloaded to 250% strain and held, the stress remains constant, as shown in figure 7.14b. Unloading further to 100% or 65% strain causes the stress to increase with time. It can be infered that at 250% strain the rate of unloading is equal to that of recovery in the sample, and that below this strain the rate of unloading exceeds that of recovery.

It should be noted that 250% strain is about where features begin to reappear in SAXS upon unloading from 600% strain such that the microstructure is being rebuilt. It is possible that the two events may share a causality relationship, such that smaller scale reorganization and perfection of the structure may sample require longer relaxation time constants than those associated with the rate of the unloading.

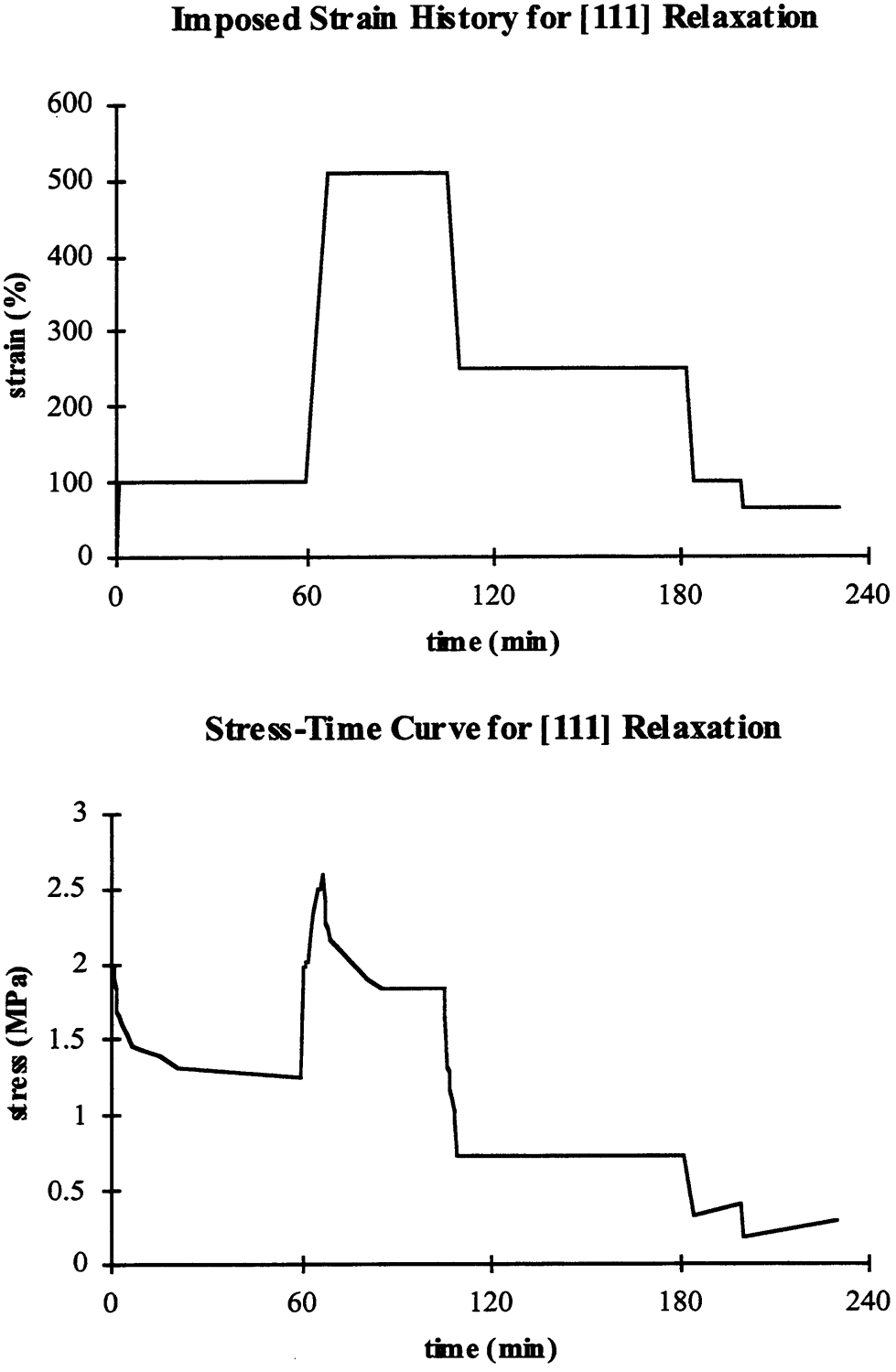

Figure 7.14: a) (top) Imposed strain-vs-time history stress-relaxation study of the [111] direction. b) (bottom) Stress-time response to the imposed steps of strain.

7.5.5 Discussion

The deformation mechanisms of the DG stretched in the [111] direction can now be considered from the geometry of the DG in the [111] direction, along with the TEM and SAXS results presented, as well as insight from past studies on the deformation behavior of cylinders and lamellae parallel to the axes or layers. It can be interpreted that in the elastic regime (<1%), the strains are accomodated by beam bending or the opening of the hinges that struts make with one another in this direction. Subsequent yielding occurs in grains which are oriented best with the stress axis. The yielding and necking process initates flow and plasticity of the PS domains, similar to the plasticity experienced in fibrils when PS crazes, as the struts are on the same size scale as these fibrils. Higher strains then cause pullout in the unentangled PS domains, which cause the domains to draw down and eventually separate. TEM shows that samples nominally stretched to 300% consist of both highly elongated and discontinous PS domains. This draw-down and separation is consistent with the previous studies on cylinders and lamellae stretched parallel to the axes or layers (as discussed in section 7.4), which were dubbed "break up". Stress-relaxation during stretching is due to the time-dependent response of the viscoelastic composite. This viscoelasticity is also evident in the behavior of the composite upon unloading. Upon unloading the entangled rubber PI chains provide the retractive force. The plastically deformed and drawn PS domains recover over time, thereby forming the original domain structure, as exhibited full microscopic, as well as macroscopic, recovery of the sample.

7.6 Deformation of Oriented DG in the Transverse Direction

The mechanical properties are listed in table 7.1. The tensile modulus along the transverse is approximately 10 MPa, about 20% of that in the [111] direction. Yielding occurs diffusely, without the presence of necking or drawing, a phenomenon also observed in stretching perpendicular to the axes of cylinders and perpendicular to the layers of lamellae. The hysteresis in the stress-strain curve is approximately 40% and a weak Mullins effect is observed. These both suggest that perhaps more of the rubber is carrying the deformation at high strains, since the deformation behavior in this direction is more akin to that of a gum vulcanizate, whereas the [111] deformation behavior was much more "plastic". In order to verify such a hypothesis, the structure in the transverse direction will be observed first, followed by in situ SAXS and TEM results.

7.6.1 Description of the Transverse Direction

For loads applied along the transverse direction, the most direct continuous PS path is much more serpentine than that in the [111] direction. The initial deformation along transverse may be somewhat akin to uncoiling a set of loose springs. However, more importantly is the fact that the transverse direction consists of {211} planes with misorientations around the [111] direction. These {211} planes in turn consist of high PS connectivity [111] domains, and the {211} planes are those of highest PS content. The struts forming <111> paths stay intact, and large strain deformation is accomodated by buckling under the lateral compression.

7.6.2 In-situ SAXS of Deformation in the Transverse Direction

Figure 7.15 shows a stress-strain curve of the DG deformed in the transverse direction and selected SAXS patterns are shown in figures 2c i-iv. The mechanical properties are listed in Table 7.1. The tensile modulus for the transverse stretch is approximately 10 MPa, about 1/5 less than that in the flow direction with no necking during deformation. Yielding occurs at ~10% at approximately 0.74 MPa. The hysteresis of the stress-strain curve is approximately 40%, with a weak Mullins effect, and a residual strain upon unloading of approximately 20%. All three of these features are markedly less than in the flow direction and closer to that typical of a gum vulcanizate.

The SAXS patterns show that Bragg-like reflections persist throughout deformation even to 600% strain. Streaks perpendicular to the stretching direction and continuous across the equator gradually develop from the (211) reflection. They first become easily discernible at 70-80% strain and move closer together in proportion to the macroscopic strain in the sample. The streaks exhibit higher intensity near their tips with increasing

strain and become reminiscent of a 4-point pattern. The SAXS patterns also contain broad regions of intensity which lie on a well-defined ring which persists at constant q throughout the elongation. At the highest strain the ring is comprised of a set of faint layer lines, which move closer together and increase in number with increasing strain. In the SAXS pattern after unloading, with approximately 10% residual strain, the main features of the original SAXS pattern have returned. After annealing the pattern is again nearly identical to the original starting SAXS pattern.

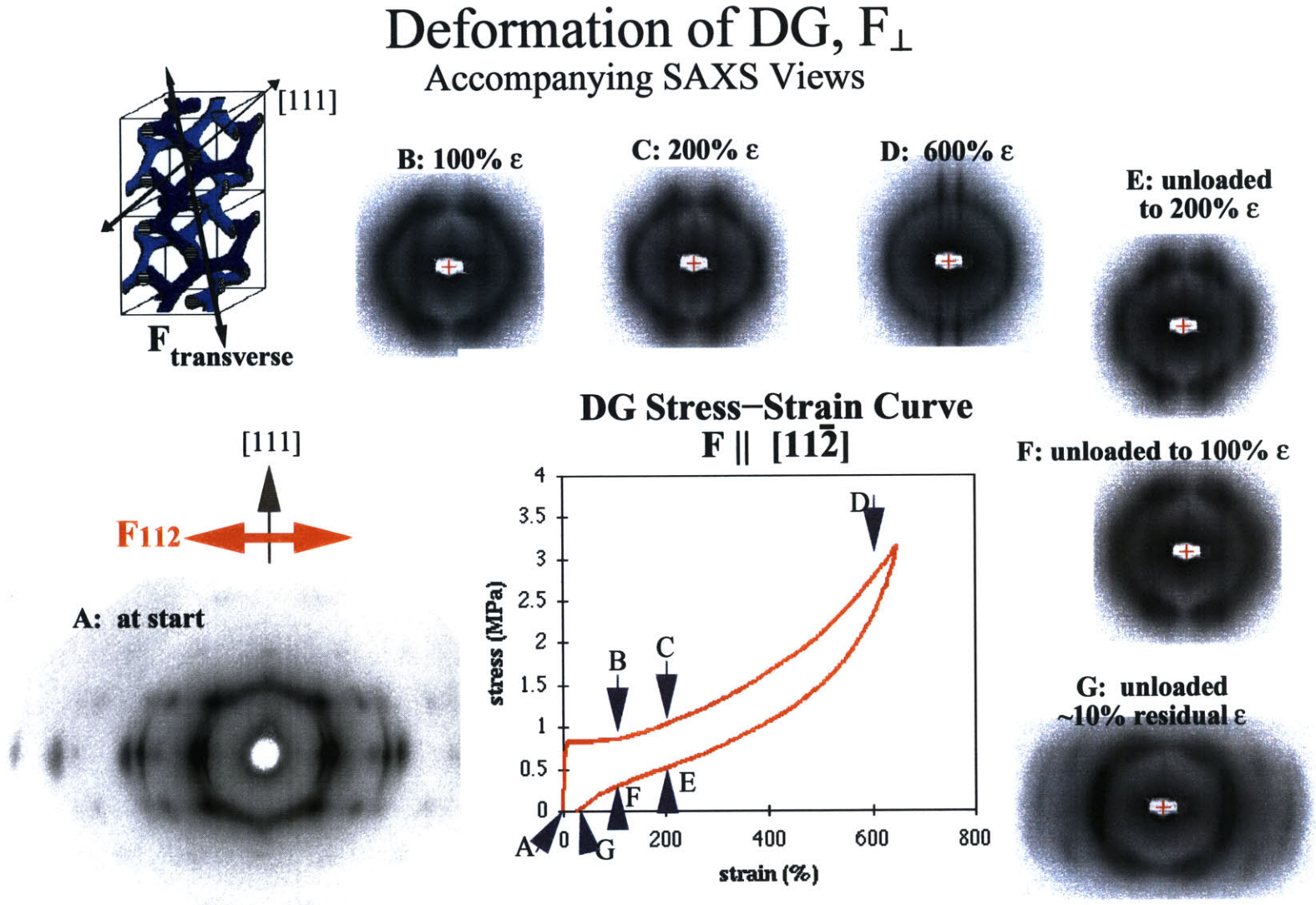

Figure 7.15: Stress–strain curve of roll cast annealed 34%S SIS DG stretched transverse to the [111] roll cast direction (center), with accompanying SAXS patterns at different points along the stress–strain curve..

7.6.3 TEM of DG Deformed in the Transverse Direction

Figures 7.16 show TEM images of roll cast oriented DG stretched in the transverse direction and viewed through the film. The sample shown in figure 7.16b was stretched to 150% strain and irradiated with 80 Mrad of 200 Mev electrons. Nominal residual stress is 125%. The sample shown in figure 7.16c was stretched to 450% and irradiated, and retained nominally 300% strain. Both images indicate that buckling of planes is occuring.

Aged glassy polymers always undergo yielding (McClintock and Argon, 1966) when deformed because the yielding process is akin to that of production of free volume in order to initiate flow. The samples mentioned in this thesis been annealed for 2 weeks at 120°C in order to induce the phase transformation, such that the PS domains have been aged. However, the presence or absence of a neck in an aged sample indicates whether the yielding process is distributed or whether it is simultaneous. The development of sharp neck, as in the isotropic and [111] stretches, indicates homogeneous yielding, in that the elements of a localized region yield simultaneously. Before yielding, all of the reinforcing elements had borne the load equally. The absence of a neck during yielding, as in the transverse stretches, indicates a distributed yielding process, in which highly variable stress concentrations and local bearing of load occurs.

Yield in the transverse loading then is associated with initiation of the buckling process. However, yielding in the tranverse direction is not accompanied by a necking and a drop in the load carrying abilities because it is a distributed rather than a simultaneous process. Because there are different grains of DG with misorientations about the [111] axis, some grains whose orientations are favorable for buckling will buckle at lower strains than other grains. Defects within a grain would also be buckling initiators. Also because of the distributed yielding there is not a characteristic wavelength or periodicity associated with the buckling, as there would be for a perfect single crystal.

The periodicity in the direction of the stretch direction is associated with the {211} planes which lie perpendicular to the stretch axis. There is a well-defined periodicity of these planes at all strains, as evidenced by the faint layer lines at all strains. Measured q-values of the most prominent streak at different strain values indicate that the interlayer spacings increase with increasing strain by an amount proportional to the strain.

The periodicity perpendicular to the stretch direction is associated with planes which lie parallel to the stretch axis. At low strains these are well correlated, as evidenced by the Bragg-peak-tipped ends of the streaks, but this correlation is lost with increasing strain, as evidenced by the broadening of the tips at higher strains. This could be due to the buckling of these high density PS planes in a manner similar to lamellae and cylinders stretched in the transverse directions as seen by Honeker and Albalak, respectively. This stress is

relieved by deforming the grains via buckling and rotating the planes towards the stretch axis. The correlations between planes which lie parallel to the stretch direction become interrupted in a manner analogous to stacking faults.

In order to correlate the components of the SAXS patterns with real space structures, FFTs were taken of the TEM images. The components of interest in the diffraction patterns were then isolated and inverse-transformed. Figures 7.17a-g show the FFTs and inverse FFTs of the TEM micrographs of samples defromed in the transverse direction to 125% strain, and figures 7.18a-g show the same for samples deformed to 300% strain. Figure 7.17c-d and 7.18c-d show that the main components of the SAXS patterns of samples stretched in the transverse direction belong to the {110} planes. Figures 7.17e-f and 7.18e-f show that the heavy tipped ends arise from the buckling, as the inverse FFTs of only these components show the zig-zag structures of the buckling. Figures 7.17g-h and 7.18g-h show that the streaks arise from the disorder of the buckling waves, which are most likely due to either grain boundaries or defects within the grains initiating the buckling.

When the sample stretched in the transverse direction is unloaded, the sample retains strains of approximately 10%, similar to that of a gum vulcanizate. Because so much of the deformation was taken up by buckling, the immediate recovery is more complete than in the [111] stretch in which deformation was taken up by plastic deformation of the struts and breakage.

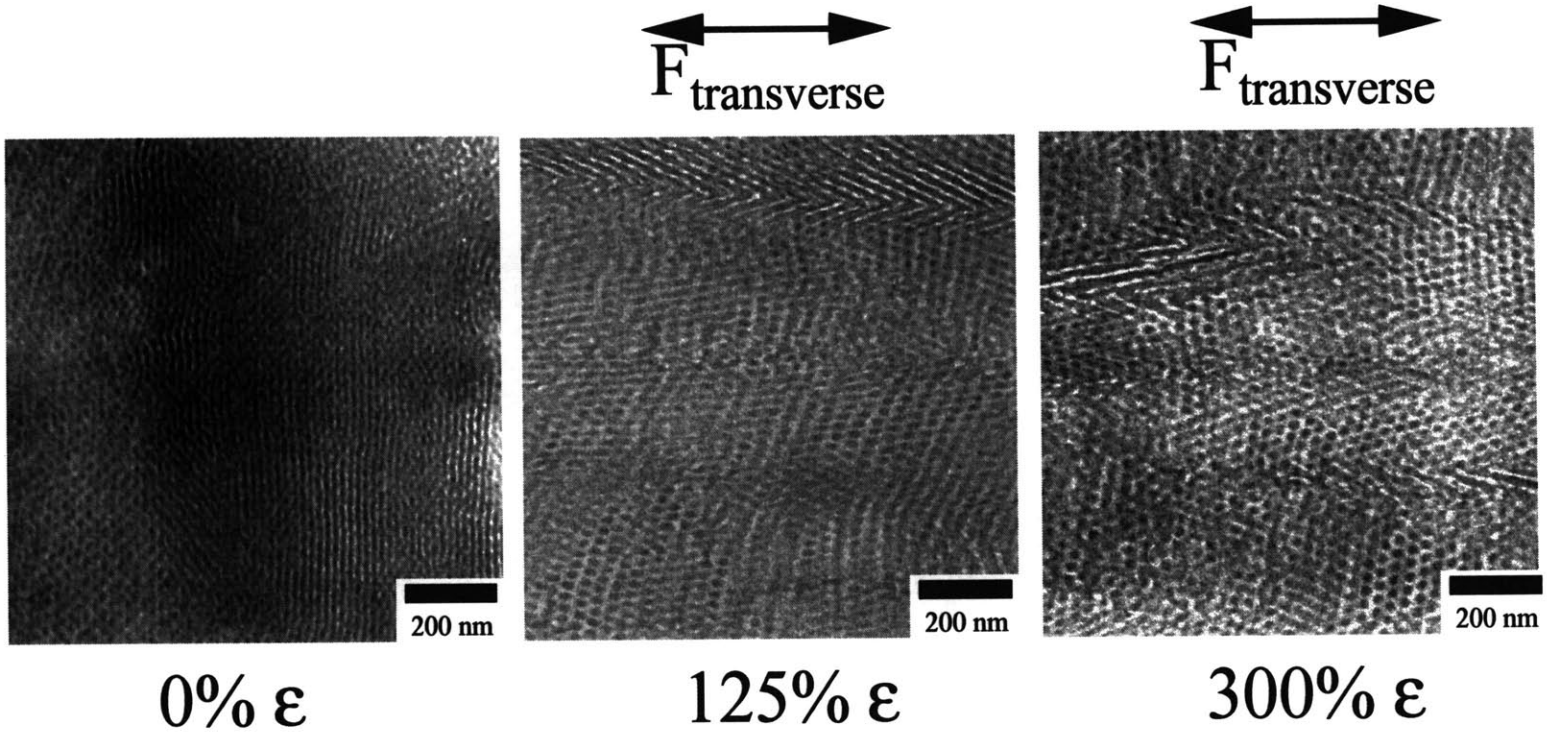

Figure 7.16: TEM micrographs of the DG stretched transverse to the flow direction at various strains. The [111] roll cast direction is along the vertical. Samples are viewed through the film (in the [110] direction).

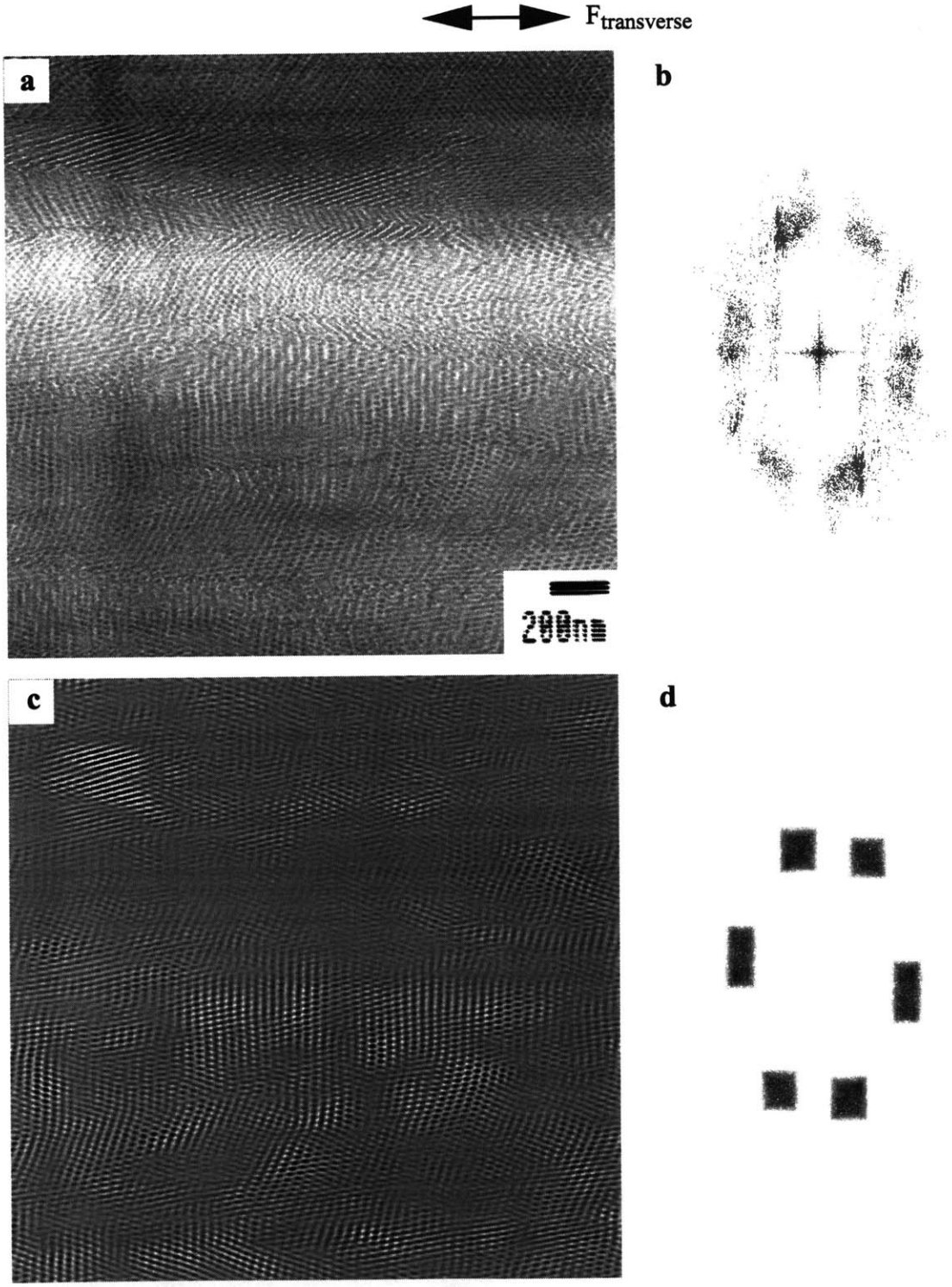

Figure 7.17: a) TEM image of roll cast 34%S SIS DG deformed 125% transverse to the roll cast direction. b) FFT of the image in figure 7.17a. d) Main components of Fourier space chosen for inverse FFT. c) Real space components corresponding to the Fourier components shown in figure 7.17.

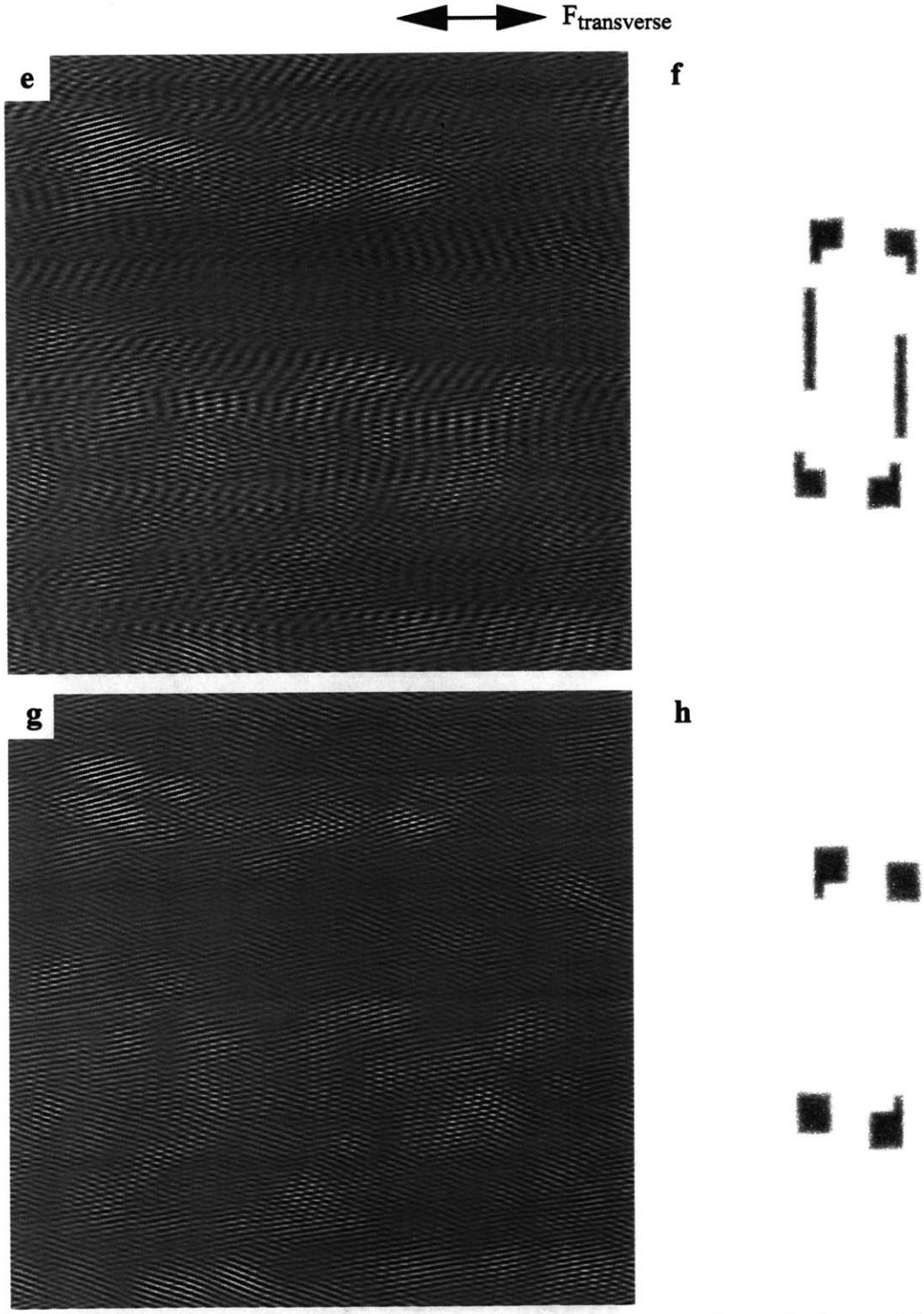

Figure 7.17: e) The streak components of Fourier space shown in figure 7.17a chosen for inverse FFT. f) Real space components corresponding to the streaks in the diffraction pattern. g) The higher–intensity ends of the streaks shown in the FFT in figure 7.17f. h) Corresponding real space components of the FFT in figure 7.17g.

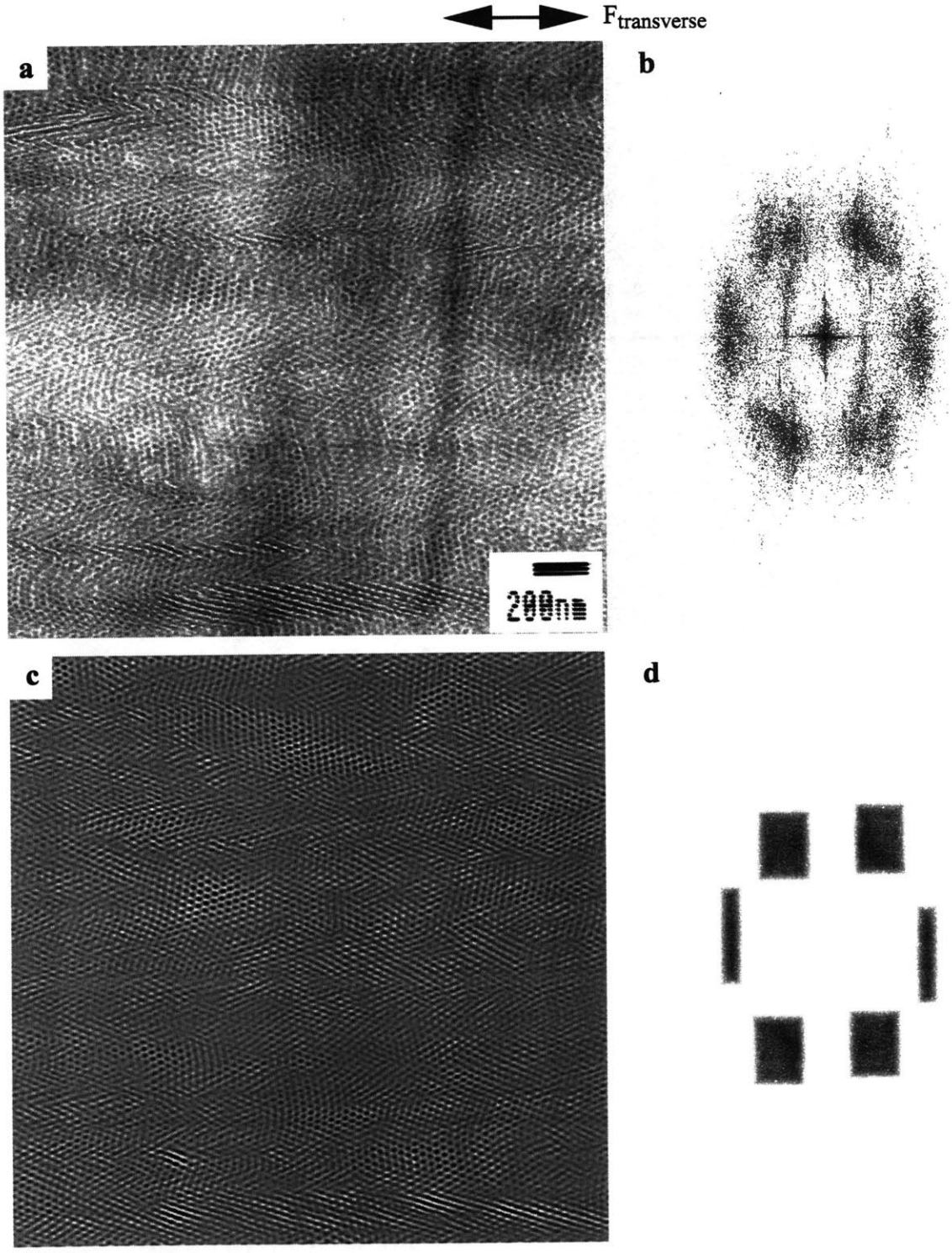

Figure 7.18: a) TEM image of roll cast 34%S SIS DG deformed 300% transverse to the roll cast direction. b) FFT of the image in figure 7.18a. d) Main components of Fourier space chosen for inverse FFT. c) Real space components corresponding to the Fourier components shown in figure 7.18d.

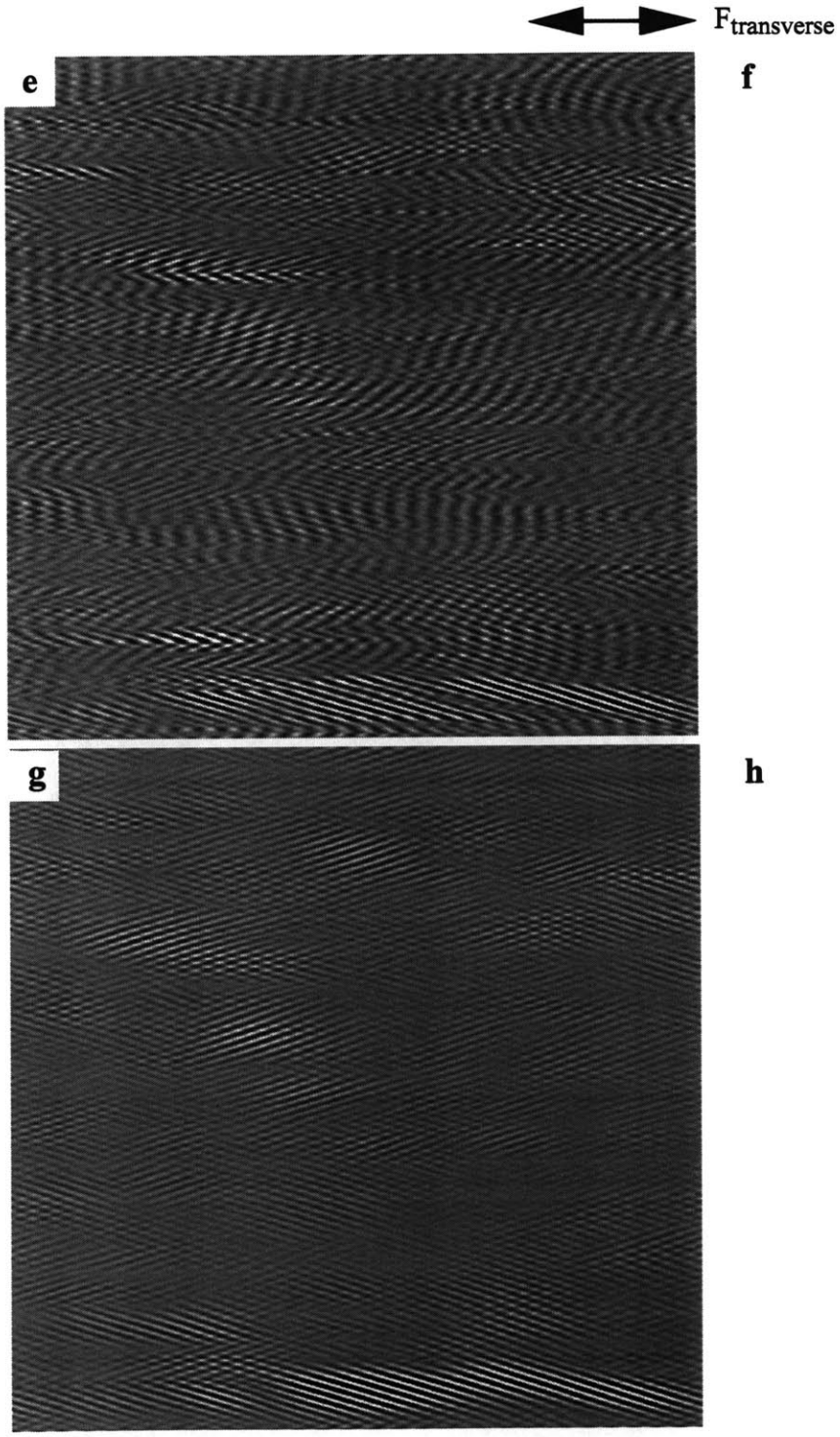

Figure 7.18: e) The streak components of Fourier space shown in figure 7.18a chosen for inverse FFT. f) Real space components corresponding to the streaks in the diffraction pattern. g) The higher–intensity ends of the streaks shown in the FFT in figure 7.18f. h) Corresponding real space components of the FFT in figure 7.18g.

7.6.4 Stress Relaxation of the Transverse Direction

Figure 7.17a shows the imposed strain-time history for a sample stretched in the transverse direction, and figure 7.17b shows the stress-time response. During loading, the stress-relaxation is greater at higher strains than at lower strains, as the structure resists stretching in the axial load direction and buckling in the transverse direction, and the stress decreases from the point of imposed strain. Upon unloading, the stress is decreased and the structure recovers from being stretched; the stress decreases from the point of unloading. At ~200% strain, the rate of unloading equals that of recovery and the stress remains constant with time after the point of imposed strain to many minutes later. This may be the strain to which the sample would like to decay given its strain history: it allows the short-term relaxations without forcing polystyrene collapse. At ~100% strain, the rate of unloading exceeds that of recovery, the structure becomes crushed. Here, the stress increases from the point of imposed strain, as the PS networks resist collapse.\

7.6.5 Discussion

The deformation mechanisms of the DG stretched in the transverse direction can now be considered from the geometry of the DG in the transverse direction, along with the TEM and SAXS results presented, as well as insight from past studies on the deformation behavior of cylinders and lamellae parallel to the axes or layers. It can be interpreted that in the elastic regime (<1%), the strains are accomodated by beam bending, elastic buckling of the continuous PS domains, or the rotation of grain structures. Yielding is associated with the buckling of the continuous [111] domains, which are now perpendicular to the stretching direction. This is similar to the phenomenon of the chevrons (buckling formations) of cylinders as reported in section 7.4. Borrowing concepts of deformation of cylinders perpendicular to the axes, subsequent yielding occurs by cooperative orientation of the buckled domains toward the stress axis. Plasticity of the PS domains is sampled in this direction as much as in the [111] stretch, but rather buckling of the continous PS domains dominates the large strain behavior. It can be imagined, however, that at high elongations of the sample, some of the buckled [111] domains rotates enough into the stress axis for the [111] PS domains to be pulled along the tight PS helices. TEM and FFTs thereof indeed provide evidence of buckling. Inverse-ffts of the streaks indicates that there is no associated characteristic buckling wavelength, but suggest that buckling is initiated at different areas due to defects and grain boundaries. Upon unloading recovery is more immediately complete than in the [111] stretch because the plasticity of the viscoelastic PS domains was not sampled to the same extent as in the [111] stretch.

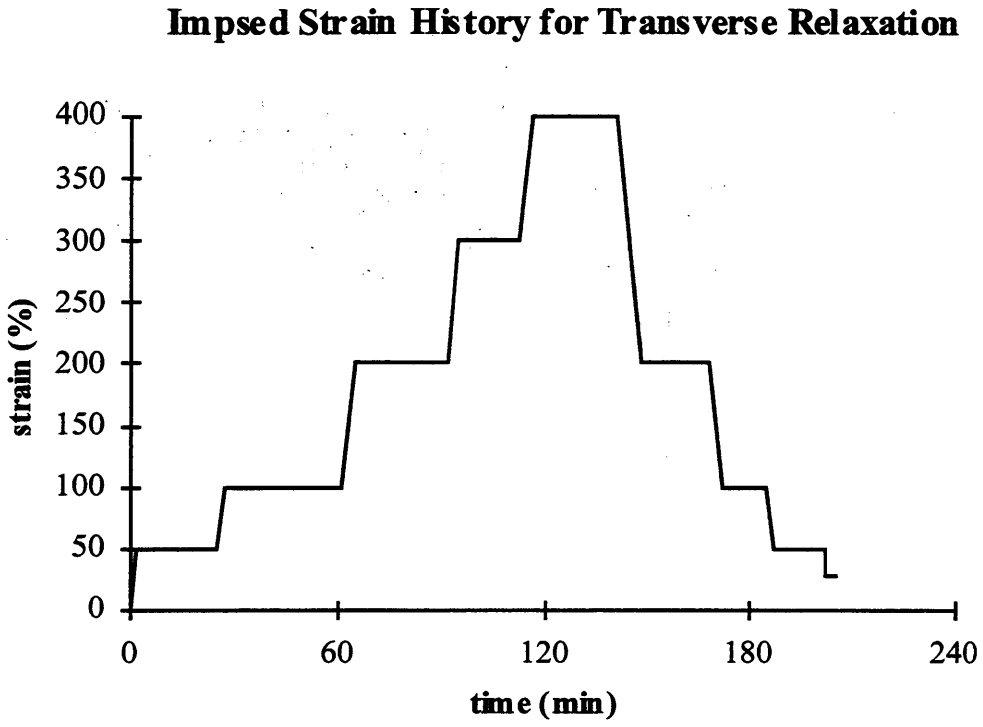

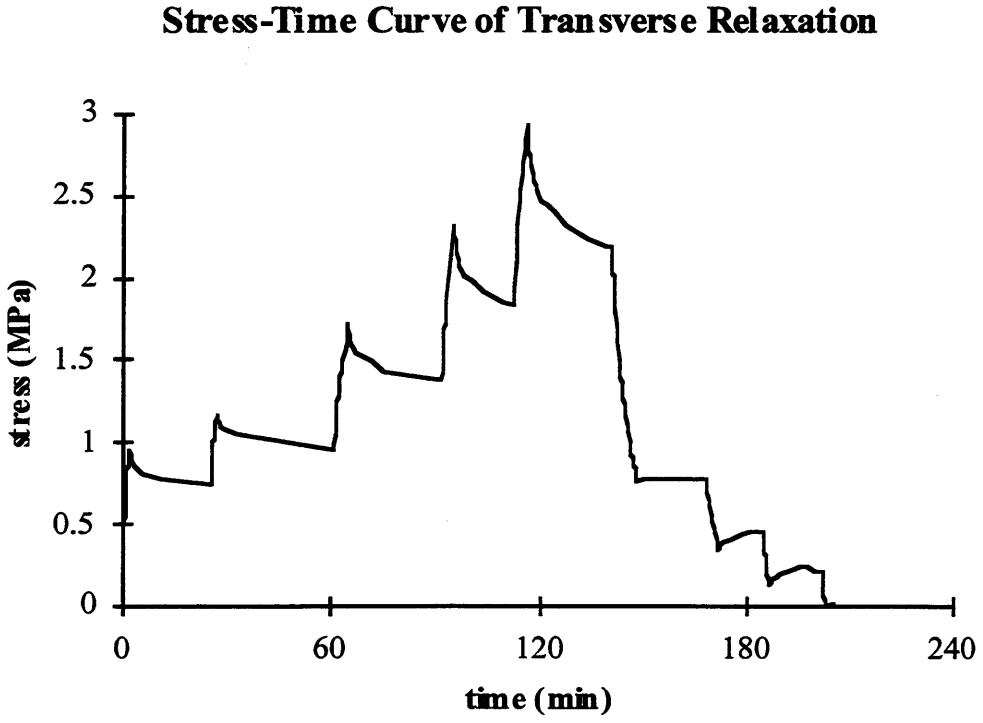

Figure 7.19: a) Imposed strain-time curve of the stress relaxation experiment in the transverse direction. b) Stress-time curve showing stress relaxation.

7.7 References

Albalak, R., Y. Cohen, B. Dair and E. L. Thomas (1999). "The High-Strain Deformation of Block Copolymer Films with Lamellar Morphology." in preparation.

Alward, D. and E. L. Thomas (1985), unpublished results.

Alward, D. B. (1985). "A Morphological Study Of A Series Of Multiarmed Star Block Copolymers Of Polyisoprene And Polystyrene". Ph. D. thesis, University of Massachusetts.

Avgeropoulos, A., B. J. Dair, N. Hadjichristidis and E. L. Thomas (1997). "The Tricontinuous Double Gyroid Cubic Phase In Triblock Copolymers Of The Aba-Type." Macromolecules **30**: 5634-5642.

Bailey, J. T., E. T. Bishop, W. R. Hendricks, G. Holden and N. R. Legge (1966). "Thermoplastic Elastomers: Physical Properties And Applications." Rubber Age **10**: 69-74.

Beahan, P., M. Bevis and D. Hull (1971). "The Morphology Of Crazes In Polystyrene." Philosophical Magazine **24**: 1267-1279.

Beahan, P., M. Bevis and D. Hull (1973). "A Comparison Of The Morphologies Of Crazes Formed In Thin Films And Bulk Specimens Of Polystyrene." Journal of Materials Science **8**(2).

Beahan, P., M. Bevis and D. Hull (1973). "Electron Microscopy Studies Of Fracture Processes In Amorphous Thermoplastics." Polymer **14**: 96-102.

Beecher, J. F., L. Marker, R. D. Bradford and S. L. Aggarwal (1969). "Morphology And Mechanical Behavior Of Block Polymers." Journal of Polymer Science Part C **26**: 117-134.

Brandt, M. and W. Ruland (1996). "Saxs Studies On The Deformation Of Macrolattices In Block Copolymers." Acta Polymerica **47**: 498-506.

Brown, H. and E. J. Kramer (1981). "Craze Microstructure From Small-Angle X-Ray Scattering." Journal of Macromolecular Science - Physics B **19**: 487-522.

Brunwin, D. M., E. Fischer and J. F. Henderson (1969). "Developments In Self-Reinforced Elastomers." Journal of Polymer Science Part C **26**: 135-147.

Childers, C. W. and G. Kraus (1967). "Properties Of Random And Block Copolymers Of Butadiene And Styrene. Iii. Three Sequence Sbs Block Polymers." Rubber Chemistry Technology **40**: 1183-1199.

Dair, B. J., E. Prasman, M. Capel and E. L. Thomas (1997). Deformation Behavior of Cubic Triblock Copolymers with Discrete or Tricontinuous Glassy Microdomains. Churchill Conference on the Deformation, Yield, and Fracture of Polymers, Cambridge, England.

Dair, B. J., E. L. Thomas, A. Avgeropoulos, N. Hadjichristidis and M. Capel (1998). Anisotropic Deformation Behavior of the Cubic Double Gyroid Phase in ABA Elastomeric Triblock Copolymers. International Symposium on Toughening of Plastics in the 1998 August Meeting of the American Chemical Society, Boston, MA.

Donald, A. M., T. Chan and E. J. Kramer (1981). "The Effect Of Film Thickness On Craze Microstructure." Journal of Materials Science **16**: 669-675

Donald, A. M. and E. J. Kramer (1981). "The Mechanism For Craze-Tip Advance In Glassy Polymers." Philosophical Magazine A **43**: 857-870.

Donald, A. M. and E. J. Kramer (1982). "Effect Of Molecular Entanglements On Craze Microstructure In Glassy Polymers." Journal of Polymer Science: Polymer Physics Edition **20**: 899-909.

Donald, A. M., E. J. Kramer and R. A. Bubeck (1982). "The Entanglement Network And Craze Micromechanics In Glassy Polymers." Journal of Polymer Science: Polymer Physics Edition **20**: 1129-1141.

Ferry, J. D. (1980). Viscoelastic Properties of Polymers. New York, John Wiley & Sons.

Fischer, E. and J. F. Henderson (1969). "The Stress-Strain-Birefringence Properties Of Styrene-Butadiene Block Copolymers." Journal of Polymer Science Part C **26**: 149-160.

Folkes, M. J., A. Keller and F. P. Scalisi (1973). "An Extrusion Technique Of "Single-Crystals" Of Block Copolymers." Colloid and Polymer Science **251**(1): 1-4.

Fujimura, M., T. Hashimoto and H. Kawai (1978). "Structural Change Accompanied By Plastic-To-Rubber Transition Of Sbs Block Copolymers." Rubber Chemistry and Technology **51**: 215-224.

Grosse-Brauckmann, K. (1997). "On Gyroid Interfaces." Journal of Colloid and Interface Science **187**: 418-428.

Hadziioannou, G., A. Mathis and A. Skoulios (1979). "'Monocristoux' De Copolymeres Trisequences Styrene/Isoprene/Styrene Presentant La Structure Cylindrique: Ii. Etude De La Deformation Par Elongation." Colloid and Polymer Science **257**: 337-343.

Hajduk, D. A., P. E. Harper, S. M. Gruner, C. C. Honeker, E. L. Thomas and L. J. Fetters (1995). "A Reevaluation Of Bicontinuous Cubic Phases In Starblock Copolymers." Macromolecules **28**: 2570-2573.

Hashimoto, T., M. Fujimura, K. Saijo, H. Kawai, J. Diamant and M. Shen (1979). "Strain-Induced Plastic-To-Rubber Transition Of A Sbs Block Copolymer And Its Blend With Ps" in Multiphase Polymers. S. L. Cooper and G. M. Estes, ACS Advances in Chemistry Series: 257-275.

Henderson, J. F., K. H. Grundy and E. Fischer (1968). "Stress-Birefringence Properties Of S-I Block Copolymers." Journal of Polymer Science Part C **16**: 3121-3131.

Hendus, H., K.-H. Illers and E. Ropte (1966). "Strukturuntersuchungen An SBS Blockcopolymeren." Colloid and Polymer Science **216-217**: 110-119.

Holden, G., E. T. Bishop and N. R. Legge (1969). "Thermoplastic Elastomers." Journal of Polymer Science Part C **26**: 37-57.

Holden, G. and N. R. Legge (1996). "Styrenic Thermoplastic Elastomers" in Thermoplastic Elastomers. G. Holden, N. R. Legge, R. P. Quirk and H. E. Schroeder. New York, Hanser Publishers: 48-69.

Honeker, C. C. (1997). Large Strain Deformation Behavior of Oriented Triblock Copolymer Cylinders. PhD. thesis, Massachusetts Institute of Technology.

Honeker, C. C. and E. L. Thomas (1996). "Impact Of Morphological Orientation In Determining Mechanical Properties In Block Copolymers Systems." Chemistry of Materials **8**(8): 1702-1714.

Inoue, T., M. Moritani, T. Hashimoto and H. Kawai (1971). "Deformation Mechanism Of Elastomeric Block Copolymers Having Spherical Domains Of Hard Segments Under Uniaxial Tensile Stress." Macromolecules **4**: 500-507.

Kambour, R. P. (1964). "Structure And Properties Of Crazes In Polycarbonate And Other Glassy Polymers." Polymer **5**: 143-155.

Kambour, R. P. and A. S. Holik (1969). "Electron Microscopy Of Crazes In Glassy Polymers: Use Of Reinforcing Impregnants During Microtomy." Journal of Polymer Science A2 **7**: 1393-1403.

Kambour, R. P. and R. R. Russell (1971). "Electron Microscopy Of Crazes In Polystyrene And Rubber-Modified Polystyrene: Use Of Iodine-Sulphur Eutectic As A Craze Reinforcing Agent." Polymer **12**: 237-246.

Keller, A., E. Pedemonte and F. M. Willmouth (1970). "Macro-lattice from segregated amorphous phases of a three block copolymer." Nature **225**: 538-539.

Kinning, D. J., E. L. Thomas, D. B. Alward, L. J. Fetters and D. L. J. Handlin (1986). "Sharpness Of The Functionality Induced Structural Transition In Poly(Styrene-Isoprene) Star Block Copolymers." Macromolecules **19**: 1288-1290.

Kraus, G., C. W. Childers and J. T. Gruver (1967). "Properties Of Random And Block Copolymers Of Butadiene And Styrene. I. Dynamic Properties And Glassy Transition Temperatures." J. Appl. Polym. Sci. **11**: 1581-1591.

Lauterwasser, B. D. and E. J. Kramer (1979). "Microscopic Mechanisms And Mechanics Of Craze Growth And Fracture." Philosophical Magazine A **39**: 469-495.

Livigni, R. A., L. Marker, G. Shkapenko and S. L. Aggarwal (1967). Structure and Transition Behavior of Isoprene-Styrene Copolymers of Different Sequence Length. American Chemical Society Symposium on Structure and Properties of Elastomers, Montreal, Canada.

McClintock, F. A. and A. S. Argon (1966). Mechanical Behavior of Materials. Reading, MA, Addison-Wesley.

Molau, G. E. (1970). "Colloidal And Morphological Behavior Of Block And Graft Copolymers" in Block Polymers. S. L. Aggarwal. New York, Plenum Press: 79-106.

Morton, M. (1983). "Structure-Property Relations In Amorphous And Crystallizable Aba Triblock Copolymers." Rubber Chemistry and Technology **56**: 1096-1110.

Morton, M., J. E. McGrath and P. C. Juliano (1969). "Structure-Property Relationships For Styrene-Diene Thermoplastic Elastomers." J. Polym. Sci. Part C **26**: 99-115.

Odell, J. A. and A. Keller (1977). "Deformation Behavior Of An Sbs Copolymer." Polymer Engineering and Science **17**(1): 544-559.

Pakula, T., K. Saijo, H. Kawai and T. Hashimoto (1985). "Deformation behavior of SBS triblock copolymer with cylindrical morphology." Macromolecules **18**: 1294-1302.

Pedemonte, E. and G. C. Alfonso (1975). "The Morphology Of Sbs Three-Block Copolymers." Macro. **8**(1): 85-86.

Pedemonte, E., A. Turturro and G. Dondero (1974). "Correlation Between Morphology And Stress-Strain Properties Of Three Block Copolymers I. Stress-Softening Effect." British Polymer Journal **6**: 277-282.

Prasman, E. and E. L. Thomas (1998). "High-Strain Tensile Deformation Of A Sphere-Forming Triblock Copolymer/Mineral Oil Blend." Journal of Polymer Science, Part B: Polymer Physics **36**: 1625-1636.

Quirk, R. P. and M. Morton (1996). "Research On Anionic Triblock Copolymers" in Thermoplastic Elastomers. New York, Hanser Publishers: 72-100.

Richards, R. W. and G. Welsh (1995). "Deformation Of Matrix Macromolecules In A Uniaxially Extended Styrene-Isoprene-Styrene Linear Triblock Copolymer." European Polymer Journal **31**(12): 1197-1206.

Sakurai, S., J. Sakamoto, M. Shibayama and S. Nomura (1993). "Effects Of Microdomain Structures On The Molecular Orientation Of Sbs Triblock Copolymer." Macro. **26**: 3351-3356.

Schoen, A. H. (1970). Infinite periodic minimal surfaces without self intersections, NASA Technical Note TN D-5541.

Seguela, R. and J. Prud'homme (1981). "Deformation Mechanism Of Thermoplastic Two-Phase Elastomers Of Lamellar Morphology Having A High Volume Fraction Of Rubbery Microphase." Macromolecules **14**: 197-202.

Senyek, M. L. (1986). "Isoprene Polymers" in Encyclopedia of Polymer Science and Technology. H. F. Mark, M. Bikales, C. G. Overberger and G. Menges. New York, John Wiley & Sons. **8:** 487-564.

Smith, T. L. (1970). "Time-Dependent Mechanical Properties Of Elastomeric Block Polymers In Large Tensile Deformations" in Block Polymers. S. L. Aggarwal. New York, Plenum Press: 137-151.

Smith, T. L. and R. A. Dickie (1969). "Viscoelastic And Ultimate Tensile Properties Of Sbs Block Copolymers." Journal of Polymer Science Part C **26**: 163-187.

Tarasov, S. G., D. Y. Tsvankin and Y. K. Godovsky (1978). "The Structural Changes During The Deformation Of Oriented And Isotropic B-S Block Copolymers." Polymer Science USSR **20**: 1728-1739.

Thomas, E. L. and R. J. Albalak "Manuscript In Preparation." .

Ward, I. M. (1975). Mechanical Properties of Solid Polymers. New York, John Wiley & Sons.

Chapter 8: Predicting the <111> Modulus

As mentioned in chapter 7, the influence of both shear and flow produces highly oriented cylinders along the flow direction. Upon annealing, <111> directions of DG nucleate and grow from the cylinder axes. Although grains of DG may be misoriented around the flow axis, the <111> direction of the DG is nonetheless very reliably oriented along the flow direction. Hence some predictions can be made of the <111> modulus based on the structure of the DG in this direction.

Section 8.1 first predicts a relative <111> DG modulus based on that of cylinders. Because of the epitaxial relationship between the cylinder axes and the <111> direction of the DG and because the <111> DG direction contains the tightest-wound helices of continuous PS paths, the modulus of DG can be predicted from considerations of the geometries of the two in their analogous directions.

Section 8.2 predicts an absolute <111> DG modulus from beam bending theory, as well as from the geometry of the basic units of structure. As mentioned in section 2.7.2, Gibson and Ashby (1997) found that cellular materials consisting of interconnected struts deform elastically by bending of the struts. It was with the same Prof. Gibson in the Department of Materials Science and Engineering that these beam-bending approximations to the deformation behavior of DG in the <111> were developed.

8.1 Relative Modulus of DG Along <111> Versus Cylinders Along the Axis

8.1.1 General Case

The modulus of DG in the <111> direction can be reconciled with that observed in cylinders in the cylinder axial direction by a simple geometric argument. First, we shall take into consideration the reinforcing elements per cross-sectional area of each respective morphology in the directions of interest, and then we will consider the volume fraction of PS in each phase which contributes to the reinforcement.

Figures 8.1a and b show the cross-sections normal to the reinforcing directions of the cylinder and DG phases, respectively. This was shown in the chapter on roll cast morphology, the <111> direction of DG grows from the cylinder axis. Figure 8.1a shows a cross-sectional area normal to the axes of the cylinders. The hexagon is used to indicate the 6-fold symmetry of the non-primitive cell containing 3 cylinders -- each of the 6 corners of the hexagon contributes 1/3 of a cylinder to the hexagon, plus the cylinder in the center. Figure 8.1b shows a cross-sectional area normal to the <111> direction, i.e., the {111} plane of the DG. The hexagon shows the analogous area as covered by the hexagon in the

cylinder phase. Both hexagons have the same area in the case of epitaxial growth of DG from cylinders. The DG hexagon is also a non-primitive, translationally repetitive cell in the plane of 3-fold symmetry.

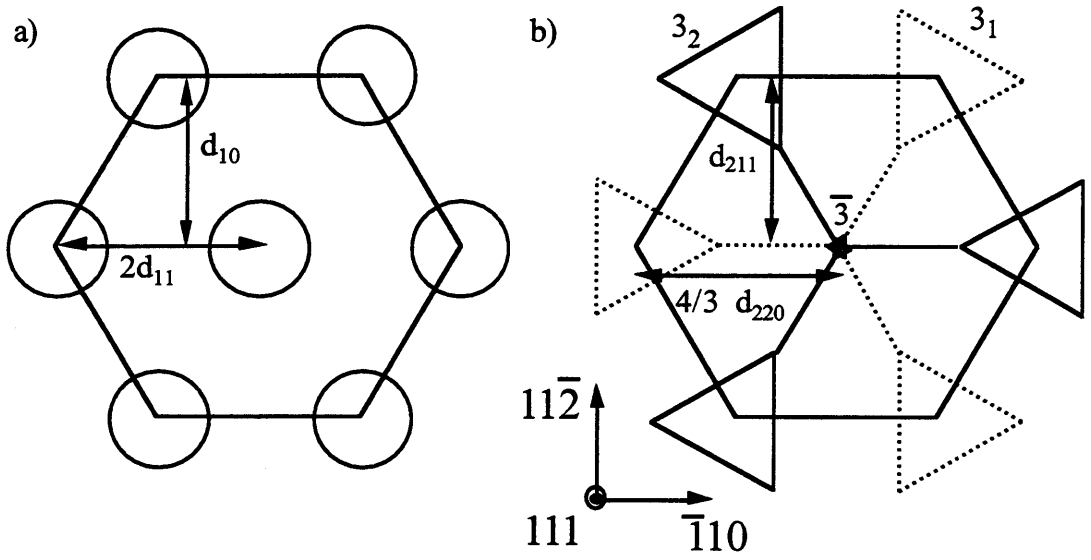

Figure 8.1: Cross-sectional area views of a) cylinders down the cylinder axes, and b) DG down the <111> direction. The area outlined in hexagons is analogous in both morphologies. The area of the cylinder hexagon with respect to cylinder spacings is $A = 6\, d_{11}\, d_{10}$, and the area of the DG hexagon with respect to DG spacings is $A = 4\, d_{220}\, d_{211}$.

In figure 8.1a three cylinders "belong" to the area covered by the hexagon: two complete cylinders from the 6 corners, and one cylinder from the center. In the transformation from the cylinder phase to the DG phase, the cylinder axes transform into connected struts along the 3_1 screw, 3_2 screw, and $\bar{3}$ axes of the DG, where only the struts along the 3_1 and 3_2 axes contribute to the reinforcing mechanical properties of the DG in the <111> direction. In figure 8.1b, only two complete 3-fold screw axes belong to the DG hexagon: one complete 3_1 and one complete 3_2 screw axis from alternating corners; the center cylinder is "replaced" in DG by a non-reinforcing $\bar{3}$ axis.

To understand why screw axes in the <111> direction are reinforcing and why the $\bar{3}$ axis is not, side views of the cylinder and DG <111> axes need to be examined. Figures 8.2a and 8.2b show the side views of the prisms having the hexagonal bases as shown in figures 8.1a and 8.1b, respectively. The cylinder phase has an arbitrary prism "height" assigned. As the cylinder phase is ideally infinite in the direction of the cylinder axis and hence has no periodicity. The DG prism, as drawn in figure 8.2b, spans 6 struts in the

<111> direction and has a height of $\sqrt{3}$ a, where "a" is the DG lattice parameter. On the corners of the prism sit 3_1 and 3_2 screw axes of alternating chirality, forming tight helices (likened to a stretched-out spring), each consisting of 6 struts, each being angled at 35° from the <111> axis, but connected to one another in the <111>.

Running through the center of the DG prism is the $\bar{3}$ axis, which consists of 4 nodes, alternating between the two chirality networks, stacked in the <111>. The nodal planes are perpendicular to the <111> axis and are not connected along the <111> direction. In fact, each node moves along the <111> according to the 3_1 or 3_2 helices to which they are connected when the material is deformed in the <111> direction. Hence the $\bar{3}$ axes do not contribute to the reinforcement of the <111> direction.

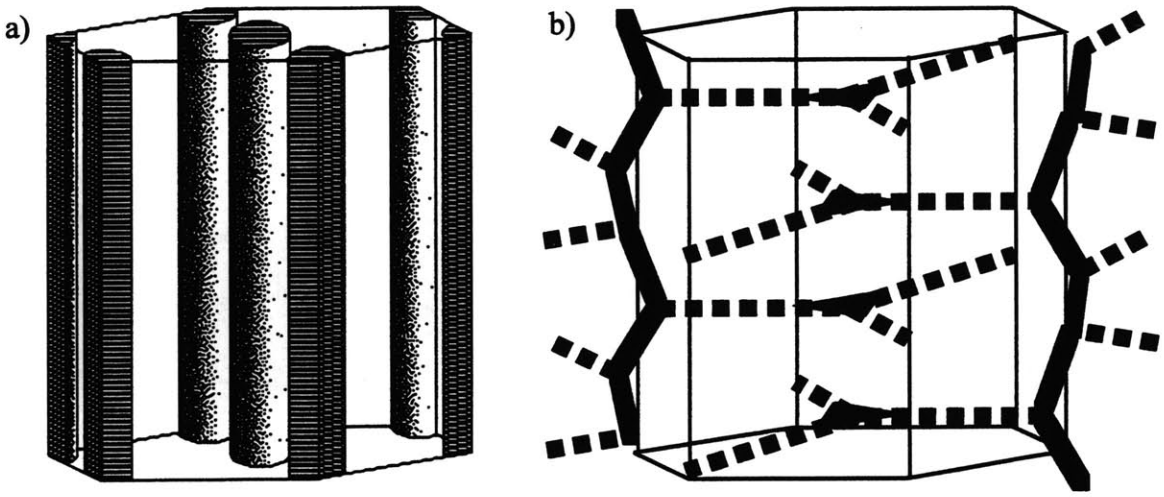

Figure 8.2. Prisms of the cylinder and DG phase with the hexagonal bases shown in figures 8.1a and 8.1b. a) The cylinder "prism". The cylinder phase has no periodicity in the direction along the axes such that the height of the "prism" can be defined arbitrarily. b) The DG prism is 6-struts deep in the <111> direction. The bolded lines indicate struts which contribute to the <111> modulus, and the dashed lines indicate struts which do not.

In figure 8.2a, the cylinder hexagon contains 3 reinforcing rods, but the DG hexagon in figure 8.2b contains 2 helices. Therefore, cylinders map onto DG helices in the <111> with only 66% efficiency. To a zeroth order approximation, the modulus of the DG should be 66% that of cylinders; i.e., the force is borne by the 3 cylinders per area of the hexagon in the case of cylinders, but by the 2 helices per area of the hexagon in the case of DG.

To find a more mathematical expression for the ratio of the moduli $\frac{E_{dg[111]}}{E_{cyl[001]}}$, let us consider a unit force applied over the area outlined by the hexagons in each case. The

modulus should scale as the number of reinforcing units per area. In cylinders, there are 3 reinforcing cylinders per hexagon of area 6 $d_{11}\ d_{10}$, whereas in DG, there are 2 reinforcing helices per hexagon of area 4 $d_{220}\ d_{211}$ such that

$$\frac{E_{dg\,[111]}}{E_{cyl\,[111]}} \propto \frac{\left(\frac{2}{4\ d_{220}\ d_{211}}\right)_{dg}}{\left(\frac{3}{6\ d_{11}\ d_{10}}\right)_{cyl}} = \frac{d_{11}\ d_{10}}{d_{220}\ d_{211}} \tag{8.1a}$$

Using the identities that $d_{11} = \frac{d_{10}}{\sqrt{3}}$ and $d_{220} = \frac{\sqrt{3}}{2} d_{211}$,(8.1a(can be simplified to

$$\frac{E_{dg\,[111]}}{E_{cyl[001]}} \propto \frac{2}{3}\left(\frac{d_{cyl\,10}}{d_{dg\,211}}\right)^2 \tag{8.1b}$$

For the special case in which the DG grows epitaxially from the cylinder phase,

$$d_{dg\,211} = d_{cyl\,10} \tag{8.2}$$

(Rançon and Charvolin) such that in (8.1b) the <111> modulus of DG can be predicted to be $\frac{2}{3}$ that of the [001] cylinder modulus.

For oriented cylinders, all of the volume fraction of the PS helps to carry the applied load along the cylinder axes. However, in oriented DG not all of the volume fraction of PS aids in strengthening the <111> direction. The <$\bar{1}$10> struts which are perpendicular to the <111> direction do not contribute to the <111> modulus. Hence the ratio of the moduli must be adjusted by a factor proportional to the volume fraction of PS actually used to strengthen the morphology in the force direction.

In order to assign the correct volume fraction of PS used to strengthen DG in the <111> direction, the fraction of struts which are in the <111> direction in a unit cell of DG needs to be determined. As shown in the prism of figure 8.2b, each helix centered on the corners of the hexagon has 6 struts in the <111> along the length of the prism. However, as only 1/3 of each helix "belongs" to the volume encompassed by the hexagon, there are

$$\left(\frac{1/3\ \text{helix}}{\text{corner}}\right)\left(6\ \frac{\text{struts}}{\text{helix}}\right)\left(6\ \frac{\text{corners}}{\text{hexagon prism}}\right) = 12\ \frac{\text{struts}}{\text{hexagon prism}}$$

which act in the reinforcement of the <111> direction. The $\bar{3}$ axis in the center of the prism consists of 4 nodes (of 3 struts each) which do not contribute to the reinforcement of the <111> direction. Within the volume of the prism are then

$$\left(\frac{4 \text{ nodes}}{\text{hexagon prism}}\right)\left(\frac{3 \text{ struts}}{\text{node}}\right) = 12 \text{ struts}$$

which do not act to reinforce the <111> direction.

In this unit cell volume (total volume is a^3, where a is the DG lattice parameter), there are a total of 24 struts, 12 of which contribute to the <111> modulus and 12 of which do not. Only 50% of the PS volume fraction actually contributes to the <111> modulus; equation (8.1b) is thus modified

$$\frac{E_{dg[111]}}{E_{cyl[10]}} = \frac{1}{3}\left(\frac{d_{cyl\,10}}{d_{dg\,211}}\right)^2\left(\frac{\phi_{dg\,ps}}{\phi_{cyl\,ps}}\right) \tag{8.1c}$$

This is a general expression to estimate the ratio of the moduli between a DG sample along the <111> and a cylinder sample along the [001] directions.

This simple model can be tested using experimentally measured properties of both roll cast DG and cylinders. The modulus of roll-cast cylinders stretched down the axis as reported by Honeker for a 29 wt. %S (26 vol. % PS, calculated using densities of $\rho_{PI} = 0.90$ g/cm^3 and $\rho_{PS} = 1.04$ g/cm^3) 15k-72k-15k SIS triblock copolymer is 120 MPa (Honeker, 1997), p244. The spacing of the (211) planes in the roll-cast 34%S (34 vol. % PS, 36 wt. % PS) 13.6k-46.4k-13.6k SIS triblock copolymer is approximately 250 Å. Using equation (8.1b) for a DG sample and a cylinder sample which are not related epitaxially, an estimate for the modulus of DG stretched in the <111> direction is

$$E_{dg\,[111]} = \frac{1}{3}\left(\frac{270\text{ Å}}{250\text{ Å}}\right)^2\left(\frac{0.33}{0.26}\right)(120\text{ MPa}) = 59\text{ MPa} \tag{8.1d}$$

The experimentally observed modulus of the roll-cast DG stretched along the <111> is 48±9 MPa. The predicted modulus is within the same order of magnitude and comes within 22% of the experimental value. This simple model has shown to be quite accurate in

its ability to predict the modulus of DG in the <111> direction based on properties of highly textured cylinders and DG.

8.2 Estimating an Absolute Modulus from Beam Theory

In this section, the modulus of DG will be predicted based on fundamental mechanics, in particular, on a cantilever beam analysis. We assume the struts to be circular in cross section. In the first analysis, we make simplifying assumptions of a constant diameter along the length and of a large length-to-diameter ratio, which allows us to consider only bending deflections, ignoring those due to axial and shear components. In the second analysis, we refine the strut model to take into account the variation of the strut diameter along the length of the strut, as well as axial and shear deflections accompanying a small length-to-diameter ratio of the struts.

8.2.1 General Cantilever Beam Bending

The maximum bending deflection, δ, of the end of a cantilever of length L having a material modulus E, from a force applied at the end, as shown in figure 8.3, can be described by the second-order differential,

$$\frac{d^2\delta}{dx^2} = -\frac{M(x)}{E\ I(x)} \tag{8.3}$$

where

$$M(x) = F(L-x) \tag{8.4}$$

is the moment felt by the cantilever at point x along the length due to the force applied at the end, and

$$I(x) = \frac{1}{4}\pi\ r(x)^4 \tag{8.5}$$

is the moment of inertia of the cross section at x having radius r(x).

For the case where we approximate the struts to have a uniform thickness throughout its length, I is a constant, and (8.3) can be easily solved. The deflection, δ, can then be described as

$$\delta = \frac{F\ L^3}{3\ E_s\ I}. \tag{8.6}$$

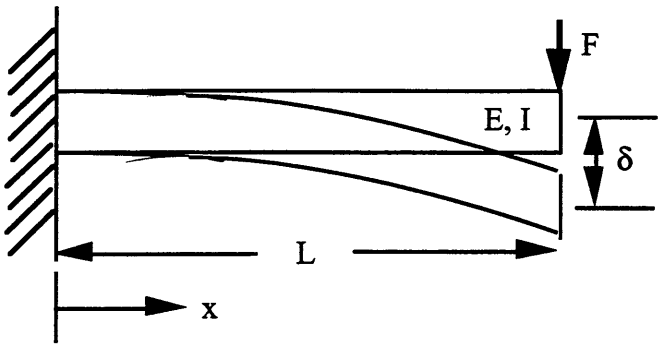

Figure 8.3. A schematic of a simple cantilever of length L, and material properties E and I, loaded with force F at the end. The maximum deflection occurs at the end and is given by equation (8.5).

A beam loaded at an angle θ, as shown in figure 8.4a, has components of axial and shear deflection as well as bending. Figure 8.4b shows the components of the force causing the various deflections. The bending deflection arises from the component F cos θ, which is normal to the strut or cantilever direction. The shear and axial deflections arise from the component F sin θ, which is in the direction of the strut. In particular, the deflections are given as

$$\delta_{bend} = \frac{(F \sin\theta) L^3}{3 E I} \tag{8.7a}$$

$$\delta_{axial} = \frac{(F \cos\theta) L}{A E} \tag{8.7b}$$

$$\delta_{shear} = \frac{(F \cos\theta) L}{A G}, \tag{8.7c}$$

where E is the Young's modulus, A is the cross-sectional area of the beam, and G is the shear modulus. For an isotropic material, the shear modulus is given by

$$G = \frac{E}{2(1+\nu)}$$

where ν is Poisson's ratio. For most materials, but not including rubbers, $\nu = \frac{1}{3}$, such that $G = \frac{3}{8}E$, and $\delta_{shear} = \frac{8}{3}\delta_{axial}$.

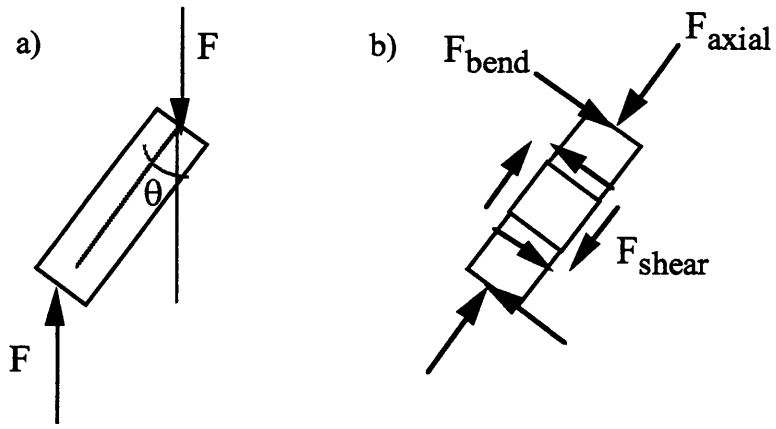

Figure 8.4 a) A beam loaded at an angle θ from the axis of the beam.
b) The forces can be resolved into the bending, axial, and shear components.

The ratios of the deflections for a rod with circular cross-section are given by

$$\frac{\delta_{axial}}{\delta_{bend}} = \frac{3}{4}\frac{r^2}{L^2}\frac{1}{\tan\theta} \tag{8.8}$$

and

$$\frac{\delta_{shear}}{\delta_{bend}} = 2\frac{r^2}{L^2}\frac{1}{\tan\theta}. \tag{8.9}$$

For typical bending geometries where $\theta = 90°$ (as in figure 8.3) and where the rod is long ($L >> r$), the deformation is dominated by bending. Hence, the axial and shear deflections can be neglected.

8.2.2 Application to Struts

8.2.2.1 Struts as Uniform Rods Deformed by Pure Bending

We will first generalize the strut to have a uniform diameter profile along the length of the rod. Figure 8.5a shows a DG helix in the <111> direction, and figure 8.5b shows a side view. In this simplified case, the force can be thought to be applied to the top of one strut, and the bottom of the same is fixed such that only the top end is allowed to deflect. The struts are also angled at 35° from the <111> axis, such that the force is applied at an angle, as is shown in figure 8.5c. As discussed in the previous section, all deflections exist: axial, shear, and bending, as described by (8.7a-c). However, we will make here

first the assumption that the deflection of the beam is dominated by bending, assuming L >> r .

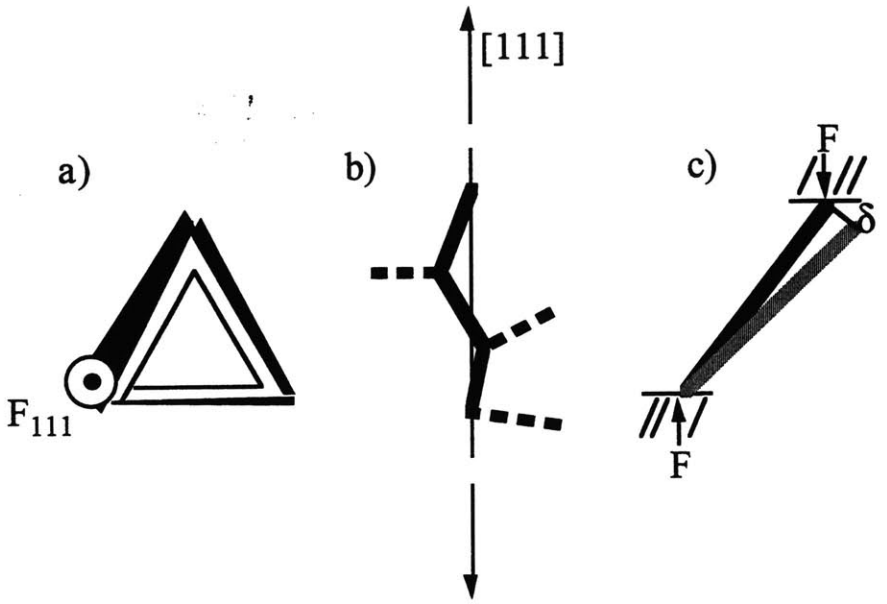

Figure 8.5: Simplified views of struts as sticks. a) A view down the <111> direction of a reinforcing helix comprised of struts angled at 35° to the <111> direction. b) A side view of the same. The bold lines denote struts which participate in strengthening the <111>, while the dashed lines indicate struts which do not. c) Loading conditions of a typical strut. The black strut denotes the original strut, whereas the grey strut denotes the deflected strut.

A beam fixed at both ends with one end allowed to deflect vertically is essentially two beams, each with length $\frac{L}{2}$, such that the total bending deflection of the beam with length L is

$$\delta_L = 2\,\frac{F\left(\frac{L}{2}\right)^3}{3\,E_s\,I} = \frac{F\,L^3}{12\,E_s\,I}\,. \tag{8.10}$$

For a cantilever which is angled at 35° to the force axis, the component of the force causing bending is F sin 35°, as illustrated in figure 8.6a, such that the resulting bending deflection is

$$\delta_L = \frac{F\,L^3}{12\,E_s\,I}\,\sin 35°\,. \tag{8.11}$$

Assuming that the struts have a circular cross-section, the moment of inertia, I, is given as

$$I = \frac{1}{4}\pi r^4, \tag{8.5b}$$

giving

$$\delta_L = \frac{F L^3}{3 \pi E_s r^4} \sin 35°. \tag{8.6b}$$

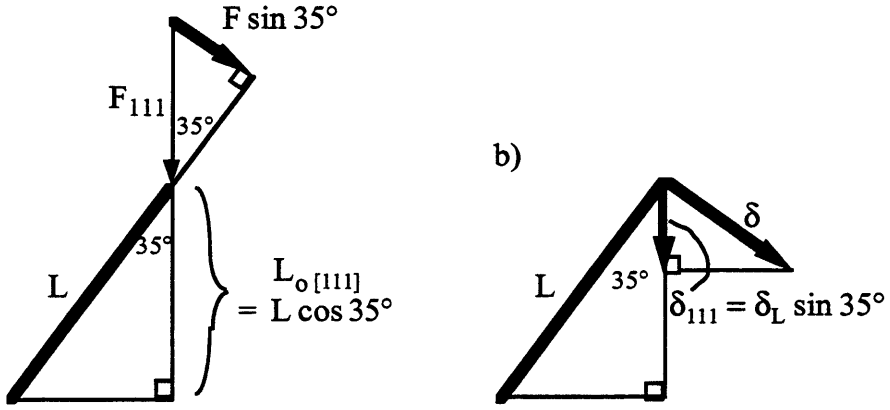

Figure 8.6: a) A schematic of a strut and the applied force. The strut is angled at 35° to the <111> (force) axis such that the bending component of the force (applied normal to the strut "cantilever") is $F_\perp = F \sin 35°$. The initial length of the strut in the <111> direction is $L_{O\,[111]} = L \cos 35°$.
b) A schematic of a strut and the bending deflection resulting from the force applied as in 8.6a. The component of the deflection in the <111> direction is $\delta_{111} = \delta_L \sin 35°$.

The strain $\varepsilon = \frac{\Delta L}{L_o}$ in the <111> direction is given as $\varepsilon = \frac{\delta_{111}}{L_{O\,[111]}}$, where δ_{111} is the deflection in the <111> direction, and $L_{O\,[111]}$ is the initial length of the strut in the <111>. From the relations of resolved length and deflection (as shown in figures 8.6a and 8.6b), $L_{O\,[111]} = L \cos 35°$ and $\delta_{111} = \delta_L \sin 35°$; combined with equation (8.6b),

$$\varepsilon = \frac{\delta_L \sin 35°}{L \cos 35°} = \frac{\delta_L}{L} \tan 35° = \frac{F L^2}{3 \pi E_s r^4} (\sin 35°)(\tan 35°) \tag{8.12}$$

The stress in the sample is $\frac{F}{A}$, where A is the area over which the force acts, which, in this case, is the area per reinforcing helix. We take the area as the area of the hexagon "belonging" to one helix instead of just the area that the polystyrene helix occupies. This area is given by the product of the total area of the hexagon and the area fraction of the PS, because the experimental modulus is found as the force over the entire area of a sample, and not just the smaller area which the <111> PS helices take up. As shown in the {111} projection of DG, there are 2 reinforcing helices per hexagon of area 4 $d_{220}\, d_{211}$. The area per reinforcing helix is hence 2 $d_{220}\, d_{211}$, and the stress is given as

$$\sigma = \frac{F}{A} = \frac{F}{2\, d_{220}\, d_{211}} \tag{8.13}$$

The modulus is given by

$$E = \frac{\sigma}{\varepsilon}$$

$$E = \frac{\left(\frac{F}{2\, d_{220}\, d_{211}}\right)}{\frac{F\, L^2}{3\, \pi\, E_s\, r^4}\,(\sin 35°)(\tan 35°)} = \frac{3\, \pi\, E_s\, r^4}{2\, d_{220}\, d_{211}\, L^2\,(\sin 35°)(\tan 35°)} \tag{8.14}$$

Using the relation that L = 3d = 6r for DG, the above equation can be rewritten

$$E = \frac{3\, \pi\, E_s\, L^2}{(2)(1296)\, d_{220}\, d_{211}\,(\sin 35°)(\tan 35°)} \tag{8.15}$$

From the observed roll-cast $d_{dg\ 211}$ = 250 Å, the lattice parameter, a, of a roll-cast sample is found to be 620 Å. Using the fact that the length of each strut is $\frac{\sqrt{2}\, a}{4}$, as shown in section 3.5, L = 220 Å. Using this result for L and the other observed quantities of d_{220} = 220 Å, d_{211} = 250 Å, and E_S = 3000 MPa (for PS), the predicted modulus is E = 23 MPa, which is 52% lower than the experimantally observed modulus. In the next section, the modulus of the strut and loading models are refined to take into account the factors which were disregarded in this initial estimate.

Incorporation of Strut Diameter Variation and Axial and Shear Deflections

Here, we will analyze the modulus problem taking into account the non-uniformity of the strut diameter with strut length based on TEMsim level set simulations of the DG surface and later incorporate axial and shear deformations into the estimate of the modulus.

Actual struts vary in radius along its length and the diameter = $\frac{L}{3}$ only at the center of the strut for the composition of DG at 34 vol. % PS (Grosse-Brauckmann, 1997). Figure 8.7 shows a trace of the level set approximation for the surface of a DG strut, simulated using the TEMsim program. Since the radius r(x) is a function of position along the length, the moment of inertia, I(x) is also function of position along the length, and equation 8.5 is no longer necessarily easily solvable.

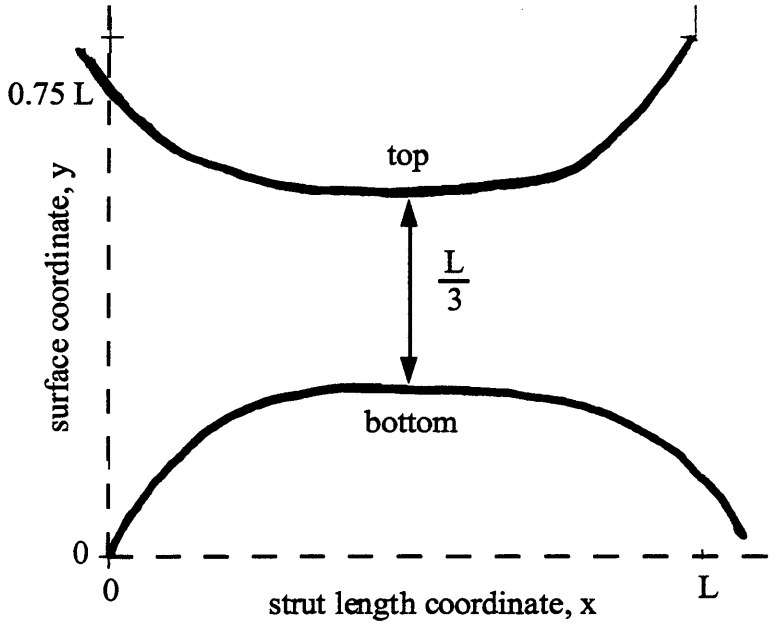

Figure 8.7: A sketch of the DG strut as drawn from a TEMsim DG (011) surface projection with t = ± 1.0 (corresponding to a DG triblock with volume fractions 17% PS - 66% PI - 17% PS, for a total 34 wt% PS). The x-axis is scaled such that the full length of the strut is L, and the y-axis is scaled such that the diameter of the center of the strut is L/3.

In order to take the variation of strut radius into account, r(x) was found by the following method: Unscannit ™ was used to assign coordinates along both the top and bottom surfaces of the strut, with the x-axis scaled such that the total length of the strut spans L and the y-axis scaled such that the diameter of the center of the strut spans L/3. The radius of the strut at a given length L_1 was found as half of the distance between the top and bottom surfaces, i.e.,

$$r@L_1 = \frac{top@L_1 - bottom@L_1}{2}.$$

The radius as a function of strut length is plotted in figure 8.8. A fourth-order polynomial,

$$r(x) = 0.39 - 1.59\,x + 4.31\,x^2 - 5.44\,x^3 + 2.72\,x^4 \qquad (8.16)$$

was found to be the lowest order polynomial having $R^2 > 0.999$. This best fit to the curve, as shown in figure 8.8, is hardly distinguishable from the r(x) data found from TEMsim.

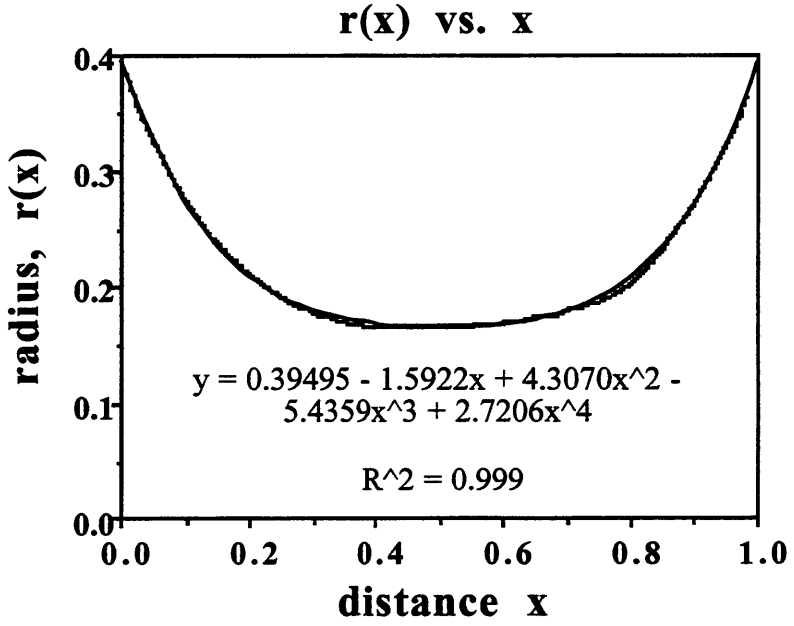

Figure 8.8: The r(x) (found from a trace of the TEMsim level set model) and 4th order polynomial fit for the radius of a DG strut as a function of strut length.

As before, the deflection δ will be considered for only half of the full strut length, and the full deflection will be taken as $\delta_t = 2\,\delta$. The moment of inertia I(x) was calculated as in (8.5b), and I(x) vs. x is plotted in figure 8.9a by using values found in figure 8.8. The bending moment M(x) is plotted in figure 8.9b.

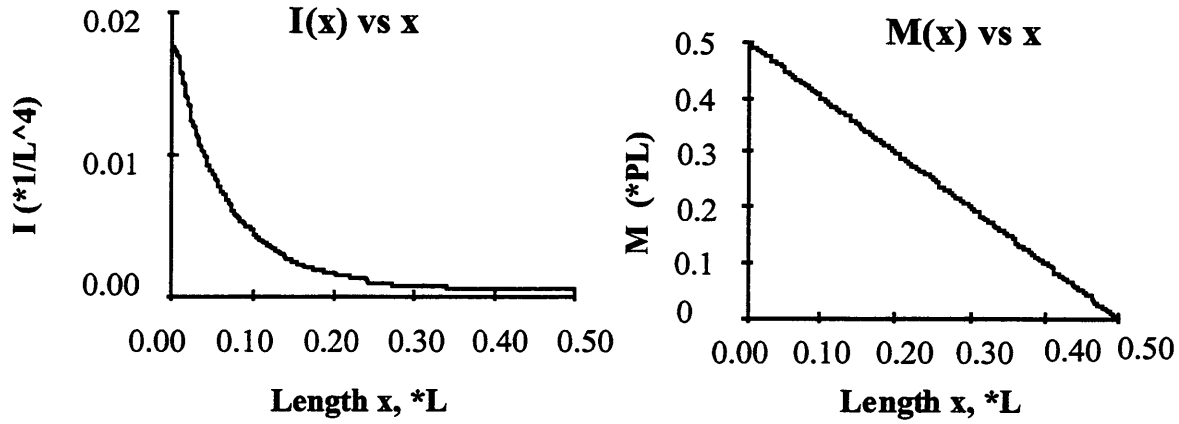

Figure 8.9: a) The moment of inertia I(x) is given as $I(x) = \frac{1}{4}\pi r(x)^4$, where r(x) varies with distance according to figure 8.8. The units of I scale as L^4 because r(x) is scaled with respect to the length of the cantilever, L. b) The bending moment M(x) is given as $M(x) = P\left(\frac{L}{2} - x\right)$.

Substituting in expressions for M(x) and I(x), (8.8) becomes

$$\frac{d^2\delta}{dx^2} = -\frac{M(x)}{E\,I(x)} = -\frac{P\left(\frac{L}{2} - x\right)}{E\left(\frac{1}{4}\pi r(x)^4\right)} \tag{8.17}$$

The equation for r(x) is a fourth-order polynomial; the $r(x)^4$ factor in the denominator hence expands out to include factors of x^{16}. Thus, both the art of finding a solution and the solution itself to (8.17) for the deflection are both mathematically and computationally rigorous. Therefore, an alternative graphical method of finding the deflection of the beam will be presented here.

The deflection of a cantilever can be determined graphically using the "moment-area method" (ref: Timoshenko, SP, Gere, JM, Mechanics of Materials, 4th Ed. 1997), ideally valid for a linear elastic material assuming shear deformations are negligible. The method is shown graphically for a simple cantilever of uniform thickness in figure 8.10. The deflection δ of a linear elastic material, assuming shear deformations are negligible, can be found as

$$\delta = \left(\begin{array}{c}\text{area under the} \\ \frac{M}{EI}\text{ vs length curve}\end{array}\right)\left(\begin{array}{c}\text{moment arm} \\ \text{from the centroid of the area} \\ \text{to the point of applied load}\end{array}\right). \tag{8.18}$$

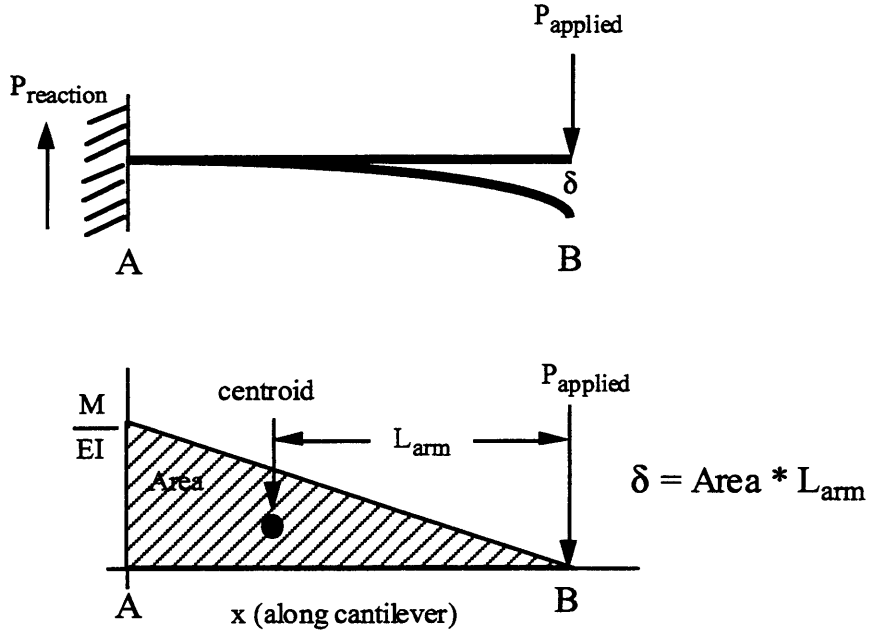

Figure 8.10: The moment-area method provides a graphical method for finding the deflection of a linear elastic beam from a force applied at the end of the beam. The deflection is given as the area under the (M / E I) curve (shaded) and the moment arm from the centroid of the area to the point of applied load.

Using the values found in figures 8.9 a and b and E_{PS} = 3000 MPa, M/EI was plotted as a function of distance along the cantilever, and is given in figure 8.11.

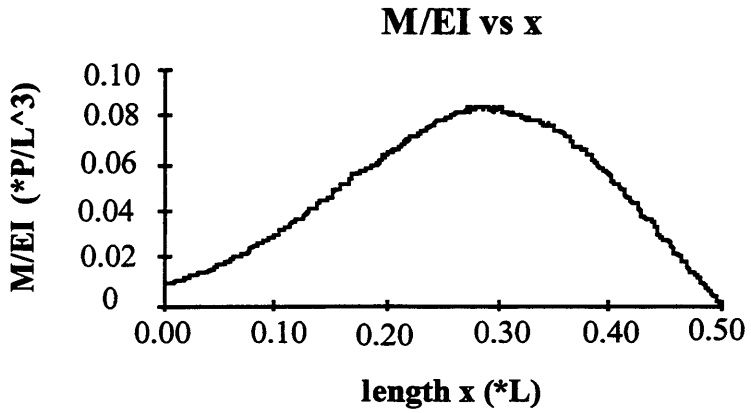

Figure 8.11: M/EI as a function of length along the cantilever, as plotted using values found in figures 8.9 a and b, and E_{PS} = 3000 MPa. r(x), I(x), and hence M/EI (x) are all scaled to units of length of the cantilever, L.

The M/EI vs. x curve was divided into intervals of $dx < 0.00074\ l$. The area of each interval, A_i was found by approximating the intervals as trapezoids such that $A_i = \frac{1}{2}(y_i + y_{i+1})(dx_i)$. The total area, $A = \sum_i A_i$, was found to be $A = 0.024 \frac{P}{L^2}$.

The x-coordinate of the centroid of the area, $\bar{x}$, was found using the definition

$$\bar{x} = \frac{\sum_i \bar{x}_i A_i}{\sum_i A_i},$$

where $\bar{x}_i$ is the centroid of the area A_i (the centroids $\bar{x}_i$ of the i-th interval were approximated to be half-way of the interval; i.e., at $\frac{x_i + x_{i+1}}{2}$). The centroid was found to be at $\bar{x} = 0.27\ L$, such that the moment arm from the centroid to the point of applied load is $L_{arm} = \frac{L}{2} - 0.27\ L = 0.23\ L$.

The deflection δ of the strut cantilever from a force applied normal to the cantilever beam is

$$\delta = \left(0.024 \frac{P}{L^2}\right)(0.23\ L) = 0.0056 \frac{P}{L} \tag{8.19}$$

Since the strut is actually at a 35° angle from the <111> direction, the component of the load which gives rise to a deflection is actually F sin 35° such that the deflection is

$$\delta = 0.0056 \frac{P}{L} \sin 35° = 0.0064 \frac{P}{L} \tag{8.19b}$$

Following a similar argument as given in the above section and using this new deflection, the better estimate for modulus of DG in the <111> direction is 96 MPa.

Assumptions in the Beam Theory Analysis

The following analysis assumes that the DG struts are approximated as cantilevers, hinged on both sides such that each half of a strut can be analyzed as a cantilever with the force applied at one end (i.e., the thinner end of the half). The cantilever boundary

condition is justified by the following argument: the struts flare out on both sides into a rather fat, thick node, as shown in figure 8.12.

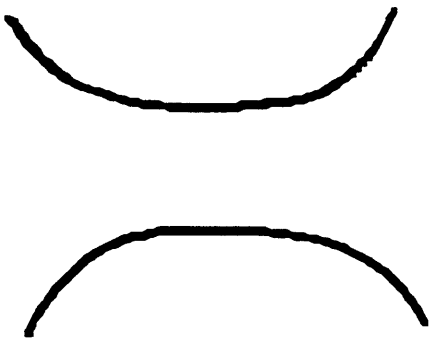

Figure 8.12: A schematic of a strut

Any deformation due to an applied load will be taken up at the thinner portion of the strut, away from the thicker nodal end. The nodal end of the strut can be considered to be firmly embedded in its position, as would the end of a cantilever attached to the wall, as shown in figures 8.13a-b.

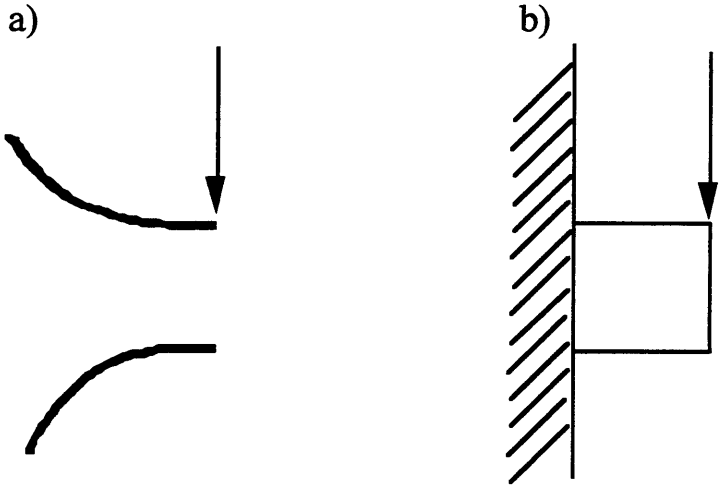

Figures 8.13 a-b: A strut can be modeled as a cantilever; the nodal end anchors the strut, and any deformation due to an applied load is taken up by the thinner end. Therefore, the strut can be approximated as a cantilever beam, with the force applied at the thinner portion.

This analysis is also based on the assumption that the main method of deformation is through bending of the DG struts/cantilevers. Axial and shear deformations also result from the applied force; in particular, the (F cos 55°) component of the force gives rise to

$$\delta_{axial} = \frac{(F\sin 55^\circ)L}{AE} \tag{8.20}$$

Observing that

$$\delta_{bend} = \frac{(F\cos 55^\circ)L^3}{3EI} = \frac{(F\cos 55^\circ)L^3}{3E(\frac{1}{4}\pi r^4)}, \tag{8.21}$$

δ_{axial} and δ_{shear} can be written in terms of δ_{bend} according to

$$\frac{\delta_{axial}}{\delta_{bend}} = \frac{\dfrac{(F\sin\theta)L}{AE}}{\dfrac{(F\cos\theta)L^3}{3EI}} = \frac{\dfrac{(F\sin 55^\circ)L}{AE}}{\dfrac{(F\cos 55^\circ)L^3}{3E(\frac{1}{4}\pi r^4)}} = \frac{3}{4}\left(\frac{r}{L}\right)^2 \tan 55^\circ \tag{8.22}$$

$$\frac{\delta_{shear}}{\delta_{bend}} = \frac{8}{3}\frac{\delta_{axial}}{\delta_{bend}} = 2\left(\frac{r}{L}\right)^2 \tan 55^\circ. \tag{8.23}$$

Taking the variation of $\frac{r}{L}$ versus x into account, $\frac{\delta_{axial}}{\delta_{bend}}$ was found graphically by plotting values of $\frac{3}{4}\left(\frac{r}{L}\right)^2 \tan 55^\circ$ versus x using the values of $\frac{r}{L}$ found in figure 8.8, and subsequently summing over the intervals Δx; i.e.,

$$\frac{\delta_{axial}}{\delta_{bend}} = \sum_{x=0}^{L} \frac{3}{4}\left(\frac{r(x)}{L}\right)^2 \tan 55^\circ(\Delta x) = 0.0548 \tag{8.24}$$

and

$$\frac{\delta_{shear}}{\delta_{bend}} = \frac{8}{3}\frac{\delta_{axial}}{\delta_{bend}} = 0.146. \tag{8.25}$$

The shear deformation is 15% of the bending deformation, and the axial deformation is only 5.5% of the bending deformation. Hence, the following conclusions can be made: the

main mode of deformation is by the bending of the struts and the moment-area method used to find δ_{bend} is also valid.

Using the value of δ_{bend}= 0.00640, and $\frac{F}{L}$ found from (8.18),

$$\delta_{axial} = 0.000350\frac{F}{L} \tag{8.26}$$

$$\delta_{shear} = 0.000935\frac{F}{L} \tag{8.27}$$

The total strain in the <111> direction is found as the sum of the contributions of the <111> components of the bend, axial, and shear deformations,

$$\varepsilon_{total} = \varepsilon_{bend} + \varepsilon_{axial} + \varepsilon_{shear} \tag{8.28}$$

The component of the bending deflection in the <111> direction is $\delta_{bend,111} = \delta_{bend}(\cos 55°)$, while the component of the axial and shear deflections are $\delta_{axial,111} = \delta_{axial}(\sin 55°)$ and $\delta_{shear,111} = \delta_{shear}(\sin 55°)$, respectively. The total strain is hence given by

$$\varepsilon_{total} = \frac{\Delta L}{L_0} = \frac{\delta_{total,111}}{L\sin 55°} = \frac{1}{L}\left[\frac{\delta_{bend,111}}{\tan 55°} + \delta_{axial} + \delta_{shear}\right] = 0.00576\frac{F}{L^2}\ . \tag{8.29}$$

A schematic representation of the axial, bending, and shear deflections is shown in figure 8.14. Using this new deflection, the better estimate for modulus of DG in the <111> direction is 75 MPa, which is a mere factor of 1.6 different than the observed modulus of 48 MPa. Again, the experimentally observed modulus is 48 MPa, only a factor of 2 less than the predicted; the predicted value is in the same order of magnitude as the observed. The fact that roll cast DG is not a perfect crystal and that inhomogeneities exist from the roll-casting process, the annealing process, sample handling, and tensile testing may account for the factor of 2.

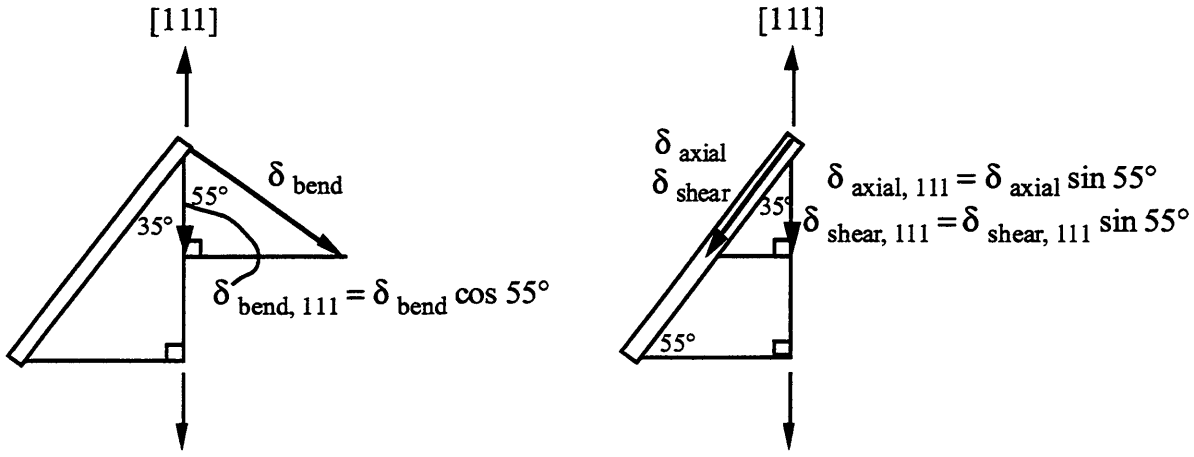

Figure 8.14: Representation of axial, bending, and shear deflections.

8.3 References

Gibson, L. J. and M. F. Ashby (1997). Cellular Solids. Cambridge, UK, Cambridge University Press.

Grosse-Brauckmann, K. (1997). "On Gyroid Interfaces." Journal of Colloid and Interface Science **187**: 418-428.

Honeker, C. C. (1997). Large Strain Deformation Behavior of Oriented Triblock Copolymer Cylinders. PhD. thesis, Massachusetts Institute of Technology.

Rançon, Y. and J. Charvolin (1988). "Epitaxial Relationships During Phase Transformations in a Lyotropic Liquid Crystal." Journal of Physical Chemistry **92**: 2646-2651.

Chapter 9: Conclusions and Future Outlook

9.1 Conclusions

The goals of the project were as follows: to obtain an elastomeric SIS triblock copolymer with a tricontinuous topologically connected cubic phase; to orient and form a textured sample; and to characterize the anisotropic deformation behavior via in-situ synchrotron SAXS, TEM, and tensile testing. A novel phase was expected to exist in the composition window of 33-37%S based on diblock copolymer phase diagrams. Therefore, two PI-rich (64 and 66 volume %) SIS triblock copolymers were obtained with typical molecular weights and compositions for commercial thermoplastic elasomers. The morphology was characterized by a combination of TEM, SAXS, TEMsim, laser diffraction and FFT's. Consideration of the first two peaks with q2/q1 = 1.155 from SAXS of these samples narrowed the possibilities to eight cubic space groups. Examination of the symmetries found in different TEM projections as well as observed connectivity of the morphology allowed identification of the sample as belonging to the Ia3d space group. Comparisons of the high -symmetry TEM images with simulated projections of level set DD and DG models resulted in positive identification of the DG phase.

Roll casting was then used to orient the materials. The 34%S SIS sample roll cast into cylinders while 36%S SIS roll cast into lamellae. The transition mechanism from cylinders to DG upon annealing is direct, whereas that from lamellae to DG involves a long-lived metastable state. Because of the ambiguity of the annealed morphology produced from roll cast lamellae, and because oriented DG samples were desired, only the roll cast 34%S SIS samples were used in subsequent experiments. The roll cast cylinder axes nucleated and grew into <111>-type DG directions. The final DG annealed morphology consists of {110} planes, twinned due to the degeneracy inherent in the 2-fold symmetry of the original cylindrical structures.

The mechanical properties and deformation microstructures were investigated via simultaneous load-deformation measurements and SAXS. Data were recorded as the samples were deformed to 600% strain in either the flow direction or transverse to the flow direction, that is along the [111] of the DG or perpedicular to it. The roll cast-annealled DG SAXS pattern is very rich, having high order reflections both in the roll cast direction and perpendicular to it. Upon deformation in the [111] direction, the sample has a sharp yield followed by necking. This necking behavior is accompanied by a loss of characteristic Bragg peaks, which are then replaced by a diffuse scattering pattern with two main streaks normal to the stretching direction. With unloading of the sample, Bragg features return but

approximately 100% residual strain remains in the material. Upon deformation in the transverse direction, the sample shows no distinct yield but rather exhibits a diffuse yield transition. Bragg peaks and Bragg streaks in the SAXS patterns of these samples persist, even to the maximum 600% strain. The residual strain upon unloading is much lower in this direction, showing only 20% hysteresis. When both types of samples are annealled, both the macroscopic (represented by sample dimensions) and microscopic (as indicated by SAXS) recovery is complete.

To correlate the diffraction patterns with real-space equivalents, deformed samples were irradiated with high energy electrons, microtomed, and then examined via TEM. Yielding in the [111] direction is accompanied by plastic deformation of the PS domains which form tightly wound helices alligned in this direction. During necking and higher strains, elongation and drawing of the PS domains occurs, with pullout of the PS endblocks at the highest loadings. Strain transverse to the [111] is accomodated by rotation of the domains into the stretch direction. Higher strains cause buckling of the continuous [111] PS helices, followed by cooperative rotation towards the stretch axis.

The high anisotropy of the DG morphology results in distinct differences in the mechanical properties of oriented samples in different directions. The modulus in the [111] direction is 5 times larger than in the transverse direction, and the material exhibits 50% higher mechanical hysteresis.

All these characteristics are due to the high PS connectivity in the flow direction, and no continuous PS domains in the transverse direction which leads to dramatic and significantly different deformation modes, SAXS characteristics, and TEM images during deformation.

9.2 Future Outlook

This section presents some of the possible projects or collaborations that could stem from either this thesis project or from the projects I started during my tenure with Prof. Thomas.

Dexco Collaboration

One of the main objectives for polymer engineers is to optimize molecular weight to be high enough for good entanglement and mechanical properties, yet low enough for ease of control over synthesis and processing. As reported in section 5.3, the Dexco company (an industrial producer of SIS thermoplastic elastomers) synthesized three SIS triblocks as a possible collaboration between the company and MIT in search of DG. However, the triblocks they synthesized had molecular weights too high for the DG phase to form. The 34% styrene SIS polymer from the University of Athens having molecular weight ~75

kg/mol, showed that when roll-cast and annealed, the highly-oriented double gyroid morphology is formed. This material shows a good balance between mechanical behavior and processability. A lower molecular weight material will not be as well entangled, while a higher molecular weight material may not exhibit the DG morphology, and at the same time, will be more difficult to process. To this date an industrial DG triblock has not yet been synthesized, though the desired composition and molecular weight is known. In collaboration with Dexco or another industrial producer, materials or products with novel mechanical properties can be made.

Elastic Constants of DG

As was discussed in section 2.8, the cubic DG structure has 3 independent elastic constants, which are, for example, S_{11}, S_{12}, and S_{44}. In section 7.1, the tensile moduli are given of DG in two orthogonal directions. Only the shear modulus remains to be measured in order to have three mechanical quantities available for extracting the elastic constants. The properties in shear can be found via torsion, which requires a cylindrical rod or plug of oriented material. Because none of the original two grams of 13.6/46.4/13.6 kg/mol SIS material remains, the challenges are to have more material synthesized (which may be remedied if Dexco were able to supply a kilogram) and to orient the material such that a rod or a plug sample geometry can be made. However, by overcoming these challenges, the reward would be great, since two of three mechanical measurements required have already been made in this thesis. With knowledge of all three elastic constants, quantitative predictions of the mechanical behavior in any given direction can be made.

Phase Behavior of the Triblock DG

Theoretically predicting the phase behavior of triblock copolymers, especially in the composition window of the novel phases, would be both scientifically and commercially important. Currently the only theoretical phase diagrams which include the novel phases for block copolymer systems are for diblock and starblock copolymers (Matsen and Schick, 1994). The last theoretical predictions for phase behavior of triblock copolymers were done in 1989, before the novel phases were found (Mayes and Olvera de la Cruz, 1989). Figure 5.17 of this thesis contains molecular weight-composition-phase information for the symmetric triblock copolymer materials used in this thesis to map out roughly where DG is observed. Because triblock copolymers are industrially mainstays, it would be commercially beneficial to be able to predict the phase behavior of the block copolymers based on composition and molecular weight.

Doublet Issue

It also remains to be elucidated the issue surrounding the inner peak of the equatorial doublet in roll cast materials. This phenomenon is noticed in both DG and in cylinders, as seen in section 6.3 and in Christian Honeker's thesis (chapter 8). These peaks correspond to structures whose spacing is larger than that of the largest interlayer spacings inherent in the materials and is presumably associated with the roll casting process.

Morphology of Roll Cast Annealed 36 and/or the Mechanical Properties of the HPL Phase

The HPL phase has been observed to be a long-lived metastable phase in soft condensed matter in transit from equilibrium lamellar to DG phases. There may be applications in which the metastable phase would be kinetically hindered from transforming to the equilibrium one for the lifetime of the application or product. Therefore, it may be interesting to investigate the properties of the HPL phase, such as the end conditions for stability in high molecular weight materials, orientation behavior, and mechanical properties, especially compared to those of lamellae and DG.

Behavior of Roll Casting Conditions on the Orientation Behavior of the DG Phase

It has been found that roll cast cylinders and lamellae can have different orientations depending on the processing conditions. Because the DG is such a complex structure and because different orientations of its cylinder and lamellar precursors can be achieved by fine tuning the roll cast conditions, the orientation behavior of DG roll cast with different conditions can be studied.

Mineral Oil Blends

It would be interesting on an industrial standpoint to study triblock copolymer - mineral oil blends. Mineral oil is generally an undesirable by-product of the refining process, but by using it as an additive, it can not only lower the neat block polymer materials costs but also put an unwanted material to good use. There have been already some morphology and mechanical properties studies on various block copolymer systems with mineral oil (Ceausescu, Bordieanu, Ghioca, Cerchez, Buzdugan, and Stancu, 1983,1984; Polizzi, Stribeck, and Zachmann, 1988, 1989; Stribeck, Boesecke, and Polizzi, 1989; Flosenzier and Torkelson, 1992; Prasman, 1997; Prasman and Thomas,

1998). In our lab, mineral oil blend samples having DG morphology have been made, but the roll casting parameters need to be fine tuned in order to produce good films. Ideally these films would not have to be temperature annealed because the mineral oil reduces the entanglement density enough to provide mobility for the struts and domains. Preliminary studies of stretches of isotropic polygranular mineral oil blends having DG morphology show that their stress-strain behavior depends on the morphology. However, it would be interesting to study how oriented mineral oil filled DG deforms and the effect of osmotic pressures exerted by the PS struts on the mineral oil due to Poisson effects when the DG is stretched.

High Temperature Stretching

The mini-stretcher was modified to include high temperature capabilities such that stretching of block copolymers above their Tg could be carried out. A preliminary in-situ SAXS high temperature stretching experiment was conducted on cylinder materials at 85°C. Some problems that need to be overcome are the inability of the load cell to read the load at high temperature and the inability of the temperature box to withstand higher than 130°C temperatures (polycarbonate box). Once these difficulties are resolved, it becomes possible to monitor the response and interactions of the two phases as they transition through the Tg's of the components while simultaneously undergoing deformation. In particular, the mechanisms of deformation will be less viscoelastic at high temperatures such that the pullout and recovery behavior of the material could be quite different than that seen below Tg.

Finite Element Modeling of the Deformation of Block Copolymer Morphologies

Finite element modelling (FEM) of the deformation behavior of block copolymers is ripe for study, since the deformation behavior of all of the equilibrium block copolymer morphologies, oriented and textured, have been studied. FEM can be a powerful tool to gain insight into the mechanisms of deformation behavior. From FEM simulations, effects of defects, grain boundaries, and different orientations of the microstructure on the deformation behavior can be modelled. As the simplest problem, two-dimensional meshes can be written for approximations of the classical phases. More complex geometries, such as 3-dimensional representations with included defects, can then be modelled and the results compared with the experimental data. The novel DG phase can first be approximated in 2D by meshing out two-dimensional co-continuous phases. A bigger

challenge (perhaps worthy of a thesis in itself), however, is the meshing of the complex surface of the three-dimensional DG morphology.

Ultimate Tensile Properties

Many studies have been done on ultimate tensile properties of the classical block copolymer morphologies, and this is a general engineering quantity of interest. However, ultimate tensile properties are statistical in nature, requiring many tests (and hence much polymer) for statistically significant values. Strains-at-break depend on many factors, such as rate, grip method, impurities and defects. Therefore, once substantial quantities of triblocks in the composition range for DG have been obtained, the tensile properties can be determined.

9.3 References

Ceausescu, E., R. Bordeianu, P. Ghioca, E. Buzdugan, R. Stancu and I. Cerchez (1984). "Dilute Block Copolymer Systems. Properties Of Oil-Extended Butadiene-Styrene Block Copolymers." Pure & Applied Chemistry **56**(3): 319-328.

Ceausescu, E., R. Bordeianu, P. Ghioca, I. Cerchez, E. Buzdugan and R. Stancu (1983). "Dilute Block Copolymer Systems Ii. Tensile Modulus Of Oil-Extended Butadiene-Styrene Block Copolymers At Large Strains." Revue Roumaine de Chimie **28**(4): 299-323.

Flosenzier, L. S. and J. M. Torkelson (1992). "Influence Of Molecular Weight And Composition Of The Morphology And Mechanical Properties Of Sbs-Polystyrene-Mineral Oil Blends." Macro **25**: 735-742.

Matsen, M. W. and M. Schick (1994). "Microphase Separation In Starblock Copolymer Melts." Macromolecules **27**: 6761-6767.

Mayes, A. M. and M. Olvera de la Cruz (1989). "Microphase Separation In Multiblock Copolymer Melts." Journal of Chemical Physics **91**(11): 7228-7235.

Polizzi, S., N. Stribeck and H. G. Zachmann (1988). "Structure And Properties Of Oil Extended Styrene Butadiene Block Copolymers." Polymer Composites **9**(6): 434-442.

Polizzi, S., N. Stribeck, H. G. Zachmann and B. R. (1989). "Morphological Changes In Sbs Block Copolymers Caused By Oil Extension As Determined By Absolute Small Angle X-Ray Scattering." Colloid and Polymer Science **267**(4): 281-291.

Prasman, E. (1997). Morphology and mechanical behavior of oriented blends of styrene - isoprene - styrene triblock copolymer and mineral oil. Masters thesis, Massachusetts Institute of Technology.

Prasman, E. and E. L. Thomas (1998). "High-Strain Tensile Deformation Of A Sphere-Forming Triblock Copolymer/Mineral Oil Blend." Journal of Polymer Science, Part B: Polymer Physics **36**: 1625-1636.

Stribeck, N., P. Boesecke and S. Polizzi (1989). "Saxs Investigation On The Influence Of Oil Dilution On Morphological Changes In A Sbs Block Copolymer During The First Draw Cycle." Colloid & Polym. Sci. **267**: 687-701.